FINAL TECHNICAL REPORT

DEVELOPMENT OF EARTHQUAKE GROUND SHAKING HAZARD MAPS FOR THE YELLOWSTONE-JACKSON HOLE-STAR VALLEY, WYOMING

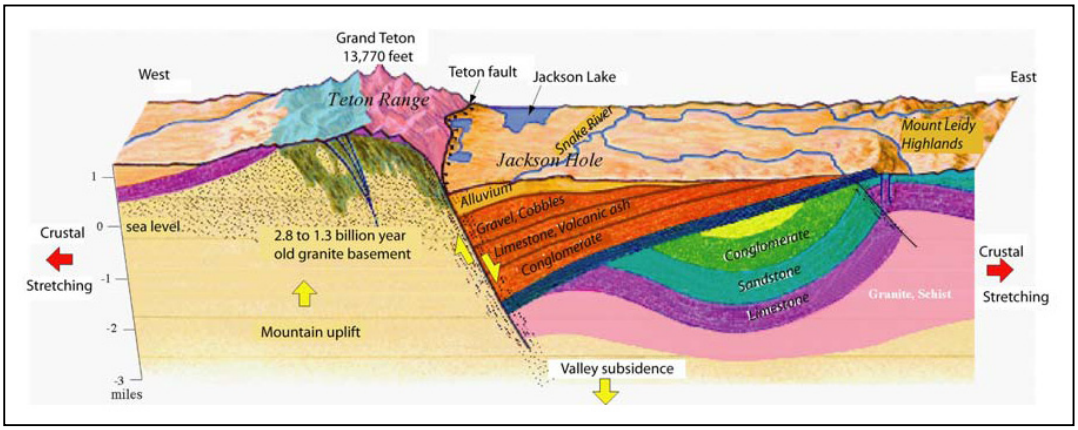

Submitted to the

U.S. Geological Survey

Under the National Earthquake Hazards Reduction Program

Program Element II Evaluate Urban Hazard and Risk

USGS Award 05HQGR0026

Prepared by

Bonnie Jean Pickering White

Department of Geology and Geophysics
The University of Utah
Salt Lake City, UT 94112

and

Robert B. Smith

Department of Geology and Geophysics
The University of Utah
Salt Lake City, UT 94112

Principal Investigator

Ivan Wong

Seismic Hazards Group
URS Corporation
1333 Broadway, Suite 800, Oakland, CA 94612
Phone: (510) 874-3014, Fax: (510) 874-3268
E-mail: ivan_wong@urscorp.com

26 September 2006

This research was supported by the U. S. Geological Survey (USGS), Department of the Interior, under USGS Award Number 05HQGR0026. The views and conclusions contained in this document are those of the authors and should not be interpreted as necessarily representing the official policies, either expressed or implied of the U.S. Government.

PREFACE

The Yellowstone-Jackson Hole-Star Valley corridor is located within the seismically and tectonically active Intermountain Seismic Belt in westernmost Wyoming and eastern Idaho. The corridor has the highest seismic hazard in the Intermountain U.S. based on the U.S. Geological Survey's National Hazard Maps. The region contains the heavily visited Yellowstone and Teton National Parks and the rapidly growing areas of Jackson Hole and Star Valley. Although there has only been one large earthquake in this region in historical times (1959 moment magnitude [**M**] 7.5 Hebgen Lake), abundant geologic evidence exists for the past occurrence of surface-faulting earthquakes of **M** 7 or greater. In addition, background seismicity not associated with known faults and whose maximum magnitude is about **M** 6½ is relatively abundant within this portion of the Intermountain Seismic Belt and must be considered in seismic hazard evaluations.

A Project Team of URS Corporation, the University of Utah, the U.S. Geological Survey (USGS), and Pacific Engineering & Analysis has proposed to develop a series of 12 deterministic earthquake scenario and probabilistic ground shaking maps for the Yellowstone-Jackson Hole-Star Valley corridor. Ground motions will be estimated based on the most up-to-date information on seismic sources, crustal attenuation and near-surface geology. Given the location of the corridor adjacent to major faults such as the Teton and Grand Valley faults, seismic hazard evaluations need to not only consider the hazards from numerous seismic sources, but also address the near-source effects on ground motions such as hanging wall and rupture directivity effects, as well as soil amplification effects.

In December 2004, URS and the University of Utah received funding to support an initial task of the whole project, the analysis of the Jackson Lake seismographic data. The work was performed by Ms. Bonnie Jean Pickering White, a graduate student in the Department of Geology and Geophysics at the University of Utah. She was supervised by Dr. Robert Smith.

The enclosed Master of Science Thesis by Ms. Pickering White describes the analysis of the Jackson Lake network as well as additional analyses of the seismotectonic setting of the Teton region.

SEISMICITY, SEISMOTECTONICS AND PRELIMINARY EARTHQUAKE HAZARD ANALYSIS OF THE TETON REGION, WYOMING

by

Bonnie Jean Pickering White

A thesis submitted to the faculty of
The University of Utah
in partial fulfillment of the requirements for the degree of

Master of Science

in

Geophysics

Department of Geology and Geophysics

The University of Utah

August 2006

ABSTRACT

The U.S. Bureau of Reclamation (BoR) released their recorded earthquakes in the Teton region from 1986 to 2002 that focused on the seismic safety of Jackson Lake dam. The historic seismically quiescent Teton fault zone was the main focus of the seismic monitoring, but the data provided broad coverage of the general Teton Range, Jackson Hole and surrounding areas. The main objectives of this study were to generate an accurate hypocenter and magnitude list of regional earthquakes, analyze tomographic imaging to determine a three-dimensional P-wave velocity model, and integrate these data with GPS measurements of ground motion to better understand the seismotectonics of the Teton Region. These data provide key information for the seismic hazard analysis of the area. Seismicity was recorded on up to 20 short-period and 5 broadband seismographs focusing on the effects of earthquake hazards of the BoR operated Jackson Lake, Palisades and Grassley Lake dams. Data available for the study included seismic station coordinates, P-wave picked arrival times, and hypocenters of 8,000+ earthquakes located by a one-dimensional velocity model from 1986 to 2002 of magnitude $0.1 < M < 4.7$. The P-wave data that initially had been determined by automated first arrival picks were repicked manually with an average picking error of < 0.12s for 10% of all the events including $M > 2.0$. This data quality check was vital to ascertain that the uncertainties were acceptable for the tomographic algorithm. The P-wave arrival time data were then used to produce a new catalog of 8,537 precisely located earthquakes with

hypocenter location uncertainties using a nonlinear probabilistic method and tomography-determined three-dimensional velocity model. Hypocenter residuals in time were improved by 59%. The resulting stress-field orientations derived from accurate focal mechanisms revealed dominantly east-west extension across the Teton fault with a northeast-southwest stress orientation along the northern Teton fault area and southern Yellowstone region. We noted that there was no correlation of hypocenters with the down dip projection of the Teton fault. On the other hand, ground deformation data from GPS and leveling data revealed an unexpected result suggesting a reverse loading of east-west compression in the vicinity of on the Teton fault. Combined results from the 1987-2003 campaign GPS surveys, showed an average valley floor uplift of ~0.5-1.5 mm/yr and a valley floor west motion of ~1 mm/yr with respect to the mountain block. These observations may reveal a cause of the seismic quiescence of the Teton fault compared to its Late Quaternary fault loading rate ~2-3 mm/yr. The three-dimensional tomography image revealed two notable large low velocity zones at 0 km (sea level) to 5 km depth, centered beneath the Jackson Lake dam and beneath the southern end of Jackson Hole. P-wave velocities of 4.2 km/s to 4.6 km/s correlate with low gravity anomalies of -245 mgal centered near the Jackson Lake Dam and -225 mgals located near the town of Jackson, WY. The combination of the accurate hypocenter and accurate magnitudes along with the seismotectonic analysis helped to refine location and geometry of the background seismicity as key input for a probabilistic earthquake hazards analysis. The preliminary probabilistic seismic hazard analysis was conducted for four sites in the Jackson Hole valley along with regional hazard maps for the greater Teton and Yellowstone area. Preliminary results show the largest peak ground acceleration hazard

is located around the Teton fault due to its large average 1.3 mm/yr slip rate, which is the largest slip rate in the greater Teton and Yellowstone region.

TABLE OF CONTENTS

LIST OF FIGURES

Figure

LIST OF TABLES

Table

ACKNOWLEDGEMENTS

I am first and foremost indebted to the undying support, patience, and love of my family: John David and Nancy Pickering, John Pickering Jr., and my wonderful husband Travis White. Their wisdom and strength were the rock that supported and carried me during the long hours I spent working in the office and writing continuously at home. They kept me motivated and always provided a much needed laugh when life was becoming too serious. Without my family the goal of obtaining my Masters would have been an empty accomplishment.

There are very special individuals who deserve recognition with regard to my studies of the Teton fault and completion of my Masters in geophysics. Most notably is Dr. Robert B. Smith. He has been instrumental in providing guidance, facilitating access to the Bureau of Reclamation's Teton Seismic data set, and aid in the funding of this research. Dr. Smith has provided a wealth of knowledge, insight, and affection for the Tetons and I am humbled that he has allowed me to work and learn from him for the past three years. I must also say working with Dr. Smith has allowed multiple opportunities to be presented to me, and I will be forever in his debt.

Dr. Stephan Husen has also been instrumental in the completion of this research. I can truly say that without his help, support, and guidance this research would have never been completed. His insight and advice on generating velocity models and working with various earthquake relocation methods has been superior and greatly

appreciated. I also must add that he did not allow me to simply go through the motions of earthquake relocation, and instead always made me stop and think first about the importance and meaning of each step. Learning from Dr. Husen has definitely made a memorable mark on my life, and he is certainly a mentor I will always admire.

Dr. Ron Bruhn also provided valuable insight and advice on analysis of normal fault geometry and structural mechanics of the greater Teton region. He helped to ground-truth to some of the observations of the geophysical models with geologic observations. Ivan Wong also gave support and insight in the completion of this research. He brought the realization of the importance of the relocated earthquake catalog to the completion of the Probabilistic Seismic Hazard Analysis, which he will continue on with after my work is done. Dr. Jim Pechmann has also provided guidance in matters of magnitude calibration, and has always provided an open door for me to ask any questions. I must also recognize the guidance I received from Dr. Greg Waite on focal mechanisms and inverting them for stress field orientations. I also want to thank Charlotte Rowe, Art Sylvester, Tim Ahern, Norm Abrahamson and Nick Gregor for their help with the cross correlation codes, leveling line data, P-wave data formatting, and probabilistic seismic hazard codes.

My research has benefited greatly from the cooperation with the U.S. Bureau of Reclamation in Denver, CO. Chris Wood, Dan O'Connell, and Lisa Block were instrumental in the aiding of providing the earthquake data recorded by the Jackson Lake Seismic Network operated by the Bureau of Reclamation from 1986-2002. Their support and excellent work operating and picking first arrivals of seismic events in the Tetons is much appreciated.

I must also thank my fellow graduate students who aided me in my research and insured my survival in graduate school as a happy experience. To all of my office-mates; Greg Waite, Michael Jordan, Christine Puskas, Wu-Lung Chan, Aaron DeNosaquo, Katrina Settles, and Jamie Farrell, I must say all of you made coming to school every day more enjoyable.

I appreciate the support of my graduate program by a Fellowship and teaching award of the University of Utah Department of Geology and Geophysics. My research was funded by in part by the USGS NEHRP #05HQGR0026, and by Yellowstone research foundation funds of Dr. Robert B. Smith with computation support by the University of Utah.

CHAPTER 1

INTRODUCTION

The Teton Range is a youthful normal-fault bounded mountain block in the western United States that is located near the intersection of the Basin Range, Idaho-Wyoming thrust belt, Rocky Mountain foreland, and Snake River Plain-Yellowstone tectonic provinces in northwestern Wyoming (Figure 1.1). It is one of the easternmost and youngest faults of the Basin-Range with the stable Laramide uplifts and an overthrust belt to the east. The seismotectonics of the Teton Range and its historic seismic quiescence, above M 3.0 along the Teton fault, has suggested theories as to the stability of the region and the possibility of a large future earthquake occurring on the Teton fault.

The greater study region consists of the Teton Range, the valley of Jackson Hole, southern Yellowstone and the northern Star Valley area. This region forms an important part of the Intermountain Seismic Belt, extending southward 130 km from the Yellowstone volcanic system to the northern Star Valley area of Wyoming and Idaho.

The Teton fault bounds the east side of the Teton Range and is a typical major Basin-Range normal fault that extends 55 km north-south (Figure 1.2). On the basis of its length, this structure has been considered capable of generating a maximum credible earthquake of M_L 7.5 or M_w 7.3 [*Gilbert et al.,* 1983]. The historic seismic record, however, suggests that the Teton fault is seismically quiescent and occupies a notable

Figure 1.1. Western U.S. tectonic provinces and study area location. The Teton Range and study area for this research is located in the western United States in northwestern Wyoming, near the intersection of the Basin Range, Idaho-Wyoming thrust belt, Rocky Mountain foreland, and Yellowstone-Snake River Plain (YSRP) tectonic provinces. The study area is marked in blue outlining the Grand Teton and Yellowstone National Parks.

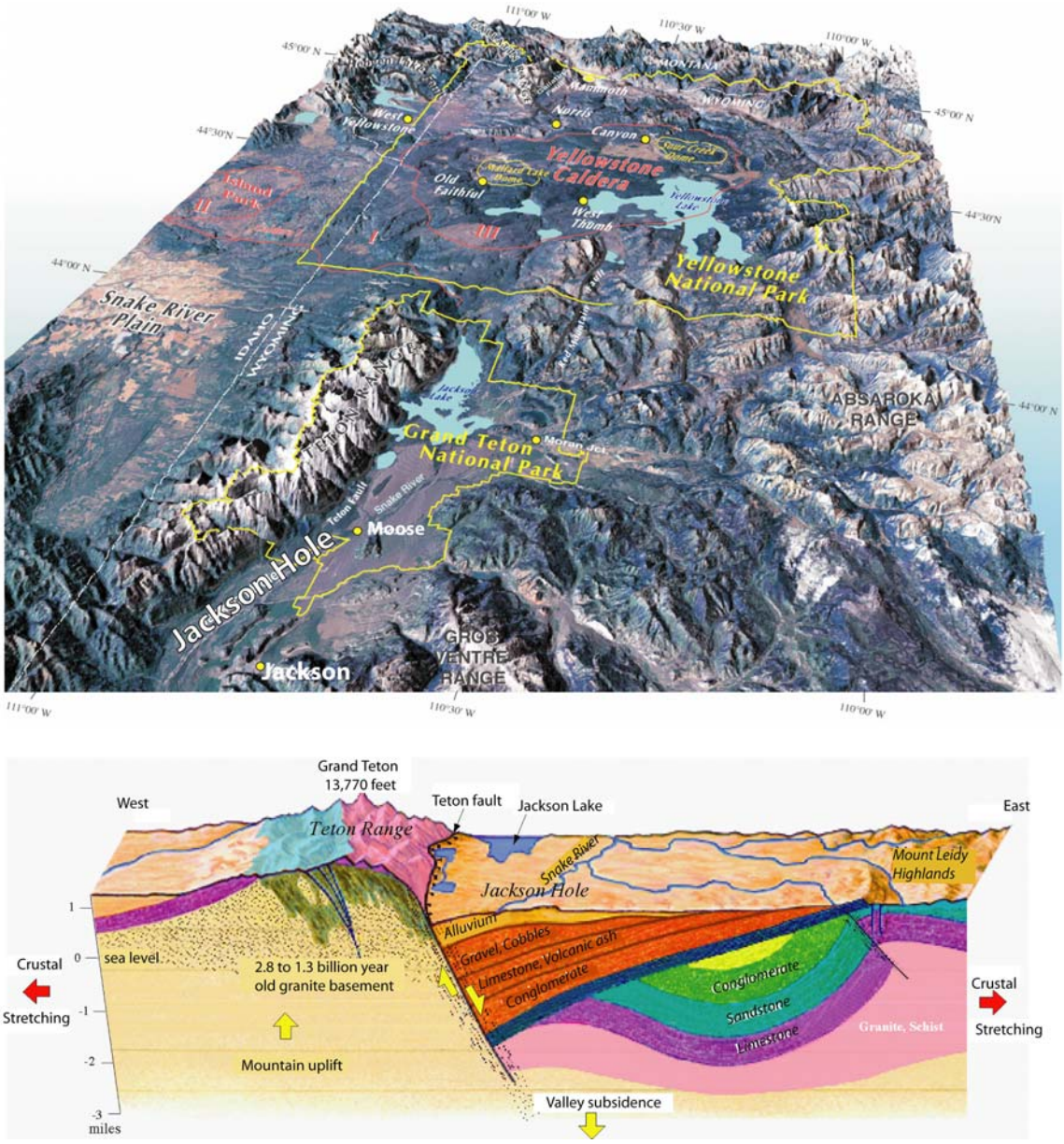

Figure 1.2. Teton and Yellowstone satellite image with geologic cross section through the Teton region. The greater Teton region is comprised of the Teton Mountain Range, Jackson Hole valley, and southern Yellowstone areas (top figure). The majority of the Teton Range and Jackson Hole valley lie inside the Grand Teton National Park boundary outlined in yellow. The town of Jackson, WY is located south of the park entrance at Moose, WY. Yellowstone National Park is directly north of the Teton Range and is outlined in yellow. The lower figure shows the geologic cross section from *Smith and Siegel* [2000] who produced an artistic view of the geologic profile from the Teton Range through the Jackson Hole valley that simplifies the previous works of *Love* [1989 and 1989] and *Byrd* [1995]. The Teton Range's highest peak is Grand Teton at 13,770 ft. The Teton fault shows an arbitrary dip of about 60 degrees down towards the east.

seismic gap at the M 3+ level [*Smith*, 1988]. If the seismic gap interpretation is accurate, then the Teton fault may be locked, and the gap would be expected to generate moderate to large earthquakes in the future.

Earthquake hazards associated with the Teton fault are evident by comparing the geology and seismotectonics of the Teton fault with the Hebgen Lake, MT, and Borah Peak, ID, faults. These faults were associated with the two largest historic ruptures of the eastern Basin-Range; the Ms 7.3 1983 Borah Peak, Idaho, earthquake [*Richins et al.*, 1987; *Smith et al.*, 1985; *Doser and Smith*, 1983] and the M_L 7.5 1959 Hebgen Lake, Montana, earthquake [*Doser*, 1985]. The Borah Peak earthquake and Hebgen Lake earthquake produced scarps of 2.7 m and 6.1 m. Holocene fault scarps of 30 m are seen along the Teton fault and are hypothesized to have been created by 5 to 15 Hebgen Lake sized earthquakes with 2-6 m of offset for each event [*Smith et al.*, 1985], which includes two trenched earthquakes along the southern Teton fault segment with one 2.8 m vertical offset M=7.1 event 7,090 years ago and a 1.3 m vertical offset M=6.8 event 4,840 years ago.

Interest in the Teton fault and its potential earthquake hazard began with the failure of the Teton dam in Idaho on June 5, 1976 only 70 km west from the Teton fault. The Teton dam failure led to concerns on the safety of Jackson Lake dam, which is located in the valley of Jackson Hole 48 km north of Jackson, Wyoming. The U.S. Bureau of Reclamation originally constructed the Jackson Lake dam in 1911 along the mouth of a natural glacier carved lake and the South Fork of the Snake River in northwestern Wyoming, 30 miles north of Jackson.

Early seismic studies of the Teton region and hazard reports conducted by the University of Utah in the 1970s led to more permanent seismograph installations in 1986 by the Bureau of Reclamation as well as a rehabilitation of the Jackson Lake dam structure. Fault trenching, gravity profiles, topographic measurements, and seismic refraction studies have all been conducted for the Teton fault and greater Teton region by *Byrd et al*. [1994] from the University of Utah in the 1990s. The U.S. Bureau of Reclamation has also evaluated the hazard analysis of the Teton fault and the Jackson Lake Dam as internal studies. Other modern hazard analysis using dynamic models are currently being applied to the Teton fault by Dr. Ralph Archuleta at the University of California Santa Barbara. However, it is in this inclusive study that we attempt to bring all of this information together with a new relocated earthquake catalog and three-dimensional (3-D) velocity model as a first step for a new complete probabilistic seismic hazard analysis of the greater Teton region.

To evaluate the earthquake potential and relative seismic hazard of the Teton region, especially on the Teton fault, an updated earthquake catalog of the Teton region was needed to understand the seismic patterns associated with the known faulting structures in the region. From 1986 to 2002 the U.S. Bureau of Reclamation constructed and operated the Jackson Lake seismic network (JLSN) that recorded 8,537 events of $0.1 < M < 4.7$ on 20 short-period and 5 broadband seismographs. This network focused on the effects of seismicity on the Jackson Lake dam located in Jackson Hole valley. These earthquakes were located using a one-dimensional (1-D) P- and S-wave velocity model for the region and was used in strong ground motion studies conducted by the Bureau of Reclamation to evaluate the safety of the Jackson Lake dam.

The objective of our study was to develop a new earthquake catalog of the Teton region using new probabilistic nonlinear relocation methods [*Lomax*, 2001] and incorporating a tomographically determined 3-D velocity model. The new seismic data allowed a more accurate assessment of the regional Teton seismicity and its relationship to the seismic sources using high precision hypocenters and 3-D tomographic images. Hypocenter locations in the Teton Region have improved in accuracy using the 3-D velocity model and probabilistic relocation method by reducing the P-wave arrival time residuals by 59% relative to the original Bureau of Reclamation's 1-D hypocenter locations. Hypocenter residuals improved from initial average RMS values of 0.24 s to final average RMS values of 0.097 s.

Several methods were used to develop our new earthquake data. First the seismic data obtained from the Bureau of Reclamation were analyzed and errors in the automatic picking algorithm were determined. Then cross-correlation of the waveforms was conducted to improve the first arrival P-wave picks using the methods of *Rowe* [2000]. The high quality data were then used for the development of a minimum 1-D velocity model of the Teton region. The high quality data subset consisted of 445 events with at least 10 zero-weighted first motion observations, RMS time residuals < 0.5, azimuthal gap < 160 deg, and the closest station to epicenter distance < 20km. Seismic refraction surveys conducted by *Behrendt et al.* [1968], then reinterpreted by *Byrd* [1995], and phosphate mining blasts recorded by the JLSN were used as constraints when determining the solution quality of the 1-D velocity model. The next step was to use the new 1-D velocity model and generate an initial 3-D velocity grid for the whole region. Solution quality tests were conducted to insure the final 3-D velocity model's resolution

capabilities and stability. All Teton seismic events were then relocated using a probabilistic nonlinear relocation method [*Husen and Smith*, 2004] and the new 3-D velocity model. Only the highest quality relocated events with the least amount of hypocenter error associated with each earthquake were used to assess epicentral patterns, fault behavior, and focal depth relationships for the Teton region. Focal mechanisms were computed for these high quality events as well as stress-field solutions for different subregions with in the greater Teton region using the methods of *Horiuchi et al.* [1995], *Gephart* [1990a], and *Waite and Smith* [2004]. Magnitudes originally determined by the BoR were then compared with recorded Teton earthquakes and calibrated local magnitudes determined by the University of Utah Seismograph Stations to ensure there were no large discrepancies between the two magnitude calibration scales. Finally, a catalog of high precision earthquakes in the Teton region was developed with defined tomographic images and focal mechanisms.

In this study, my objectives are to present the methodology and new relocated earthquake catalog and 3-D velocity model for the Teton region. I will also combine results from geologic, geodetic, geophysical, and leveling studies to help refine the seismotectonic understanding of the Teton fault. Finally I will provide fault-stress loading conditions, and key input into the probabilistic earthquake hazards analysis.

CHAPTER 2

SEISMOTECTONICS OF THE TETON REGION

2.1. Geology and Tectonic History

The Teton Range is one of the most impressive neotectonic features in the western United States. The north-south Teton Range is located near the intersection of the Basin Range, Idaho-Wyoming thrust belt, Rocky Mountain foreland, and Snake River Plain-Yellowstone tectonic provinces in northwestern Wyoming (Figure 1.1). The range is located in the Intermountain Seismic Belt [*Smith and Sbar*, 1974], which is a major zone of earthquake activity that extends 1,300 km from Arizona through Utah, eastern Idaho, western Wyoming, and western Montana (Figure 2.1).

The Teton fault runs north-south and extends 55 km along the eastern base of the Teton Range, and has produced a steep escarpment on the westward tilted fault block that forms the range (Figure 1.2). The southern and middle segments of the Teton fault extend 42km from the town of Wilson, WY north to the south end of Jackson Lake (Figure 2.2). These sections of the fault have shown fission track ages between 85 to 65 Ma indicating the timing of uplift in the Teton Range which shows 2 km of vertical relief along the Teton fault escarpment [*Roberts and Burbank*, 1993]. The northern Teton fault segment shows younger dates between 26 to 67 Ma. The fault branches into two segments near the northern end of Jackson Lake (Figure 2.2). The northern segment

Figure 2.1. Epicenter map of the Intermountain Seismic Belt. The Teton Region and study area, marked by the black box, is within the Intermountain Seismic Belt [*Smith and Sbar*, 1974], which is a major zone of seismic activity that extends 1,300 km from Arizona through Utah, eastern Idaho, western Wyoming, and western Montana. Earthquake epicenters from 1850-2004 are displayed as red dots. State boundaries are represented by blue lines. Large historic events are labeled and represented by the yellow stars.

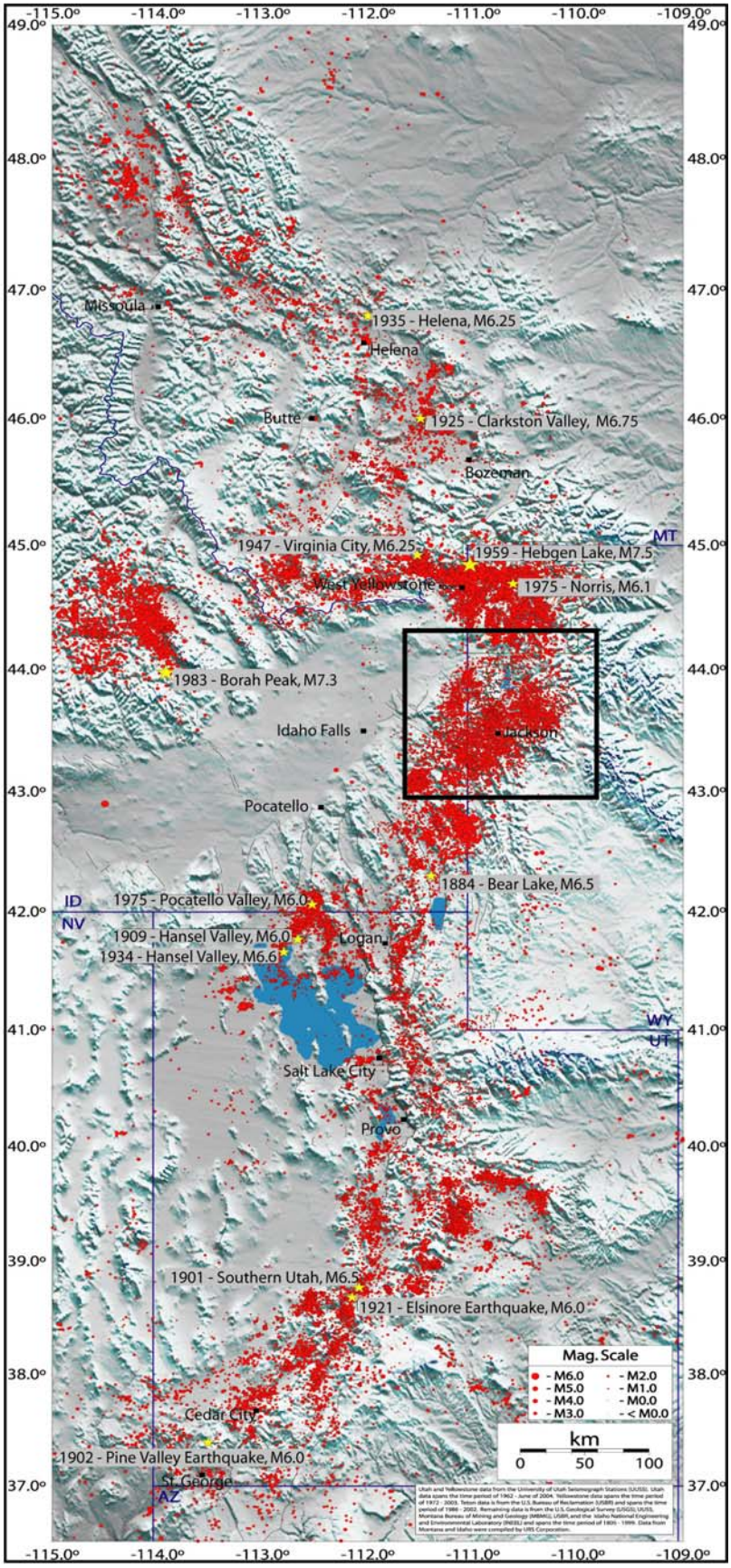
-115.0°
-114.0°
-113.0°
-112.0°
-111.0°
-110.0°
-109.0°
49.0°
48.0°
47.0°
46.0°
45.0°
44.0°
43.0°
42.0°
41.0°
40.0°
39.0°
38.0°
37.0°
Missoula
1935 - Helena, M6.25
Helena
Butte
1925 - Clarkston Valley, M6.75
Bozeman
MT
1947 - Virginia City, M6.25
1959 - Hebgen Lake, M7.5
West Yellowstone
1975 - Norris, M6.1
1983 - Borah Peak, M7.3
Idaho Falls
Jackson
Pocatello
1884 - Bear Lake, M6.5
ID
NV
1975 - Pocatello Valley, M6.0
1909 - Hansel Valley, M6.0
1934 - Hansel Valley, M6.6
Logan
WY
UT
Salt Lake City
Provo
1901 - Southern Utah, M6.5
1921 - Elsinore Earthquake, M6.0
Mag. Scale
- M6.0
- M5.0
- M4.0
- M3.0
- M2.0
- M1.0
- M0.0
- < M0.0
km
0
50
100
Cedar City
1902 - Pine Valley Earthquake, M6.0
St. George
AZ

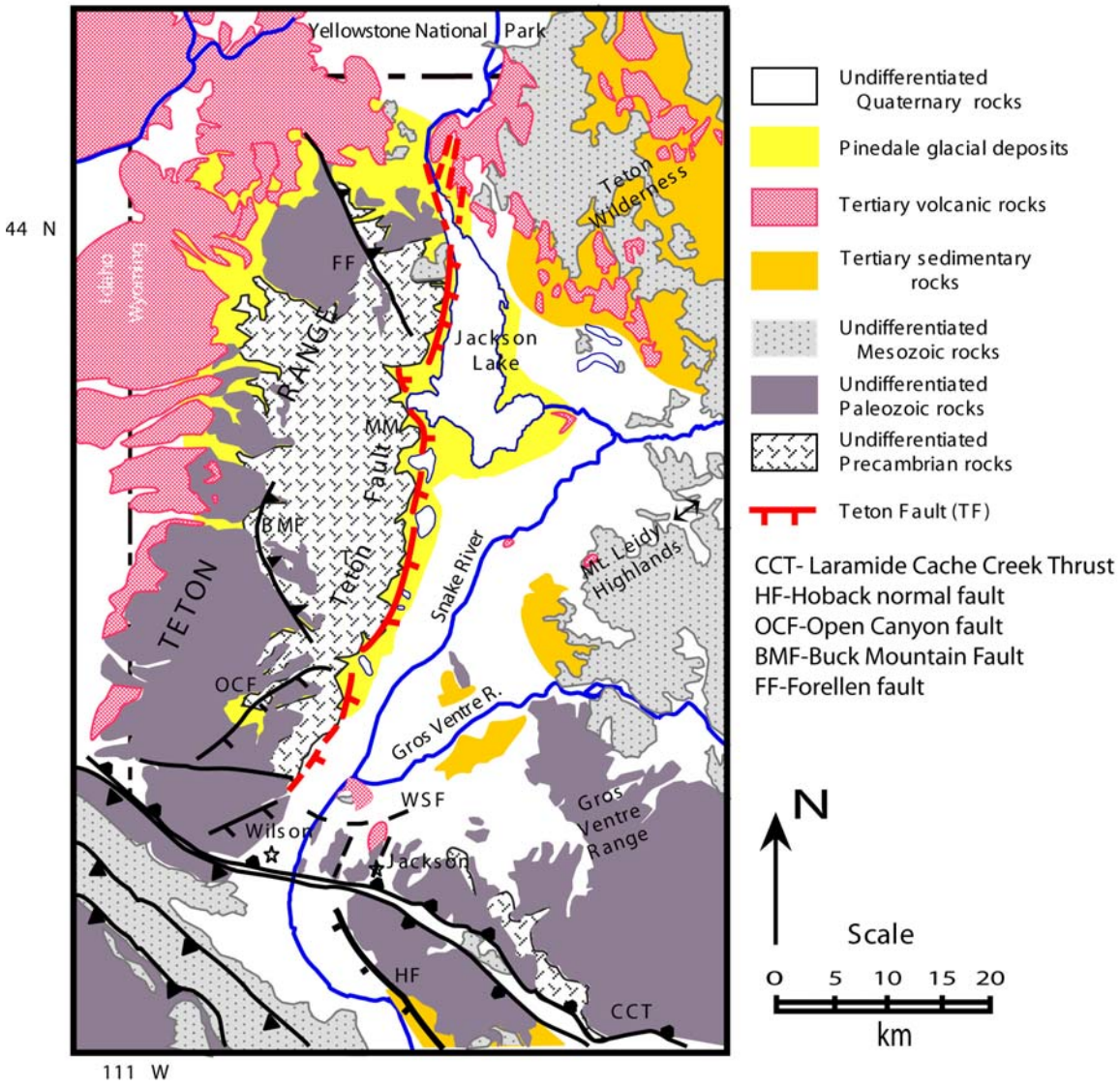

Figure 2.2. Geologic and fault map of the Teton region. The geology is modified after *Love* et al. [1992] and Teton fault trace is from *Smith et al.* [1993]. The major faults and geologic formations are labeled in the key above.

appears to die out under the 70,000-yr-old Pitchstone Plateau rhyolite flows [*Christiansen and Blank*, 1972]. The eastern segment of the fault merges into the remains of a ring-fracture system formed during the collapse of Yellowstone's first caldera cycle 1.9 Ma [*Christiansen and Blank*, 1972].

The Teton normal fault is the principal structure responsible for the Late Miocene to Holocene footwall uplift of the Teton Range and hanging wall subsidence of the Jackson Hole valley (Figure 2.2). However, structural evolution of the range has been influenced by four major post-Paleozoic events [*Smith et al.*, 1990a]: 1) Mesozoic to early Tertiary, east-west compression due to the Idaho-Wyoming thrust belt or Laramide orogeny; 2) late Tertiary, Basin-Range crustal extension producing the Teton fault and Teton Range with 6-9 km of stratigraphic displacement; 3) late Cenozoic volcanism and crustal deformation due to the nearby Snake River Plain-Yellowstone volcanic system; and 4) extensive silicic volcanism from the Yellowstone Plateau, including the Quaternary Huckleberry Ridge tuff that caps the north end of the Teton Range and is exposed in various outcrops in the northern end of Jackson Hole [*Smith et al.*, 1990a]. The structural evolution of the Teton Range has produced a unique drainage system that does not follow the range crest but is located ~5 km to the west of the Range's highest peaks (Figure 2.3).

Vertical fault displacement along the Teton fault was initiated less than 7 to 9 Ma, with cumulative vertical displacement estimated to be about 6 to 9km [*Byrd and Smith*, 1995]. Displacements of alluvial fans and glacial moraines at the base of the Teton Range show evidence of continued movement along the fault during the Pleistocene and Holocene time periods. A series of 3 to 52 m high fault scarps delineate the postglacial

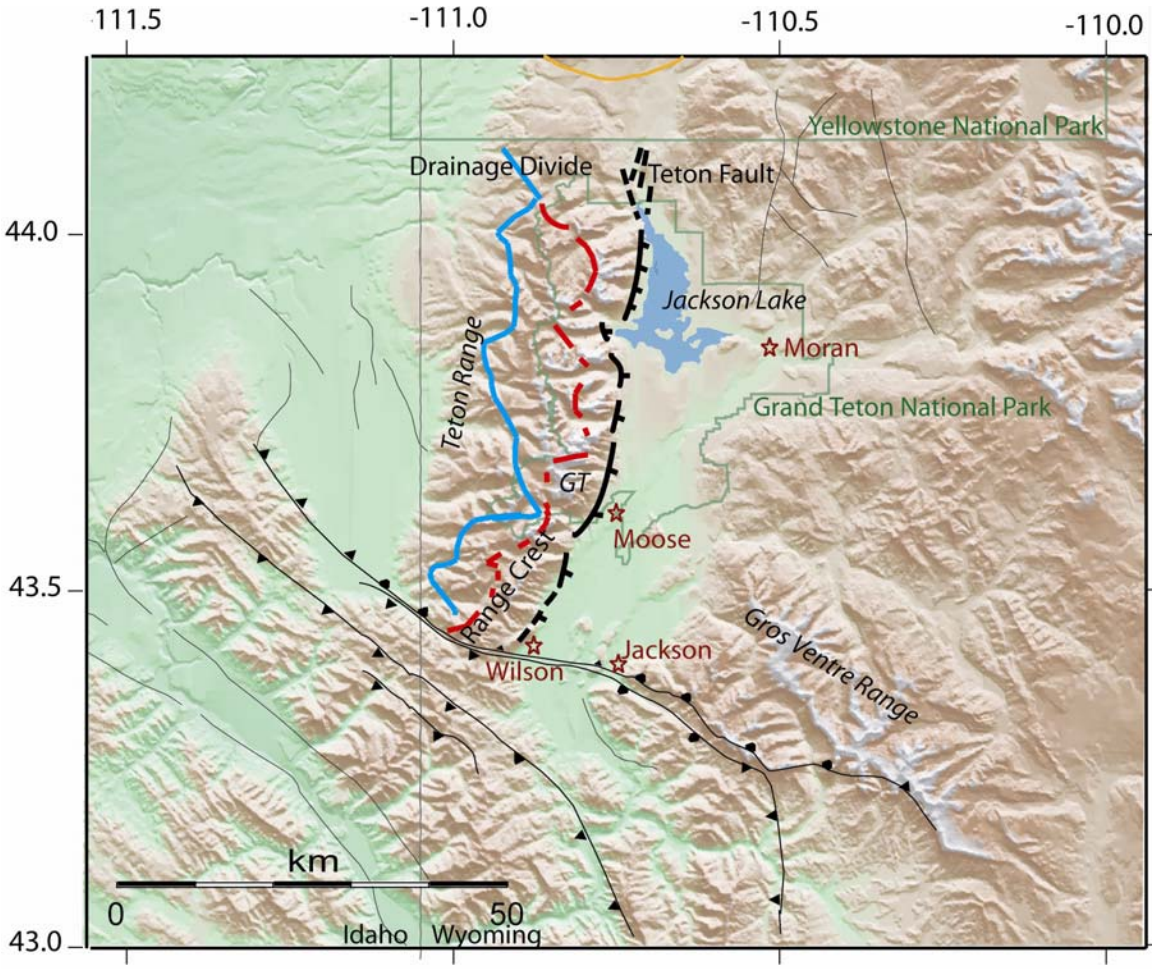

Figure 2.3. Drainage divide and range crest map of the Teton Mountains. The highest peak in the Teton Range is labeled GT (Grand Teton). The drainage divide is outlined in blue and the range crest is outlined in red.

(~14,000 yr) trace of the Teton fault and confirm that the fault has been subject to several postglacial ground rupturing earthquakes [*Gilbert et al*., 1983*; Susong et al*., 1987; *Smith et al*., 1989, 1993a]. There has been about 2 km of movement along the fault since the eruption of the Huckleberry Ridge tuff, 1.9 Ma [*Christiansen and Blank*, 1972], giving an estimated average prehistoric slip rate of 0.45 to 2.4 mm/yr along [e.g. *Gilbert et al*., 1983; *Smith et al*., 1989, 1993a].

Based on trenching results and detailed mapping, the Teton fault's youngest deformation corresponded to two paleoearthquakes M=7.1 7,090 years ago and M=6.8 4,840 years ago [*Byrd*, 1991]. Gravity and seismic refraction models using paleomagnetic data from the Huckleberry Ridge tuff were also developed by *Byrd et al.* [1994]. His models suggest a total normal fault separation of 2.5 to 3.5 km has accumulated across the Teton fault in the past 2.0 Ma [*Byrd et al*., 1994].

Modern studies [*Sylvester et al.*, 2004] of the Teton fault used geodetic methods including 1st-order leveling-lines that extend from the Teton Range in Granite Canyon east across the middle section of the Teton fault to the south side of Jenny Lake in the Jackson Hole valley. Leveling results have recently shown that the alluvium-filled valley of the hanging-wall rose and fell 8-10 mm relative to bedrock between 1988 and 1993 [*Sylvester et al.*, 2004]. In 1997, a 2 km wide zone adjacent to the Teton fault rose 12 mm relative to the 1993 survey [*Sylvester et al.*, 2004]. The 1997 uplift of the valley floor and subsidence zone may reflect an unexpected, reverse loading and local crustal shortening between 1995 and 2000 as indicated by GPS surveys [*Sylvester et al*., 2004]. The GPS campaign network in the Teton region has also displayed results of reverse loading across the Teton fault. Combined results from the 1987-2003 campaign GPS

surveys display an average valley floor uplift of ~0.5-1.5 mm/yr and a valley floor western horizontal motion of 1±0.5 mm/yr.

Smith and Siegel [2000] produced a 3-D view of the geologic profile from the Teton Range through the Jackson Hole valley that simplifies the previous works of *Love* [1989] and *Byrd* [1995] (Figure 1.2). The footwall of the Teton fault is comprised of the Teton Range, which consists of a core of Achaean igneous and metamorphic rocks, unconformably overlain by west-dipping Paleozoic strata that are unconformably capped by Late Miocene to Quaternary volcanic rocks [*Byrd*, 1995]. Exposures of Mesozoic and Tertiary age strata are limited to relatively minor outcrops at the north end of the range [*Love et al*., 1992]. The hanging-wall of the Teton fault, the Jackson Hole valley, is interpreted to be an asymmetric, west-dipping, sedimentary basin underlain by a relatively continuous succession of Paleozoic through Tertiary strata that are exposed in the Gros Ventre Range [*Love*, 1989]. These sedimentary strata are overlain by Late Miocene to Quaternary lacustrine, volcaniclastic, glacial, fluvial, and alluvial deposits (Figure 2.2) [e.g., *Love et al*., 1992].

The hanging-wall of the Teton fault is bounded by the eastern uplift Hoback normal fault in the southeastern end of Jackson Hole (Figure 2.2). The Hoback fault has a total displacement of 3,000 m with 15 m of measured displacement on post-15,000-yr old loess [*Love et al.*, 1973]. Displacements along the Teton and Hoback faults appear to die out as they converge on the east-west trending Cache Creek thrust near Jackson, a major fault formed during the Laramide orogeny that may have been active as late as Pliocene time [*Love et al.*, 1973]. The interaction between the late Quaternary Teton and

Hoback normal faults and the older Laramide Cache Creek thrust structure are poorly understood.

2.2. Historic and Regional Seismicity

The Teton region is located within the central part of the 1,300 km long, Intermountain seismic Belt (ISB), a diffuse zone of shallow earthquakes (focal depths less than 20 km) that represents the boundary between the Basin and Range physiographic province and the Rocky Mountains [*Smith and Arabasz*, 1991]. Although large earthquakes have not occurred in the Teton region in historic time, other large earthquakes have occurred in the central ISB, including the Ms = 7.5, 1959 Hebgen Lake, Montana, earthquake located 90 km northwest of the Teton Range, and the Ms = 7.3, 1983 Borah Peak, Idaho, earthquake located 200 km west of the Teton Range. Displacements of late Quaternary deposits indicate that multiple large Hebgen Lake Ms 7.5 size earthquakes have occurred along the Teton fault in order to generate these large Holocene fault offsets [*Gilbet et al*., 1983].

Although inhabitants of the Teton-Jackson Hole region have felt small earthquakes since the late 1800s, no earthquake has exceeded an intensity of VI on the modified Mercalli scale [*Coffman and von Hake*, 1973]. From 1923 to 1975, felt earthquakes occurred primarily in the central Gros Ventre Range, southern Jackson Hole, and Driggs, Idaho regions [*Smith et al*., 1976]. The earliest published discussion of historical earthquakes was given by *Blackwelder* [1926], who described a slight earthquake in Jackson, on September 3, 1925 [*Smith et al.,* 1976]. The next account of earthquakes was given by *Fryxell* [1933], who documented several felt shocks in the

Gros Ventre Canyon, January 25-28, 1932 [*Smith et al*., 1976]. The most recent documented earthquake sequence [*Gale*, 1940] consisted of three shocks during the autumn of 1939. These shocks did not produce any damage, and from felt reports were judged to be near or just southwest of Jackson [*Smith et al*., 1976]. Historical accounts of these earthquakes do not suggest that the earthquakes occurred along the Teton fault zone [*Smith et al*., 1976].

The apparent lack of seismicity along the Teton fault may be due to the sparsity or lack of instrumentation in the Teton region until the early 1960s. A skeleton network of U. S. seismograph stations, at a station spacing of ~2,000 km, was established in the U.S. and revealed a relatively low rate of seismicity for this region. Epicenter accuracy of this early network was ~500 km at the Ms ≥ 4.0 thresholds [*Smith and Sbar*, 1974]. By the early 1970s and mid 1980s seismograph station coverage increased significantly by installation of regional seismograph networks such the U. S. Bureau of Reclamation's Jackson Lake seismic array and the USGS supported University of Utah's Yellowstone and Utah arrays. These networks provided epicenter accuracy to ± 2-4 km [*Doser and Smith*, 1983; *Wood*, 1988; *Smith and Arabasz*, 1991]. The magnitude of completeness of the Teton catalog with time was set by the Bureau of Reclamation to be at the magnitude cutoff of 2.0. All events with magnitudes of 2.0 or larger had manually picked P-wave times with picking errors less than 0.06 s.

All of these networks document the paucity of earthquakes that may possibly be attributed to the Teton fault, as shown by the Bureau of Reclamation's recorded Teton region earthquakes at 20 stations from 1986-2002 in Figure 2.4. Projections of a 45-75˚

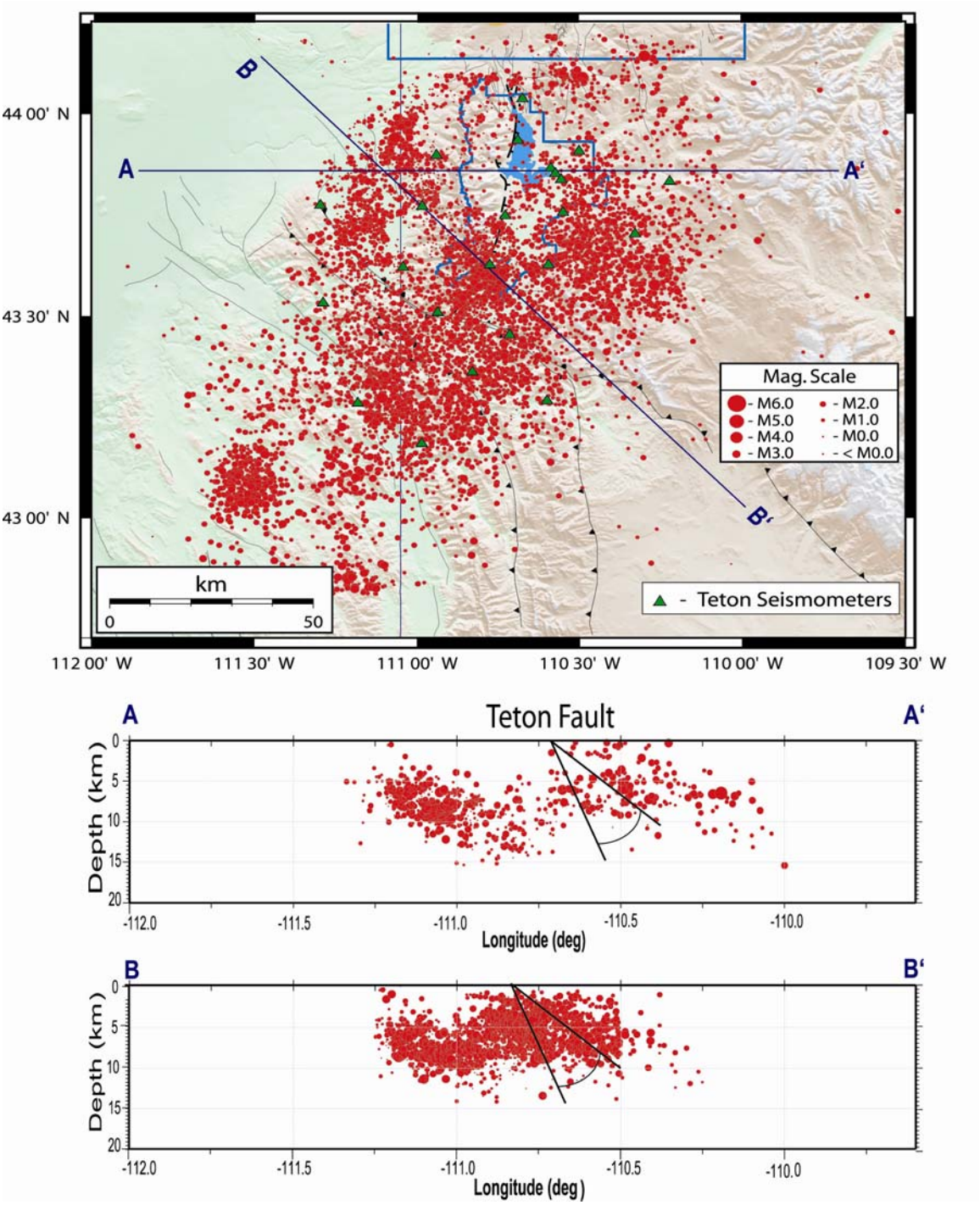

Figure 2.4. Original hypocenters of earthquakes in Grand Teton National Park from 1986-2002 recorded and located by the U.S. Bureau of Reclamation. The hypocenters are represented by red circles shown in both plain view and vertical cross sectional depth view. The Teton fault is outlined in black and the National Parks are outlined in dark blue. The Teton fault is projected at depth at about 45-75˚ east-dipping. There are no earthquakes that align with the downward projection of the Teton fault.

east-dipping fault into the earthquake focal depths show the fault surface at depths of 10 to 15 km, indicating these earthquakes did not occur on the down-dip, eastward projection of the Teton fault (Figure 2.4). The dip angle of the Teton fault is not well defined, so a range of angles was used to account for all possible angles associated with the normal dipping Teton fault. The most recent studies on the dipping angle of the Teton fault by *Byrd* [1995] showed that angles between 45-75˚ using a boundary element model for kinematic faults were the most likely to cause the observed height changes across the length of the Teton leveling line that traversed the central Teton fault segment. The earthquakes that are not occurring along the Teton fault may be related to movement on related, yet unknown, structures in the hanging-wall.

Focal mechanisms and GPS strain rates of the Yellowstone Plateau and southeastern Idaho surrounding the Teton region suggest east-west to northeast extension [*Smith and Arabasz*, 1991; *Smith and Braile*, 1994] that were interpreted as a manifestation of Basin-Range intraplate extension. There have been few focal mechanisms published for the Teton region except for the fault plane solutions for small earthquakes (M < 4) in the Gros Ventre Range [*Doser and Smith*, 1983; *Wood*, 1988] that showed oblique-normal faulting solutions. These regional strain data for the Teton region were consistent with the regional east-west to northeast extension in the Basin and Range providence. Low strain rates converted from the seismic moment rate to displacement rates of 0.01 mm/yr or less are associated with east-west crustal extension [*Eddington et al.,* 1987; *Doser and Smith*, 1983; *Wood,* 1988].

The central ISB (Figures 2.1 and 2.4) seismicity rates clearly show a seismic quiescence along the Teton fault. There are several hypotheses that may account for the

observed seismic quiescence and low strain rates across the Teton fault: 1) the Teton fault may indeed be quiescent, accumulating strain energy prior to a future earthquake; 2) the fault may be releasing strain through aseismic fault creep, although there is no evidence for this; 3) the short period of historic seismologic observations and poor epicentral control before 1962 preclude accurate assessment of the long-term seismicity; 4) the Teton fault may no longer be active and is not storing significant strain energy required for earthquake nucleation but that is unlikely given its profound late Quaternary history; or 5) the regional background seismicity surrounding the fault may be effectively relieving stress accumulation directly on the fault [*Smith et al*., 1993b]. These hypotheses are logical and reasonable explanations of the seismic quiescence along the Teton fault. However, we believe the Teton fault is still an active structure that is capable of generating large future earthquakes.

2.3. Jackson Lake Seismic Network Data

The seismic data used for this study came from the U. S. Bureau of Reclamation (BoR). The BoR seismic data consisted of seismic waveform data, first arrival P-wave picks, and an earthquake catalog that was determined using a 1-D velocity model. The BoR operated the Jackson Lake Seismic Network from April 1986 to December 2002 and the number of stations and geometry of the network varied throughout that period. Initially, the network consisted of 16 short-period (1Hz) vertical-component (Geotech model S-13) seismograph stations (Figure 2.5). An additional four stations were installed in 1990 to improve monitoring coverage, totaling 20 stations. Prior to October 2000, the network used analog telemetry between station sites and communications collection

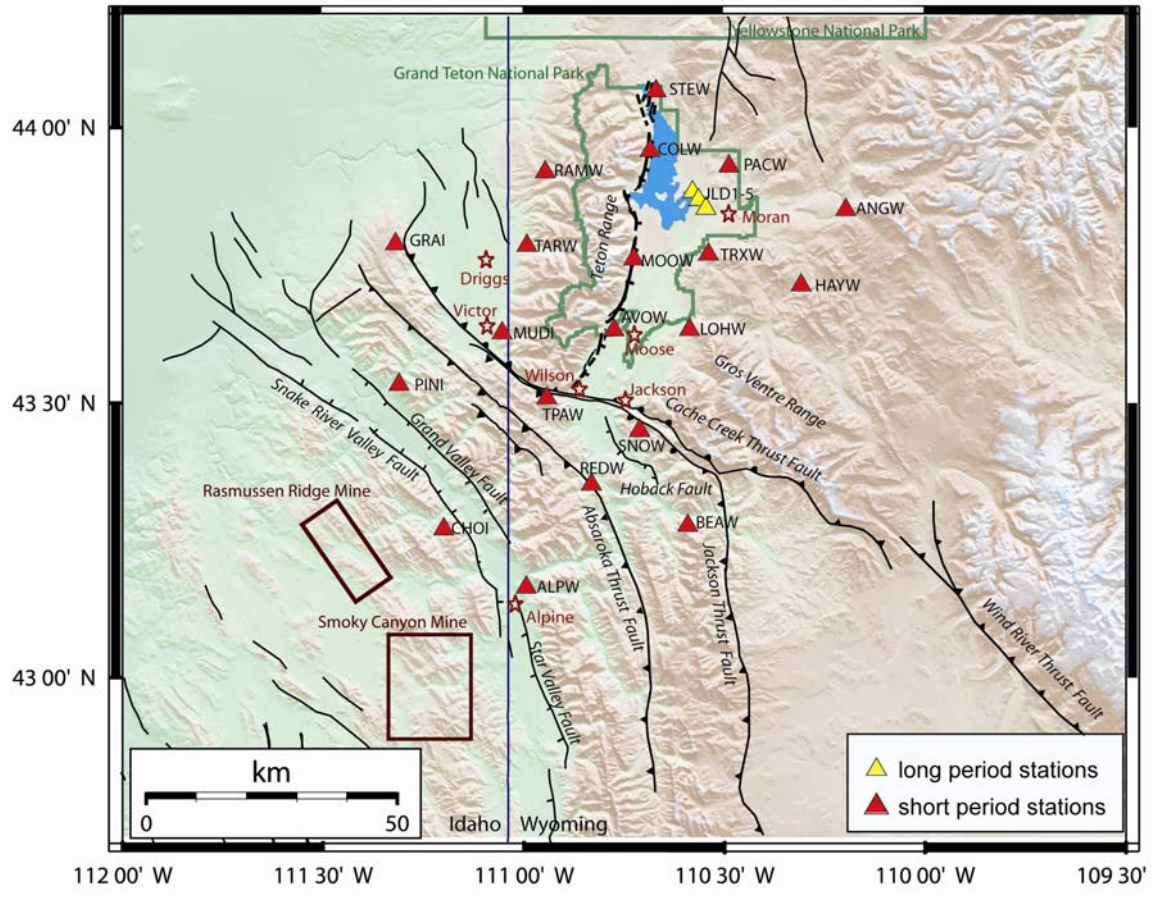

Figure 2.5. The Jackson Lake Seismic Network, 1986-2002. All the short period seismometers were operating at the same time after 1990, and the long period stations were operating from 1996-2001. Seismometers are represented by red and yellow triangles. The major faults in the area are shown by the black lines, and the outline of the Grand Teton National Park is shown in dark green. Towns are shown by the brown stars. Phosphate mines in Idaho are shown by dark brown boxes.

facilities located in the field [*Wood,* 1988]. From 2000 to 2002 the data were digitized at the communications collection facilities in the field. Signal-to-noise ratios were greatly improved by reducing analog data transfers to relatively short transmission paths via FM radio between the seismograph station and the field communication collection facilities [*O'Connell et al.*, 2003]. Five digital broadband three-component velocity seismographs were installed from 1996 to 2001 on or near Jackson Lake Dam to provide site response recordings of local earthquakes (Figure 2.5).

More than 8,000+ events were recorded by the Jackson Lake Seismic network from 1986-2002 ranging in magnitude from 0.1-4.7 (Figure 2.6). The large spike in seismicity during the fourth quarter of 1992 was most likely due to mine blasts taking place near the Smoky Canyon Mine in western Idaho from November 11th- 30th. However, we were unable to confirm that the Smoky Canyon Mine or any of the other phosphate mines in the area was blasting during that time frame. The cluster of events during the month of November all had large gaps associated with their hypocenter locations implying that even though their depths were not shallow at 0 km there is still a chance they are due to mining activity. Another possibility is that this cluster of events is a swarm or mainshock-forshock sequence. However, the cluster of events did not represent a typical mainshock-forshock sequence, but a series of 200 plus events occurred in this short time frame with the largest event being a magnitude 4.0.

Over the total number of recorded earthquakes, fewer than 3,000 events were greater than magnitude 2.0. The largest event recorded in the area was a magnitude 4.7 on December 28, 1993 in the Gros Ventre range, Wyoming. All earthquakes were automatically processed in real time, and phase arrivals for all local earthquakes equal to

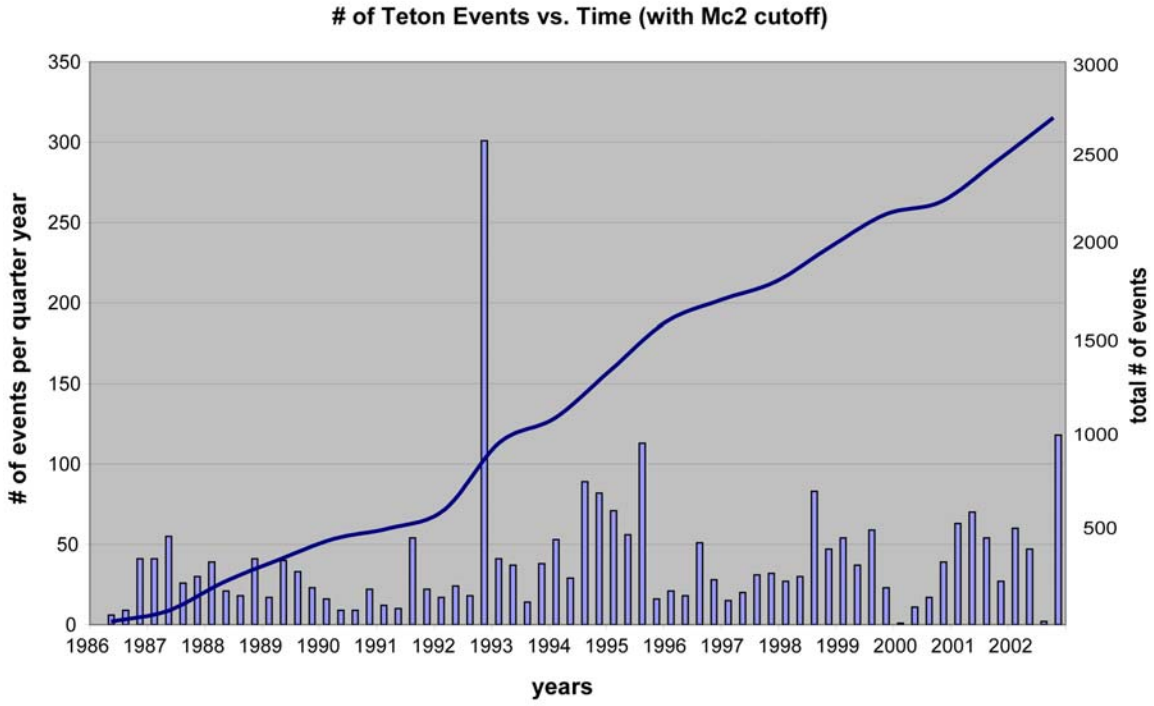

Figure 2.6. Total number of earthquakes per quarter year with magnitudes greater than 2.0 recorded by the Jackson Lake Seismic Network from 1986-2002. More than 2,500 + events were recorded ranging in magnitude from 2.0-4.7. The maximum number of events recorded in one quarter was 301 earthquakes in the last quarter of 1992 which is mainly due to mine blasting taking from November 11th-30th near or at the Smoky Canyon Phosphate Mine. The total cumulative number of earthquakes is represented by the solid blue line.

or greater than magnitude 2 along with selected smaller events were manually picked and reprocessed. Routine processing for the BoR included phase picking, magnitude estimation, 1-D hypocenter location, focal mechanism determination, and seismic moment estimation.

In this study, about 10% of the events and all events over magnitude 2.0 were analyzed by eye using a program called XPED, developed by the University of Washington, to assure the quality of the first arrival P-wave picks that were completed by the BoR's manual and automated picking methodology. XPED is a seismic analysis tool that allows users to manually pick first P-and S-wave arrivals by viewing the waveforms for each event that was recorded at each of the stations in the network. From this analysis it was clear that the BoR did an exceptional job of picking phase arrivals using the two picking methodologies. The final arrival time residual weighting scheme for the BoR picking arrivals is shown in Table 2.1. The error in seconds for the picking times is small from a minimum of 0.03 s to a maximum of 0.3 s with an average picking error of 0.15 s. This demonstrates the precision that was taken in analyzing these phase arrival times. The average RMS value for the 8,537 BoR 1-D hypocenter locations was 0.12, with a total of 95,091 P-wave picks and 37,177 S-wave picks. These events were used in the determination of the new relocated Teton earthquake catalog.

Table 2.1. Weight settings determined by picking errors in seconds

Weights	Picking Error in Seconds
0	0.03
1	0.06
2	0.15
3	0.30

CHAPTER 3

METHODOLOGY AND RESULTS

Traditional earthquake relocation procedures involving linearized location algorithms and 1-D velocity models generally limit the accuracy of absolute, single-event locations because they do not account for the complexity of the velocity structure in all dimensions. New improvements in hypocenter location schemes for local and regional networks have been derived from the improved velocity modeling via joint hypocenter determination and local 3-D tomography [*Kissling,* 1988, *Husen and Smith*, 2004].

The accuracy of the earthquake locations depends not only on the station geometry and location algorithm, but also on the accuracy of the arrival times of the first P-wave and later S-wave arrivals and the characterization of the seismic velocity structure. Using human analysts and automated picking software there are timing inconsistencies, and the recording environment of each site and size of the earthquake cause variations in the signal-to-noise ratio. It is possible to directly address picking inconsistencies by using signal processing methods to adjust the picks for consistency among events with waveform similarity [*Dodge et al*., 1995; *Rubin and Gillard*, 1998; *Rowe*, 2000]. This method can only be employed if there are enough waveforms in the data that are similar to one another to represent a similarity of arrival character. Once

picking inconsistencies are minimized, the determination of a minimum 1-D and 3-D velocity models can be achieved.

To complete the task of developing a new relocated earthquake catalog for the Teton region, several processing steps will be applied. First, I applied a cross-correlation procedure to enhance the first P wave arrivals of the entire data set using a program developed by *Rowe* [2002]. This procedure is described in section 3.1. Second, I determined the minimum 1-D velocity model described in section 3.2 needed as input to the 3-D inversion. The final 3-D tomography was then calculated using the minimum 1-D model and station corrections as described in section 3.3. Absolute hypocenter locations were calculated using the 3-D velocity model and nonlinear earthquake location algorithm NonLinLoc [*Lomax et al*., 2000] summarized in section 3.4. Once the final relocated Teton catalog was determined, the relative local magnitude scale, M_L, determined by the U.S. Bureau of Reclamation was evaluated as explained in section 3.5. Recomputed take-off angles from the relocated hypocenter files were used for focal mechanism determination that aided in the construction of stress field inversions for the Teton region as explained in section 3.6. The programs utilized, basic theoretical ideas and results of each of these relocation and catalog generating methodologies are discussed in the following sections.

3.1. Cross-Correlation of Seismic Waveforms

Cross-correlation of waveforms determines relative time delays. These time delays are related differential travel times between pairs of seismic events at the same station. They are often used as input data to improve earthquake relocation results. To improve our

picking data we employed this method of cross-correlation using the code CCHAR by *Rowe* [2002]. Rowe's automatic correlation and clustering-based method was developed for reducing the picking inconsistency in large seismic data sets. Similar to other quantitative waveform correlation methods for precise relocation, the algorithm simultaneously analyzes traces from many events on a station-by-station basis [*Dodge et al*., 1995].

3.1.1. Theory

Dealing with large seismic data sets provides a challenge in which you cannot solve the full data set in one step. In Rowe's code, this problem is dealt with by first dividing the data set into subgroups or clusters that show similar waveforms. The whole location processing flow is schematically shown in Figure 3.1. The initial step is preliminary cross-correlation, where the clusters are formed and a master station is selected. The master station is defined as one station centrally located in the network that records most of the arrivals clearly without large amounts of noise**.** Before the preliminary cross-correlation of a desired phase, the time window and exponent of coherency for adaptive filtering were selected. The catalog was then separated by a hierarchical pair group clustering algorithm that is explained in detail by *Rowe* [2000]. The program uses a flexible combinational weighting method to weight earthquakes into individual clusters. The clustering process is necessary to group individual earthquakes into clusters of other earthquakes that all show similar waveforms. After the clustering process, a relative lag estimation is conducted among traces within each cluster**.** All phases are cross-correlated and optimal pick adjustments are determined in samples that are typically milliseconds. The correlation window length, generally a short time

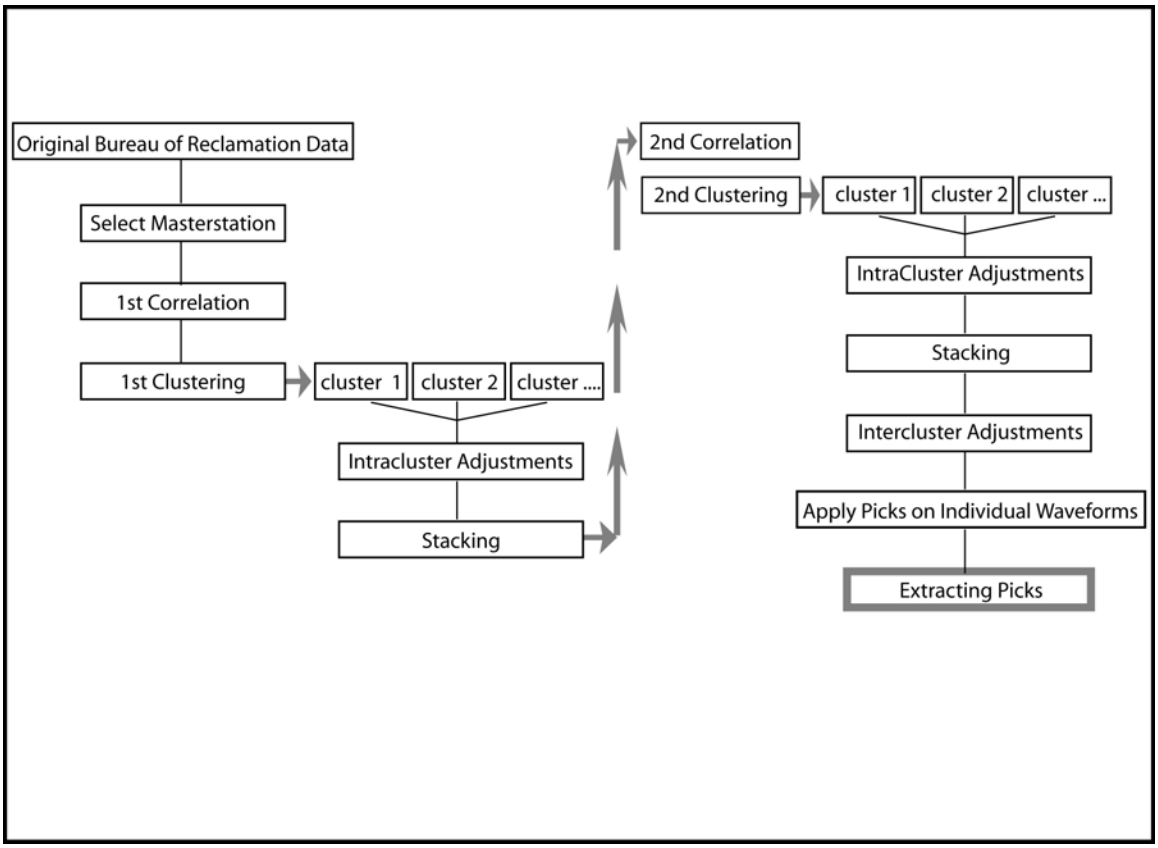

Figure 3.1. Schematic flow chart of the cross-correlation process using CCHAR [*Rowe*, 2000]. First earthquakes are clustered based on waveform similarity. Initial picks get refined and are used in the determination of the regional velocity models.

window of 64 milliseconds in duration is set to isolate the direct phase arrival, and can strongly affect waveform alignment and therefore has to be determined carefully [*Rowe*, 2000]. The cross-correlation coefficient cutoff for clustering must also be set accordingly. Relative time lag adjustments are first estimated for all phases within a cluster. These adjustments are necessary after all traces in a cluster have been aligned to one another thereby creating some traces to be shifted in time from their original arrival times.

Once relative lag adjustments are determined pick adjustments for all similar waveforms in each cluster are determined then stacked to create one waveform for each cluster [*Rowe*, 2000]. The corrected picks provide precise relative arrival times within a cluster; however, intercluster relationships must be addressed to achieve consistent intercluster picks, which correct the intercluster spatial relationship [*Matter*, 2005]. To address this issue, individual picks were adjusted and realigned waveforms were stacked to provide a composite representative waveform for each cluster, which then was analyzed for intercluster adjustments [*Matter*, 2005]. The lag and pick adjustments are once again applied to and estimated for each waveform in each cluster and then given the newer more precise picking times. The adjusted pick times are then used in determining the minimum 1-D velocity model.

3.1.2. Master Station Selection and Clustering Results

The master station for the Teton seismic network, MOOW, was chosen based on the station's data quality, waveform heterogeneity, number of recorded events, and the ability to produce as few orphan events as possible during the clustering process. This

station had 20% more recorded events than the majority of the other stations and has been operating for the entire duration of Jackson Lake seismic network. The data quality and waveform heterogeneity for the events recorded at this station showed clear first arrivals with minimal noise.

The preliminary cross-correlation procedure was employed using a time window of 64 ms that was determined by viewing the frequency of the incoming waves defined by a correlation length that encompassed the first arrival of the P wave. The cross-correlation coefficient cutoff value for clustering, which determines the threshold for clustering similar waveforms together, was set to 0.8, which *Rowe et al.* [2002] found to produce the best results with respect to the number of clusters and orphan events. Using these values and the master station, the preliminary cross-correlation was determined and all waveforms within each cluster were stacked.

To reduce the number of clusters a second correlation and clustering process were performed using the stacked waveforms as input [*Matter*, 2005]. These new events in each cluster were stacked once again and the final waveform for each cluster was determined and these new combined clusters were called megaclusters. Table 3.1 shows the clustering results for MOOW. The master station recorded 7,964 events out of 8,537 events. After the first clustering 2,403 clusters were found, and 1607 orphan events were not associated with any of the clusters. The second correlation and clustering of the stacked waveforms revealed a total of 834 megaclusters with only 483 events as orphans. The correlation window length was 64 ms. The cutoff coefficient for the clustering was 0.8. The table shows the station name, the number of recorded events, the mean

Table 3.1. Preliminary cross-correlation using the master station MOOW

Station	Events	1. Corr. Coeff	Clusters	2. Corr. Coeff	Clusters	Orphans
MOOW	7,964	0.872	2403	0.860	834	483

correlation coefficient after each correlation, the number of clusters after each clustering, and the total number of orphans after two clustering iterations.

Given the large number of 834 megaclusters shown in Table 3.1, I decided to only evaluate those megaclusters with at least 30 events. *Rowe et al.* [2002] suggested that it is not valuable to continue with the intracluster adjustments for megaclusters with fewer than 10-30 events. We chose to continue with only megaclusters that contained 30 or more earthquake waveforms. This reduced the number to 6 megaclusters, containing 64 events (megacluster1), 35 events (megacluster 2), 31 events (megacluster 3), 72 events (megacluster 4), 47 events (megacluster 5), and 68 events (megacluster 6). The final clustering of the entire data set was applied to all other stations, and therefore each station that recorded events in that cluster became a member of one of the six megaclusters.

Before continuing with the cross-correlation process, I evaluated more closely the individual megaclusters and their event correlations in time and space. Figure 3.2 shows the number of earthquakes per quarter year for all the events in megaclusters 1-6. These plots show that families of similar waveforms are not clustering in time. Instead, most of the clusters show activity for more than one time period. Figure 3.3 shows the spatial distribution of all the events in these 6 megaclusters. Each cluster is color coordinated

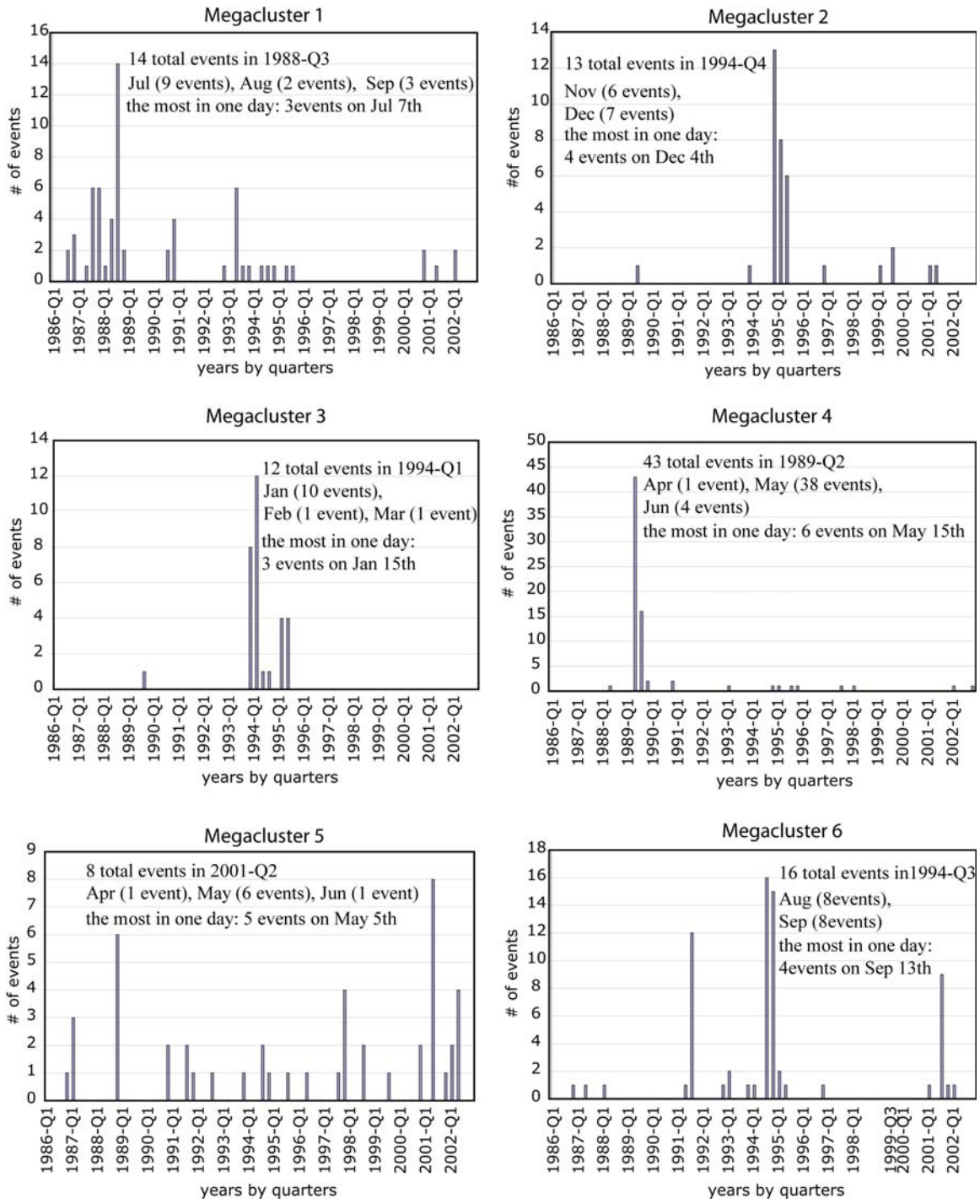

Figure 3.2. The number of earthquakes per quarter year of all six megaclusters. These plots show the that families of similar waveforms are not clustering in time. Most of the clusters show activity for more than one time period. The larger spikes in number of events in a given quarter year are labeled with how many events occurred in each month and the maximum number of events that occurred in one day.

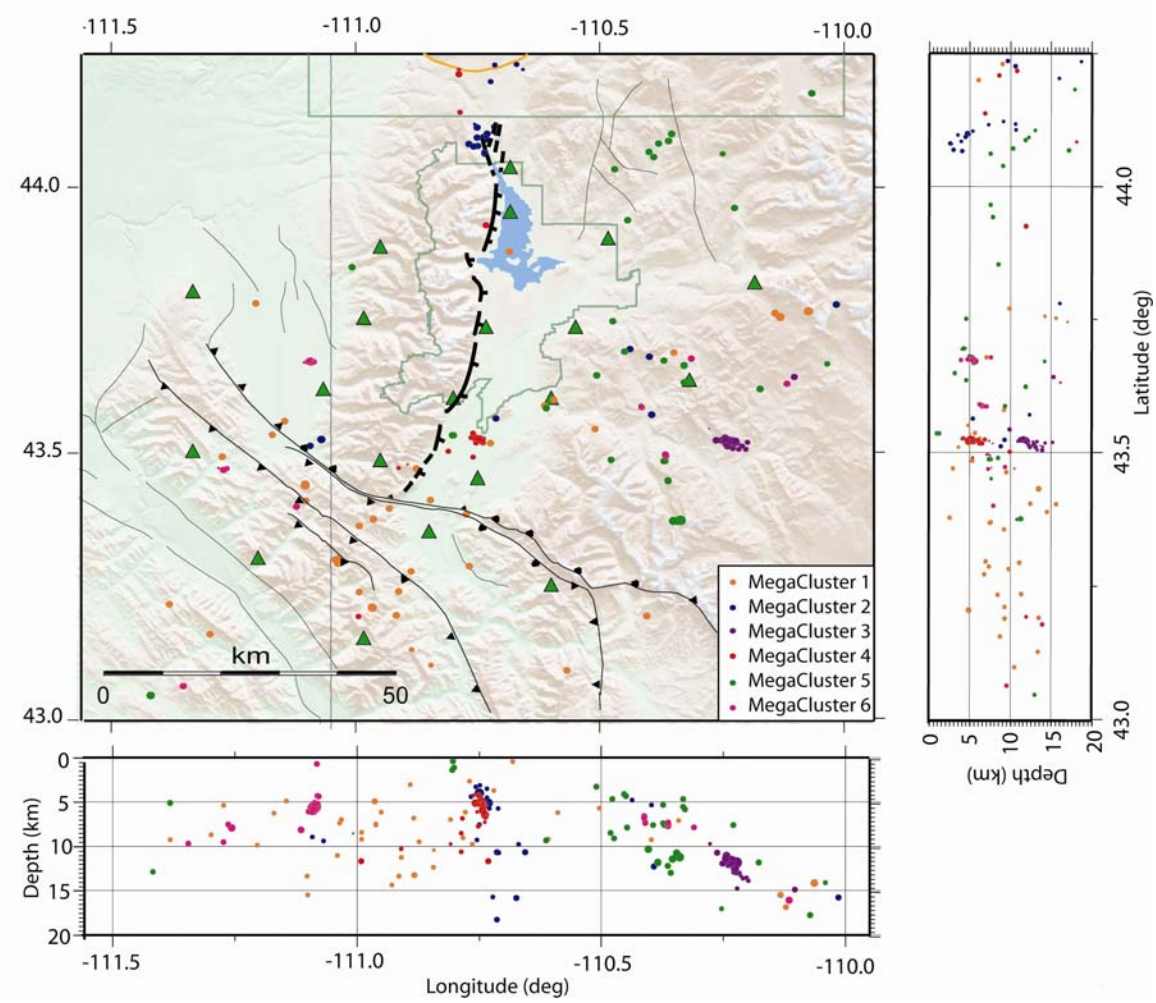

Figure 3.3. The hypocenters of all events in each of the six megaclusters. These plots show that families of similar waveforms are not clustering strongly in space. Most of the clusters show activity in more than one area. The megaclusters are color coordinated as displayed in the key. Seismic stations are shown by the green triangles. The bold black fault is the Teton fault and the smaller black faults are the Cache Creek, Jackson, and Absaroka thrust fault system. All other regional faults are gray.

and from this map view it is obvious that many of the events in each megacluster are not correlating with each other in space.

This is perplexing since earthquakes that show similar waveforms should have similar focal mechanisms and should be located close together. If they are not located close together, then path effects should perturb the waveforms. Perhaps the waveforms were not similar enough to provide a similar focal mechanism. It is also possible that this spatial observation is a consequence of the stacking procedure in which similar waveforms are mixed and correlated with less similar waveforms.

The observations we made in the previous results and figures display a concern regarding continuing on with the intracluster adjustments. In Figure 3.3 most of the clustered events are located outside the Jackson Lake seismic network. Therefore, the hypocenter locations of these events are poorly constrained and should not be used in the inversion to derive the 1-D and 3-D tomographic models. There are few megaclusters located inside the network that could possibly satisfy the criteria to be used in the tomography inversions. Given that only about 17% of the total seismicity recorded were in the megaclusters, the percentage of well-located clustered events could be even less. Therefore, we concluded that we could not improve the picks by cross-correlation better than we had originally picked.

3.2. Minimum One-Dimensional Velocity Model

Seismic tomography applied to the solid Earth is a nonlinear process [*Pavlis and Booker*, 1980]. The inverse problem of the 1-D local earthquake tomography is formulated as a linear approximation to a nonlinear function [*Kissling*, 1994]. Through

the use of this formulation, hypocenters and 1-D velocity model parameters, including station corrections, are determined and used as the initial reference model for the 3-D inversion. The resulting velocity model from the joint inversion of travel time data is defined as the "minimum 1-D model" [*Kissling*, 1988]. The minimum 1-D model calculated for the greater Teton area is described in this chapter and gives rise to the initial starting model for the 3-D inversion.

3.2.1. Theory

The coupled hypocenter-velocity problem is important to solve for when inverting for a minimum 1-D velocity model. There is more than just one unknown parameter and both the hypocenter locations and the velocity model are important unknowns. The determination of the minimum 1-D model was calculated using the program VELEST. The VELEST program is a FORTRAN77 routine that has been designed to derive 1-D velocity models for earthquake location procedures and as an initial reference model for seismic tomography [*Kissling et al.,* 1994]. VELEST iteratively solves the coupled hypocenter-velocity problem by simultaneously inverting for hypocentral parameters, seismic velocities, and station corrections. In both cases the forward problem is solved by full inversion of the damped least squares matrix.

Since the inverse problem is nonlinear, the solution is obtained iteratively, where one-iteration consists of solving both the forward problem and the inverse problem. For solving the location problem for local earthquakes, an additional singular value decomposition of the symmetric matrix is performed in order to calculate the eigenvalues, but this is only done in single-event mode. The calculation of the minimum

1-D model requires multiple iterations to select and test control parameters appropriate to the data set and problem. The complete explanation of the theory of solving the coupled hypocenter velocity model problem in the VELEST program is explained in great detail by *Kissling* [1988] and *Kissling et al.* [1994].

3.2.2. Calculation of the Minimum 1-D Model:

Results and Performance Tests

The first step in determining the minimum 1-D velocity model is to establish an *a priori* 1-D model. All available *a priori* information regarding the layered velocity model of the Teton area was obtained through researching previous studies on the area and communication with the Bureau of Reclamation regarding velocity models that were originally used to locate earthquakes in the region.

Previous studies by *Behrendt* [1968] and *Byrd* [1991] used seismic refraction data determined velocity models for the area south of the Jackson Lake. Their results provide P-wave velocity values for three layers. Three profiles were recorded using a series of eight linear geophone arrays that extended 27 km NE-SW from the Teton range front to the east side of Jackson Hole [*Byrd*, 1991]. The inverse-ray tracing models computed by *Byrd* [1991] revealed various velocity models for the basin down to a depth of 3 km. Byrd's velocity values, given a 75˚ E dip of the Teton fault, show 2.2 km/s at 0.8 km, 4.52 km/s at 1.6 km, and 6.14 km/s at 2.4 km. Combing this shallow velocity control from *Byrd* [1991] with the preexisting velocity model used by the Bureau of Reclamation to locate their earthquakes [*O'Connell et al.*, 2003] an *a priori* 1-D velocity model was determined. The final *a priori* information that was gathered was the reference station

for the inversion. The seismic station MOOW was chosen to be the reference station for its reliability and central location in the Jackson Lake seismic network (Figure 3.4), and its recording of more events than any other station in the network. Together, the model and the reference station comprise the *a priori* 1-D model (Figure 3.5) [*Kissling et al.,* 1994].

The second step in determining the minimum 1-D model is to establish the geometry and velocity intervals of plausible 1-D models. The complete data for the Teton region from April 1986 to December 2002 consisted of 8,537 located events obtained by the Bureau of Reclamation's Jackson Lake seismic network (Figure 3.6). The data were sorted to select the highest quality subset that could be used to determine the minimum 1-D model. Because of the inherent coupling between seismic velocities and hypocenter location only the highest-quality data could be used. The criteria for the highest quality provided a subset of 445 events with at least 10 zero-weighted first motion observations, RMS < 0.5, azimuthal gap < 160 degrees, and closest station to epicenter distance < 20 km. This high quality dataset as shown in Figure 3.7 was inverted for P-wave velocities and station corrections using the *a priori* 1-D model. For the inversion of this high quality set a damping coefficient of 0.01 was used for hypocentral parameters and the station delays and 1.0 for the velocity parameters. The hypocenters, station delays, and velocity parameters were inverted every iteration. This procedure was repeated with new updated velocities in the reference 1-D model, new station delays, and new hypocenter locations. The number of total iterations of this procedure increased until the RMS value reached a minimum after which perturbations

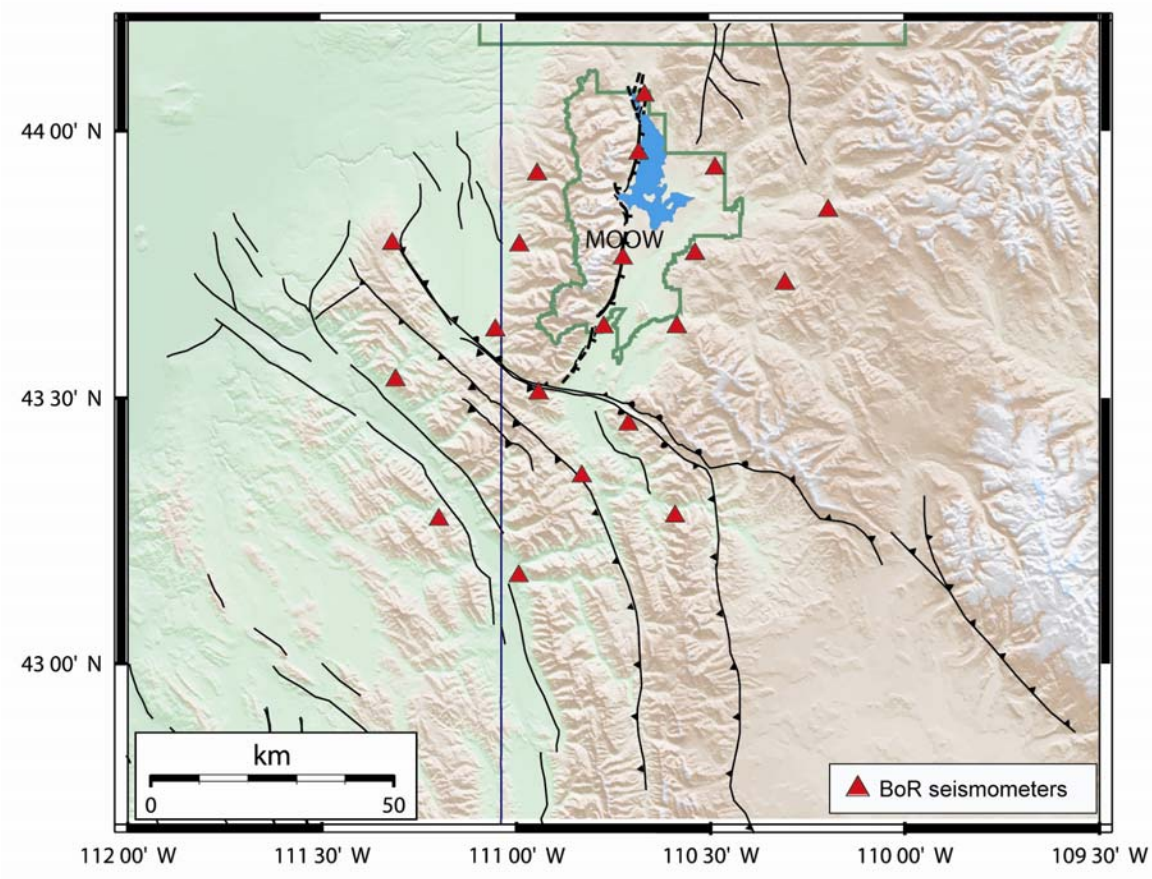

Figure 3.4. The seismic network of Grand Teton National Park. The Bureau of Reclamation operated the Jackson Lake Seismic Network from April, 1986 to December, 2002. The location of seismographs in the Jackson Lake Seismic Network is shown by the red triangles, with the station MOOW in the center of the network.

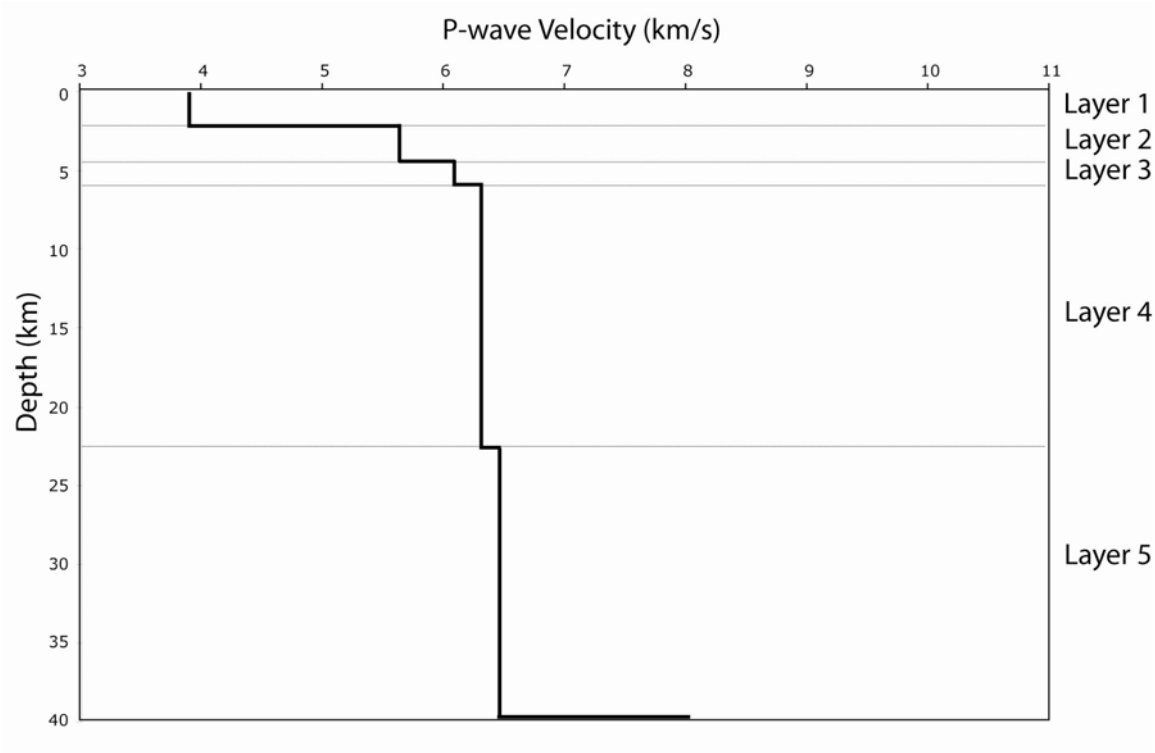

Figure 3.5. The original *a priori* model used in the VELEST program. This model was derived using information from the Bureau of Reclamation, *Byrd's* [1991] refraction inversion results, and information from the University of Utah Seismograph Station.

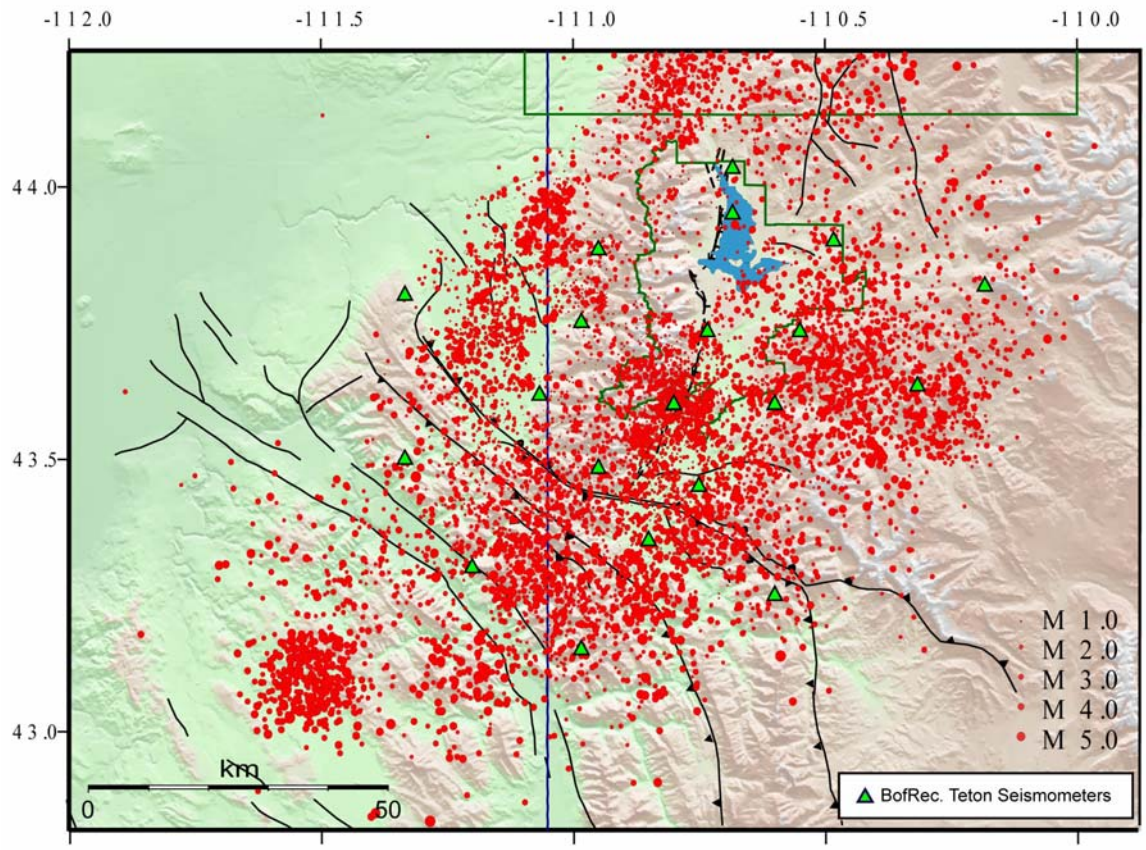

Figure 3.6. The seismic record for the greater Teton region from April 1986 to December 2002. The seismic record consists of 8,537 events as obtained and originally located by the Bureau of Reclamation's Jackson Lake Seismic Network.

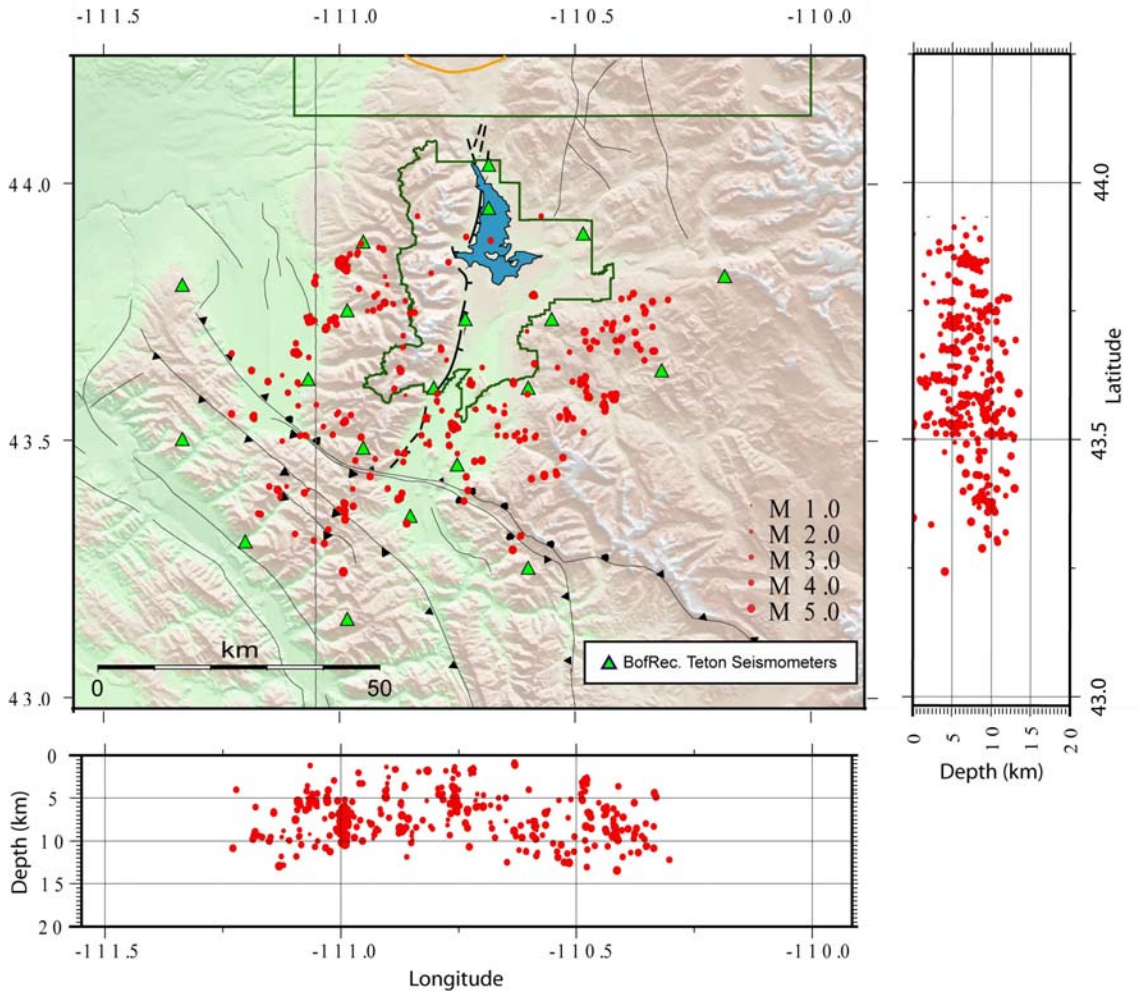

Figure 3.7. High quality earthquake data subset. The events in this subset consist of 445 total earthquakes with at least 10 zero-weighted first motion observation, an RMS value < 0.5, an azimuthal gap < 160 degrees, and the closest station to epicenter < 20 km. All the events are well with in the boundaries of the seismic network and they all have shallow depths that do not reach depths past 15 km. These hypocenter locations were determined by the Bureau of Reclamation's velocity model which is almost identical to the *a priori* model used in this paper to determine the minimum 1D model.

became statistically insignificant, yet the RMS value still remained above the predetermined picking error of the first P-wave arrival.

Given that the high quality subset used in this inversion had to contain at least 10 zero-weighted P picks the predetermined picking error for all the locations was about ±0.03 s as determined by C. Wood at the Bureau of Reclamation. The goal of this trial and error approach was to evaluate the solution space to estimate the global minimum and minimize the travel-time residuals. We simply looked for models (hypocenter locations, velocities, and station delays) that fit our data the best. Once the earthquake locations, station delays, and velocity values did not change significantly after each iteration and the total RMS value of all the events dropped significantly with respect to the first locations and the station corrections made geologic sense, then the resulting model was called the "updated *a priori* 1-D model with corresponding station delays" [*Kissling et al*., 1994].

The third step in determining the minimum 1-D model is to relocate all the earthquakes using the updated *a priori* 1-D P-wave velocity model including station delays in single-event mode (fixing the station and velocity parameters). The same high quality data set (445 events, 7,645 zero weighted P-wave arrival) was relocated, as was used in computing the updated *a priori* 1-D model.

The final step in determining the minimum 1-D model is to calculate the minimum 1-D model for the high quality data subset. This was similar to step two. However, in this step other initial velocity models were run in the inversion while keeping the same layering model but changing the velocity values. This method of varying the velocity models tests to see how well they converge to one local minima

given a wide range of varying input models. The damping parameters were set to 0.01 for the hypocentral and station delays, and 1.0 for velocity parameters.

Figure 3.8 shows the wide range of input velocity models holding the geometry fixed as well as the output models from the inversion of those models. Notice that not all outputs converge to this minima and could be caught on a local minima. The converging output models all reveal very low total RMS values around 0.05 s that are still larger than the 0.03 s P-wave picking error of the high quality earthquakes used in this inversion. The output models in this converged minima were averaged to determine a minimum 1-D model and tests were performed to determine the stability of the result. To test the true convergence of this 1-D model a high-low test was performed.

The high-low test displays one input velocity model that is identical to the averaged general 1-D model, but its velocity values have been systematically shifted by -2 km/s, and the other input velocity model that is identical but systematically shifted by +3 km/s. The reason for shifting the velocity models by -2 km/s and +3 km/s is to test the wide range of the velocity model space, given that these shifts are large as a percentage of the velocity. Both of these input models were inverted using the same damping parameters and methodology as explained above (inverting for velocity, stations, and hypocenters). Figure 3.9 shows how these input models converge back to the same minima and how low their corresponding total RMS values are. The second stability test performed on the average general 1-D model was to randomly shift the latitude and longitude of the epicenters by ± 0.6 decimal degrees (or ± 66.6 km latitude and ± 24.2 km longitude).

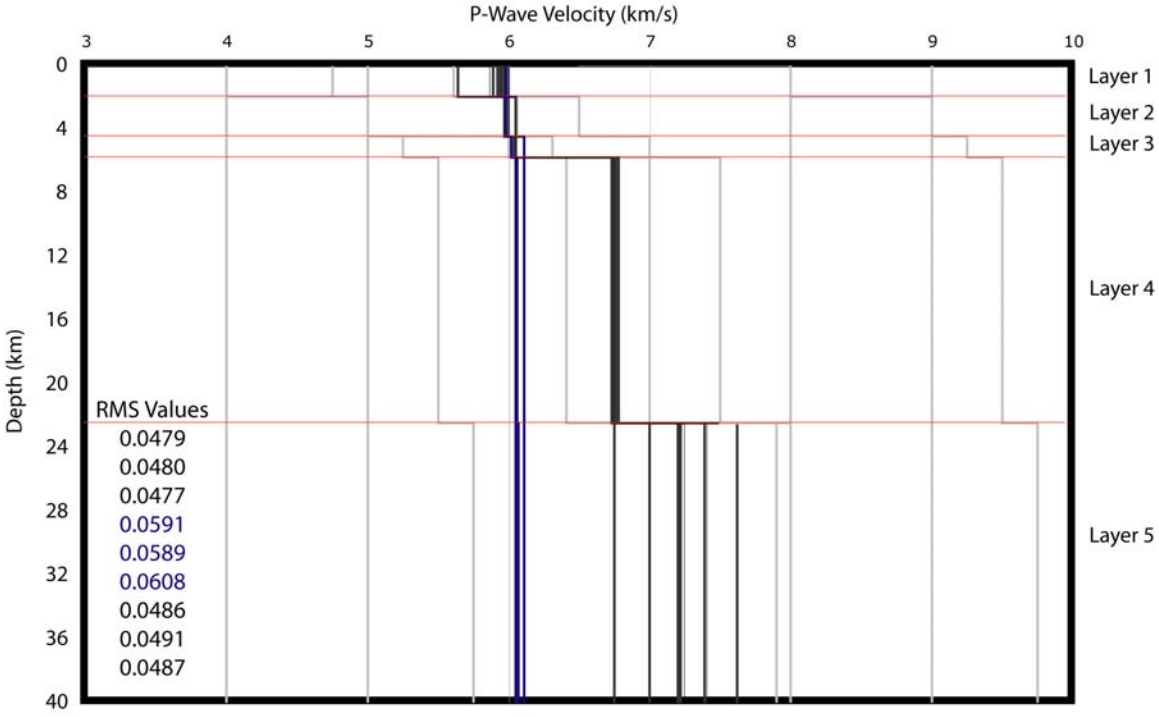

Figure 3.8. Input and output 1-D velocity models created using VELEST. The input models are displayed as solid light gray lines and the output models are represented by the blue and black solid lines. A wide range of input models displays how well all the models converge to one general minima. Notice that all outputs do not converge to this minima and could be caught on a local minima like those above caught at 6 km/s from 4 km to 40 km depth. The converging output models show very low RMS values yet they are still above the P-wave picking error. The larger RMS values in blue belong to those blue output models caught on the local minima that do not converge with the other models. The dark red horizontal lines show the tops of the new velocity layers as defined by the models.

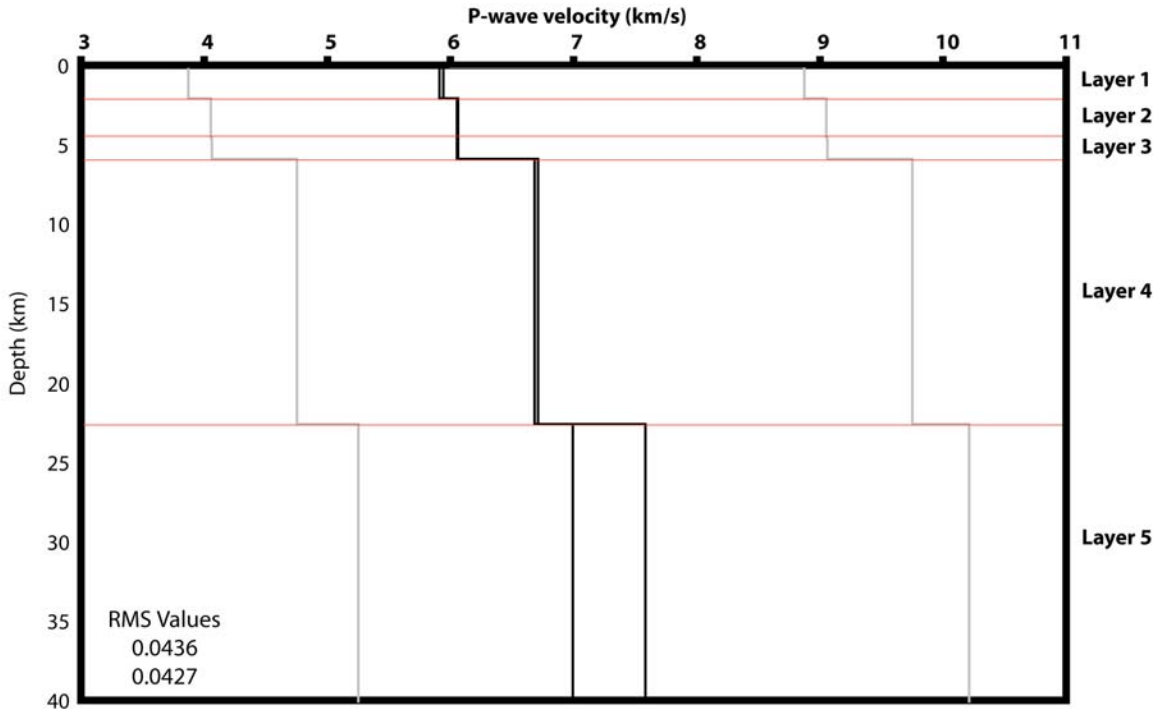

Figure 3.9. Input and output 1-D velocity models as a result of the high low stability test. The input models are displayed as light gray lines and the output models are represented by the black solid lines. The two input velocities have identical gradients. However they are systematically shifted to opposite sides of the model space to display the stability of the converged minima. Notice that the two output models converge nicely but when we pass a depth of 22 km we lose a bit of the convergence due to the lack of data.

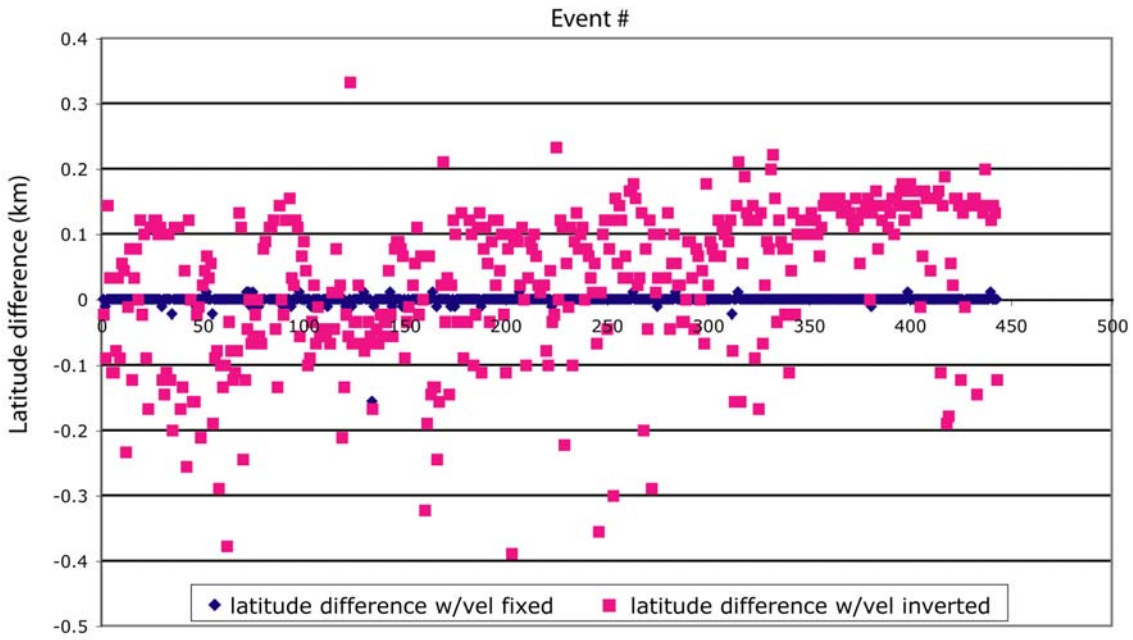

Figure 3.10. Stability test results from randomly shifted latitudes by +/- 0.6 decimal degrees (or +/- 66.6 km). The blue diamonds and pink squares display the difference between hypocenters determined by the average general 1-D velocity model and the newly relocated hypocenters by both holding the general 1-D velocity model and station residuals fixed (blue diamonds) and by jointly inverting for the velocity and station residuals (pink squares). These differences are reasonably small considering the maximum difference was allowed to vary by as much as 66.6 km. Positive difference values represent a shift of location to the north and negative values represent a southern latitude shift. Note that these hypocenters are from the high quality data subset.

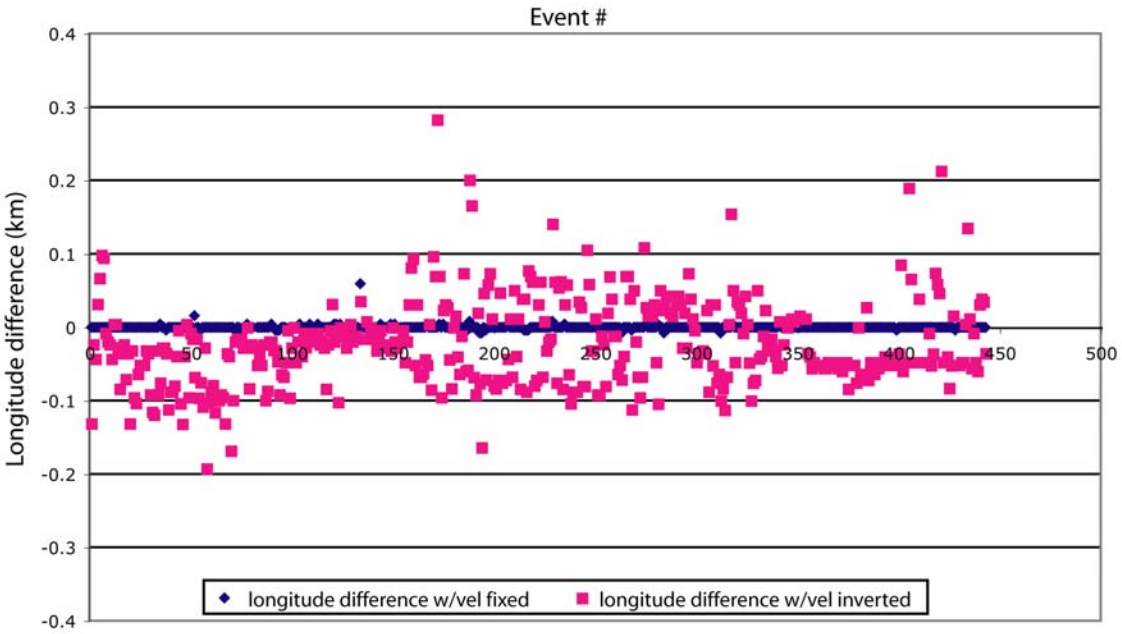

Figure 3.11. Stability test results from randomly shifted longitudes by +/- 0.6 decimal degrees (or +/- 24.2 km). The blue diamonds and pink squares display the difference between hypocenters determined by the average general 1-D velocity model and the newly relocated hypocenters by both holding the general 1-D velocity model and station residuals fixed (blue diamonds) and by jointly inverting for the velocity and station residuals (pink squares). These differences are also reasonably small considering the maximum difference was allowed to vary by as much as 24.2 km. Positive difference values represent a shift of location to the west and negative values represent an eastern longitudinal shift.

After the epicenters were randomly shifted (fixing depth) they were inverted using VELEST in single-event mode (fixing the station and velocity parameters). Figures 3.10 and 3.11 show the difference between the epicenters determined by the averaged general 1-D model and the newly relocated epicenters holding the general 1-D velocity and station residuals fixed. The third stability test used the same randomly shifted epicenters as before but inverting for velocity parameters and station delays. Using the simultaneous inversion mode all the model parameters were jointly inverted. Figures 3.10 and 3.11 also show the difference between the epicenters originally determined by the general 1-D model and the newly relocated epicenters inverting both velocity and station residuals.

The fourth stability test performed on the general 1-D model was to systematically shift the depths on all the high quality events by +5 km while holding the latitude and longitudes fixed. Once the depths were shifted the hypocenters were inverted using VELEST in single-event mode. Figure 3.12 shows the difference between the depth determined by the general 1-D P-wave model and the newly relocated depths holding the general 1-D velocity and station residuals fixed.

The fifth stability test used the same depth shifted hypocenters as before but instead of holding the general 1-D model fixed, the velocity model and station residuals were inverted as well. Using the simultaneous inversion mode, all the model parameters were jointly inverted and Figure 3.12 shows the difference between the depths originally determined by the general 1-D model and the newly relocated depths inverting both velocity and station residuals. There is much greater difference as compared to the test holding the velocity and station models fixed.

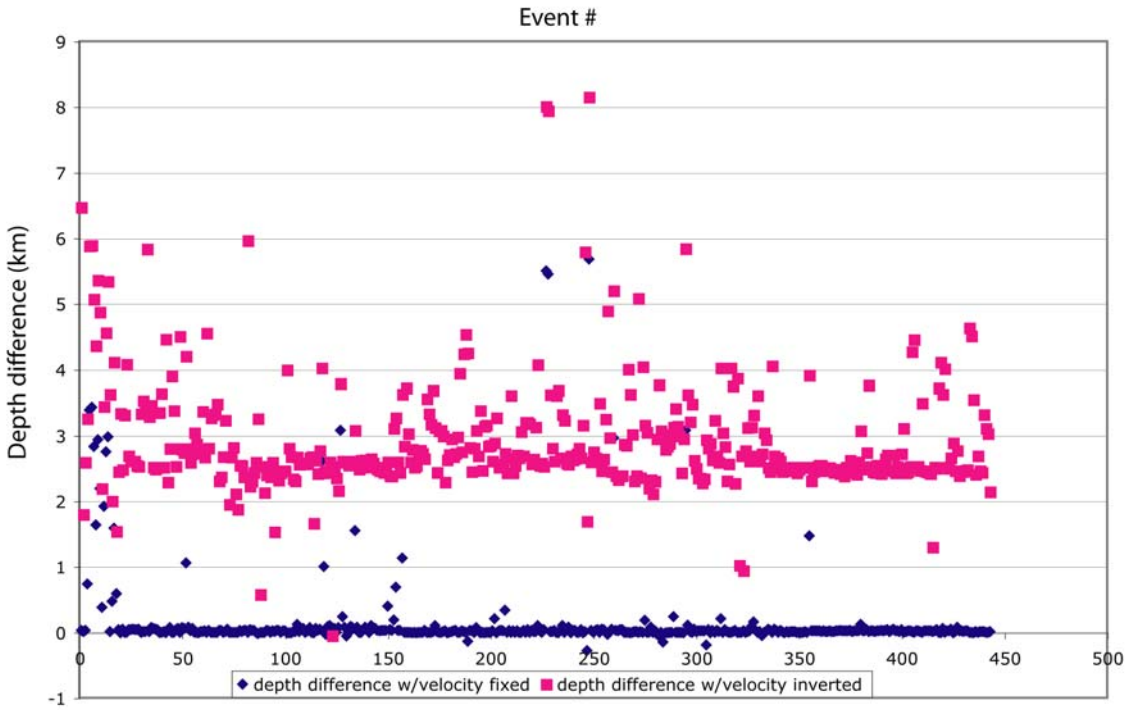

Figure 3.12. Stability test results from systematically shifted depths by + 5 km. The blue diamonds and pink squares display the difference between hypocenters determined by the average general 1-D velocity model and the newly relocated hypocenters by both holding the general 1-D velocity model and station residuals fixed (blue diamonds) and by jointly inverting for the velocity and station residuals (pink squares). The differences in depth for the events with the velocity held fixed are fair. However there are some outliers with differences greater than 3 km that raise questions on whether or not they should be included in the high quality data subset that was used to determine the minimum 1-D velocity model. The differences in depth from the events located jointly with the velocity inversion seem to have an average difference of about 3 km. This could be due to the lack of control we have on the focal depths of even the highest quality of hypocenter data. Also notice the same pattern of outliers with differences greater than 5 km. These will be addressed.

3.2.3. Discussion

The results and conclusions of the minimum 1-D model determination are summarized here. The convergence of the high-low test is very promising from depths of 0 km down to 22 km. From this test I believe that layers 1 through 4 are well resolved but in the last layer I found that I did not have any tight constraints on the true velocity values. Layers 1 through 4 contain 99% of all recorded seismicity in the Teton region at these depths giving a dense array of raypaths throughout these layers constraining the velocity model to one minimum model. However, in the last layer there are no events occurring at these depths giving little to no constraints on the velocity model at depth. At the shallow layers from 0 km to 2 km we see a lot of variance among our output models, but to help constrain these variations we used refraction data results [*Behrendt*, 1968; *Byrd*, 1991] from the Jackson Hole valley. The shift tests show promising results for the minimum 1-D model and a better understanding of our data set. One result that stands out is the depth of systematic shift tests. Notice that when we inverted for the velocity and station residuals as well as the hypocenters the depths did not come back to the original depths determined by the minimum 1-D model. However, while holding the velocity and station residuals fixed, the depths did come back to the original depths determined by the minimum 1-D model.

There are some events in the depth systematic shift tests that seem to be outliers and reach a hypocenter difference greater than 5 km. Table 3.2 lists these outliers and their qualities. These outliers are from both the depth shift tests where the velocity was held fixed and where the velocity was inverted jointly with hypocenter locations and station residuals. The outliers in Table 3.2 show events that displayed depth differences

Table 3.2. List of outliers from the systematic depth shift test

Event #	Magnitude	Depth	Gap	RMS	#of 0 Weight P Picks	Station dist. (km)
1	3.26	5.8	159	0.05	13	3.7
4	1.61	4.21	115	0.04	10	7.8
5	1.8	1.35	114	0.06	11	7.7
6	1.84	1.6	115	0.04	10	7.8
7	2.08	1.73	112	0.06	14	7.6
8	1.86	1.64	112	0.06	15	7.5
9	1.75	1.7	114	0.07	11	7.5
10	1.83	1.65	118	0.05	11	7.3
12	1.77	1.14	85	0.04	12	6
13	1.96	1.74	109	0.08	10	7.2
14	1.71	1.61	120	0.04	10	7.9
17	1.63	1.73	122	0.04	10	7.8
33	1.69	1.68	110	0.05	10	7.5
52	1.91	1.58	154	0.04	10	5
82	2.67	8.02	133	0.03	12	7.7
118	1.93	1.78	141	0.05	10	7
119	2.45	3.39	141	0.04	12	7.2
127	1.87	1.35	140	0.05	10	7.1
154	1.73	4.17	99	0.06	10	4.5
157	2.13	2.17	134	0.07	10	8.4
227	2.15	1.69	68	0.08	11	8.5
228	1.82	1.62	68	0.08	10	8.4
246	2.61	4.62	159	0.08	10	15.8
248	1.68	1.35	102	0.08	10	8.6
257	2.47	5.82	135	0.05	13	11.1
260	2.08	1.59	103	0.05	10	7.5
275	2.76	5.78	108	0.07	10	14.7
295	2.38	3.66	149	0.07	13	11.2

greater than 4.75 km for the depth shift test where the velocity was jointly inverted, and 1.75 km or greater depth differences for the shift test with the velocity held fixed.

This table also provides insight into understanding the data and the criteria that were initially set to generate the highest quality data subset. Figure 3.12 also shows these outliers and how much they vary from the mean. All of these outliers deviate from the mean greatly by more than 20%, and they all have one thing generally in common: their large distances from the epicenter to the closest station, which on average is 7 km.

The criteria for determining the highest quality data subset included the station distance being less than 20 km from the epicenter. These depth shift tests suggest that the station distance criteria must be more strict than originally planned. To resolve this problem the criteria will be changed to state that the closest station must be less than or equal to 1.5 times the focal depth. These new criteria should help point out data were the focal depths are best resolved, and thereby giving the highest quality subset of hypocenters. These new criteria were used to test the accuracy of the minimum 1-D model. Using the new subset, the velocity model output was almost identical to the original minimum 1-D model. Given this confidence in the stability of the minimum 1-D model and how well it satisfied all the tests, this model became our final minimum 1-D model.

The final station delays for the final minimum 1-D model are shown in Figure 3.13. Note that all the stations have positive station delays and therefore must lie on local low-velocity areas with respect to the reference station and the velocity of the first layer. These station corrections correlate with the near surface geology since the reference

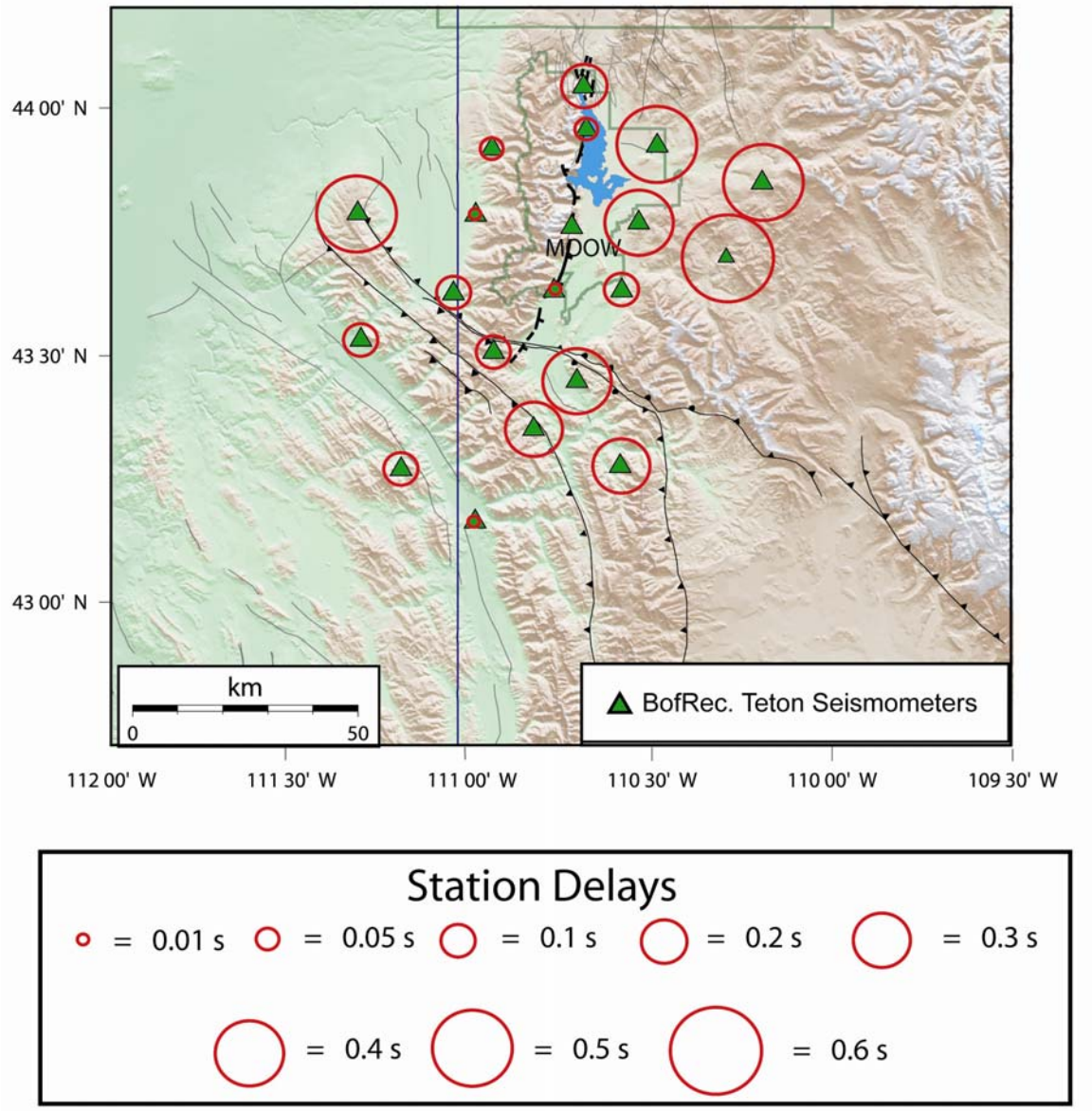

Figure 3.13. The final station residuals generated from the minimum 1-D velocity model. All the stations have positive travel time residuals and therefore must lie on local low velocity areas with respect to the reference station, MOOW, located in the center of the network along the Teton fault. The station delay for the reference station is always zero.

station MOOW is located on the bedrock of the Teton Range near the Teton fault and all other stations are located in small sediment valleys through out the region. Having determined the final minimum 1-D velocity model and corresponding station delays, I found that from the stability tests that there are some things we can resolve and some that we cannot. I then began with multiple *a priori* models and they were not all as consistent as this final model. Given that this model has some velocity layers that we were unable to resolve, it is still the model that best resembles the *a priori* information and therefore is our minimum 1-D model. Table 3.3 shows the final minimum 1-D model as it will be used as the initial starting model for the 3D velocity model.

3.3. Three-Dimensional P-Wave Tomography

The minimum 1-D model discussed in the previous section was used as the initial starting model for the 3-D inversion of the hypocenter locations and P-wave velocities. Through a series of steps, as described in this chapter, this 1-D model will be extrapolated onto a 3-D velocity grid and into the final 3-D tomographic image. A series of integrity tests will be performed to confirm the quality of this final velocity model to gain a better understanding of the crustal structure of the Teton area.

Table 3.3. The final minimum 1-D velocity model

Minimum 1-D Model		
Layer	Depth	P-wave Velocity
1	0	3.79
2	2	5.92
3	4.5	6.04
4	5.8	6.05
5	22.5	6.60
6	40	7.28

3.3.1. Theory

Determining the 3-D velocity model requires solving for the coupled hypocenter-velocity problem. The arrival time of a seismic wave generated by an earthquake is a nonlinear function of the station coordinates, the hypocentral parameters (including origin time and geographic coordinates), and the velocity field [*Kissling et al*., 1994]. The arrival times and station locations are the only measurable quantities, leaving the hypocenter parameters and the velocity field as the unknowns. To jointly solve for hypocenter locations and 3-D velocity field in this nonlinear problem, we used the computer code SIMULPS14 [*Thurber*, 1983*; Eberhart-Phillips*, 1990]. This program was extended by *Haslinger and Kissling* [2001] for full 3-D ray shooting. SIMULPS14 solves the nonlinear, coupled hypocenter-velocity problem by a linearized, iterative, damped least-square scheme [*Husen*, 2003]. Each iteration inverts for Vp variations as well as for hypocenter locations. After each iteration new ray paths and new travel time residuals are computed using the updated velocity model. The complete explanation of the methodology for solving the coupled hypocenter-velocity problem in the SIMULPS14 program is given in papers by *Eberhart-Phillips* [1990] and *Thurber* [1983].

3.3.2. Calculation of the 3-D Vp Model

All 8,537 earthquakes of the Teton catalog were relocated using the minimum 1-D model and the probabilistic relocation method NonLinLoc [*Lomax et al*., 2000]. The group of high quality hypocenters that had the smallest errors associated with their 1-D locations were chosen to be used in the 3-D velocity model determination. I point out that it is important to use hypocenters that are well constrained and will not likely vary

much from their 1-D to 3-D hypocenter locations. The high-quality data to be used in the 3-D inversion for hypocenter locations and seismic velocities were chosen by both a selection criterion based on error estimates computed by probabilistic earthquake relocation [*Husen*, 2003] and traditional selection criteria.

The probabilistic selection criteria are based on using the output information such as maximum likelihood hypocenter locations, expectation hypocenter locations, and error in the vertical direction from the NonLinLoc probabilistic relocation method. The probabilistic relocation method determines both a maximum likelihood hypocenter and an expectation hypocenter location derived from predicted travel times. The maximum likelihood hypocenter is considered the optimal hypocenter location determined by the NonLinLoc program, and the expectation hypocenter location is the traditional Gaussian or normal estimators obtained from the gridded values of the normalized location probability density function.

Large differences between the maximum likelihood and the expectation hypocenter locations can result from an ill-conditioned location problem [*Lomax et al*., 2000], and location uncertainties can be strongly irregular or show multiple minima. By selecting events that have only small (less than 0.5 km) differences between their maximum likelihood and expectation hypocenter locations, we ensured these events would have good uncertainty location estimates. I discuss the NonLinLoc program and its theory in more detail in section 3.4.

To ensure the high quality events with small differences, I selected hypocenters that had a difference of less than 0.5 km between their maximum likelihood and expectation epicenters, and with a difference of less than 2 km between their depth

values. These events selected all had uncertainties that were ellipsoidal in shape, implying that the error ellipsoid is a good approximation of the true errors. In general uncertainties are ellipsoidal in shape for hypocenter locations, due to the geometry of usually small local seismic networks. Earthquakes located inside the network boundaries tend to have smaller horizontal errors associated with their epicenters and larger errors associated with the depth of the hypocenter. These errors are graphically drawn from the maximum likelihood hypocenter in 3-D with the vertical error bar being typically twice as long as the horizontal error bars. This gives the error boundaries of the hypocenter location a geometric shape of an ellipsoid.

Though these events had well-located epicentral coordinates with errors less than 1 km, the depth errors were much larger by 2 or 10 times that of the horizontal errors. This larger vertical error is the length of the major half axis of the error ellipsoid, and was also used as a key selection criteria.

Hypocenter locations fitting the prior selection criteria with a vertical error less than 5 km were selected for the high quality data to be used for the 3-D velocity inversion. This vertical error limit was selected so the high quality hypocenters would not have a depth error greater than the depth spacing in the 3-D velocity model grid. This is important to ensure the events used in the 3-D velocity inversion do not have errors that are greater than the model parameterization grid spacing. The larger the error associated with the selected hypocenters in the inversion the larger the model spacing must become. For example, a model with spacing of 5 km in the horizontal and 10 km in the vertical should only use events that have horizontal errors less than 5km and vertical errors less than 10 km. Given the parameters and these selection criteria we determined

2,056 total events were high-quality hypocenters that we could use in our 3-D velocity inversion.

These 2,056 high-quality events were compared to the 2,147 events selected by the traditional selection criteria (gap < 180°, RMS < 0.5, number of observations ≥ 8, and distance to closest station < 1.5* focal depth). All of the high-quality events determined from the probabilistic criteria also passed the traditional selection criteria. The events that passed the traditional selection criteria but failed the probabilistic selection criteria were all events that had larger picking errors and few zero-weighted P-picks. The goal of the selection criteria based on NonLinLoc is to first select those earthquakes that show uncertainties that are ellipsoidal in shape, and then choose the earthquakes with the smallest errors.

This is precisely what we are trying to achieve when using the traditional selection criteria. However, before using these other selection criteria we were not able to justify these criteria choices since we did not have the information on the full error estimates of the hypocenter locations. By using both of these selection criteria we were able to determine that the choices for the traditional selection criteria were adequate, but might contain some outliers with larger errors than expected. The final high quality events contained the smallest hypocenter error uncertainties and fit all the traditional selection criteria. In total, 2,056 events with 30,904 P-observations were used in the 3-D P-velocity inversion (Table 3.4).

The model parameterization of the 3-D model was based on the average station spacing and earthquake distribution throughout the Teton region. Two model

Table 3.4. Number of observations and unknowns for the 3-D Vp inversion

	knowns		unknowns (inverted for)			over determination Factor
	P-obs	S-obs	model	hypocentral	total	
Vp	30,904	--------	1,125	8,224	9,349	~ 3.3

parameterizations were originally planned to account for the heterogeneous earthquake and station distribution.

A coarse grid spacing of 10x10 km was chosen to account for the Teton regional area with uneven distributions of stations and earthquakes (Figure 3.14). A fine model parameterization of 5x5 km was chosen to view the area of dense station and earthquake distribution. In this paper only the coarse 10x10 km model will be discussed; however, we are in the process of running this finer model. The depth spacing for the coarse inversion varies from 5 km in the upper layers to 10 km in the lowest layers at 15 to 25 km (Figure 3.14). The velocities from the minimum 1-D model were extrapolated on the 3-D grid as shown in Figure 3.15. We choose our model parameterization by running single-iteration inversions for different model parameterizations.

The model parameterization selected represents the finest possible model parameterization without showing strong heterogeneous ray coverage (Figure 3.16) [*Husen*, 2003]. All of our model parameterizations show homogeneous ray coverage in the center of the model. However, we chose to invert first for a coarse model followed by a fine gridded model. We felt the fine grid model would only be appropriate to use in the center of the model were ray coverage is dense, and would not be useful in the outer sections of the region. Therefore, a coarse model parameterization was chosen to first determine the velocity structure of the entire region and determine if the event data had

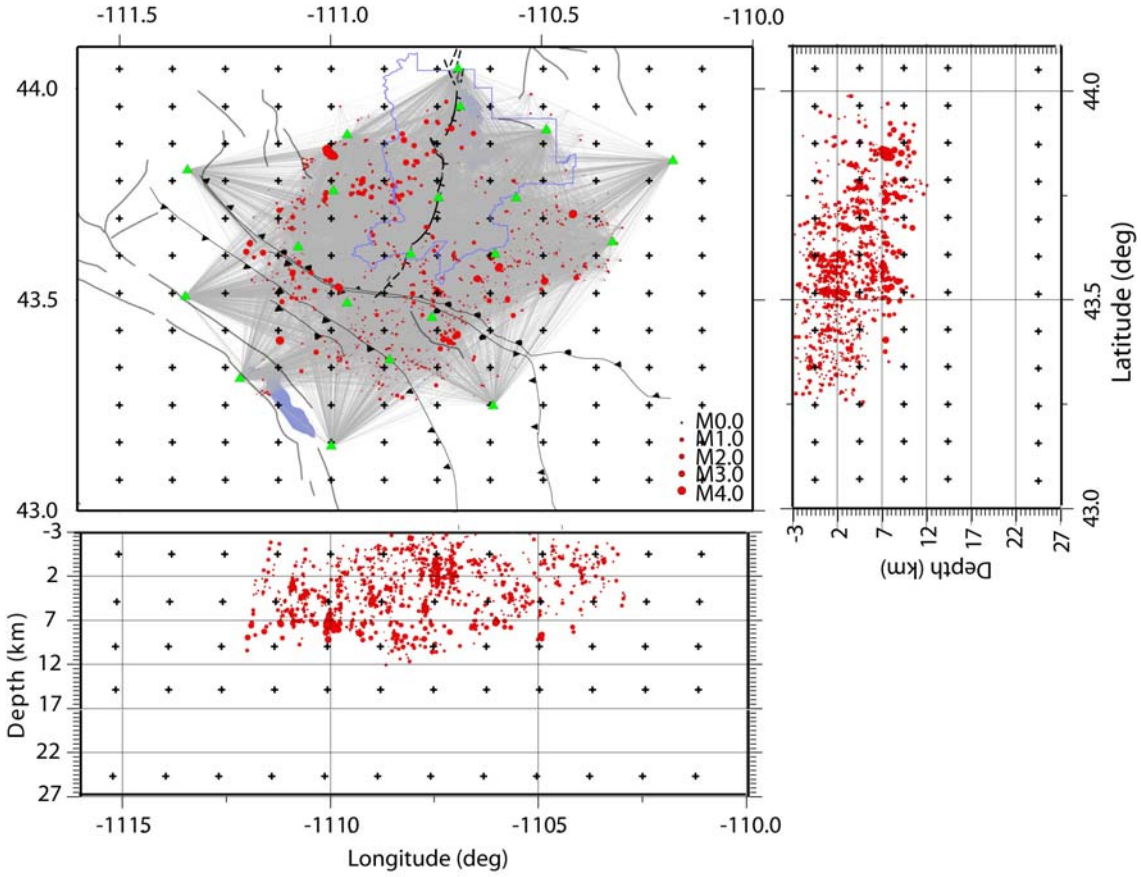

Figure 3.14. Coarse grid node layout of the Vp inversion. Grid nodes are spaced 10 km apart in the horizontal and at 5 km to 10 km in the vertical. Hypocenter locations represented by red circles were chosen for this tomographic inversion and are shown in map view and vertical cross sections in E-W and N-S directions. P-wave ray coverage is shown by the gray lines connecting the seismic stations in green with the epicenter locations. The Teton National Park is outlined by the blue lines. The thick black lines represent the regional faults with the Teton fault located in the center of the Teton National Park boundary.

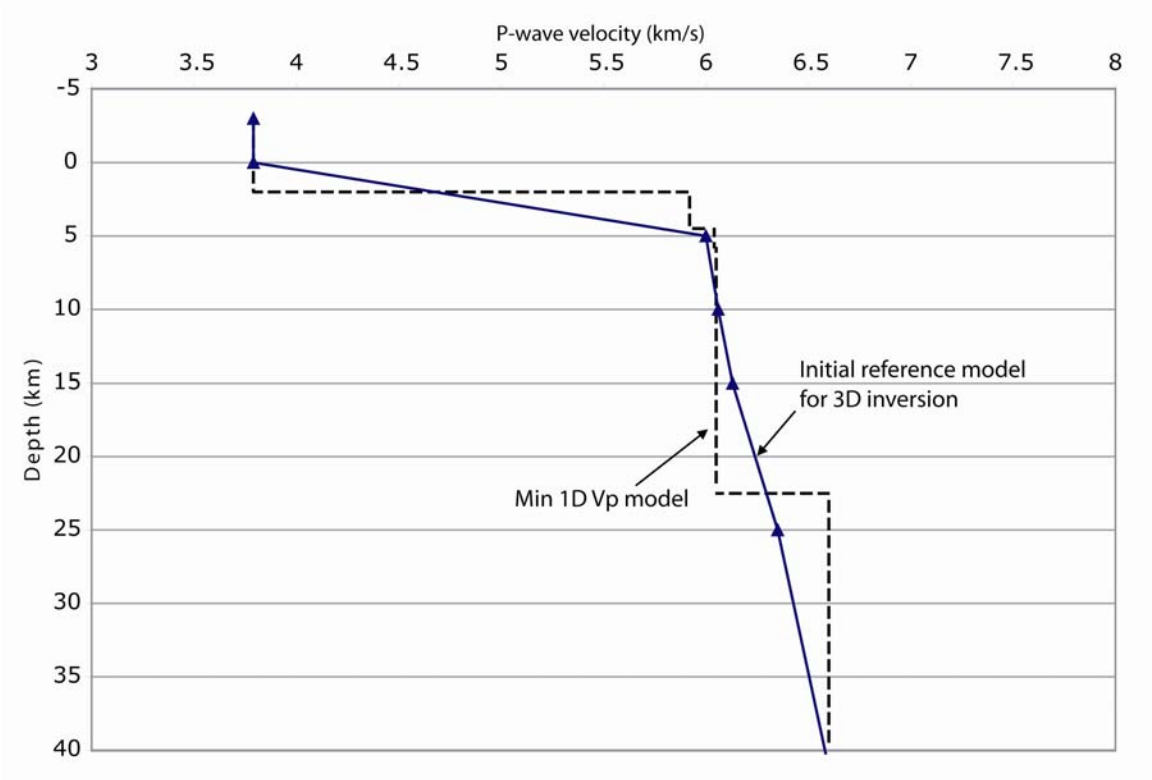

Figure 3.15. Minimum 1-D Vp model versus the initial 3-D Vp model. Minimum 1-D Vp model is represented by the dashed gray line. The initial reference model for the 3-D Vp inversion is represented by the blue line. The blue triangles denote the depth layers that have been defined and the velocity has been liner interpolated in between each defined depth layer.

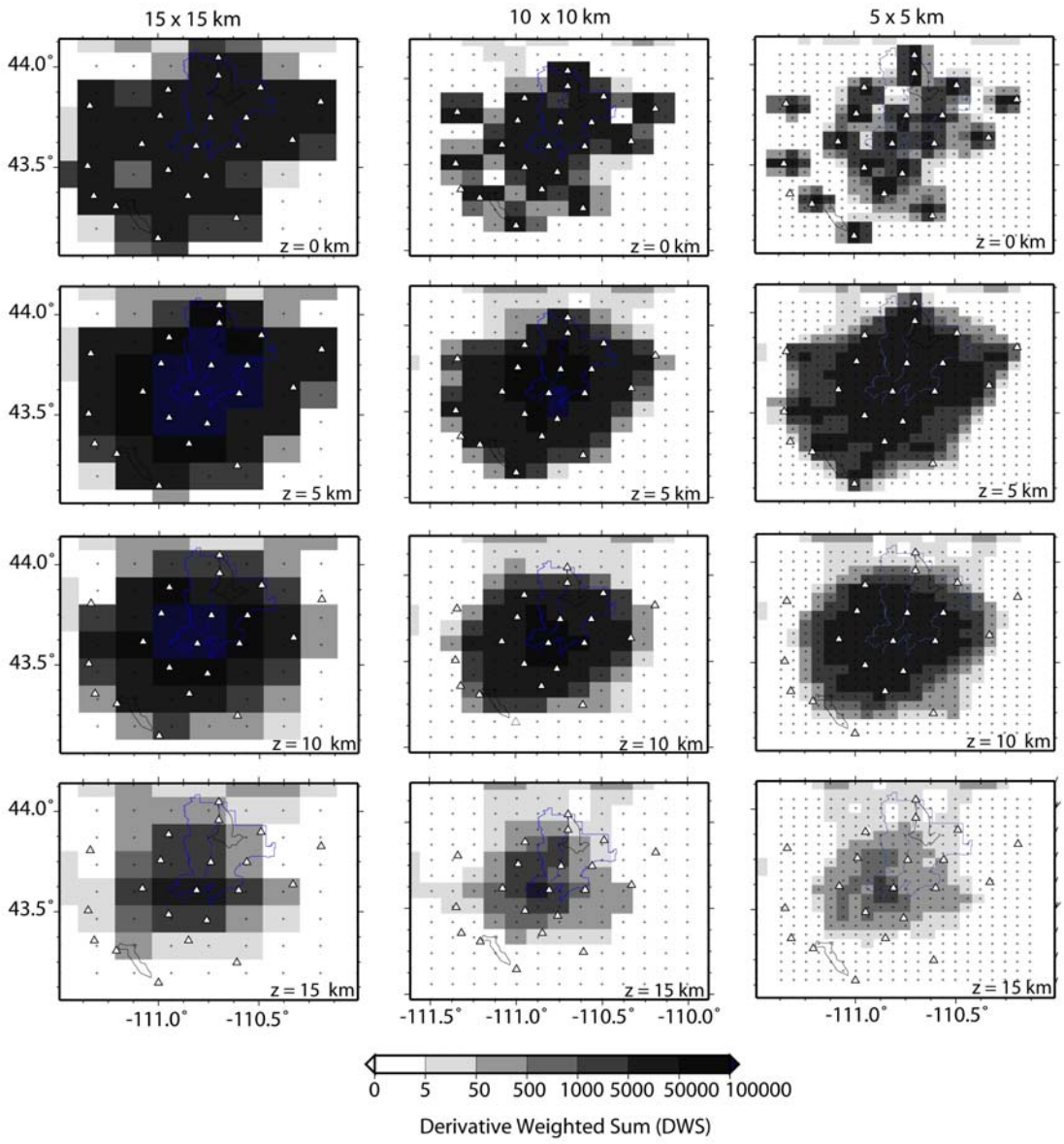

Figure 3.16. Derivative weighted sum distribution for different model parameterizations. Horizontal plane views show different depths and grid node spacings. White triangles represent seismic stations and black crosses show grid node positions. The Teton National Park is outlined in blue lines, and the Jackson Lake and Palisades Reservoir are outlined in black lines.

high resolution capabilities. The final velocity model from the coarse model can then be linearly interpolated onto the fine grid node spacing and used as an initial velocity model for the finer grid model.

Damping is a critical parameter in the inversion [*Kissling et al*., 2001], affecting both results and resolution estimates, including the diagonal element of the resolution matrix. Low damping values will lead to a complex model with a relatively large reduction in data variance, whereas high damping values will give a smooth model with a small data variance reduction [*Husen*, 1999]. A damping value that is just right will allow a large reduction in data variance but will not increase the model variance, giving a model that can image complex structures as smooth images. Following the method of *Eberthart-Phillips* [1986], a series of single iteration inversions with varying damping values were completed and a damping value of 100 was initially chosen for the 3-D P-wave inversion.

By plotting data variance against model variance, the best damping value can be selected to reduce the data variance without strongly increasing model variance (Figure 3.17) [*Eberthart-Phillips*, 1986]. We did not invert for station delays, and the results in Figure 3.17 show the data variance stayed nearly constant with decreasing damping. Therefore station delays to compensate for near-surface heterogeneities beneath the stations were not needed to stabilize the inversion process.

Tests with synthetic data as described later show decreased amplitudes of the anomalies using damping values of 100 and 500. A damping value of 500 is also well-suited for the model parameterization, as shown by the trade off-curve. Initially a damping value of 100 was chosen based solely on the trade-off curve; however, in

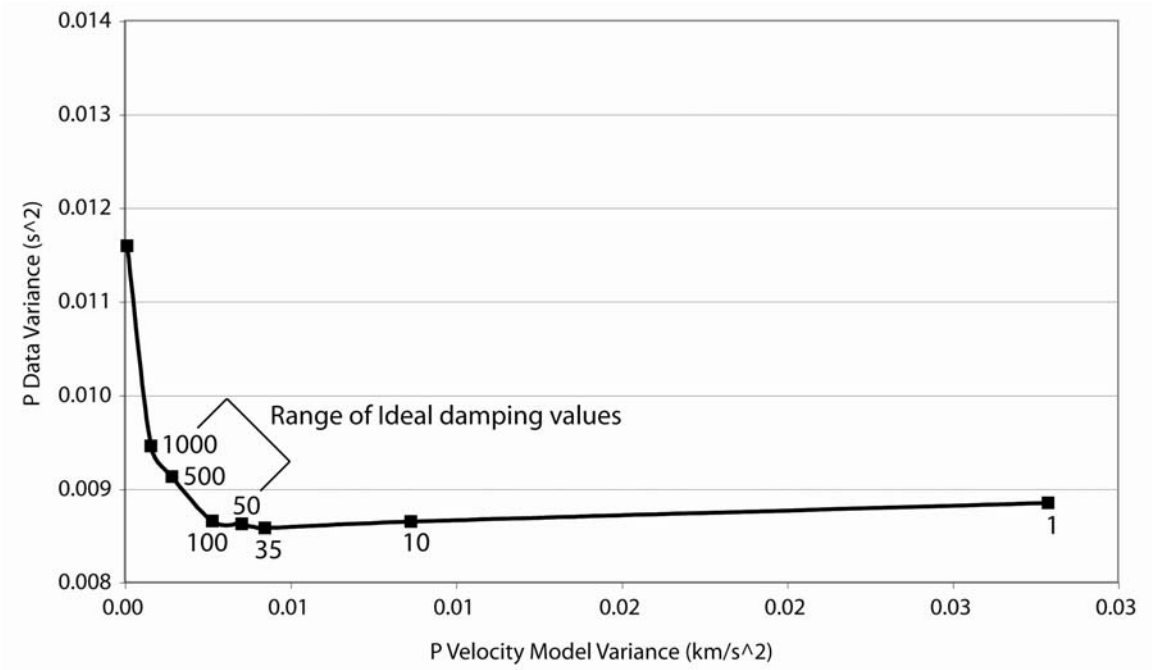

Figure 3.17. Trade-off curve to determine the damping value for Vp inversion. A series of iteration inversions were performed with these varying damping values. The damping value of 100 shows a good decrease in data variance and a decent increase in model variance. The damping value of 500 would also work for this coarse 10x10 km model parameterization.

synthetic data tests we found that using a damping value of 500 greatly reduced vertical and horizontal smearing in the velocity model while still maintaining the synthetic velocity structure.

The inversion of the coarse model with extrapolated velocities of the minimum 1-D model onto the 3-D grid converged after five iterations. The model converged after showing that RMS reduction, data variance, and model variance values were leveling out and not changing significantly from the last two iterations. This indicates that the model reached a minimum, and ideally it is the global minimum and not just a relative minimum. There was an RMS reduction of 31% and a reduction in data variance of 52% relative to the final 1-D model and an RMS reduction of 59% and data variance reduction of 88% relative to the initial 1-D *a priori* data error (Table 3.5).

Station corrections were not inverted for in the coarse grid model since all the stations used in recording the events were located inside the coarse grid model parameterization. Therefore, there was no need for station corrections to account for the velocity variations between the edge of the grid and the station. Also, all the stations in the network that recorded events for these high quality data were located on bedrock. There are two stations in the Jackson Lake seismic network that are located on soil sites near Jackson Lake Dam, but they did not record any events in the high quality data set.

Initial runs of the inversion showed a low reduction in the data variance of 10% just by relocating the hypocenter locations prior to the inversion for velocities. Hypocenter locations were shifted on average by 0.15 km in epicenter and 1.6 km in depth. This small change indicated the hypocenter locations do not depend strongly on

Table 3.5. RMS, data variance, and model variance of the first Vp inversion

1D -> 3D	RMS	data variance (s^2)	Model variance (km/s^2)
initial 1-D *a priori* data	0.24	0.078	
final 1-D data	0.14	0.019	0.0036
final 3-D data	0.097	0.009	0.0070
final reduction (rel. to initial 1-D *a priori* data)	~59%	~88%	
final reduction (rel. to final 1-D data)	~ 31%	~ 52%	

the station delays of the minimum 1-D model, which were initially set to zero in the inversion.

Velocity perturbations relative to the minimum 1-D model after five iterations are shown in Figure 3.18, and two different color scales were used in Figure 3.19. The first color scale was the standard color scale for viewing velocity perturbations. However, we found that based on our "noise level" in terms of the velocity change, we should adjust our color scale. Initially, the color scale was white from roughly -0.5% to +0.5% and at -1% to +1% we resolved high and low anomalies. However, I sensed that anomalies at 1% were not meaningful when considering the *a priori* data error and how it relates to perturbations in velocities since it was such a small velocity change.

To compute the "noise level" of our data, we considered the volume around a single model parameter and computed the travel time for a ray through the volume along the diagonal of the grid block. In our case, we had a grid spacing of 10x10x5 km and the diagonal was equal to 15.8 km. Assuming a velocity of 5.5 km/s we ended up with a travel time of 2.87 s. Then taking our average picking error of 0.15 s, we computed a

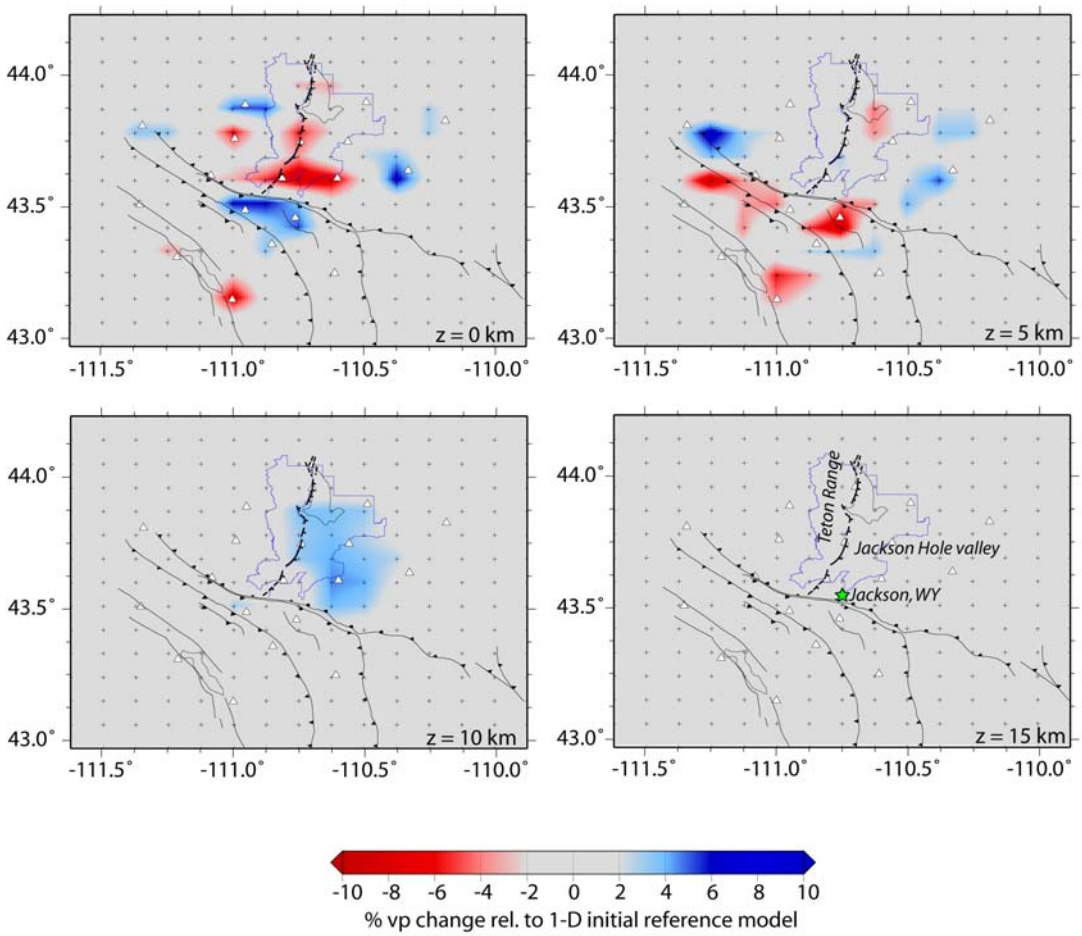

Figure 3.18. Horizontal plane view of the final 3-D inversion solution with velocity perturbations relative to those of the minimum 1-D model. The seismic stations are marked by the white triangles. The Teton National Park boundary is represented by the blue lines. The Teton fault is marked by the blue or heavy black lines. To the west of the Teton fault lies the Teton Mountains predominantly composed of Precambrian and Paleozoic bedrock. To the east of the fault lies the Jackson Hole valley composed of Tertiary and Quaternary sediments. The green star represents the town of Jackson, WY.

Figure 3.19. Horizontal plane view of the final 3-D Vp model with different color scales. Horizontal plane view of the final 3-D inversion solution with velocity perturbations relative to the minimum 1-D model. The seismic stations are marked by the white triangles. The Teton National Park boundary is represented by the blue lines. The Teton fault is marked by the dark blue lines. Figure (a) shows the velocity perturbations using the initial color scale (left column), and figure (b) shows the velocity perturbations using the updated color scale (right column) that is the same figure as in Figure 3.18.

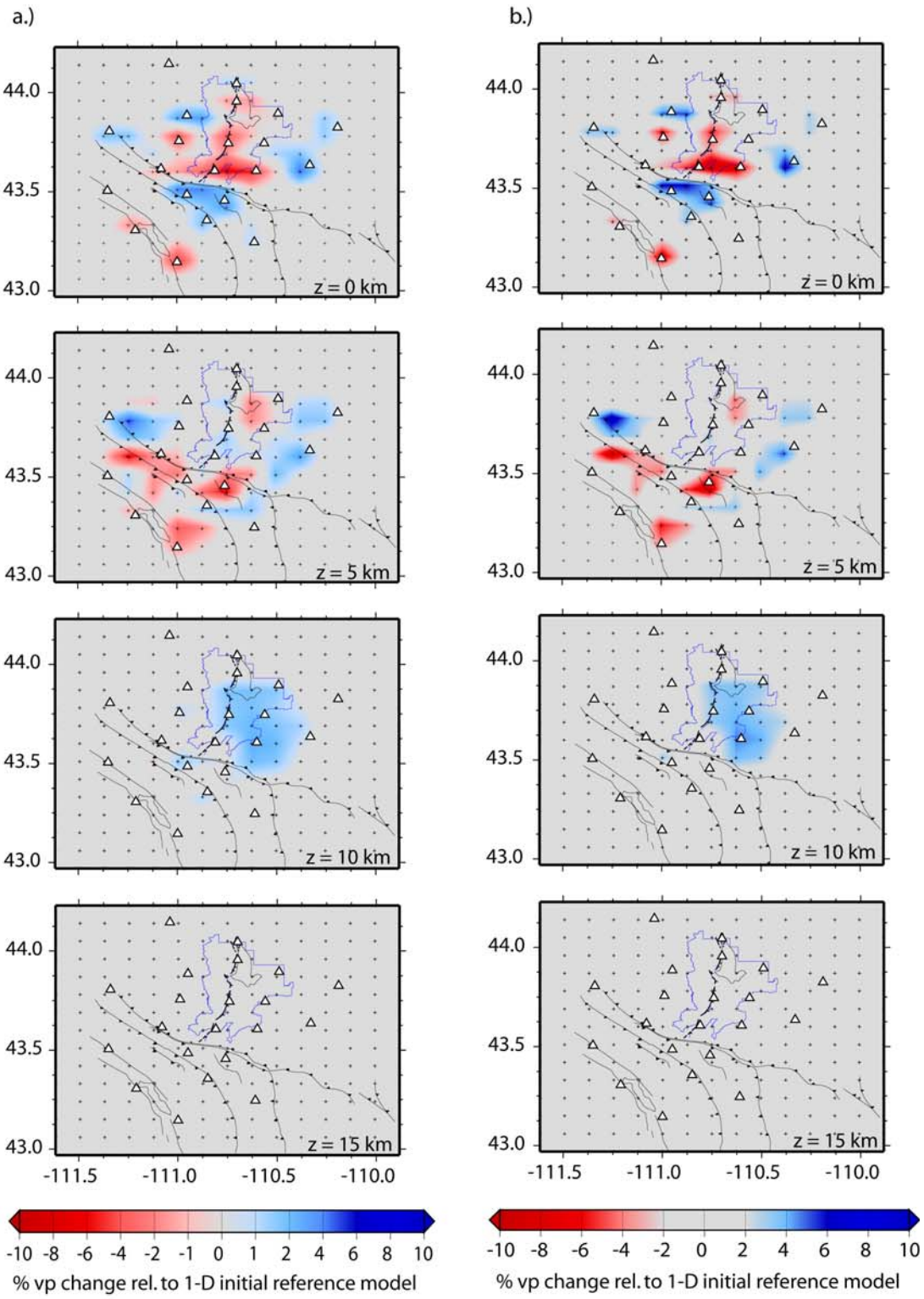
a.)
b.)
44.0
43.5
43.0
z = 0 km
z = 5 km
z = 10 km
z = 15 km
-111.5
-111.0
-110.5
-110.0
-10 -8 -6 -4 -2 -1 0 1 2 4 6 8 10
-10 -8 -6 -4 -2 0 2 4 6 8 10
% vp change rel. to 1-D initial reference model
% vp change rel. to 1-D initial reference model

noise level of 5%, or +/- 2.5%. This noise level estimate is rather conservative since we assume that the ray travels along the maximum distance in the volume, which is the diagonal. Also, for higher velocities the noise level gets smaller than this value. However, if you decrease your grid node spacing, the noise level increases. This is why you need very high-quality data with a low picking error to resolve small perturbations for small grid spacings. Therefore, we changed our color scale so that everything between -2% and +2% was white. This greatly reduced the vertical smearing between each of the horizontal layers and removed anomalies that were below the noise level.

Figures 3.18 and 3.19 show horizontal views arranged in an increasing depth from top to bottom. Model parameters associated with nodal points are overlain on the horizontal plots. At depths down to 5 km, the model perturbations occur in small anomalies distributed throughout the region on both sides of the Teton fault. These small high and low anomalies coincide with the main geomorphology units at the surface. We expected surface stratigraphy to affect the model perturbations at 5 km depth since geologic maps indicate basin depths down to 4 to 5 km depths. The patterns of anomalies are different between 0 km and 5 km due to partly to the heterogeneity of geologic structure, and also due to the sparse ray coverage at 0 km depth. The ray coverage at 5 km depth is far superior to that at 0 km, and anomalies at 0 km might not be fully imaged due to the lower resolution capabilities at this depth compared to 5 km depth. High velocities are associated with the mountain bedrock and low anomalies coincide with sediment filled valley basins. The high perturbations occurring at 10 km depth represent the bedrock below the basin fill in the Jackson Hole valley to the east of the Teton fault.

3.3.3. Resolution and Solution Quality Assessment

The tomographic inversion process can sometimes produce unrealistic model perturbations or artifacts in areas of low or possibly good resolution. The resolution of the image is limited by the distribution of the rays and the ray coverage within the target volume. The higher the ray coverage in an area, the better the resolution will be. The assessment of the solution quality is required to determine the areas of high and low resolution and detect these possible artifacts.

There are numerous tests that have been developed to assess the ray coverage, including resolution estimates such as hit count, diagonal element of the resolution matrix (RDE), spread function [*Toomey and Foulger*, 1989] and tests with synthetic data such as checkerboard sensitivity tests [*Zelt,* 1998] and characteristic model tests [*Haslinger*, 1998]. Tests with synthetic data will provide valuable information about our model parameterization, resolution capacity of the data set, and the damping value.

In this study we employed the RDE method (row of the resolution matrix) the synthetic checkerboard, and characteristic model tests to aid us in assessing the resolution of our 3-D Vp model. The RDE method is often used to assess the resolution or solution quality. Theoretically, a perfect resolution is indicated with a RDE of 1, but the RDE strongly depends on the damping and model parameterization, complicating its use for resolution assessments [*Husen*, 2002]. High damping values will lower RDE values [e.g., *Eberhart-Phillips and Reyners*, 1997], as well as a high number of model parameters [*Toomey and Foulger*, 1989]. Therefore, only a combined analysis of the hit count/DWS and RDE will yield reliable resolution estimates [*Husen et al.*, 2002].

Initially a damping value of 100 was used as well as a damping value of 500 since both were excitable values based on the trade off-curve. In Figure 3.20 the results of the checkerboard tests for these two damping values are shown, and the final checkerboard test using the 500 damping value is shown in Figure 3.21. There is not much difference between the two damping parameters except that the test using the 500 damping value has less vertical smearing and the amplitude recovery is not as strong as the test using the 100 damping value. However, both tests recover the synthetic anomaly structures and amplitudes very well, and therefore a damping value of 500 was chosen since the structures and amplitudes were recovered well without smearing.

The checkerboard test consists of a series of alternating high and low anomalies overlaid on the background of the minimum 1D model. Synthetic travel times were calculated for this model using the ART pseudo-bending method and inverted using the RKP ray shooting and ray tracing after adding Gaussian noise. Using these two different ray tracing schemes will add some additional noise, since both schemes will not compute the same travel times for the same source-receiver pairs. The first test shown in Figure 3.21 using the 500 damping parameter consisted of high and low anomalies spanning over two grid nodes in the x and y direction with one grid node separating the anomalies. The grid nodes between the anomalies were placed there to test for horizontal smearing. Amplitudes of the input synthetic anomalies were ± 10% compared to the background model. The first model shows the checkerboard anomalies at depths 0 km and 10 km, and the second model shows the anomalies at depths 5 km and 15 km. Both models left depth layers open between depth layers with anomalies to test for vertical smearing. Figure 3.22 is a similar checkerboard test, but its anomalies cover

Figure 3.20. Checkerboard test using 2x2 nodal anomalies at 100 vs. 500 damping values. The original synthetic input model of high (+10%) and low (-10%) Vp anomalies is shown by the red and blue squares. The recovered model after five iterations is shown in the horizontal planes at various depths. The black crosses mark the individual grid nodes of the model parameterization, and the white triangles mark the seismic stations. The Grand Teton National Park is outlined by the blue lines. Column (a) show anomalies at 0.0 km and 10.0 km depth using a damping parameter of 100 (left column), and column (b) show anomalies at the same depths using a damping parameter of 500 (right column).

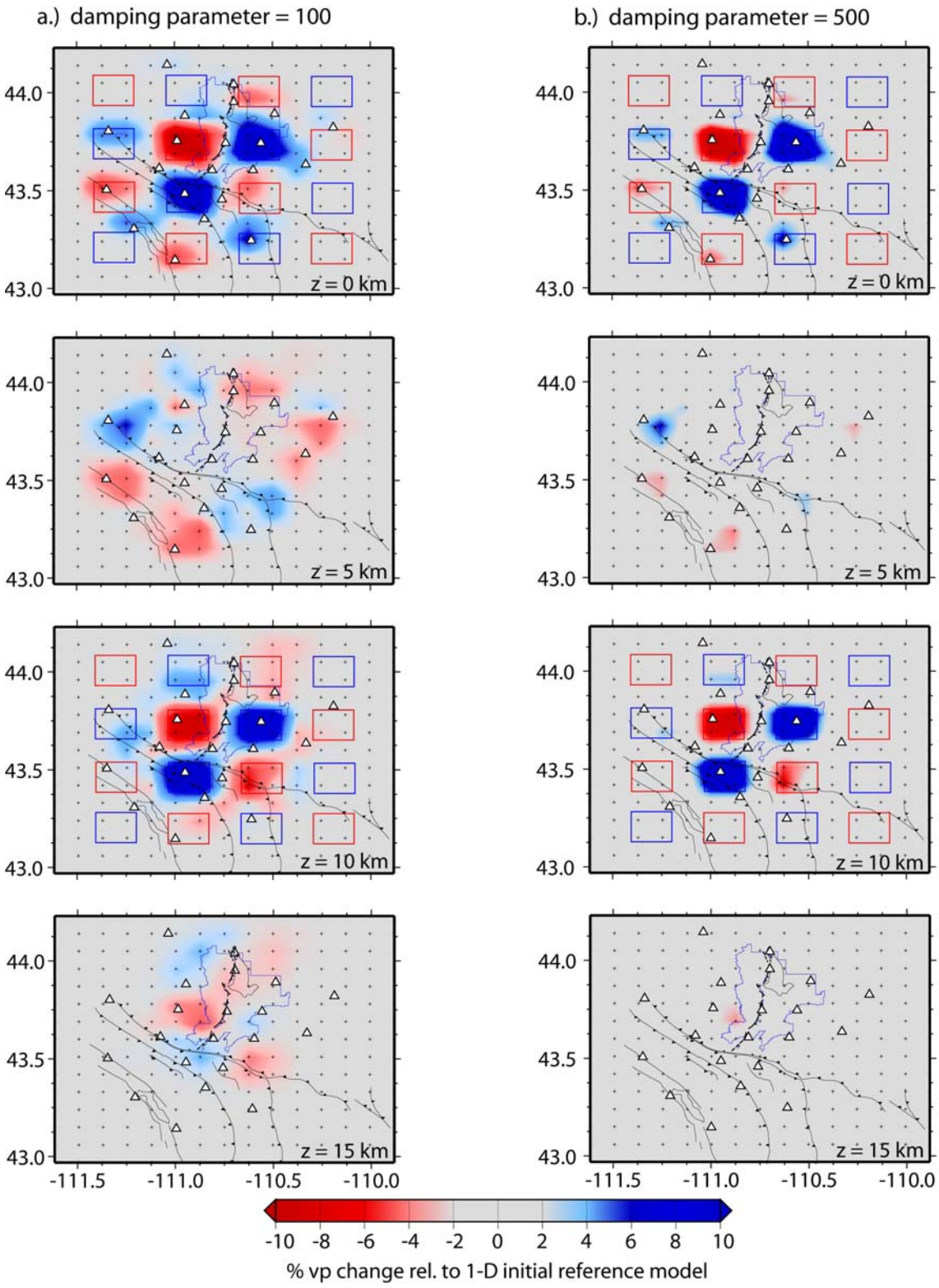
a.) damping parameter = 100
b.) damping parameter = 500
z = 0 km
z = 5 km
z = 10 km
z = 15 km
44.0
43.5
43.0
-111.5
-111.0
-110.5
-110.0
-10 -8 -6 -4 -2 0 2 4 6 8 10
% vp change rel. to 1-D initial reference model

Figure 3.21. Checkerboard test using 2x2 nodal anomalies. Assessing solution quality of Vp model using synthetic checkerboard models. The original synthetic input model of high (+10%) and low (-10%) Vp anomalies is shown by the red and blue squares. The recovered model after five iterations is shown in the horizontal planes at various depths. The black crosses mark the individual grid nodes of the model parameterization, and the white triangles mark the seismic stations. Column (a) show anomalies at 0.0 km and 10.0 km depth (left column), and column (b) show anomalies at 5.0 km and 15.0 km depth (right column).

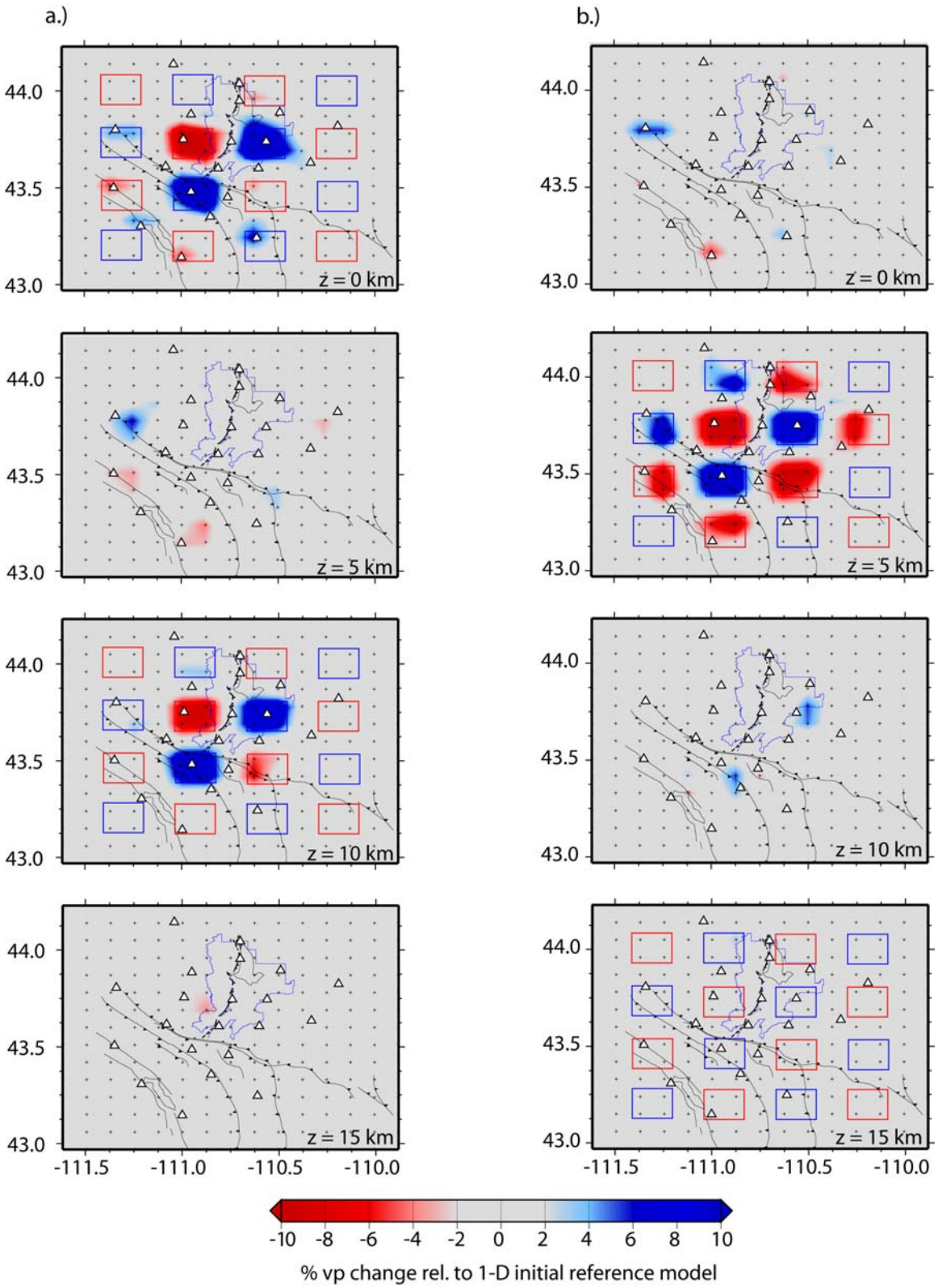
a.)
b.)
z = 0 km
z = 5 km
z = 10 km
z = 15 km
44.0
43.5
43.0
-111.5
-111.0
-110.5
-110.0
-10 -8 -6 -4 -2 0 2 4 6 8 10
% vp change rel. to 1-D initial reference model

only one grid node to test for resolution of small anomalies. Both test results show good resolution in the center of the seismic network at 0, 5, and 10 km depth. At these depths single nodes anomalies are showing almost 95% amplitude recovery. There is small horizontal smearing in the southeast corner of the model. However, the amplitudes are very small and can be ignored. There is also vertical smearing taking place especially in the larger checkerboard test. This is common to have larger amounts of vertical smearing taking place when you increase the size of the anomalies, since there are more areas where rays can travel vertically. The vertical smearing is due to mostly vertical upward traveling rays.

Checkerboard tests cannot assess the power of the data to resolve a certain structure. The ability of the data to resolve a fine-scale structure such as a checkerboard does not imply that large-scale structures can be resolved as well [*Leveque et. al,* 1993]. The characteristic model retains the size and amplitudes of anomalies seen in the inversion results but has rotated shapes and different signs for the anomalies [*Haslinger*, 1999; *Husen,* 2003]. Figure 3.23 displays the results of the synthetic characteristic model test.

Two separate characteristic tests were conducted with one having anomalies at 0 km and 10 km depths, and the other having anomalies at 5 km and 15 km depths. One grid node was left open between anomalies to test for horizontal smearing, and one depth layer was open to assess any vertical smearing. Anomalies were generally located in areas of good resolution and ray coverage as determined using the RDE values. Resolution is good at depths 0, 5, and 10 km in the center of the network. The amplitudes and anomaly shapes are recovered well in areas of high ray coverage and

Figure 3.22. Checkerboard test using 1x1 nodal anomalies. Assessing solution quality of Vp model using synthetic checkerboard models. The original synthetic input model of high (+10%) and low (-10%) Vp anomalies is shown by the red and blue squares. The recovered model after five iterations is shown in the horizontal planes at various depths. The black crosses mark the individual grid nodes of the model parameterization, and the white triangles mark the seismic stations. Figures in column (a) show anomalies at 0.0 km and 10.0 km depth (left column), and figures in column (b) show anomalies at 5.0 km and 15.0 km depth (right column).

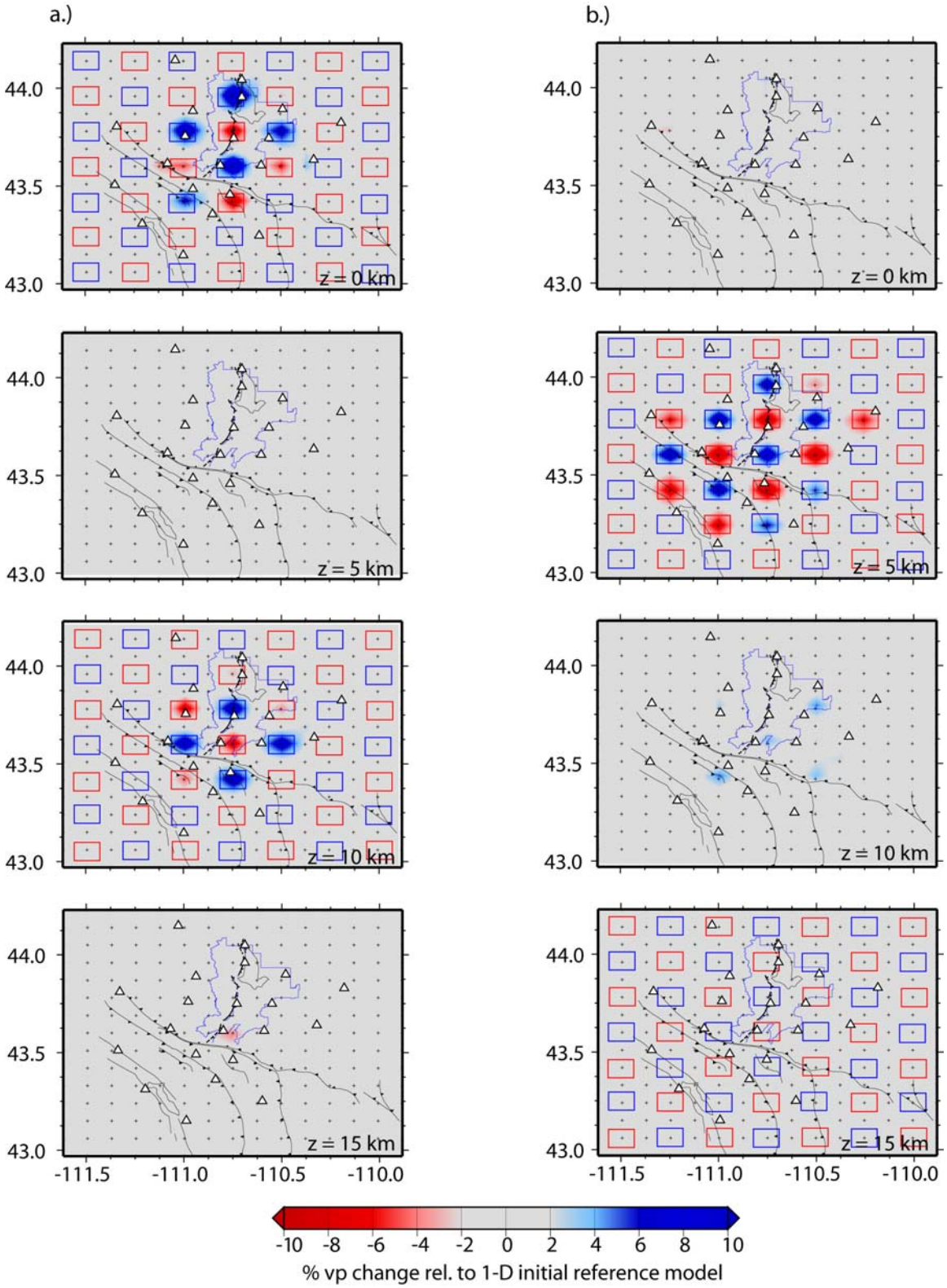
a.)
b.)
z = 0 km
z = 5 km
z = 10 km
z = 15 km
44.0
43.5
43.0
-111.5
-111.0
-110.5
-110.0
-10 -8 -6 -4 -2 0 2 4 6 8 10
% vp change rel. to 1-D initial reference model

Figure 3.23. Assessing solution quality of Vp model using synthetic characteristic models. The original synthetic input model of high (+10%) and low (-10%) Vp anomalies is shown by the red and blue squares. The recovered model after five iterations is shown in the horizontal planes at various depths. The black crosses mark the individual grid nodes of the model parameterization, and the white triangles mark the seismic stations. See text for explanation of characteristic model. Figures in column (a) show anomalies at 0.0 km and 10.0 km depth (left column), and figures in column (b) show anomalies at 5.0 km and 15.0 km depth (right column).

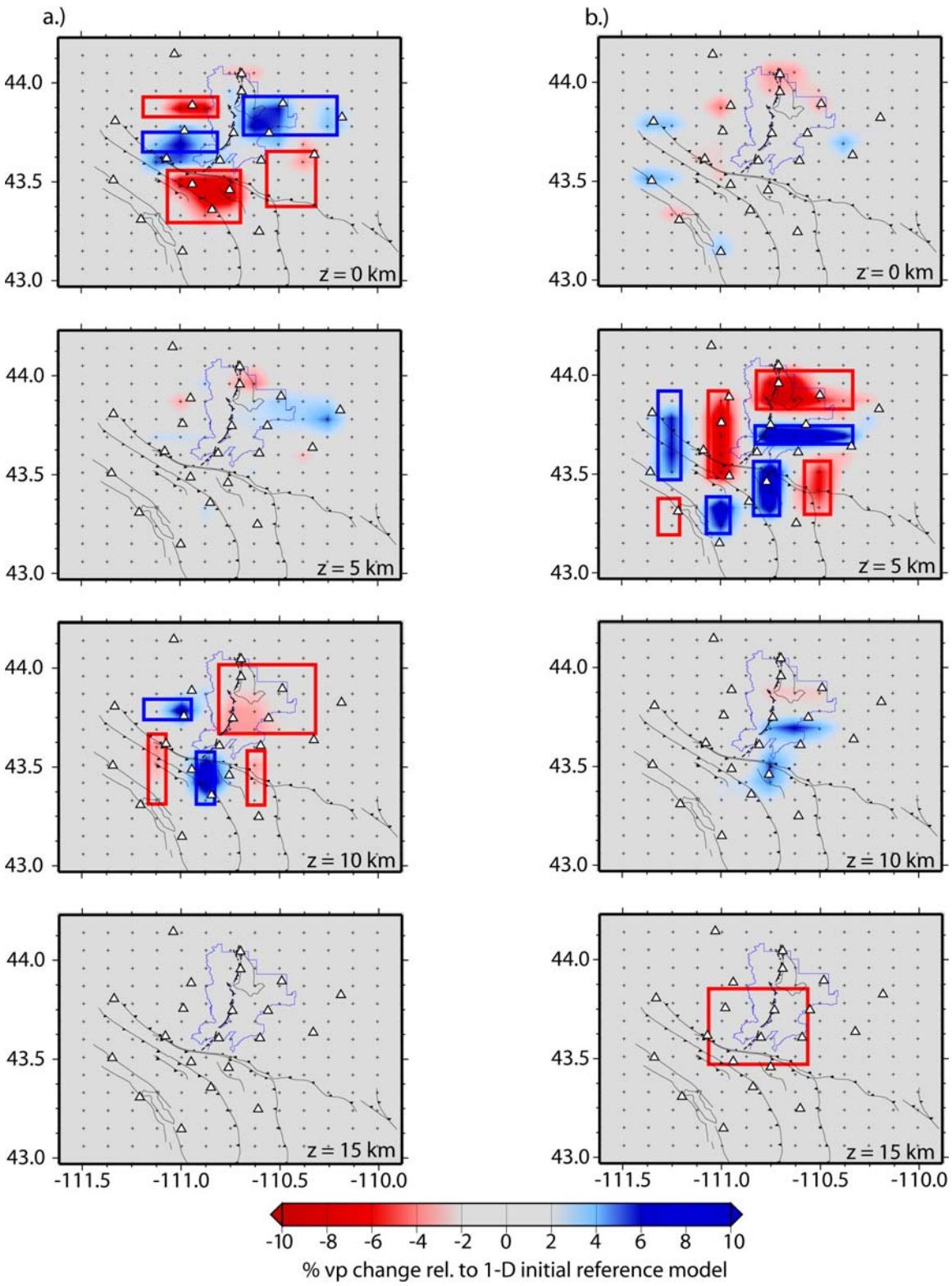
a.)
b.)
z = 0 km
z = 5 km
z = 10 km
z = 15 km
44.0
43.5
43.0
-111.5
-111.0
-110.5
-110.0
-10 -8 -6 -4 -2 0 2 4 6 8 10
% vp change rel. to 1-D initial reference model

poorly when the ray coverage decreases. Amplitude recovery in general is reduced as a consequence of damping. This affects mainly the extreme high and little anomalies. Horizontal smearing is small, and vertical smearing is the most predominant from the 5 km depth down to 10 km depth. This is due to the excellent resolution and ray coverage at 5 km depth, but at 10 km depth the resolution and ray coverage is much less.

To evaluate the effects of smearing and possible interdependence between model parameters, plots of the row of resolution matrix were generated for grid nodes in layers showing different resolutions (Figure 3.24). They clearly show the vertical smearing occurring at areas were the RDE value is the lowest. Based on the vertical and lateral extent of smearing in each of these three plots, two classes of resolution are defined. Note the dominant smearing in the vertical direction for grid nodes with good and poor resolution due to mostly upward traveling rays.

Figure 3.25 also shows the quality of the resolution capabilities of the high quality data set. This figure illustrates the correlation between high RDE values and good amplitude and structure resolution of the characteristic model. Areas of reliable resolution as determined by the synthetic tests are in general characterized by a DWS larger than 600 and an RDE larger than 0.3. Based on the results of the row of resolution matrix plots, cut-off values for good and poor resolution are defined by the RDE values (Table 3.6). Areas with good resolution determined by the synthetic tests correspond well with the areas of good resolution determined by the row of resolution matrix plots. These tests revealed that areas of reliable resolution are contained in areas with RDE

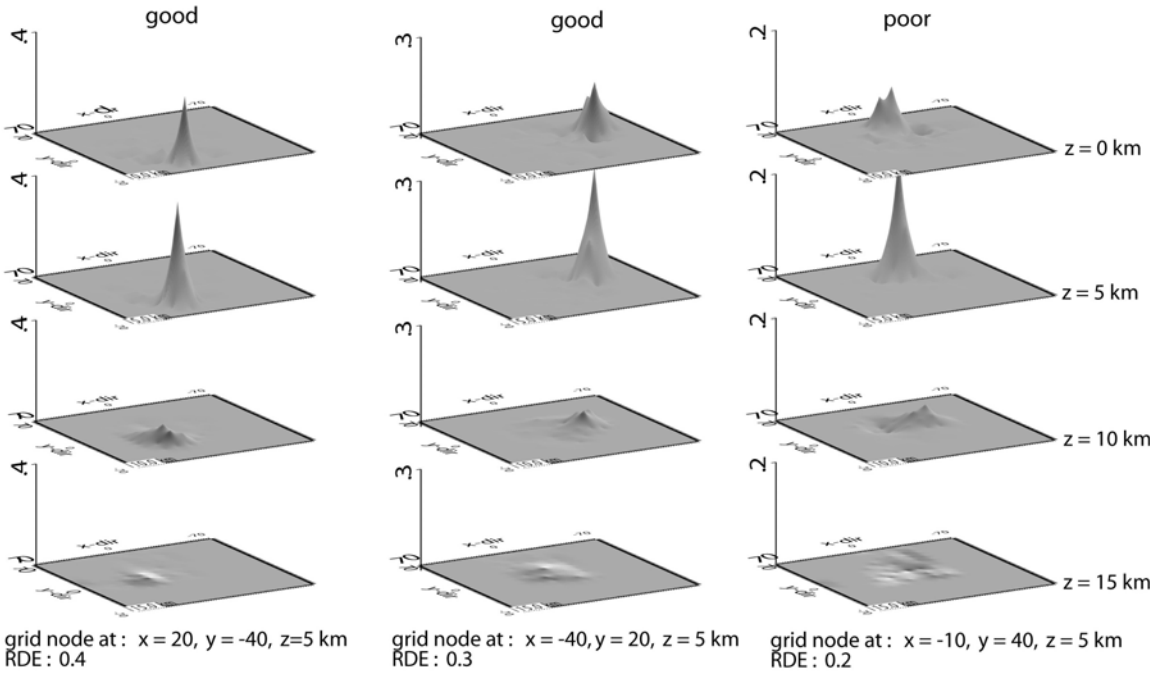

Figure 3.24. 3-D perspective view of the averaging vector (row of resolution matrix) for grid nodes in the layers showing different resolution. Based on the vertical and lateral extent, 2 classes of resolution are defined. Note the dominant smearing in the vertical direction for grid nodes with good and bad resolution due to mostly upward traveling rays.

Figure 3.25. Resolution element contours with characteristic test model output. Assessing solution quality of Vp model using synthetic characteristic models. The original synthetic input model of high (+10%) and low (-10%) Vp anomalies is shown by the red and blue squares in column (a). The recovered model after five iterations is shown in the horizontal planes at various depths. The black crosses mark the individual grid nodes of the model parameterization, and the white triangles mark the seismic stations. See text for explanation of characteristic model. Figures in column (a) show anomalies at 0.0 km and 10.0 km depth (left column), and figures in column (b) show the same anomalies with overlain RDE contours (right column).

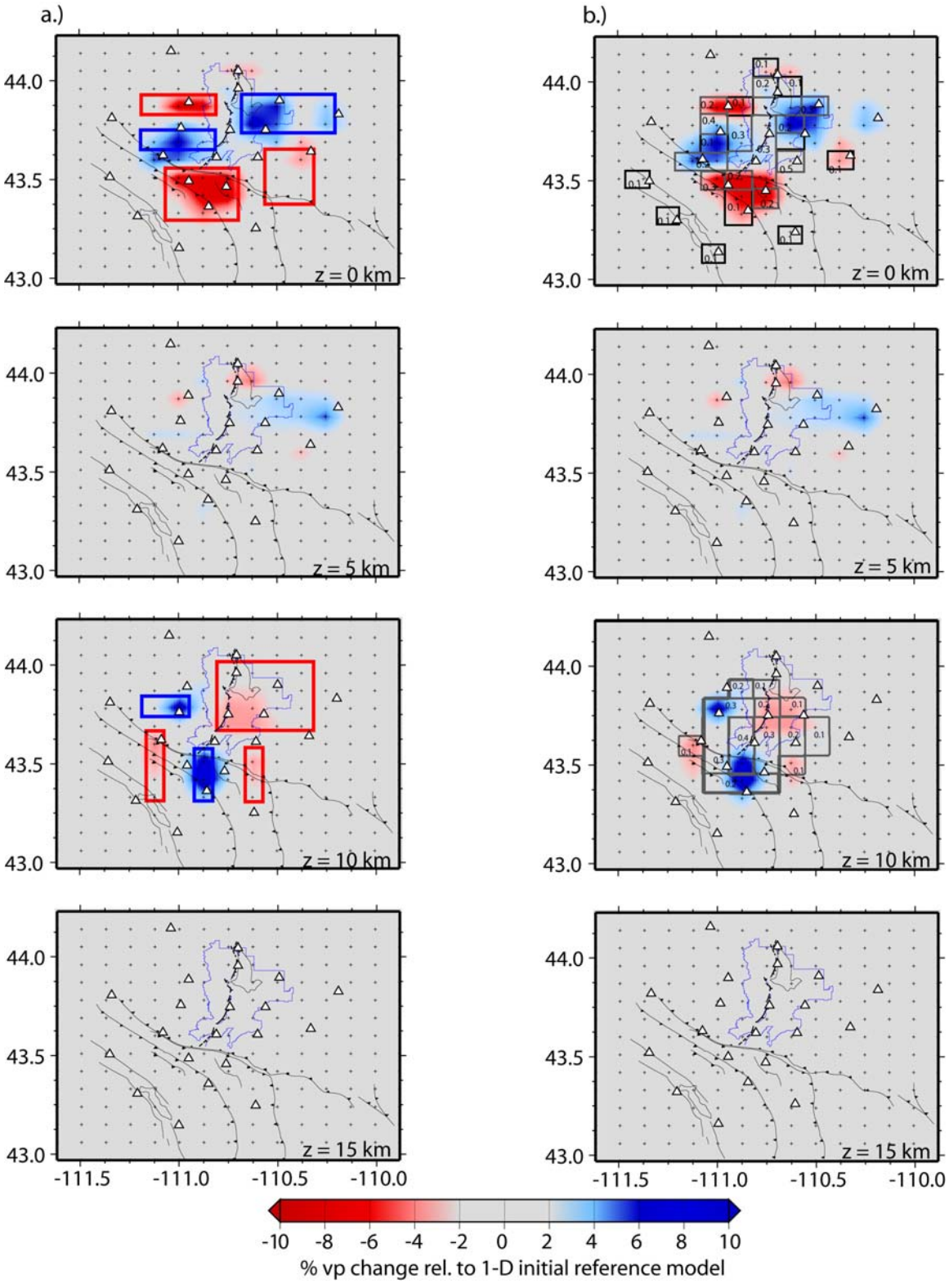
a.)
b.)
z = 0 km
z = 5 km
z = 10 km
z = 15 km
44.0
43.5
43.0
-111.5
-111.0
-110.5
-110.0
-10 -8 -6 -4 -2 0 2 4 6 8 10
% vp change rel. to 1-D initial reference model

Table 3.6. Cutoff values for RDE

Resolution	
Good	Poor
RDE > 0.3	RDE < 0.2

values of 0.3 or larger, and vertical smearing occurs mainly from 5 km depth down to 10 km depth.

3.3.4. Three-Dimensional P-wave Velocity Tomography Results

The results and conclusions of this quest for the final 3-D P-wave velocity model are summarized below. Figure 3.26 displays absolute P-wave velocities of the final 3-D velocity model for depth layers at 0 km, 5 km, 10 km, and 15 km. The final 3-D velocity model is also computed down to 25 km depth. However, as shown in the previous section the resolution capabilities are minimal past the 15 km depth due to insufficient ray coverage.

The tomographic image in Figure 3.26 (a) at 0 km depth, which is equivalent to mean sea level represents the sediment basins in the Teton region with the low velocity zones shown in dark blue. The three main basins are marked A, B, and C. Basin A reflects the Jackson Hole valley from the northern Jackson Lake to the town of Jackson, WY. Basin B represents the Teton River valley on the west side of the Teton Range. Basin C represents the Grand/Star valley near the northern and southern ends of the Palisades Reservoir and between the Grand Valley fault and Star Valley Fault. At 5 km depth, low velocity zones are still present in the Jackson Hole valley, but they are more

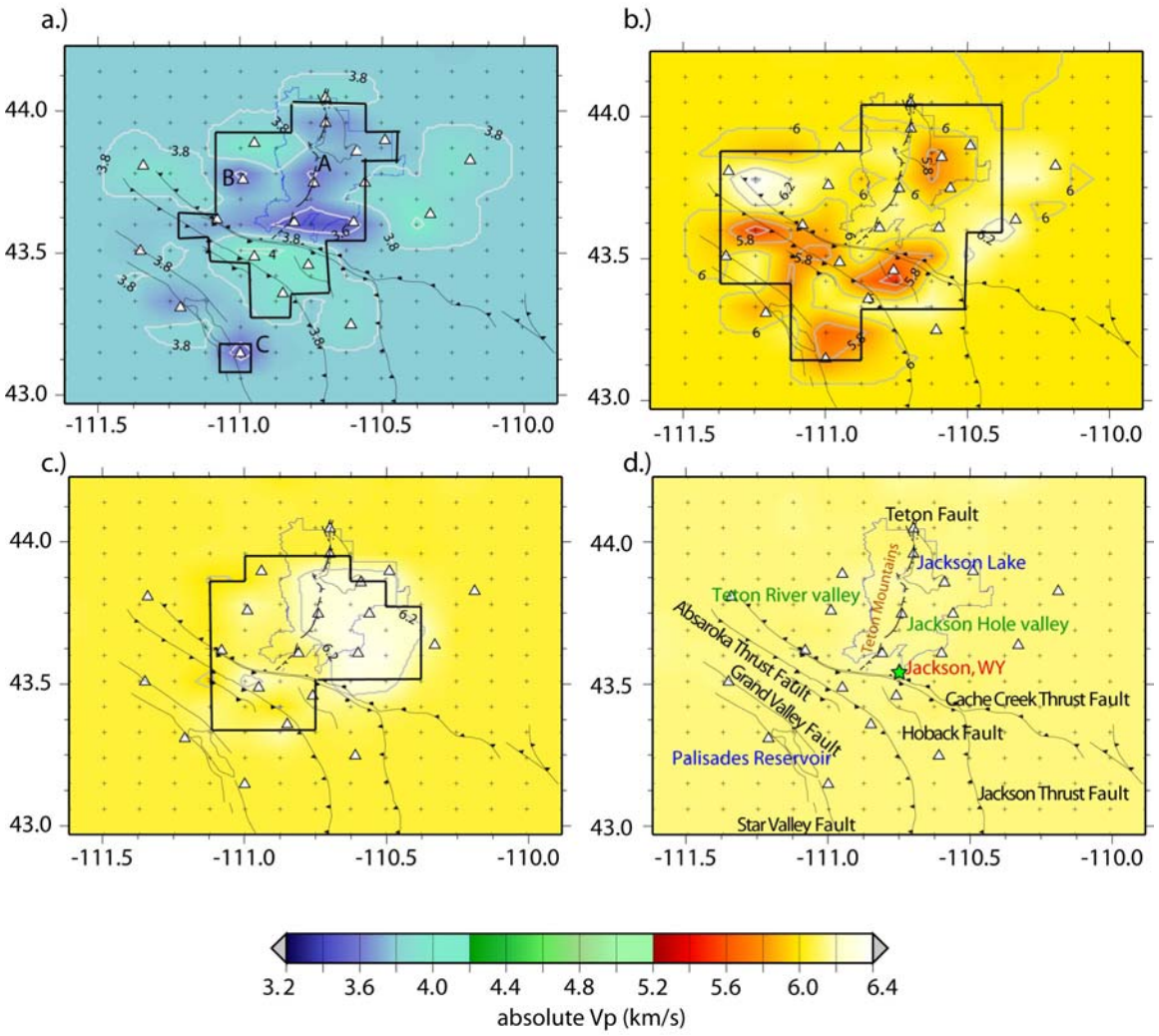

Figure 3.26. Horizontal plane view of the final 3-D inversion solution with absolute velocity values and contours. The seismic stations are marked by the white triangles. Figure (a) displays the velocity contours at 0 km (mean sea level) and area A represents the Jackson Hole valley basin, area B represents the Teton River valley basin, and area C represents the Grand valley basin. Figure (b) displays the velocity contours at 5 km depth, and figures (c) and (d) display velocity contours at 10 km and 15 km depth. Major faults and basin names are displayed in figure (d). The Teton National Park boundary is represented by the blue lines. The Teton fault is marked by the black lines. To the west of the Teton fault lie the Teton Mountains predominantly composed of Precambrian and Paleozoic bedrock that corresponds well with relatively higher velocities. To the east of the fault lies the Jackson Hole valley, composed of Tertiary and Quaternary sediments that also show a good correlation with relatively low velocities. The green star represents the town of Jackson, WY. Velocity contours show intervals of 0.2 km/s. The thin black lines represent the areas of good resolution determined by the synthetic tests and row of resolution matrix plots.

localized beneath the Jackson Lake Dam, and just south of Jackson, WY. There are two distinct patterns that are seen in the low velocity zones in the region.

Notably, there is a trend of low velocity zones from the Jackson Lake Dam low velocity body southwest of Jackson, WY and further south to the southern end of the Palisades Reservoir area. Even though the tomography indicates that these are separate low velocity zones, there may be some connection between them, but is not resolvable given the resolution capability of our data and model parameterization.

The second notable trend of these low velocity zones extends from southern Teton River valley to the southeast towards Jackson, WY. This anomaly trends almost perpendicular to the south of the southern Teton fault and notably correlates with Cache Creek Thrust faults that run along the same linear trend to the south of the Teton fault. Another point is that the sediment basin structures do not extend beneath 5 km, but lower velocity rocks might be intermixed with high velocity bedrock. The sediment basins in the Teton region are interpreted to be limited to about 2-3 km depth. At 10 km depth, there is a small high velocity zone located in the Jackson Hole valley that extends across the southern half of the Jackson Lake and into the Gros Ventre Range. This area still lies in the good resolution area and is possibly an indication of cooler higher velocity bedrock located beneath the Jackson Hole valley block.

To aid in the understanding of the tomographic velocity changes we placed constraints on crustal composition in the Teton region. Using laboratory measurements of seismic velocities by *Christensen and Mooney* [1995] we plotted the crustal rock velocities relative to the minimum 1-D velocity model at depth (Figure 3.27). The laboratory determined velocities were corrected for temperatures assuming a regional

surficial heat flow of 90 mW m^{-2} and pressure effects assuming a mean crustal density of 2.8g cm^{-3}. The important observation is that no single rock type follows the minimum 1D model for more than a few kilometers. We chose only a small number of rock compositions and metamorphic grades from *Christensen and Mooney* [1995] that best reflect the sampling of plausible rock types in the Teton region determined by *Love et al.* [1992]. Based on these observations, the upper crust appears to best fit a general suite of granitic-dioritic to quartz-rich granulitic rocks (5.5-6.2 km s^{-1}), while amphibolite to mafic granulites fit the lower crust (6.4-6.8 km s^{-1}). The correlations imply that the bulk of crustal composition varies with depth, but the correlation of velocity with composition is nonunique.

Examining the tomographic profiles across the Teton region provides a better understanding of the subsurface structure and how well we are able to resolve structures at depth. Figure 3.28 is shows the profile that runs parallel to the Teton fault from the southern to northern segment. The plot in (a) shows the location map of the profile cross section and how closely it runs along the Teton fault. The plot in (b) shows the topographic profile along the cross section in elevation meters and distance in kilometers. Plot (c) shows the tomographic profile of the cross section at depth, down to 15 km in percent P-velocity change from the minimum 1-D velocity model. Absolute P-velocity contours are overlain as well as hypocenters located within 5 km of the profile line. The bold black box designates the area of good resolution with a RDE greater than or equal to 0.3. In this figure there are low velocity zones from 0 km down to almost 2 km, which is to be expected since we are looking at a cross section running along the fault scarp. This Teton Range profile is so close to the Teton fault scarp that much of the sediment in the

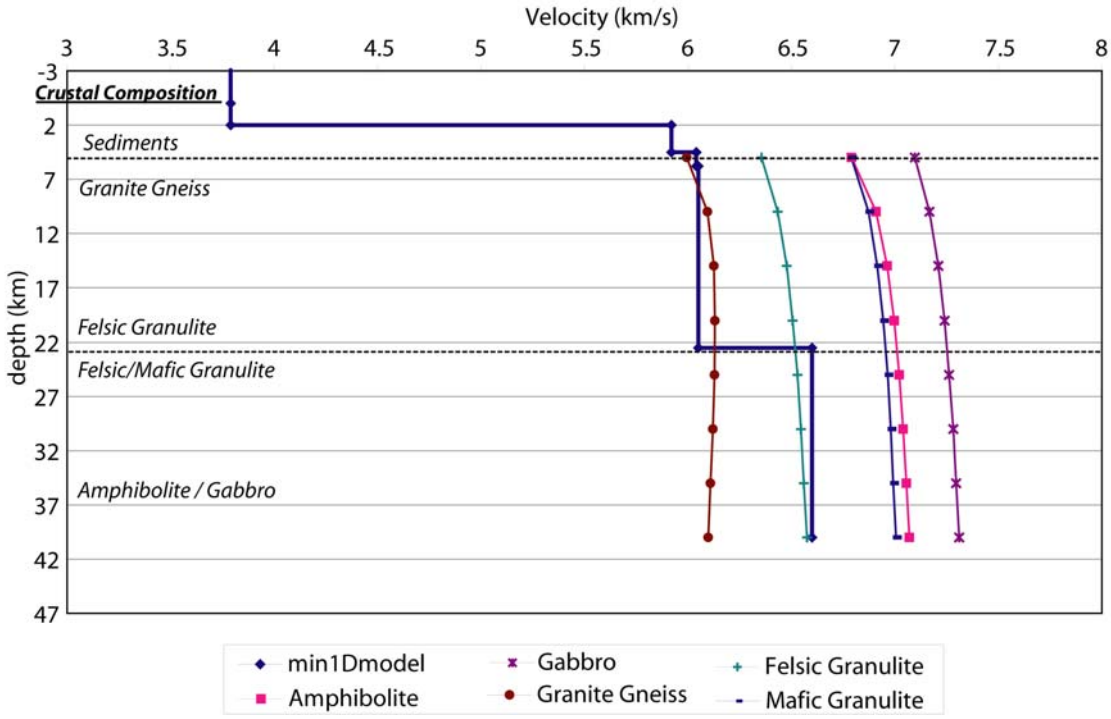

Figure 3.27. A model of the minimum 1-D Vp model with plausible continental crust and upper mantle rocks' compressional wave velocities as a function of depth. The predicted velocity-depth function of plausible continental crust and upper mantle rocks were determined by *Christensen and Mooney* [1995]. Temperature and pressure corrections with depth were made assuming a 90 mW m^{-2} surface heat flow and a mean crustal density of 2830 kg/m^3. Felsic rocks comprise the crust to a depth of 22.5 km. High grade metamorphic rocks occupy the lower crust. Rock types shown in this figure were taken from *Christensen and Mooney* [1995] and are (1) granite gneiss, Cape Ann, Massachusetts, (2) felsic granulite, New Jersey Highlands, (3) amphibolite, Indian Ocean, (4) mafic granulite, Valle d'Ossola, Italy, and (5) gabbro, Mid-Atlantic Ridge.

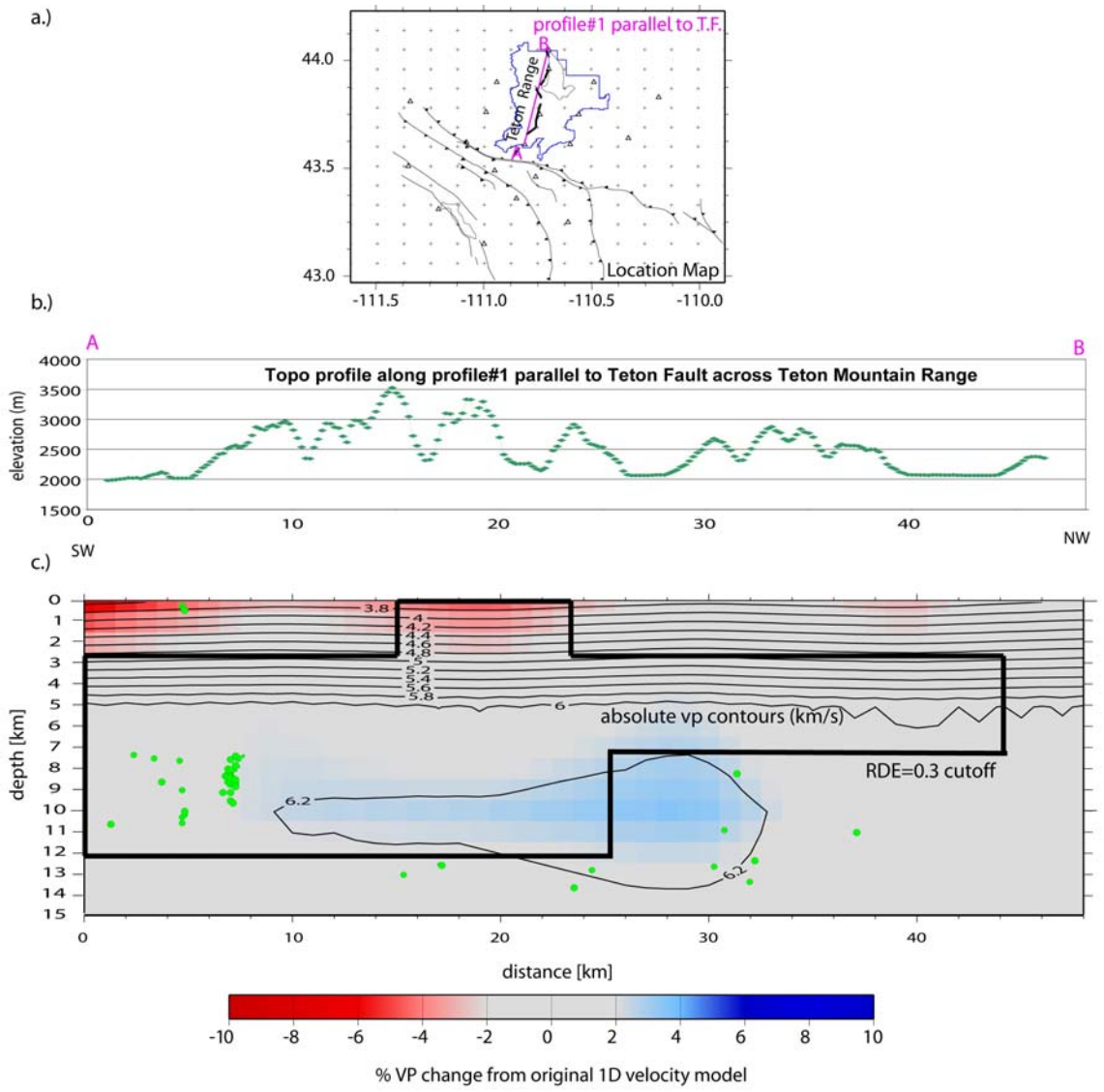

Figure 3.28. 3-D velocity model cross section parallel to the Teton fault across the Teton Range. The location map of the vertical cross section is located at the top in figure (a). The cross section location represented by the pink line continues along the A to B profile. Figure (b) shows the topographic profile along the cross section in meters. Figure (c) shows the final 3-D inversion solution with velocity perturbations shown by the red and blue color scale, and overlain absolute velocity contours. There is no vertical or horizontal exaggeration in the depth vs. distance axis. The area of good resolution is located inside the bold black lines that show the areas of RDE greater than or equal to 0.3. The hypocenter locations of the high quality events along the profile +/-5 km are shown in green circles.

first couple of kilometers is nothing more than weathered granitic, gneiss, and migmatite bedrock mixed with Quaternary sandstone and limestone sediments from the Teton range and old Pinedale glacial deposits. Also this profile runs through many small mountain valleys located between the high Teton peaks, where Quaternary sediments are transported down creek beds.

At around 7 km to 12 km there is a notable high velocity body that possibly corresponds to a granitic rock type. This could possibly be the cooler high velocity bedrock of the Teton footwall that is comprised of granite, gneiss, and migmatite. Figure 3.29 displays the cross section along a profile running parallel to the Teton fault in the Jackson Hole valley. Plots (a) and (b) once again show the location map and topographic profile along the cross section.

Plot (c) in Figure 3.29 displays the low and high velocity contrasts along the profile through the town of Jackson, WY. This tomographic image displays a localized low-velocity zone beneath the town down to almost 3 km depth, and a smaller low velocity zone beneath the Jackson Lake. These two zones could be interpreted as small localized deeper sedimentary basins with characteristics of being located in a high hazards location in the event of an earthquake along the Teton fault. One noticeable feature is the low velocity zone at the southwestern end of the profile at 4 km to 7 km depth. This is the low velocity zone that was seen in the horizontal depth slice at 5 km in Figure 3.26 that correlated with the Cache Creek Thrust faults. There is also a linear trend of hypocenter locations that run along the edge of this low velocity zone. The large high velocity body at 8 km to 12 km depth is probably the cooler dense bedrock beneath the Jackson Hole valley.

Figure 3.29. 3-D velocity model cross section parallel to the Teton fault across Jackson Hole. The location map of the vertical cross section is located at the top in figure (a). The cross section location represented by the pink line continues along the A to B profile. Figure (b) shows the topographic profile along the cross section in meters. Figure (c) shows the final 3-D inversion solution with velocity perturbations shown by the red and blue color scale, and overlain absolute velocity contours. There is a vertical exaggeration on this plot where the depth in km is 2.5x that of the distance scale in km. The area of good resolution is located inside the bold black lines that show the areas of RDE greater than or equal to 0.3. The hypocenter locations of the high quality events along the profile +/-5 km are shown in green circles. The Cache Creek and Jackson Thrust faults are projected at depth and are represented by the blue lines with black arrows showing the direction of movement by the headwall.

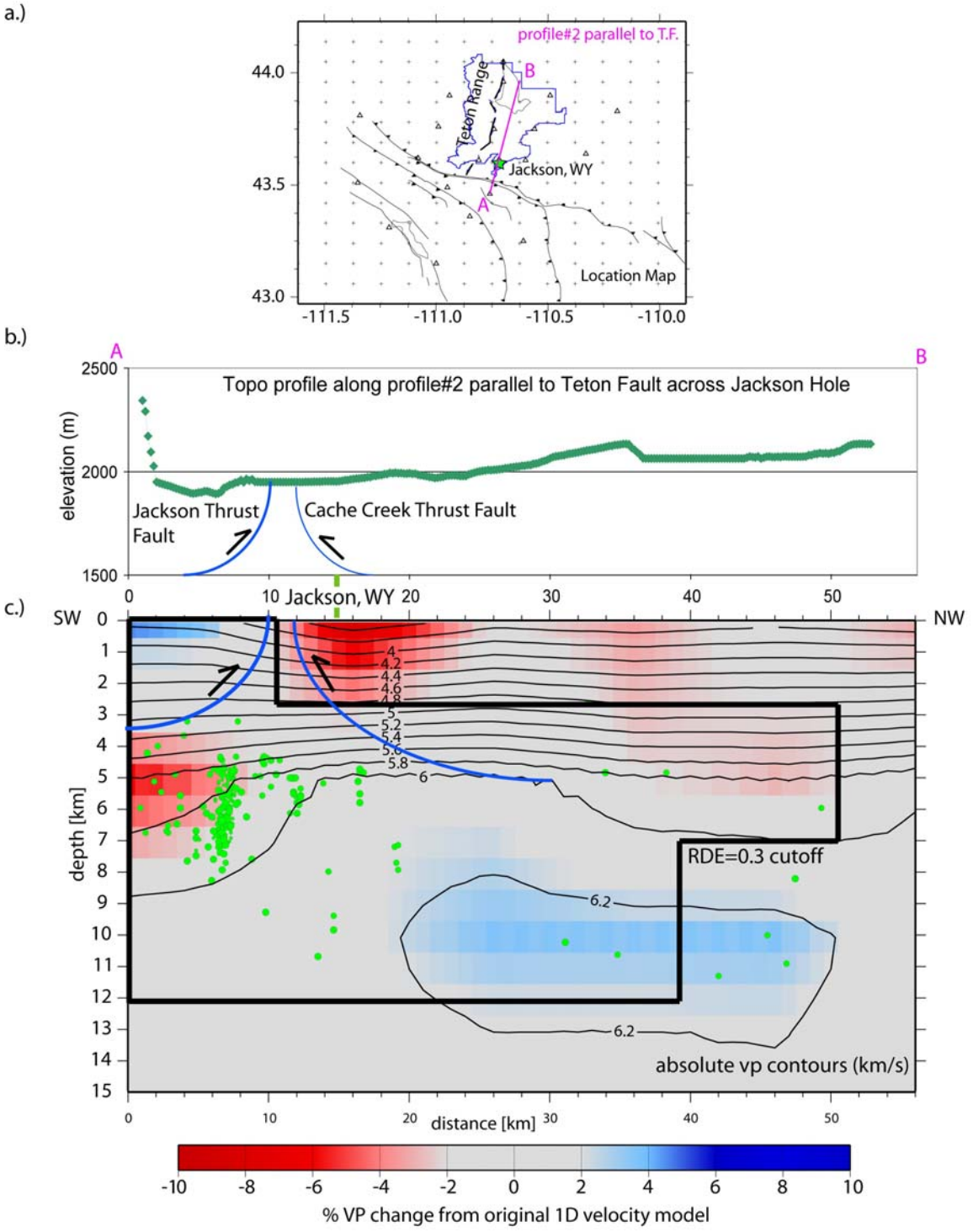
a.)
profile#2 parallel to T.F.
Teton Range
B
A
Jackson, WY
Location Map
44.0
43.5
43.0
-111.5
-111.0
-110.5
-110.0
b.)
A
B
Topo profile along profile#2 parallel to Teton Fault across Jackson Hole
elevation (m)
2500
2000
1500
Jackson Thrust Fault
Cache Creek Thrust Fault
0
10
Jackson, WY
20
30
40
50
c.)
SW
NW
depth [km]
4
4.2
4.4
4.6
4.8
5
5.2
5.4
5.6
5.8
6
6.2
RDE=0.3 cutoff
absolute vp contours (km/s)
distance [km]
-10
-8
-6
-4
-2
0
2
4
6
8
10
% VP change from original 1D velocity model

Figure 3.30 displays the cross section along a profile running perpendicular to the southern Teton fault segment. The tomographic image displays the low velocity sediment basin of the southern Jackson Hole valley near the town of the Jackson. This cross section shows the sediment filled basin down to a depth of 2.5 km. One notable observation is the linear trend of hypocenters at depths from 5 km down to 8 km along the absolute velocity contour of 6 km/s.

Figure 3.31 displays the cross section along a profile running perpendicular to the Teton fault along its northern segment. This profile also runs perpendicular to the Jackson Lake Dam. The velocity structure in this cross section displays the high velocity bedrock beneath the Teton Range, which is what we would expect. However, we do not see a clear velocity transition across the Teton fault. We were hoping to see a more defined velocity change across the fault in order to better resolve the angle of the dipping normal Teton fault. There is the low velocity zone from 3 km down to 5 km depth under the Jackson Lake Dam, and the high velocity body from 7 km down to 13 km depth beneath the valley block. We also begin to image the higher velocities in the Gros Ventre Range granite bedrock to the east the Jackson Hole valley.

3.4. Probabilistic Nonlinear Hypocenter Relocation

The Teton earthquake data was reevaluated using the algorithm, NonLinLoc [*Lomax et al*., 2000]. NonLinLoc follows the probabilistic formulation of nonlinear inverse problems by *Tarantola and Valette* [1982]. The complete description of this formulation can be found in *Tarantola and Valette* [1982] and *Moser et al.* [1992]. I will briefly describe this relocation procedure in this section and present the improvements of

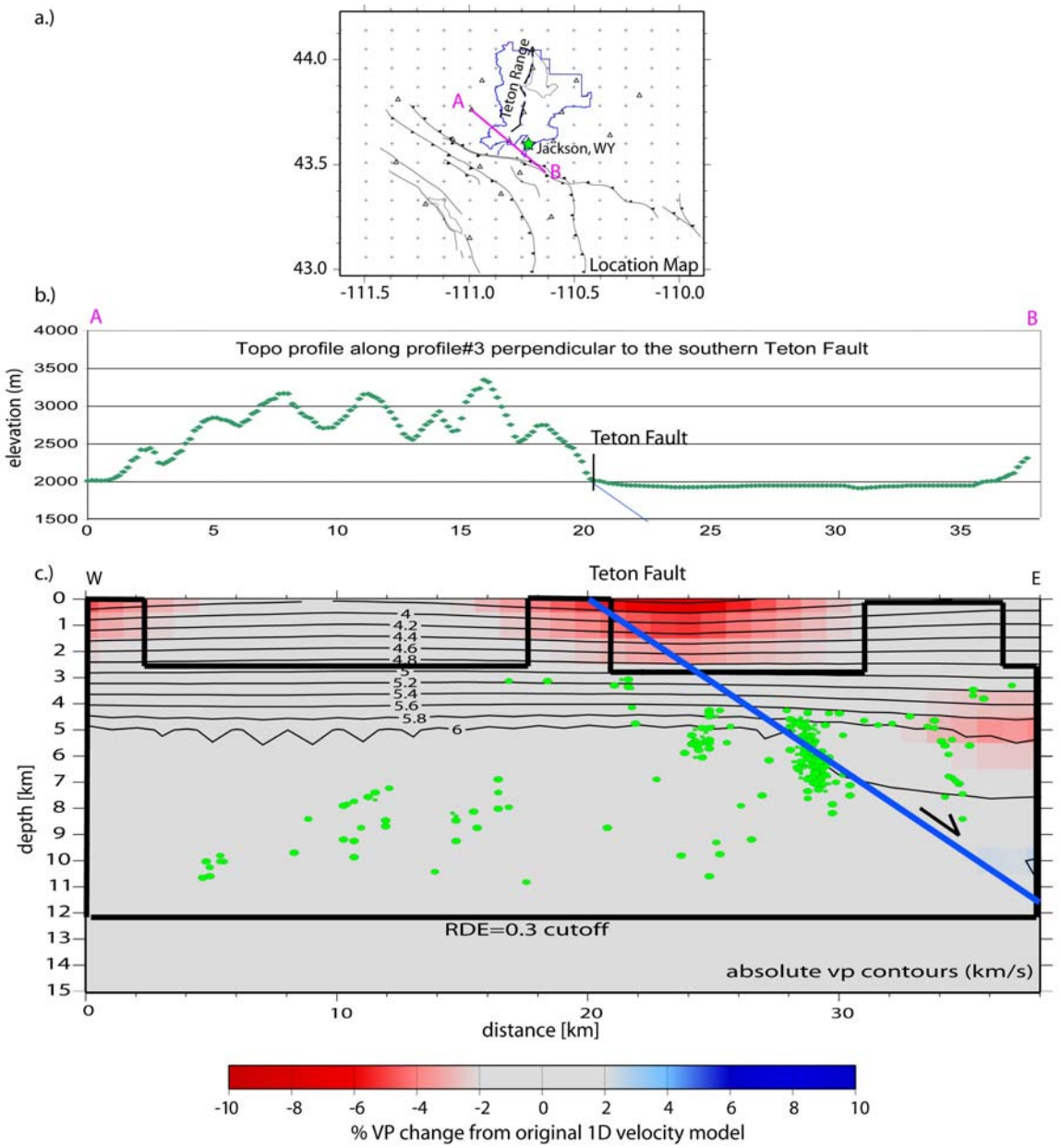

Figure 3.30. 3-D velocity model cross section perpendicular to the southern Teton fault segment. The location map of the vertical cross section is located at the top in figure (a). The cross section location represented by the pink line continues along the A to B profile. Figure (b) shows the topographic profile along the cross section in meters. Figure (c) shows the final 3-D inversion solution with velocity perturbations shown by the red and blue color scale, and overlain absolute velocity contours. There is no vertical or horizontal exaggeration between the depth and distance axis. The area of good resolution is located inside the bold black lines that show the areas of RDE greater than or equal to 0.3. The hypocenter locations of the high quality events along the profile +/-5 km are shown in green circles. The blue line represents a possible projection of the Teton fault at depth with a dipping angle of 45 degrees.

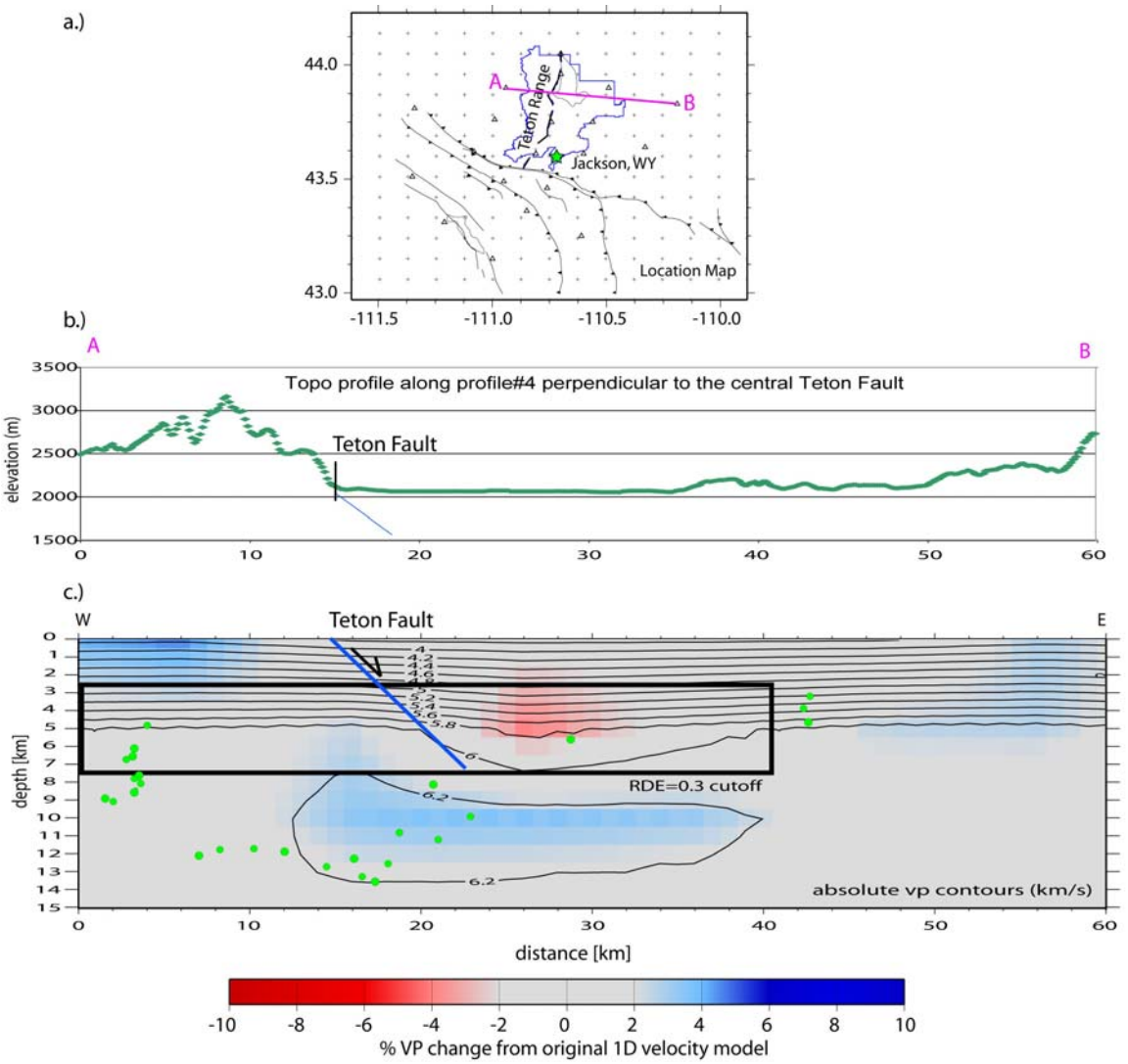

Figure 3.31. 3-D velocity model cross section perpendicular to the central Teton fault segment. The location map of the vertical cross section is located at the top in figure (a). The cross section location represented by the pink line continues along the A to B profile. Figure (b) shows the topographic profile along the cross section in meters. Figure (c) shows the final 3-D inversion solution with velocity perturbations shown by the red and blue color scale, and overlain absolute velocity contours. There is no vertical or horizontal exaggeration between the depth and distance axis. The area of good resolution is located inside the bold black lines that show the areas of RDE greater than or equal to 0.3. The hypocenter locations of the high quality events along the profile +/-5 km are shown in green circles. The blue line represents a possible projection of the Teton fault at depth with a dipping angle of 50 degrees.

the relocated hypocenters as compared to the original locations determined by the U.S. Bureau of Reclamation. I will also describe how we attempted to use a relative hypocenter relocation program called hypoDD [*Waldhauser*, 2001]. This relative hypocenter relocation was a quick test we attempted after our absolute hypocenter locations were determined using NonLinLoc, so we will only briefly discuss the theory of this program in section 3.4.3.

3.4.1. Theory

The probabilistic formulations of nonlinear inverse problems rely on the use of normalized and unnormalized probability density functions to express our knowledge about the values of parameters [*Husen*, 2003]. If the probability density functions giving *a priori* information on the model parameters and on observations are independent, and the theoretical relationship between a vector of observed data and unknown parameters can be expressed as a conditional density function, then a complete, probabilistic solution can be expressed as an a posterior probability density function (PDF) [*Tarantola and Valette*, 1982].

In earthquake relocation, the unknown parameters are the hypocentral coordinates (x, y, and z) and the origin time, t. The observed data are a set of arrival times measured at seismograph stations, and the theoretical relation gives theoretical or predicted travel times [*Husen and Smith*, 2003]. *Tarantola and Valette* [1982] described a process in which, if the theoretical relationship and observed travel times are assumed to have Gaussian uncertainties expressed by covariance matrices, and if the *a priori* information on the origin time is assumed uniform, then the *a posteriori* PDF can be evaluated

analytically in a marginal PDF for the spatial location and the origin time [*Tarantola and Valette*, 1982; *Moser et al.,* 1992].

In NonLinLoc, the PDF can be computed in three different ways [*Lomax et al*., 2001] : (1) via a grid-search algorithm using successively finer, nested grids; (2) via a Metropolis-Gibbs sampling algorithm performing a directed random walk within a spatial volume to obtain a set of samples that follow the PDF; and (3) via an Oct-Tree Importance sampling algorithm (Oct-Tree algorithm). The Oct-Tree algorithm gives accurate, efficient, and complete mapping of the PDF of the earthquake location problem [*Lomax and Curtis*, 2001]. It uses recursive subdivision and sampling of cells in 3-D to generate a cascade of sampled cells, where the number of sampled cells follows the values of the PDF at the cell center, thus leading to higher density of cells in areas of higher PDF (lower misfit) [*Husen*, 2003]. Multiple minima in the PDF are reliably detected by the grid-search algorithm but are missed by the Metropolis-Gibbs sampling algorithm [*Husen,* 2003]. The Oct-Tree algorithm outperforms the grid-search algorithm by a factor of 100 in computing time [*Lomax and Curtis*, 2001]. However, the Oct-Tree algorithm may not detect very narrow local minima in the PDF. The advantages of the Oct-Tree algorithm clearly outweigh the negative points, and therefore we used the Oct-Tree algorithm for relocating the entire earthquake catalog for the Teton region.

The *a posteriori* PDF represents a complete, probabilistic solution to the location problem, including information on uncertainty and resolution [*Lomax et al*., 2001]. Using the Oct-Tree algorithm allows us to present location uncertainties in the form of density scatter plots. These density scatter plots are obtained by drawing samples proportional to the probability [*Lomax et al*., 2000]. This means that the high density of

samples indicates a high probability for the earthquake location which is then called the maximum likelihood hypocenter location (star in Figure 3.32).

Gaussian estimates are also included in the probabilistic solution produced by NonLinLoc by determining the expected hypocenter location and the 68% confidence ellipsoid (circle in Figure 3.32) [*Lomax et al*., 2000]. These estimates may be interpreted as results by linearized location algorithms such as HYPO-71 [*Lee and Lahr*, 1972] or HYPOINVERSE [*Klein*, 1978].

3.4.2. Absolute Hypocenter Locations

A valuable advantage of the NonLinLoc program is the ability to use the 3-D velocity model determined for the Teton region in the relocation process. We relocated all 8,537 events from the catalog, 1996-2002, using the combined 3-D P wave velocity model described in the previous section and the Oct-Tree algorithm. We chose the Oct-Tree algorithm instead of the grid search since it is much faster (1/100), and it also produces similar location results as the grid search. All events were relocated using the same parameters such as initial grid size and number of samples drawn from the PDF through the entire study.

The idea of analyzing scatter plots of each of the 8,537 earthquakes to determine the location quality is impractical. Therefore, we classified all the events into four quality classes A, B, C, and D (Table 3.7). The DIFF column in Table 3.7 represents the difference between the maximum likelihood and expected hypocenter locations. The average error is determined by the average length of the three axes of the 68% error ellipsoid. This same methodology was used by *Husen and Smith* [2003].

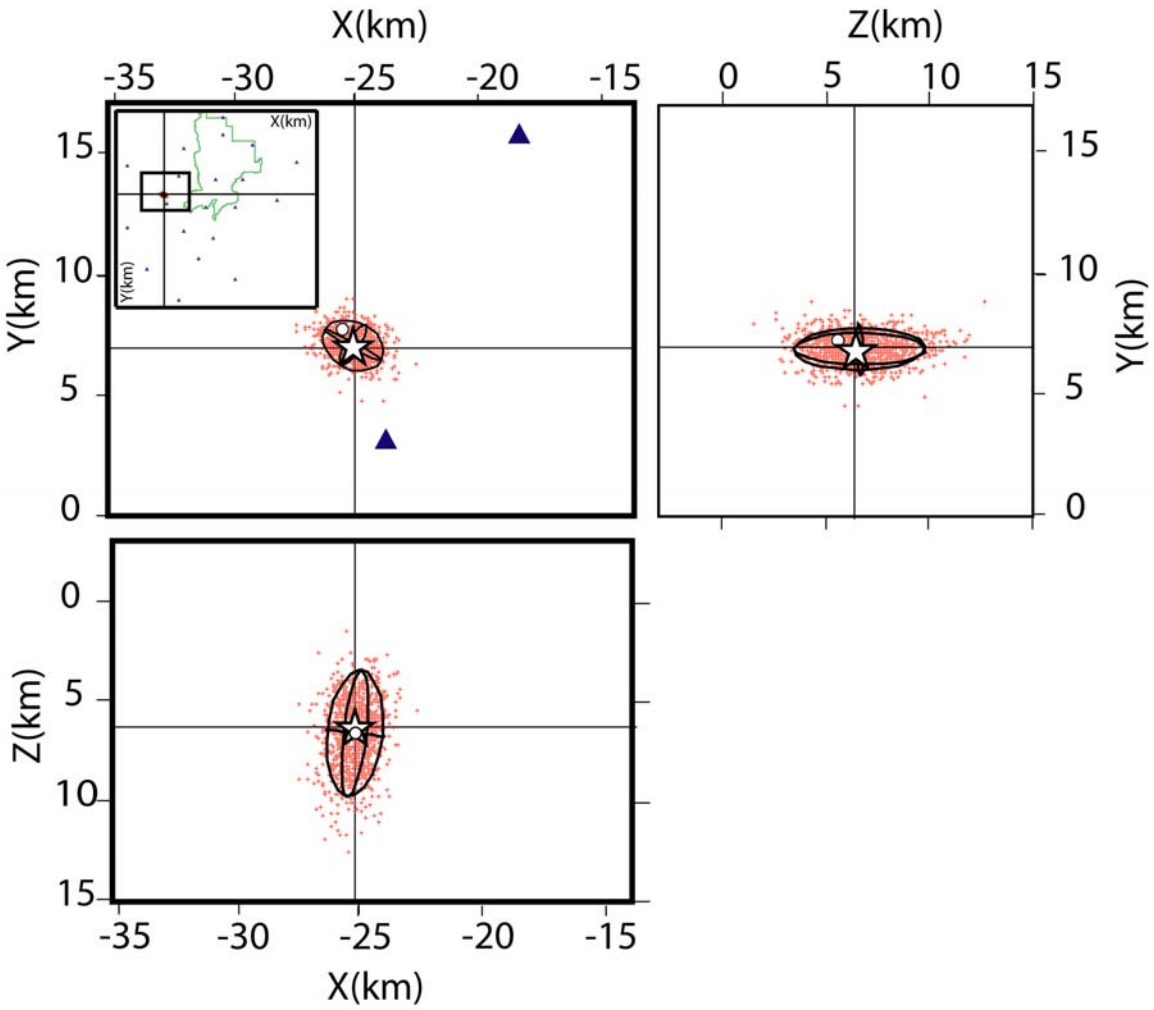

Figure 3.32. Probabilistic location uncertainties shown by density scatter plots. The plane view in the x-y direction are shown with cross sections in the x-z and y-z directions. The star indicates the maximum likelihood hypocenter location, and the circle shows the expected hypocenter location. The black triangles represent the Teton seismic stations and the black ellipsoid is the projection of the 68% confidence boundary.

Table 3.7. Quality class definitions for earthquake locations of the Teton earthquake catalog

Quality Class	Selection Criteria
A (excellent)	RMS < 0.5s, DIFF < 1.0km, average error < 3.0km
B (good)	RMS < 0.5s, DIFF < 1.0km, average error > 3.0km
C (questionable)	RMS < 0.5s, DIFF ≥ 1.0km
D (poor)	RMS ≥ 0.5s

Figure 3.33 displays the density scatter plots for each quality class. Density scatter plots display a subset of hypocenter locations determined by the probabilistic density function. The number of scatter points is proportional to the probability of the hypocenter location. The definition of the quality classes is based on a comprehensive set of uncertainty parameters computed by NonLinLoc [*Husen*, 2003]. The uncertainties used to define the classes are: the difference between the maximum likelihood and expected hypocenter locations, the total event RMS value, and the total average error determined by the average length of the three axes of the 68% error ellipsoid. The probabilistic relocation method determines both a maximum likelihood hypocenter and an expectation hypocenter location derived from predicted travel times. The maximum likelihood hypocenter is considered the optimal hypocenter location determined by the NonLinLoc program, and the expectation hypocenter location is the traditional Gaussian or normal estimators obtained from the gridded values of the normalized location probability density function. Differences greater than 2 km between the maximum likelihood and the expected hypocenter locations can result from an ill-conditioned location problem [*Lomax et al*., 2000]. If this is the case then the confidence ellipsoid is

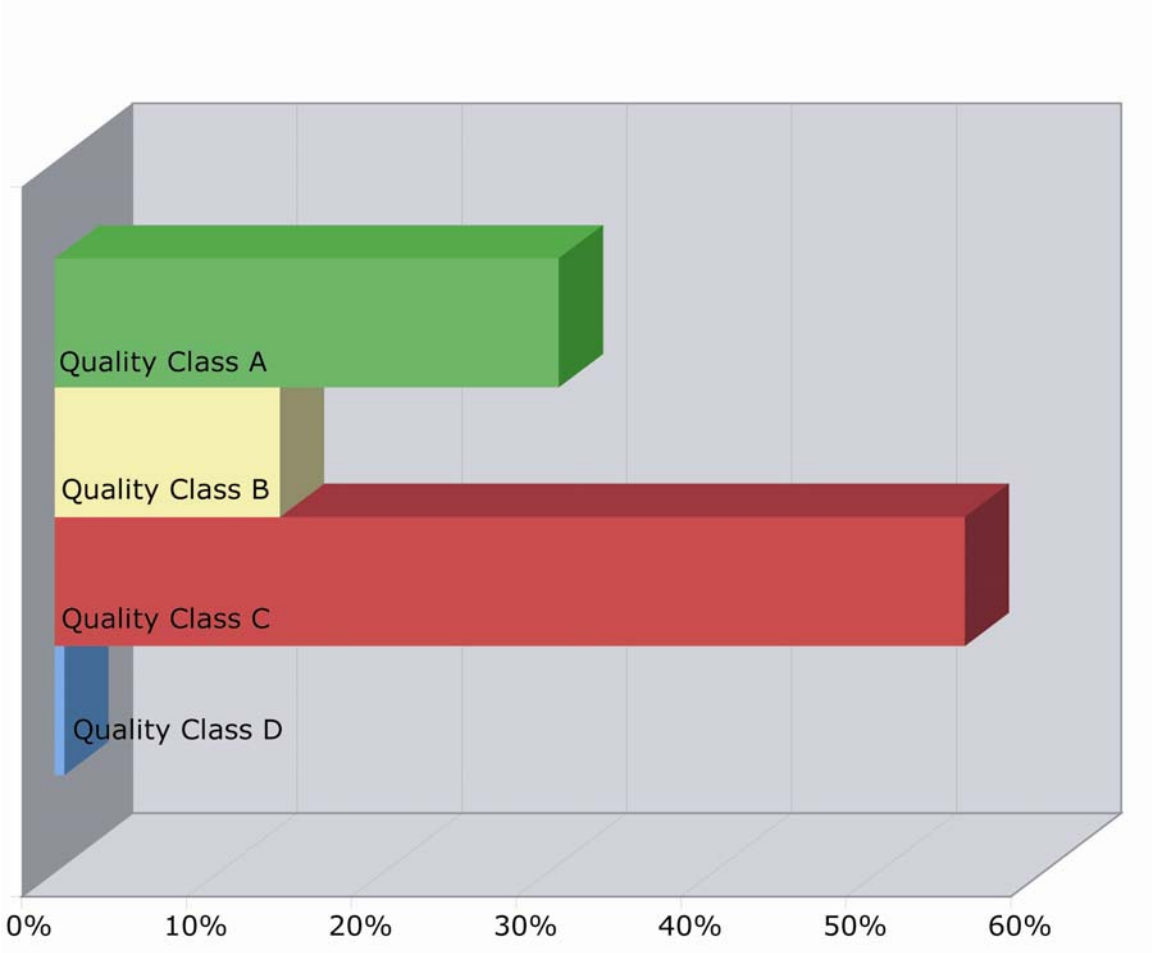

Figure 3.33. Percentage of earthquakes for each quality class for the entire relocated Teton earthquake catalog.

no longer showing adequate uncertainty estimates, since the location uncertainties can be strongly irregular or show multiple minima.

From the four quality classes, one can evaluate the percentage of earthquakes for each class (Figure 3.33). There is definitely a small number of events (less than 1%) that fall into the D quality class showing RMS values greater than 0.5 s. These large errors associated with class D could be caused by mispicked arrival times or by timing problems of the seismic data [*Husen*, 2003]. Given the large RMS values, these events were not used in interpreting the seismic profile of the Teton region.

Quality classes A, B and C all have RMS values below 0.5 s but have differences between the maximum likelihood and expected hypocenter locations. The 0.5 km difference cutoff was somewhat arbitrary, but observed scatter plots revealed that earthquakes with differences > 0.5 km had large uncertainties of several kilometers in epicenter and focal depth [*Husen*, 2003]. The scatter plot representing class C in Figure 3.34 shows the poor location uncertainties by the confidence ellipsoid. The events in class C tend to have few observations and are generally located outside the Teton seismic network giving them a poor azimuthal distribution of observations.

The last two quality classes A and B are the most reliable earthquake locations in the relocated catalog (Figure 3.34). All of these events have a well defined PDF with a minimum, and the 68% confidence ellipsoid represents the location uncertainties accurately. The difference between these two classes is defined by their average error determined by the average length of the three axes of the 68% error ellipsoid. The epicenters in both classes are well defined, but the error in depth is the separating factor. Events in class B have a larger depth error than events in class A. The difference in the

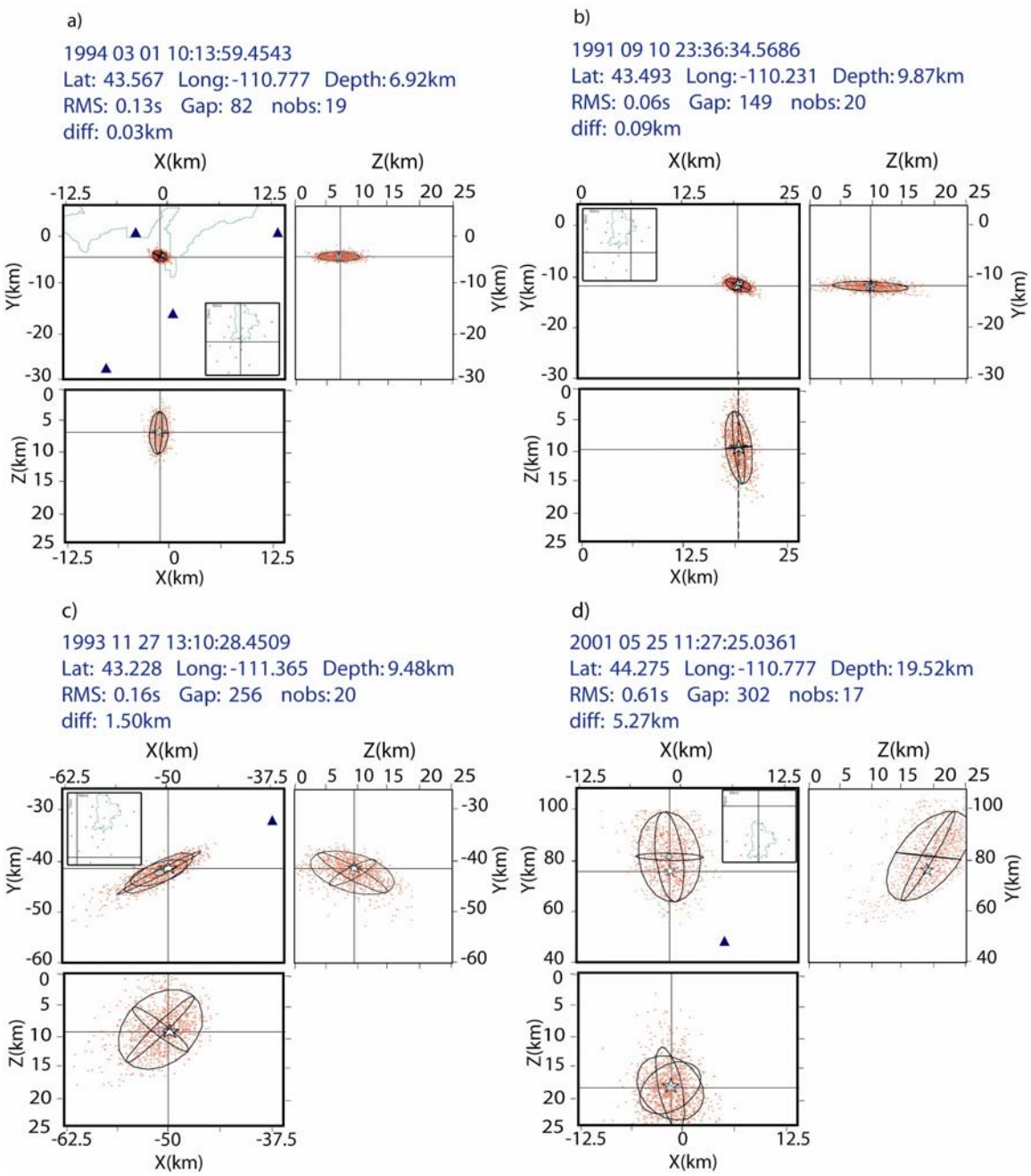

Figure 3.34. Probabilistic location uncertainties shown by density scatter plots for each quality class A, B, C, and D. The plane view in the x-y direction is shown with cross sections in the x-z and y-z directions. The star indicates the maximum likelihood hypocenter location. The blue triangles represent the Teton seismic stations and the black ellipsoid is the projection of the 68% confidence boundary. Inlays for (a), (b), (c), and (d) show an overview of the entire region. The outline of Grand Teton National Park is shown in the inlays by the thin green line.

error ellipsoids between classes A and B are clear in Figure 3.34. This larger depth error in class B is due to the lack of stations within the critical focal depth distance, giving a poor constraint on the true vertical depth.

3.4.3. Results

Hypocenter locations in the Teton Region have improved in accuracy using the 3-D velocity model and probabilistic relocation method by reducing the P-wave arrival time residuals by 59% relative to the original Bureau of Reclamation's 1-D hypocenter locations.

The results and conclusions of the final absolute hypocenter locations are summarized in this section. Figure 3.35 shows the final hypocenter locations determined by the 3-D velocity model and the NonLinLoc program. This figure shows the epicenters in the plane view of the Teton region and depth cross sections along the A to A' and B to B' profiles that run perpendicular to the Teton fault. The hypocenters along the depth section profiles show no correlation with the downward projection of the Teton fault at a 45° angle or any angle between 30° and 60°.

There are also noticeable linear trends of epicenters in the Teton region. Many of these clusters and trends also appear using the hypocenter locations obtained with the minimum 1-D model and station corrections. Hypocenters were randomly shifted by 10km and relocated using the final 3-D velocity model and NonLinLoc and the relocated hypocenters still showed linear trends of seismicity. Many of these clusters and trends do occur within a few years or event months of each other, but some linear trends tend to build over longer time periods from 1986 to 2002. One way to view these trends and

Figure 3.35. Hypocenters of all 8,537 Teton recorded earthquakes from 1986-2002 relocated by the NonLinLoc program. These hypocenters are represented by red circles shown in both plain view and vertical cross sectional depth view. The Teton fault is outlined in black and runs through the middle of Grand Teton National Park, outlined in green. The Teton fault is projected with an eastward dip of 45 degrees. There are few or no earthquakes that align with the downward projection of the Teton fault. The Jackson Lake Seismic Network stations are shown by the dark blue triangles. Linear spatial trends in epicenter locations are labeled.

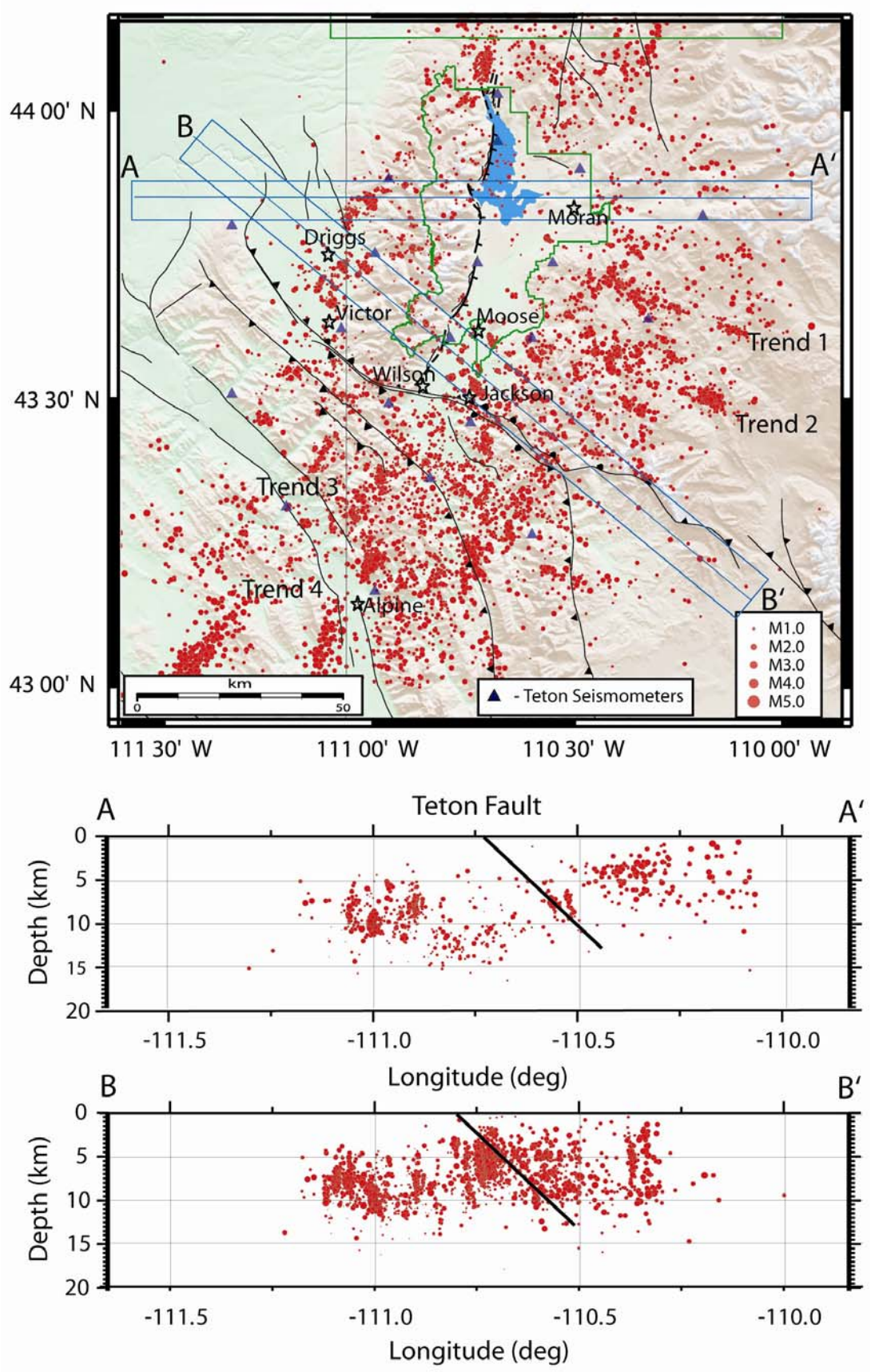
44 00' N
43 30' N
43 00' N
111 30' W
111 00' W
110 30' W
110 00' W
A
A'
B
B'
Moran
Driggs
Victor
Moose
Wilson
Jackson
Alpine
Trend 1
Trend 2
Trend 3
Trend 4
km
0
50
- Teton Seismometers
M1.0
M2.0
M3.0
M4.0
M5.0
Teton Fault
Depth (km)
Longitude (deg)
-111.5
-111.0
-110.5
-110.0
0
5
10
15
20

clusters is to plot the hypocenters by their quality classes and view only the highest precision locations to correlate with known faulting structures.

Figure 3.36 displays the hypocenter locations for all Teton region events in the highest quality class A. These hypocenter locations are the most accurate in the entire catalog and show only a few small clusters and linear trends. These are trends that could possibly be correlated with seismogenic structures and we believe they are real linear seismic trends and not artifacts. Figure 3.37 shows the hypocenter locations for all the events in the B quality class. These hypocenters are also accurate locations and will be combined with the quality class A events to aid with the determination of active faulting structures in the Teton region. There are a few trends in this quality class, but even combined class A and B events would not produce the strong clusters and trends as were seen in Figure 3.35.

Class C quality events contained the most hypocenter locations but were the second to least accurate (Figure 3.38). The epicenter plot for class C displays the majority of the clusters and trends that were dominant in the full relocated catalog hypocenter plot. We still believe these trends are imaging real structures since similar trends are seen in the higher quality hypocenter locations as well. The C quality class locations had over 1 km differences between their maximum likelihood and expectation hypocenter locations. The largest clusters of events in the lower southwestern corner of the epicenter plot are due to mining induced seismicity occurring in November of 1992. Quality class D hypocenters are shown in Figure 3.39. All 49 events are randomly distributed throughout the Teton region and all have RMS values greater than 0.5 s.

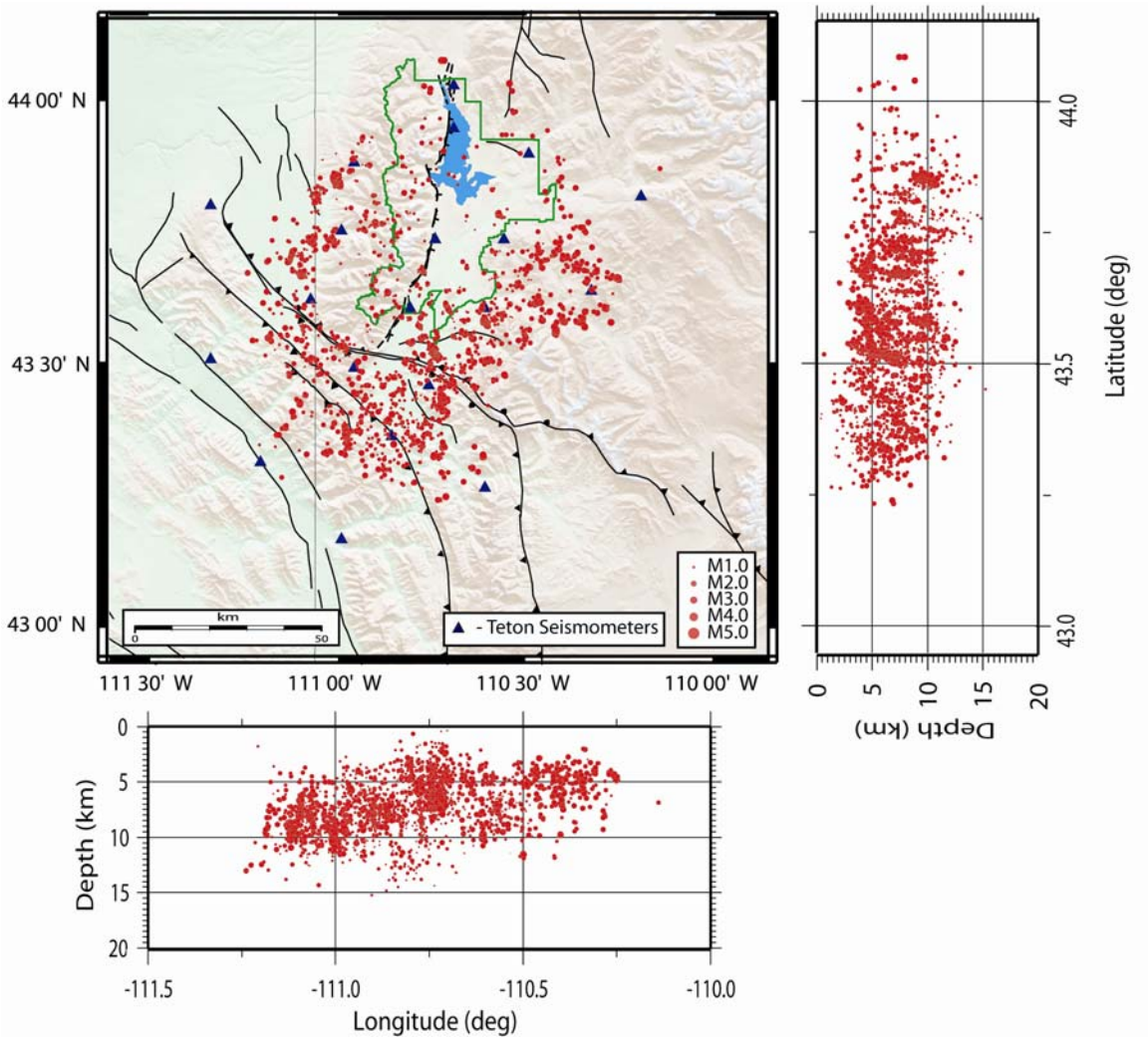

Figure 3.36. Hypocenters of quality class A relocated by the NonLinLoc program. These hypocenters are represented by red circles shown in both plain view and vertical cross sectional depth view. The Teton fault is outlined in black and runs through the middle of Grand Teton National Park that is outlined in green. The Jackson Lake Seismic Network stations are shown by the dark blue triangles. Quality class A relocated hypocenters have an RMS < 0.5, a maximum likelihood and expectational hypocenter difference < 1.0 km, and an average error < 3.0 km. These are the highest quality relocated hypocenters in the Teton catalog.

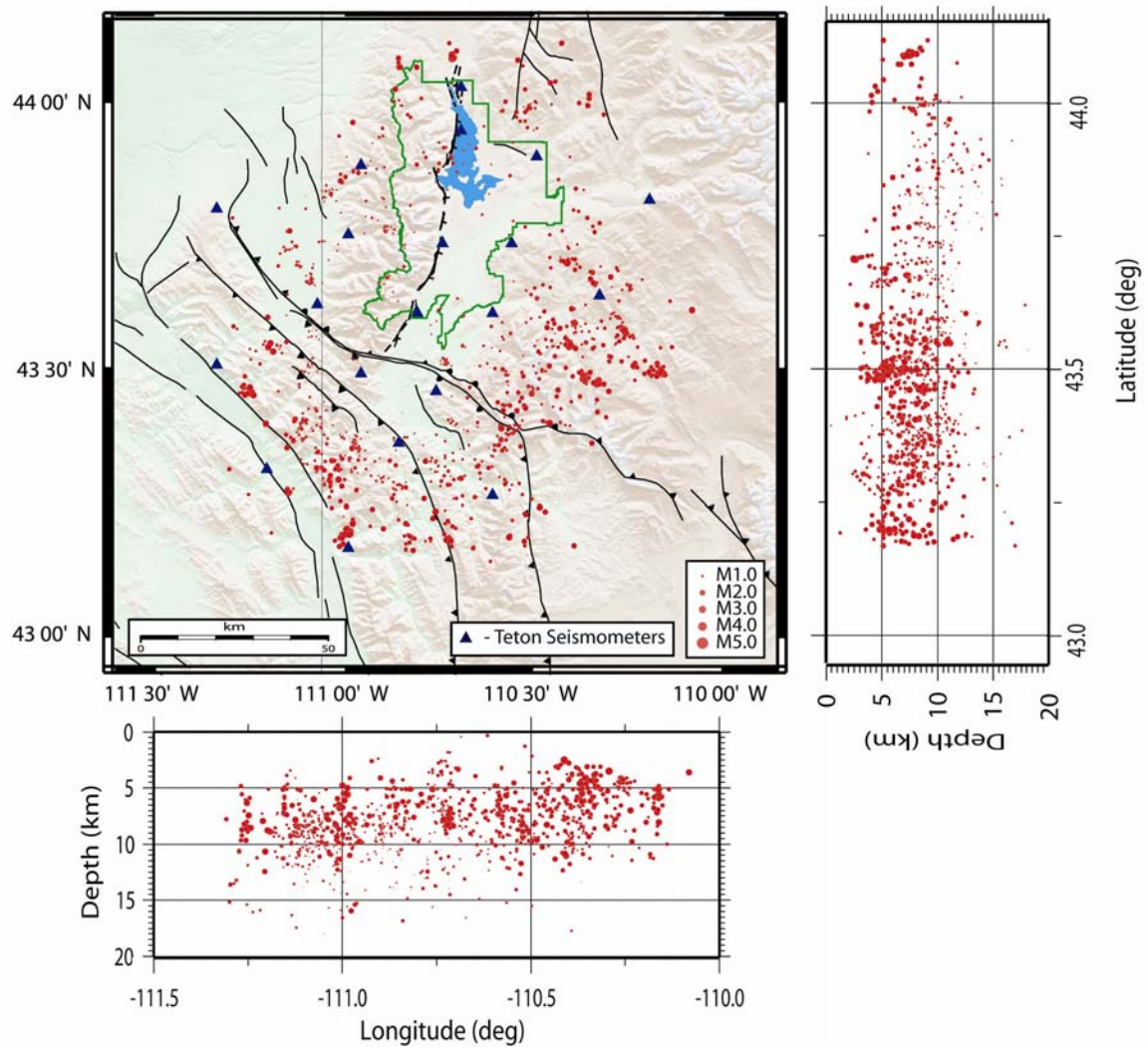

Figure 3.37. Hypocenters of quality class B relocated by the NonLinLoc program. These hypocenters are represented by red circles shown in both plain view and vertical cross sectional depth view. The Teton fault is outlined in black and runs through the middle of Grand Teton National Park that is outlined in green. The Jackson Lake Seismic Network stations are shown by the dark blue triangles. Quality class B relocated hypocenters have an RMS < 0.5, a maximum likelihood and expectational hypocenter difference < 1.0 km, and an average error > 3.0 km. These are the second highest quality relocated hypocenters in the Teton catalog.

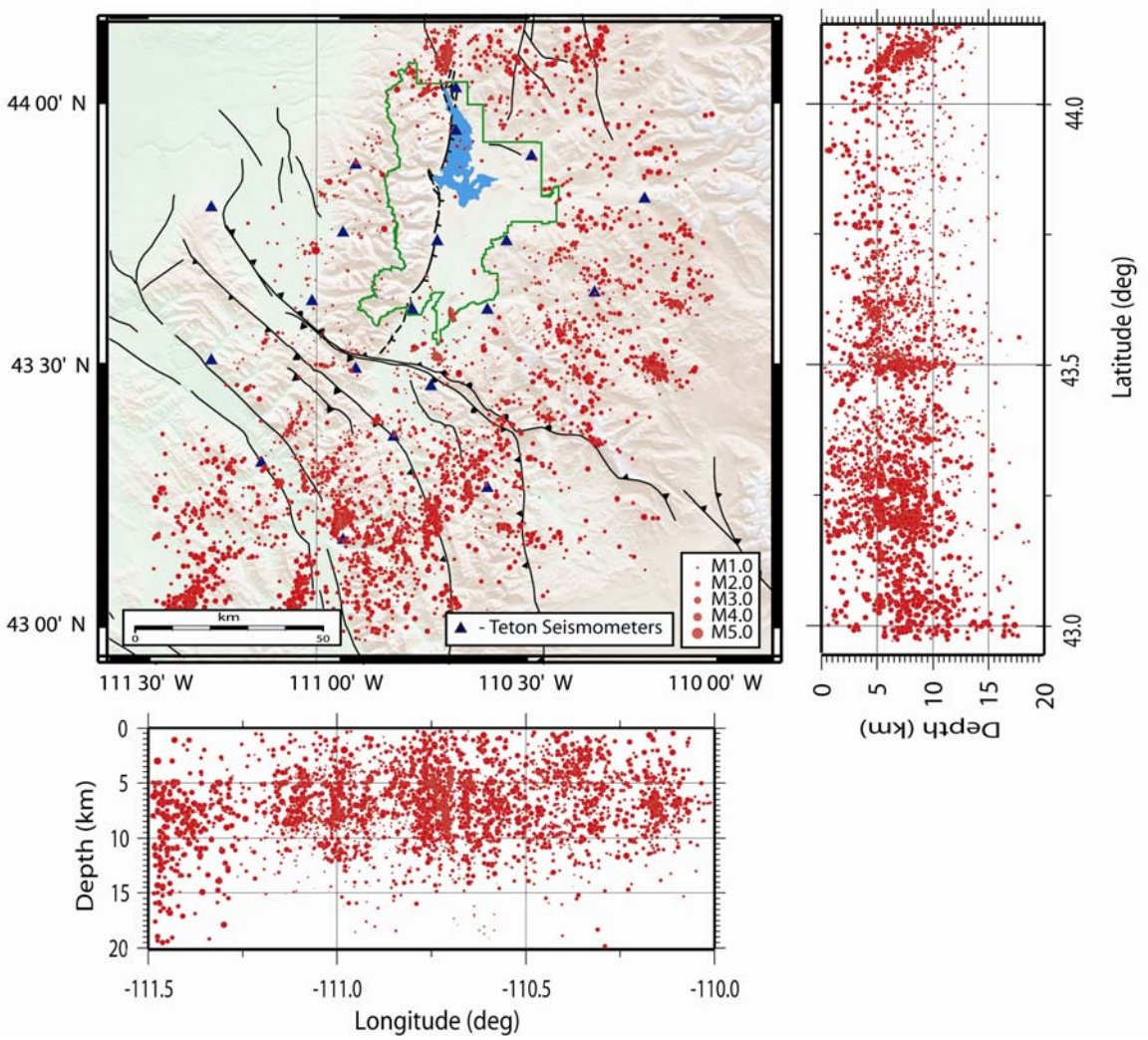

Figure 3.38. Hypocenters of quality class C relocated by the NonLinLoc program. These hypocenters are represented by red circles shown in both plain view and vertical cross sectional depth view. The Teton fault is outlined in black and runs through the middle of Grand Teton National Park that is outlined in green. The Jackson Lake Seismic Network stations are shown by the dark blue triangles. Quality class C relocated hypocenters have an RMS < 0.5, and a maximum likelihood and expectational hypocenter difference > 1.0 km.

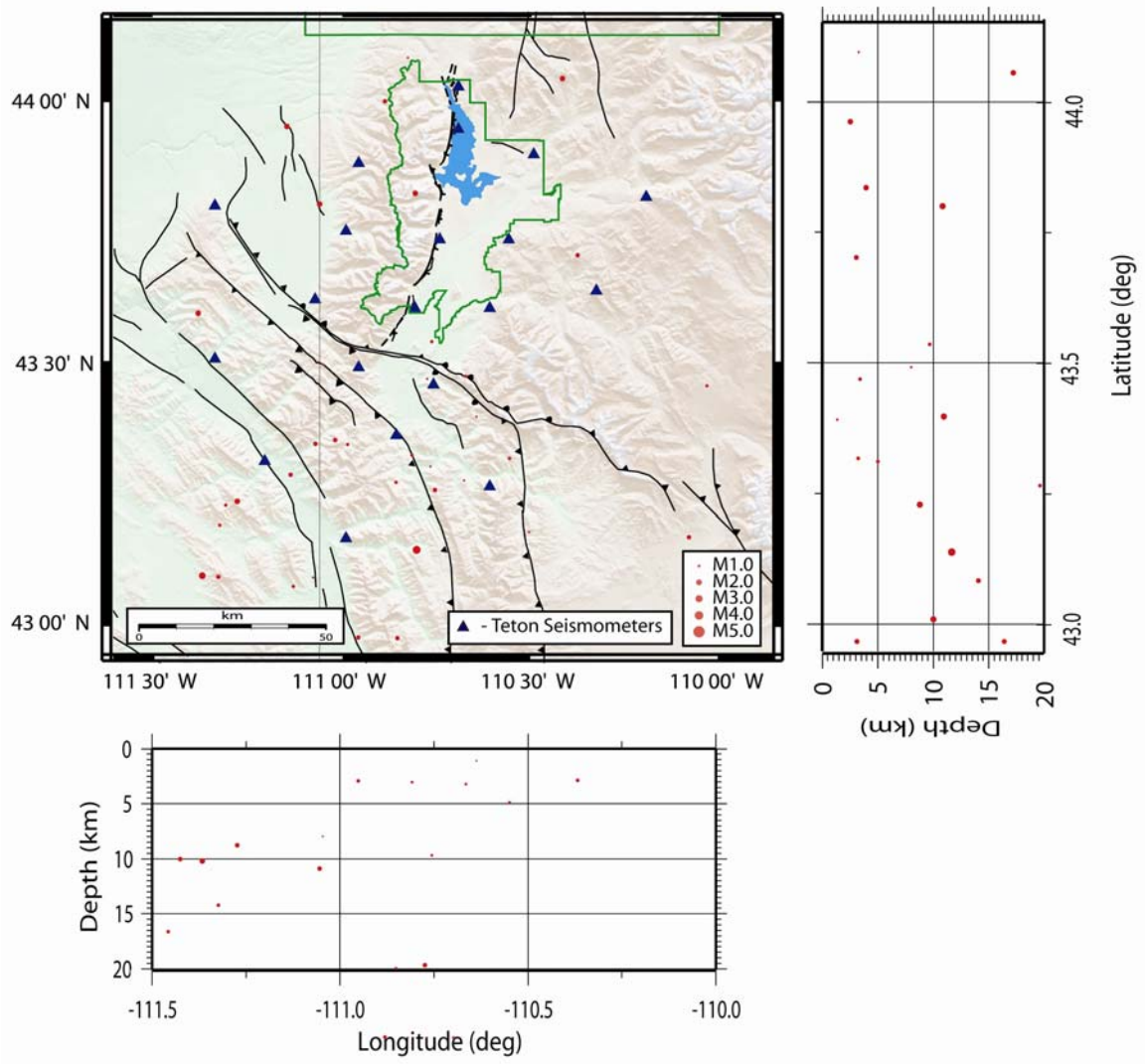

Figure 3.39. Hypocenters of quality class D relocated by the NonLinLoc program. These hypocenters are represented by red circles shown in both plain view and vertical cross sectional depth view. The Teton fault is outlined in black and runs through the middle of Grand Teton National Park that is outlined in green. The Jackson Lake Seismic Network stations are shown by the dark blue triangles. Quality class D relocated hypocenters have an RMS > 0.5.

In addition to determining the absolute hypocenter locations for all events in the Teton Bureau of Reclamation catalog, relative hypocenter locations were attempted using the new absolute locations from NonLinLoc. This double-difference method [*Waldhauser*, 2001] takes advantage of the fact that if the hypocentral separation between earthquakes is small compared to the event-station distance and to the scale length of velocity heterogeneity, ray paths between the two hypocenter locations and a common station are similar along almost the entire ray path [*Got et al*., 1994].

In this case, the difference in travel times for two events observed at one station can be attributed to the spatial offset between the events with high accuracy [*Matter*, 2005]. This methodology employs many of the similar functions such as the cross-correlation program described in the first section of this chapter. Similar to what we determined in the cross-correlation method, many of the clusters contained small numbers of events in each of them. In this program I set the minimum value of eight observations for linking two events (one observation for each degree of freedom). Furthermore, I set the maximum radius of 500 km to look for event-pairs. Almost 90% of all the relocated earthquakes were grouped in the cluster containing all the outliers that did not fit the clustering criteria. Given this information, we determined that it was not useful to continue with the relative hypocenter location process as our nonlinear locations were already more accurate by about 20%. Perhaps conducting relative hypocenter locations on individual swarms or small spatially clustered events would be useful in the future, but for the entire catalog we found it best to use only the absolute hypocenter locations for the Teton region.

3.5. Revised Coda Magnitude Scale

The revision of coda magnitude, Mc, scale is important to determine the most consistent and reliable magnitudes for earthquakes in a local region. In order to apply a new coda magnitude methodology to a network, important information must be known about the seismic station instrumentation information. Generally local magnitudes (M_L) requiring a sampling using Wood-Anderson seismometers were not available for the Teton region. In this section I will describe how we evaluated a revised coda magnitude scale for the Jackson Lake seismic network.

3.5.1. Theory

Originally coda magnitudes for all 8,537 Teton region earthquakes from April 1986 to December 2002 were to be recomputed using an improved coda magnitude equation developed by *Pechmann et al.* [2001] for the University of Utah, Utah and Yellowstone networks.

$$Mc = -2.60 + 2.44 \log\tau + 0.0040\Delta \qquad (1)$$

where τ is signal duration in seconds measured on a short period vertical component seismogram, and Δ is epicentral distance in kilometers. Signal duration is measured from the P-wave arrival to the time that the seismic signal drops below the noise level, which is defined as 0.01724 microns/s based on the median noise level for short-period analog-telemetered station in the University of Utah Seismograph Station (UUSS) regional seismic network [*Pechmann et al.*, 2001]. This methodology to recompute coda

magnitudes improved the average Mc and Ml differences ranging up to ± 0.5 magnitude units in the Utah and Yellowstone network events [*Pechmann et al*., 2001]. This same methodology was to be used in the Teton network events as well to reduce the Mc and M_L differences.

3.5.2. Coda and Local Magnitude Scale Results

In order to apply the coda magnitude calculation to the Teton network certain seismic station information is needed. The static gains of the vertical-component instruments at 5 Hz, in units of counts/micron/sec, are needed as well as the instrument response (gain verses frequency). Also the coda magnitude scale would need to be calibrated against local magnitudes determined primarily from broadband instruments. The broadband coverage from 1995 to 2002 in the Teton network was very poor, with all five stations located in one geographic location while the short period network was operating.

The original magnitudes for all the Teton network recorded events were determined by the U.S. Bureau of Reclamation, who operated the network from 1986 to 2002. They developed a relative magnitude scale that was not calibrated to adjacent networks in Yellowstone or Utah. They computed a duration magnitude scale that was relative for local events, and set up a procedure to routinely compute moment magnitudes from the long-period spectral levels and instrument response data. These magnitudes were ultimately based on short-period vertical-component seismometers.

The durations picked by the Bureau of Reclamation were done by hand using the program XPED. The calibration and gain information for each station in the network was

given to us by the BoR, and analyzed by Pechmann. To quickly assess how well the BoR's relative local magnitude scale was, we compared all Teton region earthquakes that were located by the University of Utah Seismograph Station's (UUSS) Yellowstone and Utah networks with those located by the BoR's Teton seismic network. Only events with local magnitudes for the Teton region events located by the UUSS networks were used (Figure 3.40). There were only 110 events that were recorded by the UUSS networks that match the date and time of events recorded by the Teton seismic network from 1986 to 2002. These two magnitude scales are compared in Figure 3.41.

If the magnitude scales were identical then all the magnitudes would fall along a perfect straight line with a slope of one. The results of this plot show that the magnitudes determined by the BoR match very well with the local magnitudes determined by the UUSS networks. They are not perfect along the ideal linear fitted line but there is only a maximum average of ± 0.5 magnitude units of difference between the two network magnitude scales. This difference is small enough to conclude that the magnitude scale determined by the BoR is sufficient and will be used in our later calculations of frequency of occurrence curves in developing the probabilistic seismic hazard analysis.

3.6. Recomputed Take-Off Angles and Focal Mechanism Determination

3.6.1. Theory

Double-couple focal mechanism solutions for selected events have been determined using the nonlinear grid search program FPFIT [*Reasenberg and Oppenheimer*, 1985]. This type of program systematically varies values of strike, dip and

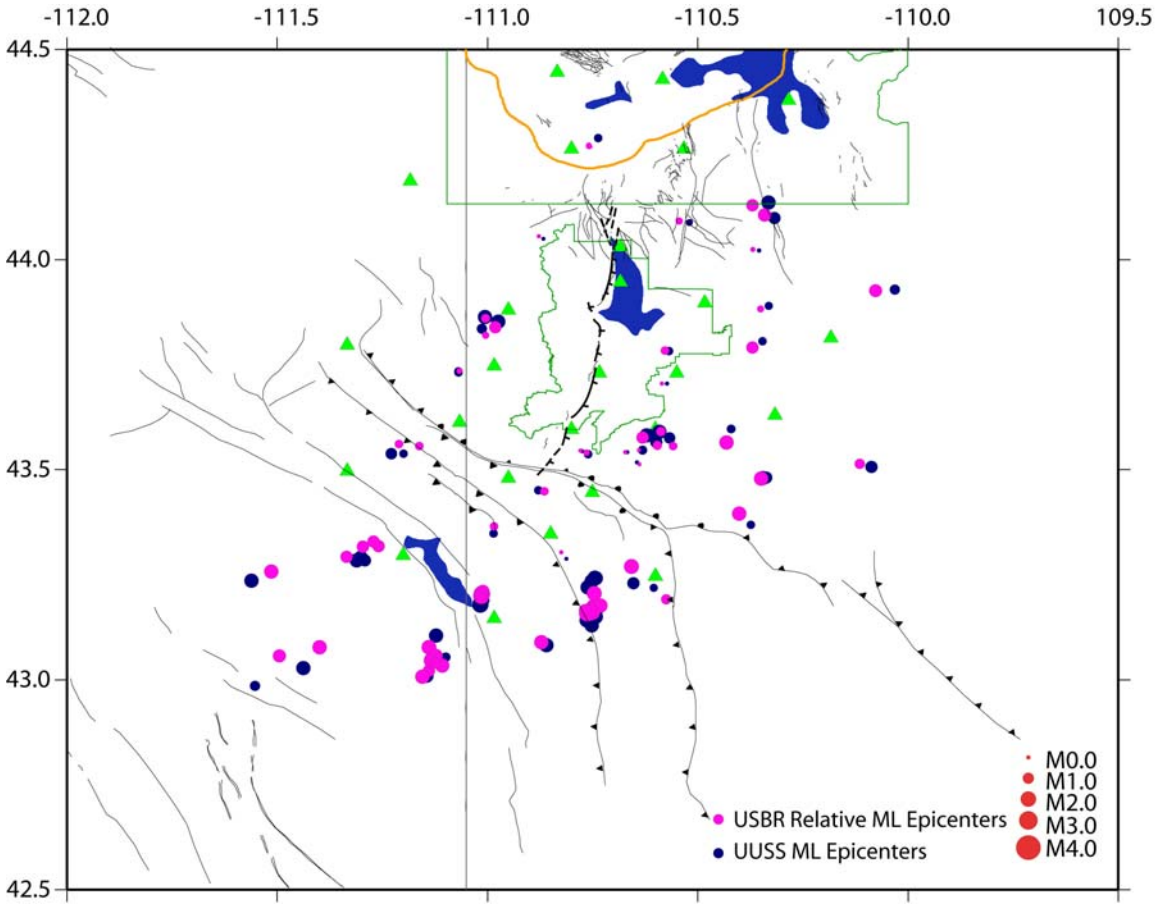

Figure 3.40. Events located by both the U.S. Bureau of Reclamation's Teton seismic network (pink circles) and the University of Utah Seismograph Station's Yellowstone and Utah networks (blue circles). One hundred and ten events were located with local magnitudes from the UUSS networks and relative local magnitudes from the U.S. BoR's Teton seismic network from 1986-2002. Seismic stations are represented by the green triangles and the magnitude scale is in the lower right corner.

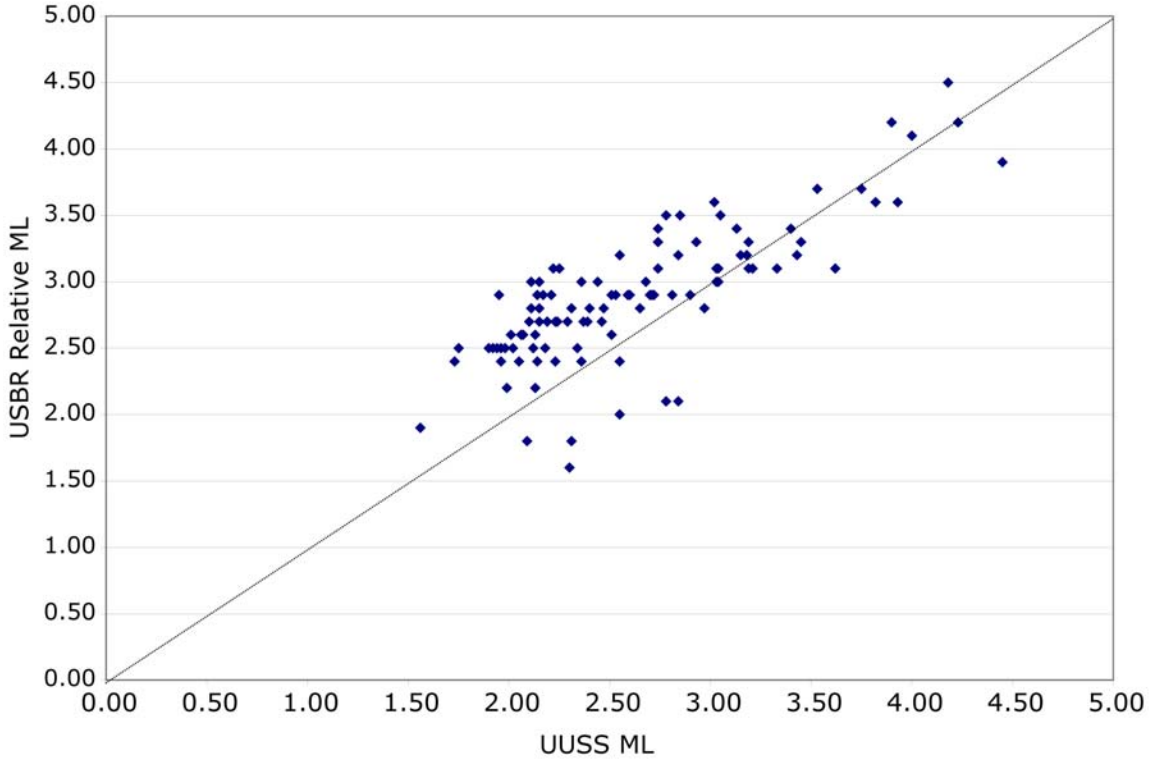

Figure 3.41. Magnitude comparison plot of events located by both the U.S. Bureau of Reclamation's Teton seismic network and the UUSS Yellowstone and Utah networks (blue diamonds). One hundred and ten events were located with local magnitudes from the UUSS networks and relative local magnitudes from the BoR's Teton seismic network from 1986-2002. The gray line represents the perfect correlation between the two different magnitude scales with a slope of one. The magnitude correlation shows the U.S. BoR's relative ML scale matches well with the UUSS ML scale. They are not perfect along the gray ideal fitting line but there is only a maximum average of 1.0 to 0.5 magnitude units of difference between the two network magnitude scales.

rake over given intervals on a grid, and determines the normalized misfit between the planes and the observed first-motion data at each interval.

We employed the algorithm MOTSI developed by *Abers and Gephart* [2001], which, given a suite of first motions, determines the focal mechanisms without regard to *a priori* stress conditions, and uses a statistical approach using P wave polarity data and take-off angles. This program was also used in calculating the stress field solutions from the focal mechanisms. *Abers and Gephardt's* [2001] algorithm follows the grid search inversion technique of *Gephart* [1990] but uses P-wave polarity data and take-off angles directly instead of focal mechanisms as input. This method assumes that the stress field is homogeneous throughout the inversion volume in both space and time and no *a priori* fault orientation information is assumed [*Waite et al.*, 2004]. The fault slip direction is defined to be parallel to the direction of maximum shear stress is maximized. Therefore, with this method the first-motion data are weighted based on the probability of a pick being correct, permitting a better estimate of the full error in the stress solution [*Waite et al.*, 2004].

3.6.2. Focal Mechanism Determination

Teton region earthquakes are moderate to small, with all magnitudes less than 4.0. Given these small magnitudes, the accurate first-motion determinations can often only be made on records from the nearest stations for a given event. Therefore, we restricted focal mechanism determination to events with at least six clear, first-motion picks. These events were also required to have their nearest station within 1.5 times the focal depth to ensure the most accurate focal depth for this study. The two selection criteria reduced the

number of events to a total of 663 events with 6,294 first motion picks. Station polarity reversal corrections did not have to be made due to the results from comparisons of regional network data with well-recorded teleseisms.

The majority of the focal mechanisms for the Teton region range from normal faulting to oblique strike slip events, with a few thrust solutions (Figure 3.42). The dip of the nodal planes in the focal mechanisms closest to the Teton fault projection show an E-dipping plane. The solutions were sorted into faulting types based on strike, dip, and rake orientation following the convention of *Aki and Richards* [1980] (Table 3.8). Since these categories are based on fault slip angles, we had to determine which of the two nodal planes was the correct fault plane in order to determine the proper rake. For each focal mechanism, the fault plane was chosen as the nodal plane that most closely matched the orientation of faults in the vicinity as mapped by *Love et al.* [1992] and others.

Table 3.8. Event types from the high quality hypocenters

Rake Angle	Type of Faulting	High Quality Events
22.5° ≥ rake > -22.5°	Left-lateral strike-slip	131
-22.5° ≥ rake > -67.5°	Oblique-normal left-lateral strike-slip	110
-67.5° ≥ rake > -112.5°	Normal	111
-112.5° ≥ rake > -157.5°	Oblique-normal right-lateral strike-slip	141
-157.5° ≥ rake > 157.5°	Right-lateral strike-slip	121
157.5° ≥ rake > 112.5°	Oblique-reverse right-lateral strike-slip	19
112.5° ≥ rake > 67.5°	Reverse	6
67.5° ≥ rake > 22.5°	Oblique-reverse left-lateral strike-slip	23

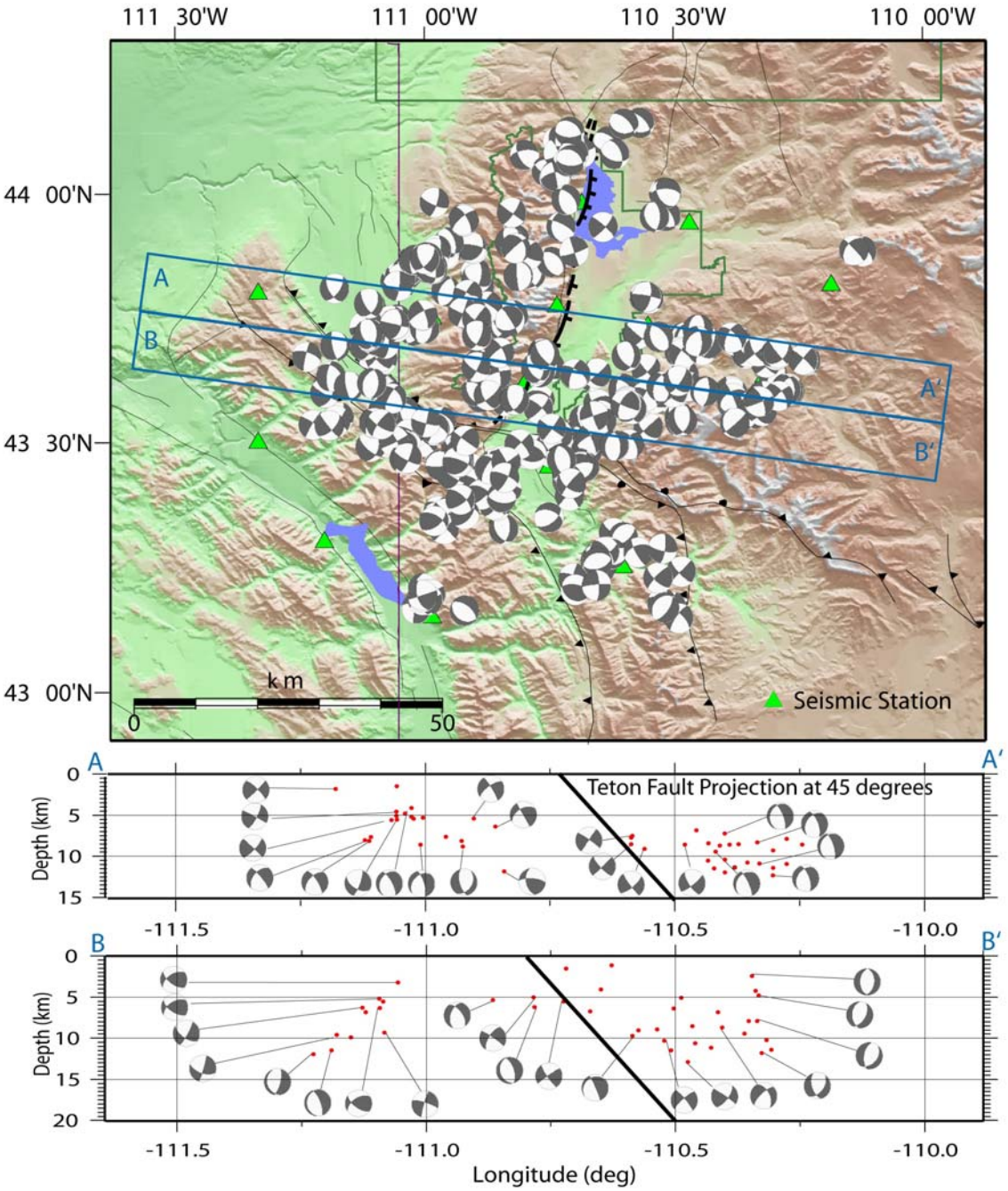

Figure 3.42. Complete set of 663 focal mechanism solutions for the time period 1986 to 2002. The U.S. Bureau of Reclamation Teton seismic stations are shown as green triangles. The Wyoming and Idaho boarder is shown by the dark maroon line. The Teton and Yellowstone National Parks are shown by the dark green lines. Cross sections from A to A' and B to B'are shown by the blue boxes. Focal mechanisms shown at depth are displayed for selected hypocenters in red with the Teton fault projected at a 45 degree angle.

3.6.3. Stress Field Inversion and Interpretation of Focal Mechanisms

The focal mechanisms for 663 events, described above, were used to evaluate the stress field of the Teton region. As I mentioned in the theory section above, the first-motion data are weighted based on the probability of a pick being correct. The highest weights are given to data that are the farthest from the nodal planes where the theoretical P wave amplitude is the largest and the probability of a mispick is the lowest. There are two parameters that describe the probability that the pick is correct. The first, α, is approximately the theoretical P wave amplitude below which the pick reliability drops off considerably (near nodal planes) [*Waite et al*., 2004]. The second, γ, is the overall estimate of mispicked data and is based on the fraction of inconsistent first motions in the entire data set [*Waite et al.*, 2004]. The Teton data set consists of events with an average of 8 first motions that are not generally uniformly distributed. We found good fits to the data using low values of α (0.01-0.05) and γ (0.01-0.05). The output α and γ values depend on the input of α and γ used in the focal mechanism determination [*Waite et al*., 2004]. We chose to be conservative and used values $\alpha = 0.05$ and $\gamma = 0.05$ for the final focal mechanism and stress tensor calculations.

To determine the stress model for the Teton region, the focal mechanism data were divided into smaller areas based on regions with similar tension (T) axes or σ_3 orientations to distinguish regions of relative homogeneous stress (Figure 3.43). Constraining all of the focal mechanisms in the data set into one stress tensor degrades the misfit due to the strong heterogeneity in the data set, but this can be corrected by subdividing the data set into areas of homogeneous stress. Stress model solutions were computed on the five smaller areas and all showed signs of homogeneity with the P and T

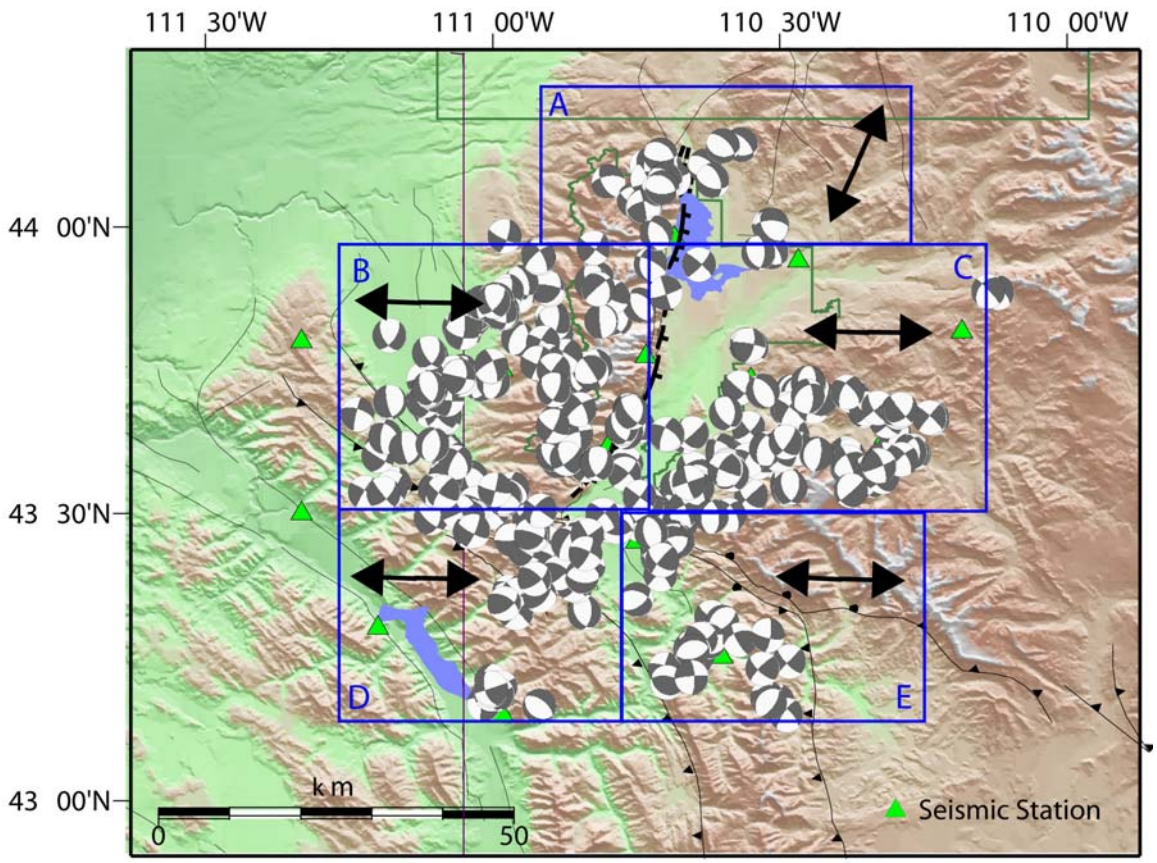

Figure 3.43. Map of areas that were used in stress tensor inversions. Focal mechanisms are shown. Note that focal mechanisms that are not within the boxes were not used in the inversions. The thick black arrows indicate the direction of σ3 and average T axis orientations derived from focal mechanisms. The subareas break the Teton fault into five blocks. Block A represents the northern part of the Teton fault where the B and C blocks represent the middle footwall and headwall sections. The D and E blocks display the σ3 stress orientations in the southern footwall and headwall sections of the Teton fault.

axis for the stress-constrained and unconstrained focal mechanisms plotted in Figure 3.44. The best fit model for each area is displayed in Table 3.9. In Table 3.9 the columns represent: NEv as the number of events; NFM as the number of first motions; NdSj > 1.0 as the number of focal mechanisms that show a fit degradation when constrained by the stress field; and NdMj < 0.9 as the number of focal mechanisms that show a change in focal mechanism when constrained by the stress field.

We compared focal mechanism solutions that were constrained to have slip in the direction of maximum shear stress with those computed independent of the stress field using two measures to quantify the differences. The first is the change in the data fit, dS, which is the means for assessing the homogeneity of the stress in an area and dS*j* is for the individual mechanisms where *j* is the number of the event. The second is the change in focal mechanism orientation, dM*j*. Identical mechanisms have dM*j* = 1.0 while mechanisms with opposite polarities, but identical fault planes have dM*j* = -1.0 [*Waite et al*., 2004].

In each area, there are small changes in *dSj*, but many events with large dM*j* changes. This can be attributed to the small number of first motions available for each event [*Waite et al*., 2004]. The number of events with dSj > 1.0 in each area is listed in Table 3.9 dSj = 1.0 and dSj = 2.0 correspond to confidence levels at which the stress homogeneity assumption can be rejected of 76% and 92%, respectively) [*Waite et al*. 2004]. Area C has the largest percentage of events with dSj > 1.0 at 4%. Generally, about 20% of the earthquakes in all the areas have dMj < 0.9, showing small variations in the nodal plane orientations. The P and T axis plots in Figure 3.44 are also used in examining the differences between the stress-constrained and unconstrained mechanisms.

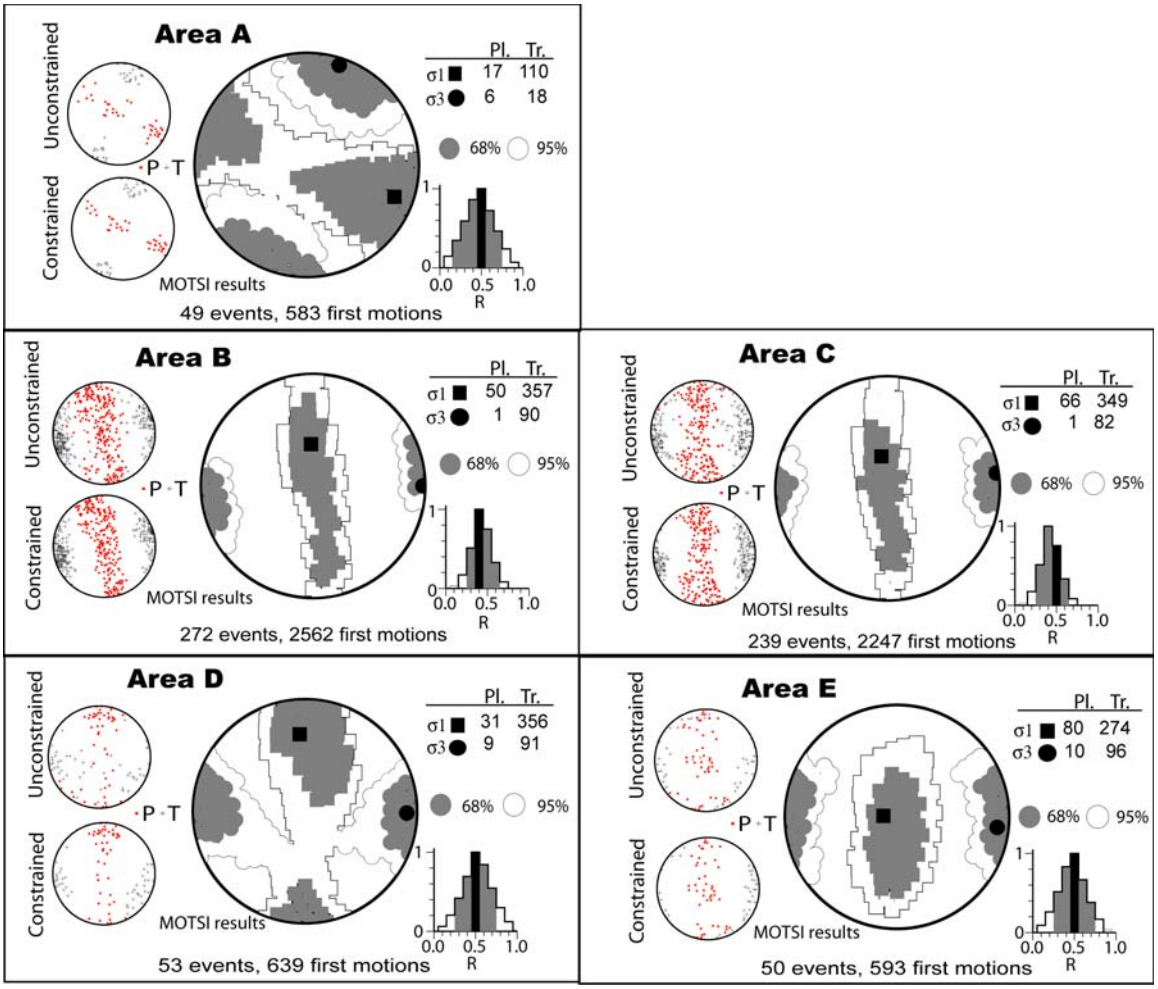

Figure 3.44. Stress field solutions computed for the five small areas A-E in the Teton region using MOTSI [*Abers and Gephart,* 2001]. The P and T axes for all earthquakes in each area are shown for focal mechanisms unconstrained and constrained by the stress solution. Best fitting σ1 and σ3 are plotted with black squares and circles. The plunge (Pl.) and trend (Tr.) of each is listed. The 68% confidence regions are shown in gray and the 95% confidence regions are white. Subdivisions were designed to minimize any possible heterogeneities in the stress field of the overall region. Areas were initially chosen based on areas of similar T axis orientations.

Table 3.9. Results of stress inversions

Area	NEv	NFM	σ_1 Pl.	Σ_1 Tr.	σ_3 Pl.	σ_3 Tr.	dS	NdSj > 1.0	NdMj < 0.9
A	49	583	17	110	6	18	1.25	0 (0%)	11 (22%)
B	272	2562	50	357	1	90	2.21	0 (0%)	80 (29%)
C	239	2247	66	349	1	82	2.81	9 (4%)	27 (11%)
D	53	639	31	356	9	91	1.84	1 (2%)	12 (23%)
E	50	593	80	274	10	96	1.94	0 (0%)	13 (26%)

It is difficult to track changes in individual mechanisms in these plots, and constraining the mechanisms tends to cluster the P and T axes [*Waite et al*., 2004].

The pattern of T axis rotation from NE-SW in area A near the Yellowstone caldera down to the predominant E-W trend in the Teton valley is reflected in the stress-field σ_3 orientations (Figure 3.43). The σ_3 orientations in all areas are well constrained and near horizontal everywhere. The stress model for area A is poorly constrained and the 68% confidence region for the σ_3 overlaps those of the other areas, but the good agreement of the best fit σ_3 with the T axes in that area, and stress inversion done in the Yellowstone region for this same area gives us some confidence that the rotation of σ_3 is realistic. Figure 3.45 displays the stress orientations and extension rates for the whole northern ISB including the new stress orientations for the Teton region [*Waite*, 1999]. This plot of stress orientations confirms that the Teton region stress field is realistic and matches the overall stress orientations of the northern ISB that is mainly dominated by the Yellowstone volcanic system. In general the east west extensional stress orientations typically known from the Basin and Range are dominate until taking a northeastern

Figure 3.45. Summary map of GPS-measured deformation rates derived from this study for the Yellowstone Snake River Plain. Average GPS rates are labeled in large font. Fault slip rates from *Byrd et al.* [1994], *Haller et al.* [2002], and *Wong et al.* [2000] were converted to horizontal extension rates assuming a fault dip of 60o and are labeled in small fonts. Fore comparison, minimum principal stress indicators from other studies are also shown. T-axis directions are from *Waite* [1999], focal mechanisms and vent alignments are from *Zoback* [1992], moment tensor solutions are from http://quakes.oce.orst.edu/moment-tensor, and mapped rift zones are from *Smith et al.* [1996].

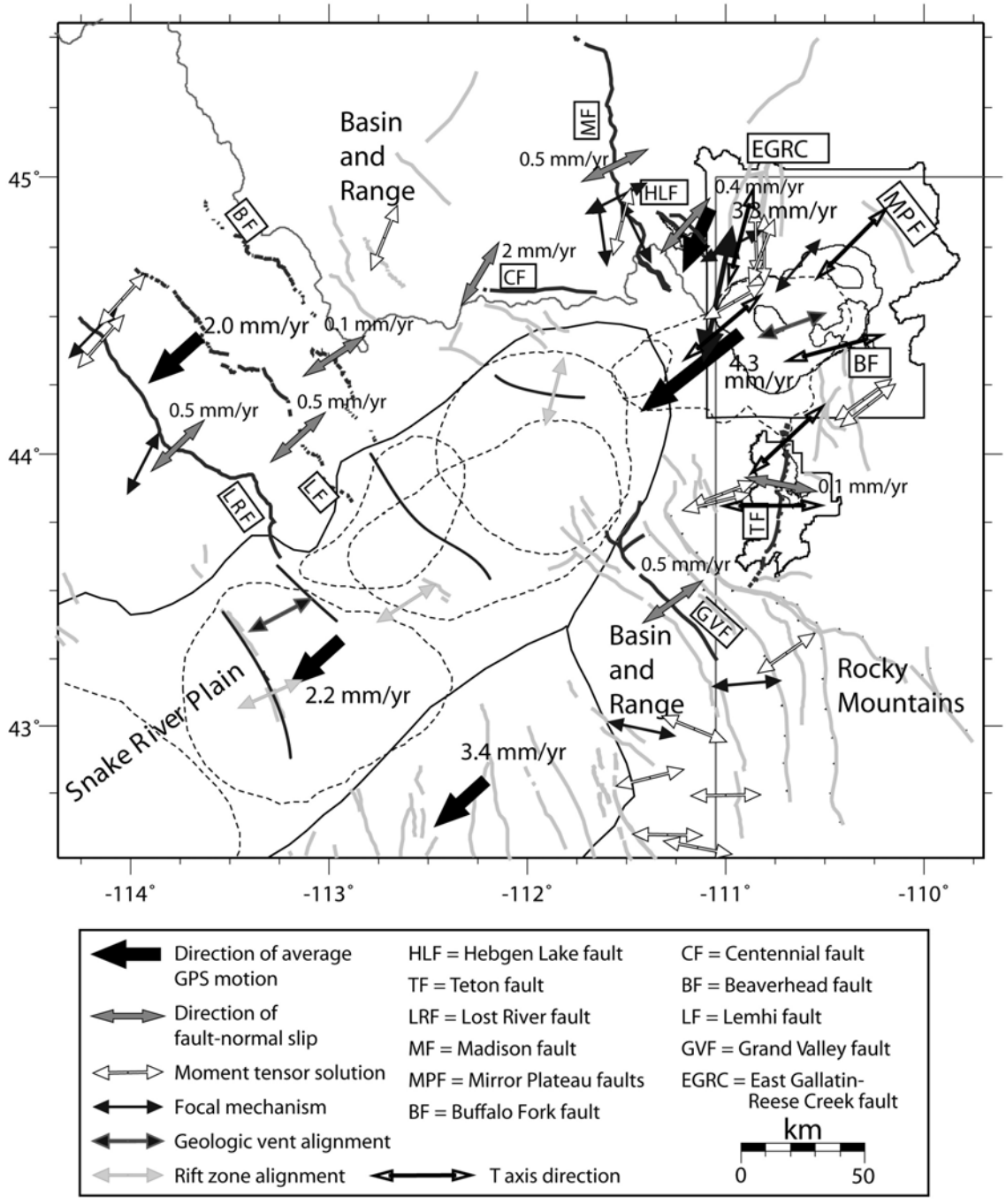
Basin
and
Range
MF
0.5 mm/yr
EGRC
HLF
0.4 mm/yr
3.8 mm/yr
MPF
BF
2 mm/yr
CF
2.0 mm/yr
0.1 mm/yr
4.3
mm/yr
BF
0.5 mm/yr
0.5 mm/yr
LRF
LF
0.1 mm/yr
TF
0.5 mm/yr
GVF
Basin
and
Range
Rocky
Mountains
Snake River Plain
2.2 mm/yr
3.4 mm/yr
45°
44°
43°
-114°
-113°
-112°
-111°
-110°
Direction of average GPS motion
Direction of fault-normal slip
Moment tensor solution
Focal mechanism
Geologic vent alignment
Rift zone alignment
T axis direction
HLF = Hebgen Lake fault
TF = Teton fault
LRF = Lost River fault
MF = Madison fault
MPF = Mirror Plateau faults
BF = Buffalo Fork fault
CF = Centennial fault
BF = Beaverhead fault
LF = Lemhi fault
GVF = Grand Valley fault
EGRC = East Gallatin-
Reese Creek fault
km
0
50

rotation in the northern Teton and Snake River Plain regions approaching the Yellowstone volcanic system. This change in stress orientation shows the dominant force the Yellowstone system has on the boundary of the Basin and Range providence stress regime and the Colorado Plateau.

CHAPTER 4

INTERPRETATION OF THE TETON EARTHQUAKE DATA

4.1. Inferring Geometry of Teton Fault Using 3-D Tomography and Seismicity

Hypocenter locations in the Teton Region have improved in accuracy using the 3-D velocity model and probabilistic relocation method by reducing the RMS value by 59% relative to the initial 1-D *a priori* data. Using only the highest two quality classes of hypocenter relocation, there are some seismic patterns that can be seen throughout the region (Figure 4.1). We believe these linear seismic trends reflect seismogenic features. For example, I note that the same linear trends in the hypocenter locations obtained using the minimum 1-D model and the trends are still there after the test using randomly shifted hypocenter locations. Also these trends are consistent over different time periods and their focal mechanisms show similar faulting types with similar strikes.

Most noticeable of these trends are the epicenter patterns in the Gros Ventre Range to the east of the Jackson Hole basin shown by trends 1 and 2 in Figure 4.1. These linear trends correlate well with southeast trending valleys throughout the Gros Ventre Range. The focal mechanisms of these earthquakes show mainly normal faulting with a small strike slip component as shown in Figure 3.43. These events in the Gros Ventre

Figure 4.1. Hypocenters of quality class A and B relocated by the NonLinLoc program. These hypocenters are represented by red circles shown in both plain view and cross sectional depth view. The Teton fault is outlined in black and runs through the middle of Grand Teton National Park, outlined in green. The Jackson Lake Seismic Network stations are shown by the dark blue triangles. Quality class A and B relocated hypocenters have an RMS < 0.5, and a maximum likelihood and expectational hypocenter difference < 1.0 km. The Teton fault is projected at depth at about 45˚ east-dipping. There are few to no earthquakes that align with the downward projection of the Teton fault. The dark green lines in the cross sections show the general seismic trend under the Teton Mountain Range.

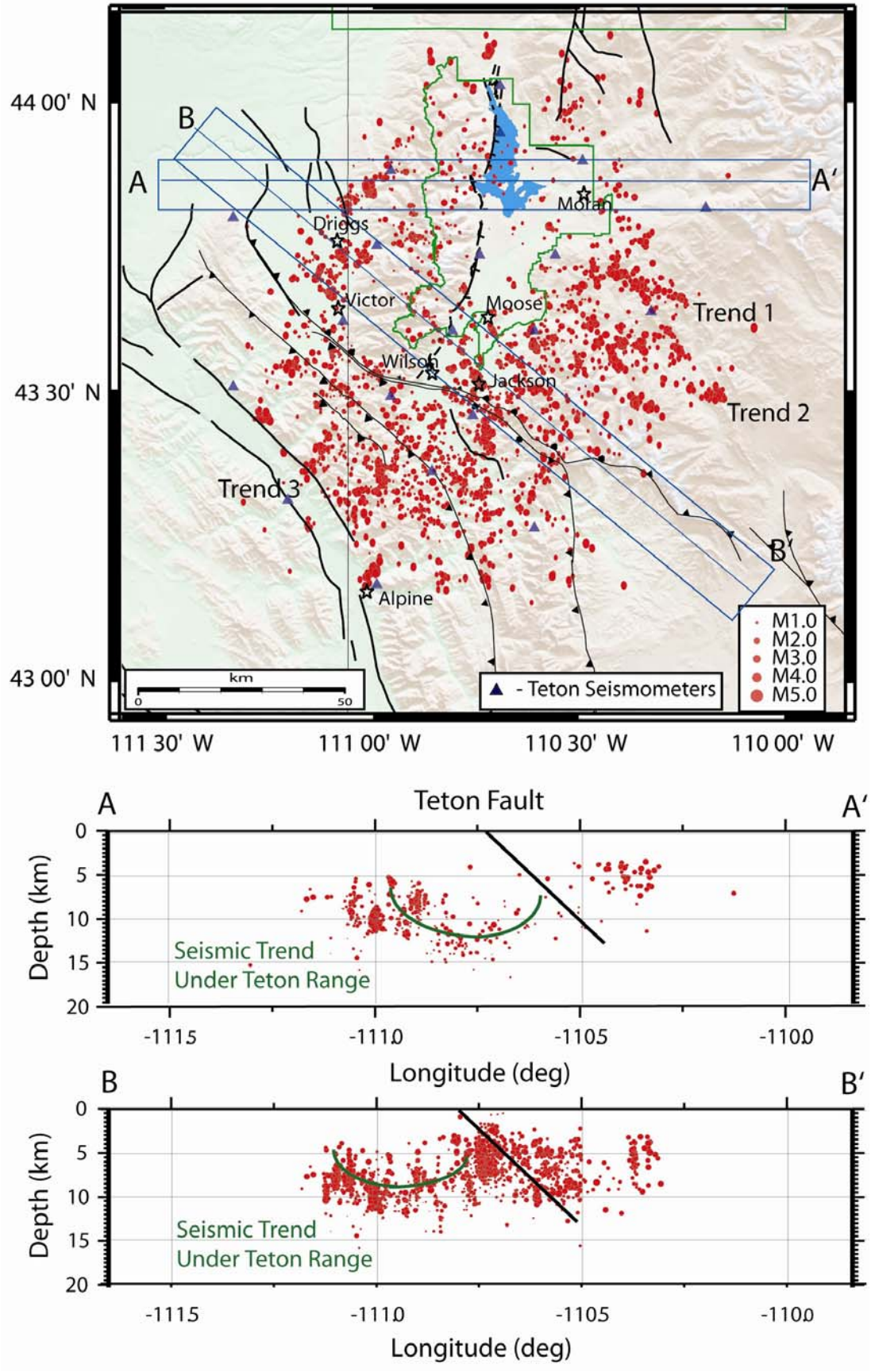
44 00' N
43 30' N
43 00' N
111 30' W
111 00' W
110 30' W
110 00' W
A
A'
B
B'
Driggs
Victor
Moose
Moran
Wilson
Jackson
Alpine
Trend 1
Trend 2
Trend 3
km
0
50
- Teton Seismometers
M1.0
M2.0
M3.0
M4.0
M5.0
Teton Fault
Depth (km)
Seismic Trend
Under Teton Range
Longitude (deg)
-1115
-1110
-1105
-1100
0
5
10
15
20

Range are the most consistent earthquakes occurring regularly over the recorded time period from 1986 to 2002. There have been few studies in the Gros Ventres that have been made public on mapped faulting structures due to the large industrial mining that is currently taking place in the region.

Other noticeable trends are the small seismic clusters between the southern ends of the Teton fault near Jackson, WY where it splays out into the southwest dipping Jackson thrust sheet, the northeast dipping Cache Creek thrust sheet and the Hoback normal fault hanging and footwalls. Though the region is seismically active in the Gros Ventre Range and south of Jackson, WY, around the Hoback normal fault and Grand Valley fault, there is clearly no seismic activity taking place along the Teton fault.

Examining the focal depth cross sections running perpendicular to the Teton fault, there is no apparent pattern of hypocenters along the down-dip projections of the Teton fault for dips ranging from 30° to 60°. One interesting observation about these cross sections is that the seismicity in the footwall seems to display a curved band beneath the Teton Range. We have theorized this seismic pattern could be outlining the root of the Teton Mountain Range as is shown in the focal depth map in Figure 4.2. Beneath the Teton Range the deviatoric stress at depth is not great enough in the root of the range, but it is great enough beneath the root and is able to create earthquakes.

Alternately, the curvature pattern could be related to flexure of the deforming footwall block from slip occurring along the Teton fault. During the uplift of the Teton mountain block along the normal fault, a rigid beam structure would have the tendency to bend in the direction of the motion, which in this case would be vertically upward. This vertical motion would cause numerous small cracks and fractures to form in the footwall

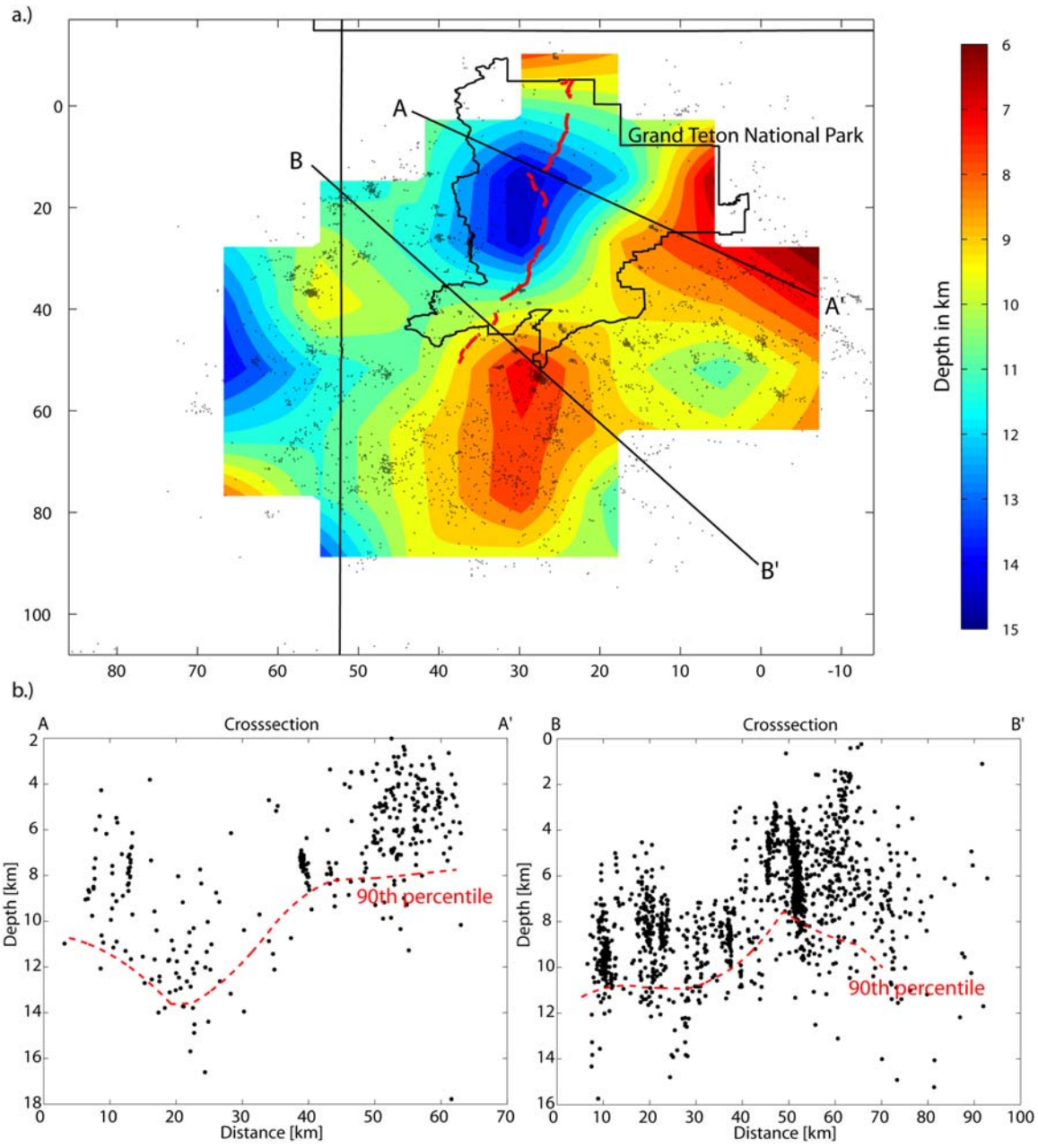

Figure 4.2. Focal depth plot of the 90th percentile of focal depth for Teton catalog using only A and B quality events. The color scale in figure (a) shows depth in kilometers. Grand Teton National Park is outlined in black and two cross sections A-A' and B-B' are labeled in black. The two cross sections in figure (b) display the focal depths along the profile running perpendicular to the Teton Fault outlined in red. The depth scale in the focal depth profiles shows a vertical exaggeration 5x the distance scale. The focal depths display no correlation with the Teton fault but perhaps correlate with the Cache Creek Thrust faults in the Gros Ventre Range.

close to the faulting plane. This might explain hypocenters that occur at shallow depths in the footwall close to the fault plane and then deepen to the west and increase in frequency below the roots of the Teton Range. However, the flexure of the Teton mountain block could in part be a resultant of the lithospheric downwarp akin to the Snake River Plain and Yellowstone volcanic hotspot track. It has been hypothesized by *Janecke* [1995] that the Teton fault is not a typical fault associated with the eastern Basin and Range but is in response to the dominate structure of the Snake River Plain. These are only two hypotheses that may explain the seismic patterns across the Teton fault. However, I believe it is a combination of both processes that have aided in creating the seismic patters across the Teton fault.

Three-dimensional P-wave velocity images of the Teton Region have displayed three low velocity bodies that are interpreted as sedimentary basins in the region at 0km depth (sea-level). These three basins; Jackson Hole valley, Teton River valley, and the Grand/Star valley basin, all have depths of about 2 to 3 km (Figure 4.3). These basins are mainly composed of Tertiary and Quaternary sediments that display a distinct P-wave velocity low compared to the surrounding cooler higher velocity bedrock.

The low velocity zones in the Jackson Hole valley seem to be stronger in the southern end of the valley where Quaternary rocks are closely oriented with older Paleozoic rocks with in the Cache Creek thrusting sheet. This strong lower velocity area is most likely due to the denser ray distribution and earthquake and station density in the area, which gave us a more reliable velocity value in this area versus the northern end of the Jackson Hole valley. Also, the tomographic model displays what seems like three individual basins in the Jackson Hole valley. We do not believe this to be true, even

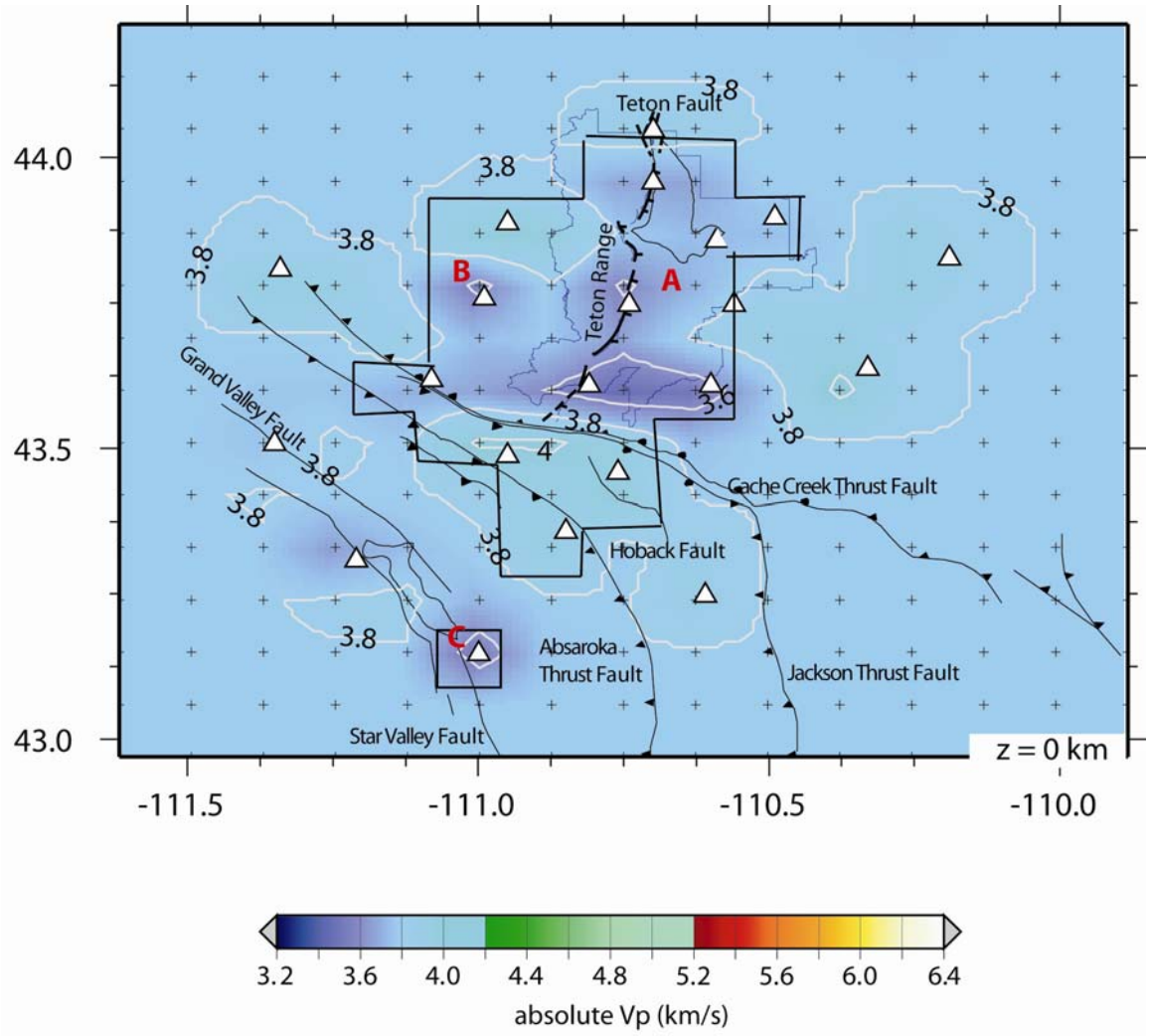

Figure 4.3. Horizontal plane view of the final 3-D inversion solution with absolute velocity values and contours at 0 km. The seismic stations are marked by the white triangles. The Teton National Park boundary is represented by the blue lines. The Teton fault is marked by the dark blue lines. To the west of the Teton fault lies the Teton mountains predominantly composed of Precambrian and Paleozoic bedrock that correspond well with relatively higher velocities. The three basins labeled A-C are mainly composed of Tertiary and Quaternary sediments that also show a good correlation with relative low velocities. The green star represents the town of Jackson, WY. Basin A represents the Jackson Hole valley. Basin B represents the Teton River valley, and basin C represents the Grand valley. Major faults are defined with the thin black lines. The thin black boxes represent the areas of good resolution determined by the synthetic tests and row of resolution matrix plots.

though it is reasonable to assume the depth of the sediment basin varies throughout the valley. We believe this image is more due to the resolution capabilities of the data set to resolve the entire large Jackson Hole valley basin as one consistent velocity structure. Therefore the low velocity zones in the Jackson Hole valley are most likely connected to one another as one individual sediment basin to the east of the Teton fault.

Velocity structure of the Teton Region at 5 km depth displays more of the underlying structure beneath the sediment basins and protruding mountainous bedrock uplifts (Figure 4.4). The most prominent features at this depth are the low velocity zones trending northwest to southeast along the boundary and just south of the Cache Creek thrust sheet that is part of the larger Sevier thrust belt in the southeast Idaho lineament. The southeast Idaho lineament is geometrically interpreted to be a lateral ramp that spans the Sevier orogenic belt of southeast Idaho and western Wyoming [*Lageson et al*., 1999]. The contractional structures within the Sevier orogeny not only plunge into the lineament from the south and north, but they seem to have lateral offset and step up to the south across the lineament [e.g., Stewart Peak culmination].

Another important fact about the southeastern Idaho lineament is that it appears to be the location of the regional bend in the central Intermountain Seismic Belt, from a northeast trend in northern Utah and southeast Idaho to a northwest trend further north of its location and not at Yellowstone, where the bend in seismicity was originally assumed to take place [*Lageson et al*., 1999]. The lineament may also account for the occurrence of numerous small earthquakes between Soda Springs, ID and Jackson, WY at depths up to 15 km (i.e., within the basement), having no apparent correlation with structure within Phanerozoic rocks [*Smith and Arabasz*, 1991]. Therefore the seismicity we see in the

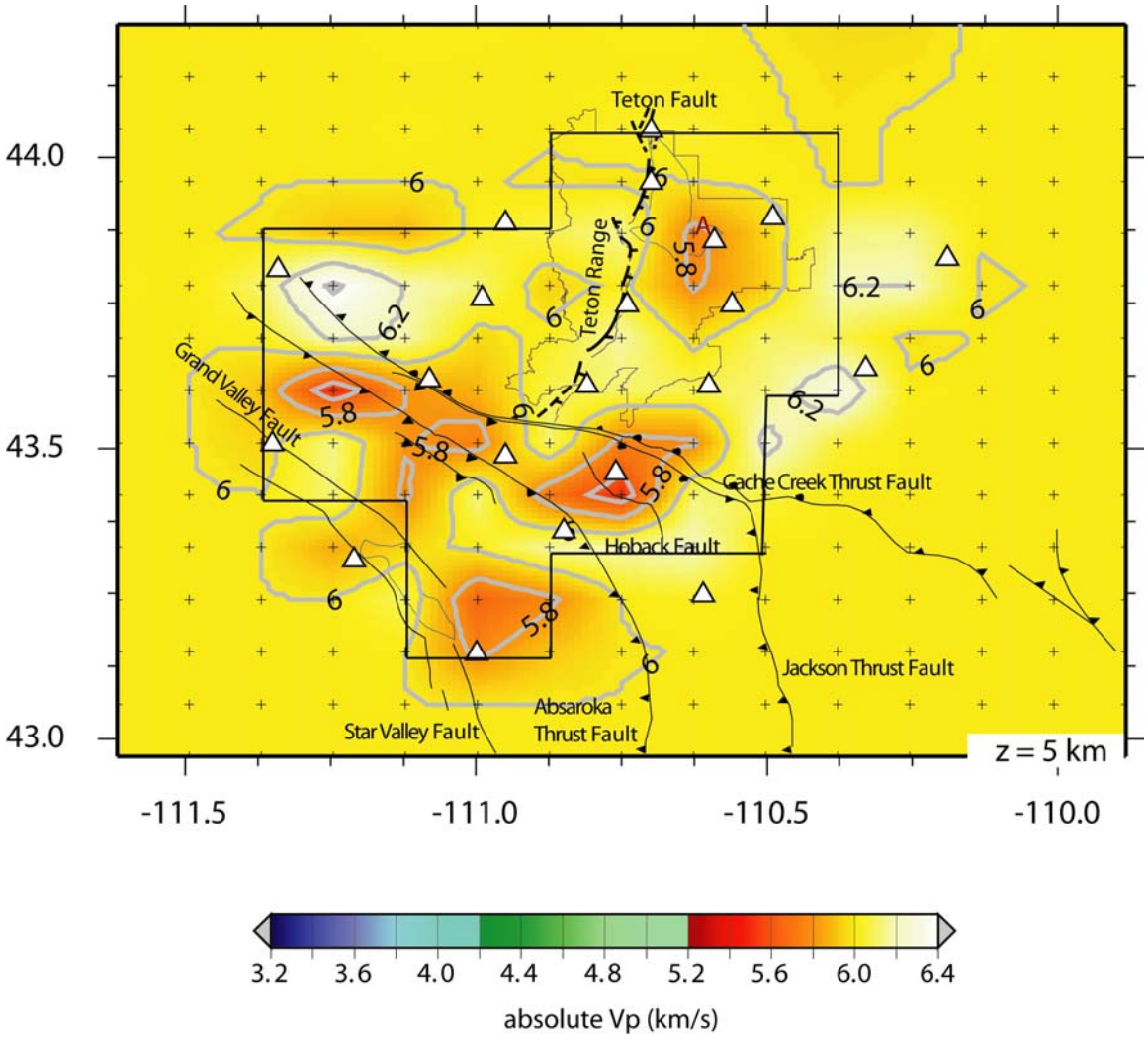

Figure 4.4. Horizontal plane view of the final 3-D inversion solution with absolute velocity values and contours at 5 km. The seismic stations are marked by the white triangles. The Teton National Park boundary is represented by the blue lines. The Teton fault is marked by the dark blue lines. To the west of the Teton fault lies the Teton mountains predominantly composed of Precambrian and Paleozoic bedrock that correspond well with relatively higher velocities. The three basins labeled A-C are mainly composed of Tertiary and Quaternary sediments that also show a good correlation with relative low velocities. The green star represents the town of Jackson, WY. Area marked A on the east side of Jackson Lake is the location of the Jackson Lake Dam. Major faults are defined with the thin black lines. The thin black boxes represent the areas of good resolution determined by the synthetic tests and row of resolution matrix plots.

southern Teton region might be more related to the underlying bedrock structures created by the Sevier thrust area, including the Cache Creek thrust faults and the Hoback listric normal fault. The low velocity zones correlating with these underlying features might be due to these thrust faults bringing up younger Mesozoic rock formations which would have lower velocities than surrounding Paleozoic rock formations at the same depth level.

Gravity models of the Teton fault using data collected by *Lavin and Bonini* [1957] *Behrendt et al.* [1968] and *Byrd* [1995] were used to generate a complete Bouguer anomaly map by V. Bankey, (U.S. Geological Survey) using a digital topographic data base to remove significant terrain corrections. *Byrd* [1995] analyzed these data to generate two-dimensional forward gravity models. His gravity modeling results showed that Jackson Hole is underlain by two distinct sedimentary basins, associated with -240 mGal and -220 mGal gravity lows, separated by a pronounced NE trending gravity high (Figure 4.5).

The basins are interpreted to be filled with 2350 kg/m^3 density rocks inferred to include the volcaniclastic and lacustrine strata of the Teewinott formations, 2.0 Ma Huckleberry Ridge Tuff, and Quaternary glacial deposits [*Byrd*, 1999]. The northern gravity low basin is centered over the east side of Jackson Lake at the Jackson Lake Dam and is up to 12 km wide, while the southern gravity low basin is centered over the southwest of Jackson Hole and extends 7 km eastward from the mountain front (Figure 4.5). The gravity low centered over the Jackson Lake Dam is also displayed in profile 1 in Figure 4.6. This profile shows the probable geologic structure beneath the dam required to obtain the gravity profile. These results help support our previous interpretation of why we resolve a low velocity body at 5 km depth beneath the dam.

Figure 4.5. Horizontal plane view of the complete Bouguer gravity anomaly of the Teton Range and Jackson Hole valley with contours every 5 mGals. The gravity stations are marked by the black circles. The Teton fault and Cache Creek Thrust faults are marked by the thin black lines. To the west of the Teton fault lies the Teton Range predominantly composed of Precambrian and Paleozoic bedrock that correspond well with relatively higher gravity anomalies. To the east of the fault lies the Jackson Hole valley composed of Tertiary and Quaternary sediments that also show a good correlation with relatively lower gravity anomalies. The green star represents the town of Jackson, WY. The letter A represents the location of the Jackson Lake Dam. Gravity profile locations are labeled by Profile #1-#4.

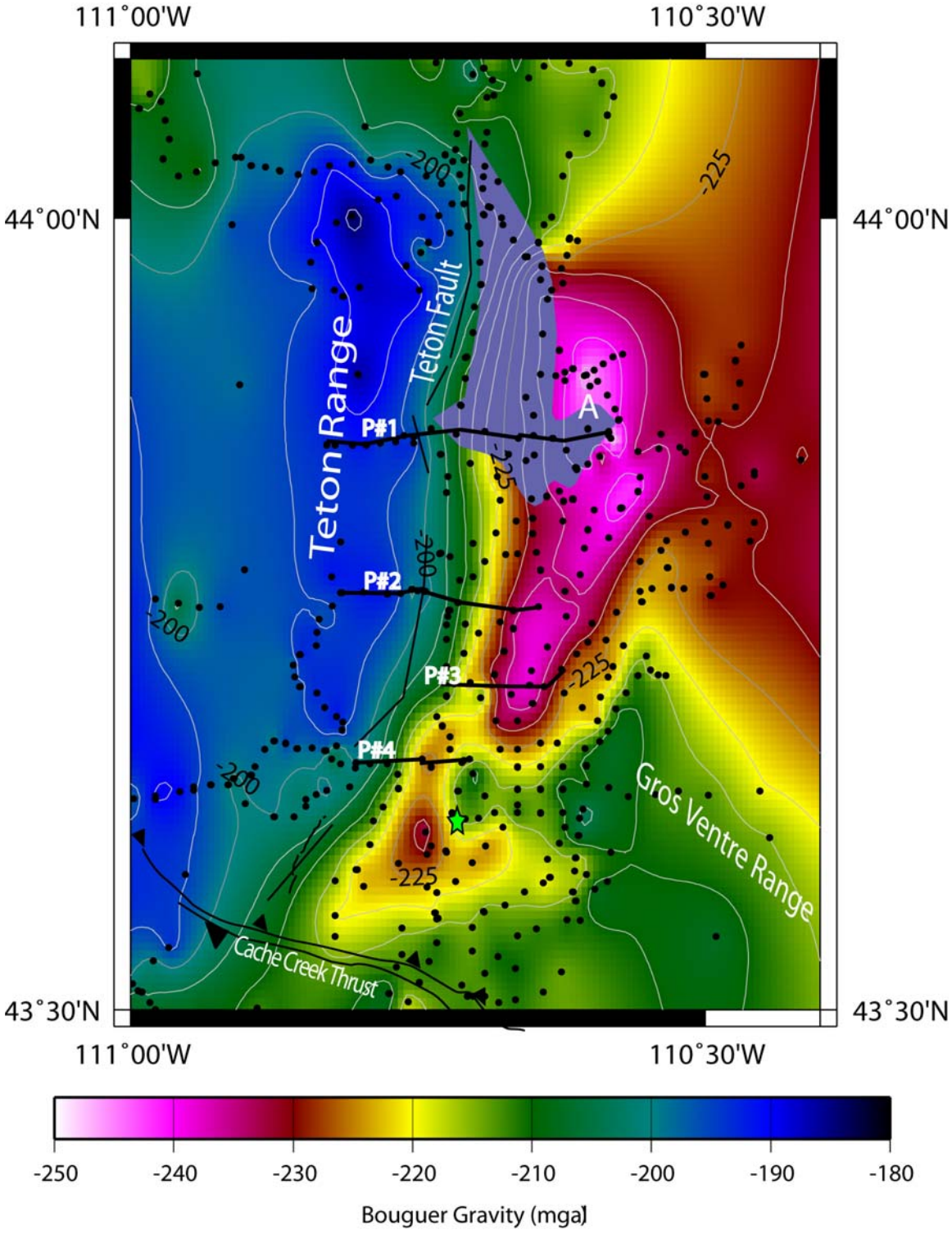
111°00'W
110°30'W
44°00'N
43°30'N
Teton Range
Teton Fault
A
P#1
P#2
P#3
P#4
-200
-225
Gros Ventre Range
Cache Creek Thrust
-250
-240
-230
-220
-210
-200
-190
-180
Bouguer Gravity (mgal)

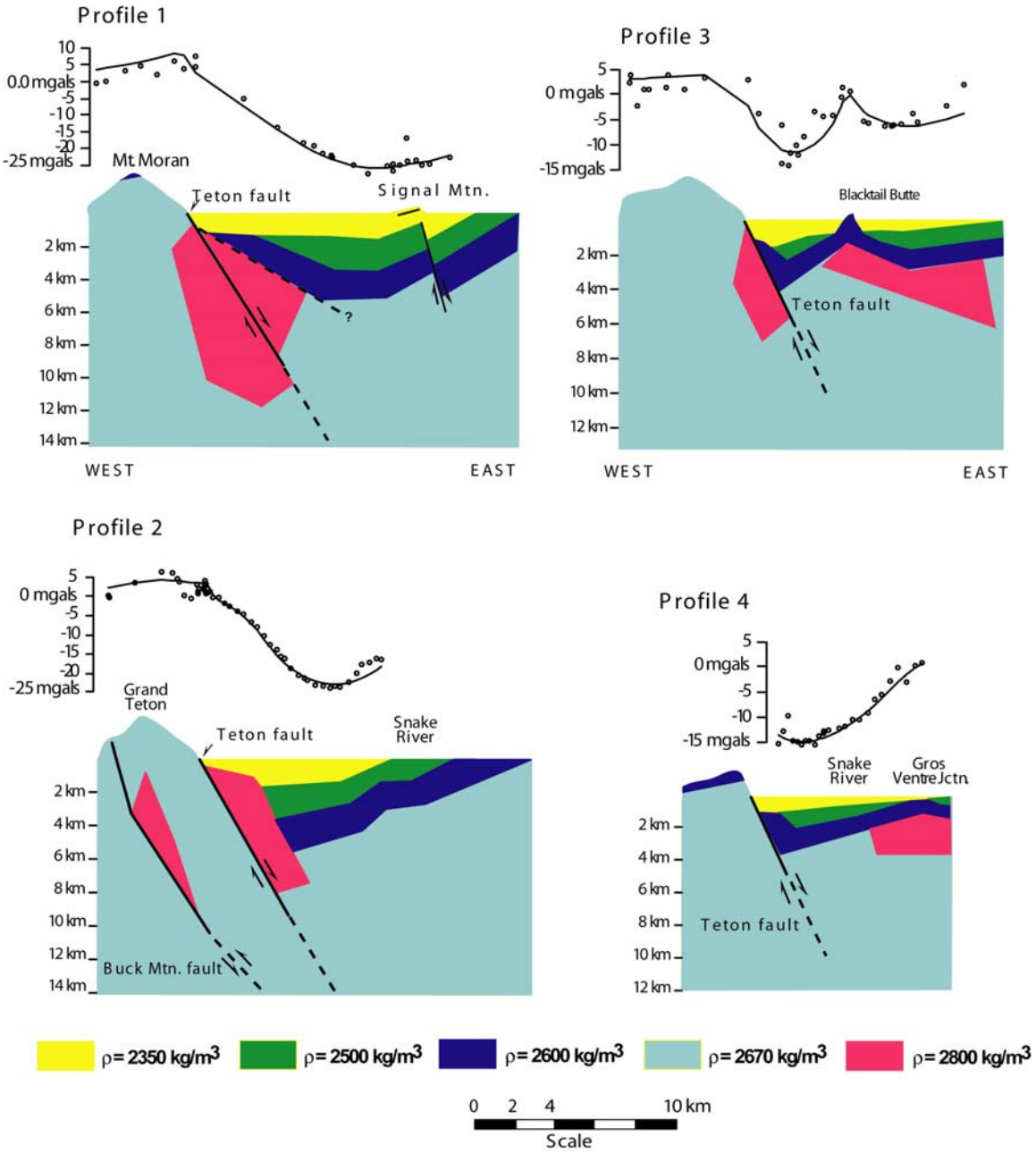

Figure 4.6. Gravity modeling results of profiles 1-4 generated by *Byrd* [1995]. Locations for these profiles are shown in Figure 4.5.

Basin depths also vary from west to east from 0.5 to 1.5 km next to the Teton fault, to 2 to 2.5 km over the centers of the basins, and 1km on the west side of Blacktail Butte (Figure 4.6). The interbasin gravity high represents an area of relatively shallow basement rocks beneath the central part of the Jackson Hole valley. High density rocks, 2800 kg/m^3, in the footwall of the Teton fault approximate the relative gravity high associated with the Teton Range (Figures 4.5 and 4.6). The gravity gradient of 3 to 6 mGal/km is characterized by a convex-upward anomaly, marking the west side of Jackson Hole and the Teton fault trace on the northern gravity profiles (Figures 4.5 and 4.6).

The forward gravity modeling by *Byrd* [1995] suggests that 1) the gravity signature of the northern Teton fault is associated with a 2 to 5 km wide zone of 2800 kg/m^3 density rocks in the footwall and hanging wall or that 2) the fault appears as a shallow, approximately 30° east-dipping structure [*Byrd,* 1995] (Figure 4.6). In the southern part of Jackson Hole, the gravity models suggest the Teton fault is a single 30° to 70° dipping structure that has juxtaposed 2670 kg/m^3 footwall rocks against 2600 kg/m^3 rocks in the hanging wall. These two gravity lows in the Jackson Hole valley correlate with seismic low velocity zones shown in Figure 4.3. Using these gravity models we can also compare them with the results of our tomography cross sections.

A notable goal of the 3-D tomographic mapping of the Teton crustal structure was to determine the dip angle of the Teton fault at depth. Evaluating the cross sections perpendicular and parallel to the Teton fault reveals that we are able to resolve a velocity change associated with the fault. We had assumed a higher velocity bedrock footwall and a lower velocity sediment hanging wall. The perpendicular cross sections do show

Figure 4.7. 3-D velocity model cross section perpendicular to the southern Teton fault. The location map of the vertical cross section is located at the top in figure (a). The cross section location represented by the pink line continues along the A to B profile. Figure (b) shows the topographic profile along the cross section in meters. Figure (c) shows the final 3-D inversion solution with velocity perturbations shown by the red and blue color scale, and overlain absolute velocity contours. There is no vertical or horizontal exaggeration between the depth and distance axis. The area of good resolution is located inside the bold black lines that show the areas of RDE greater than or equal to 0.3. The hypocenter locations of the high quality events along the profile +/-5 km are shown in green circles. The blue line represents a possible projection of the Teton fault at depth with a dipping angle of 45 degrees.

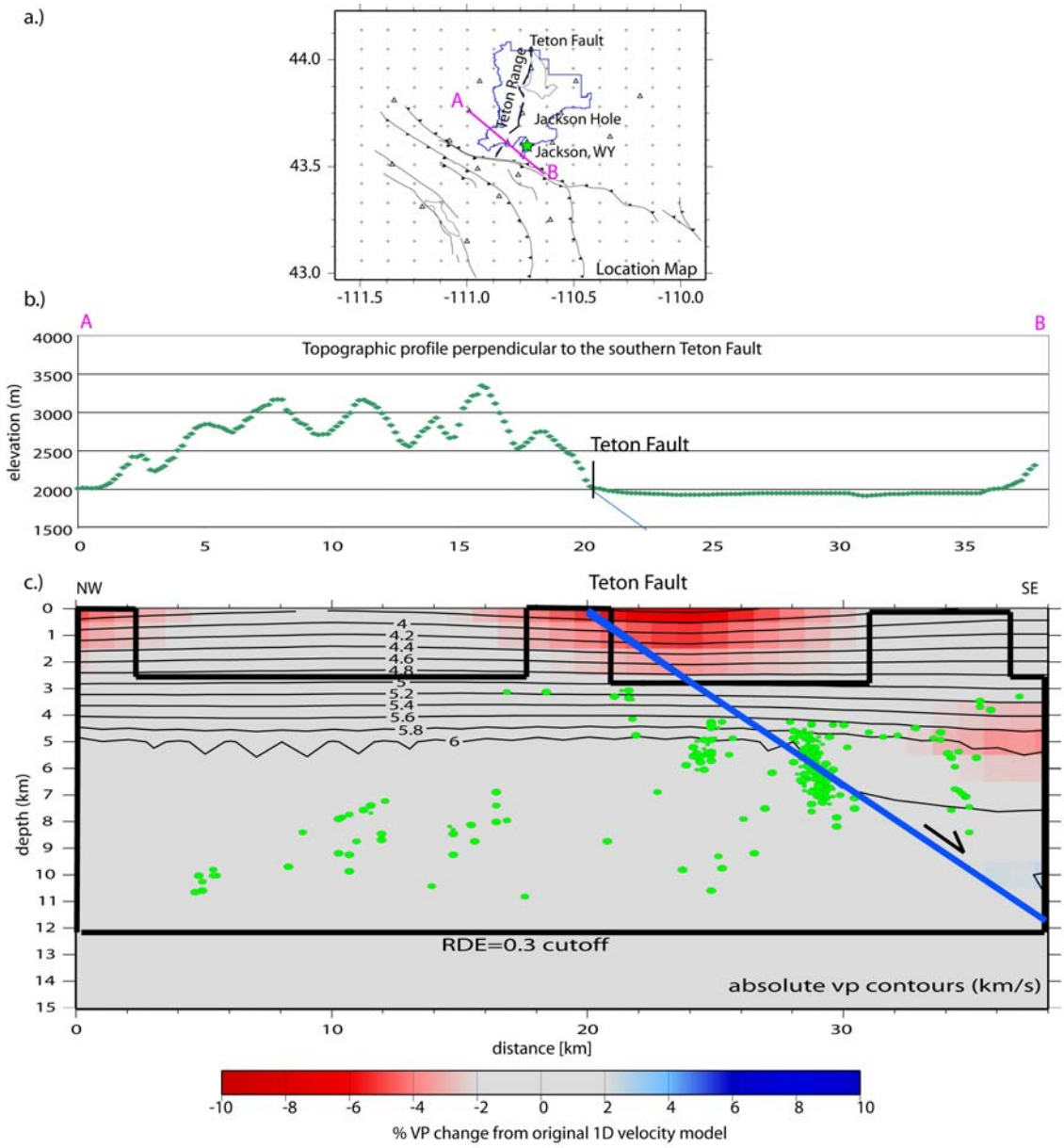
a.)
Teton Fault
Teton Range
A
Jackson Hole
Jackson, WY
B
Location Map
44.0
43.5
43.0
-111.5
-111.0
-110.5
-110.0
b.)
A
B
Topographic profile perpendicular to the southern Teton Fault
elevation (m)
Teton Fault
c.)
NW
Teton Fault
SE
depth (km)
RDE=0.3 cutoff
absolute vp contours (km/s)
distance [km]
% VP change from original 1D velocity model

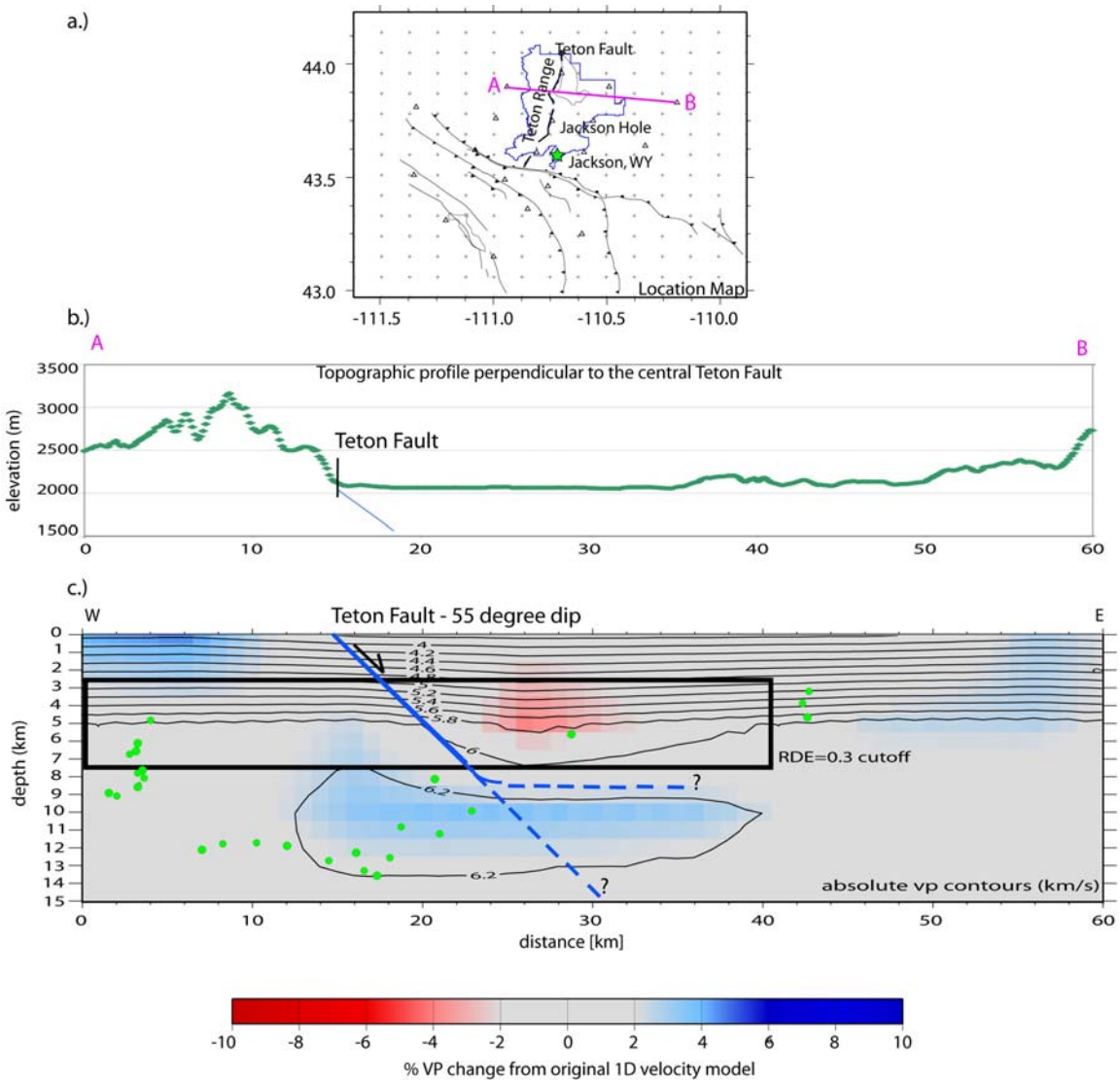

Figure 4.8. 3-D velocity model cross section perpendicular to the central Teton fault. The location map of the vertical cross section is located at the top in figure (a). The cross section location represented by the pink line continues along the A to B profile. Figure (b) shows the topographic profile along the cross section in meters. Figure (c) shows the final 3-D inversion solution with velocity perturbations shown by the red and blue color scale, and overlain absolute velocity contours. There is no vertical or horizontal exaggeration between the depth and distance axis. The area of good resolution is located inside the bold black lines that show the areas of RDE greater than or equal to 0.3. The hypocenter locations of the high quality events along the profile +/-5 km are shown in green circles. The blue line represents a possible projection of the Teton fault at depth with a dipping angle of 55 degrees.

this expected velocity change and low velocity hanging wall in Figures 4.7 and 4.8. In these figures we have projected the Teton fault at depth between 45° and 55°. These dip angles best represent the angle of dip along the Teton fault as imaged by the final 3-D velocity model.

One explanation for the lack of change is that our model parameterization is too large to resolve the structure. A smaller localized 5km x 5km model focused on the Teton fault might be able to resolve the velocity change across the fault and resolve the structure. Also waveform modeling of more of the earthquake located east of the Teton fault may provide better constraints on the Teton fault dip at depth than are currently available. We hope that our later model with finer parameterization might help with this resolution issue. Another possibility is that the data set is not able to resolve the structure due to the limited earthquake distribution in the region. Other alternatives are that there is not enough of a geologic difference between the offset layer beds close to the fault to see the transition clearly, or some other factor we have not discovered.

Examining the parallel tomographic cross sections, a noticeable high-velocity zone located between 7 km and 12 km is predominant, even though the plots do have 2.75 times the vertical exaggeration in depth as compared to the distance axis (Figure 4.9). This same anomaly is observed in both parallel cross sections at the same depth with very similar structures. Given that the anomaly is at the same depth for a cross section along the Teton fault scarp and the other cross section 5-8 km east of the fault in the Jackson Hole basin, the two anomalies might be imaging a similar high velocity

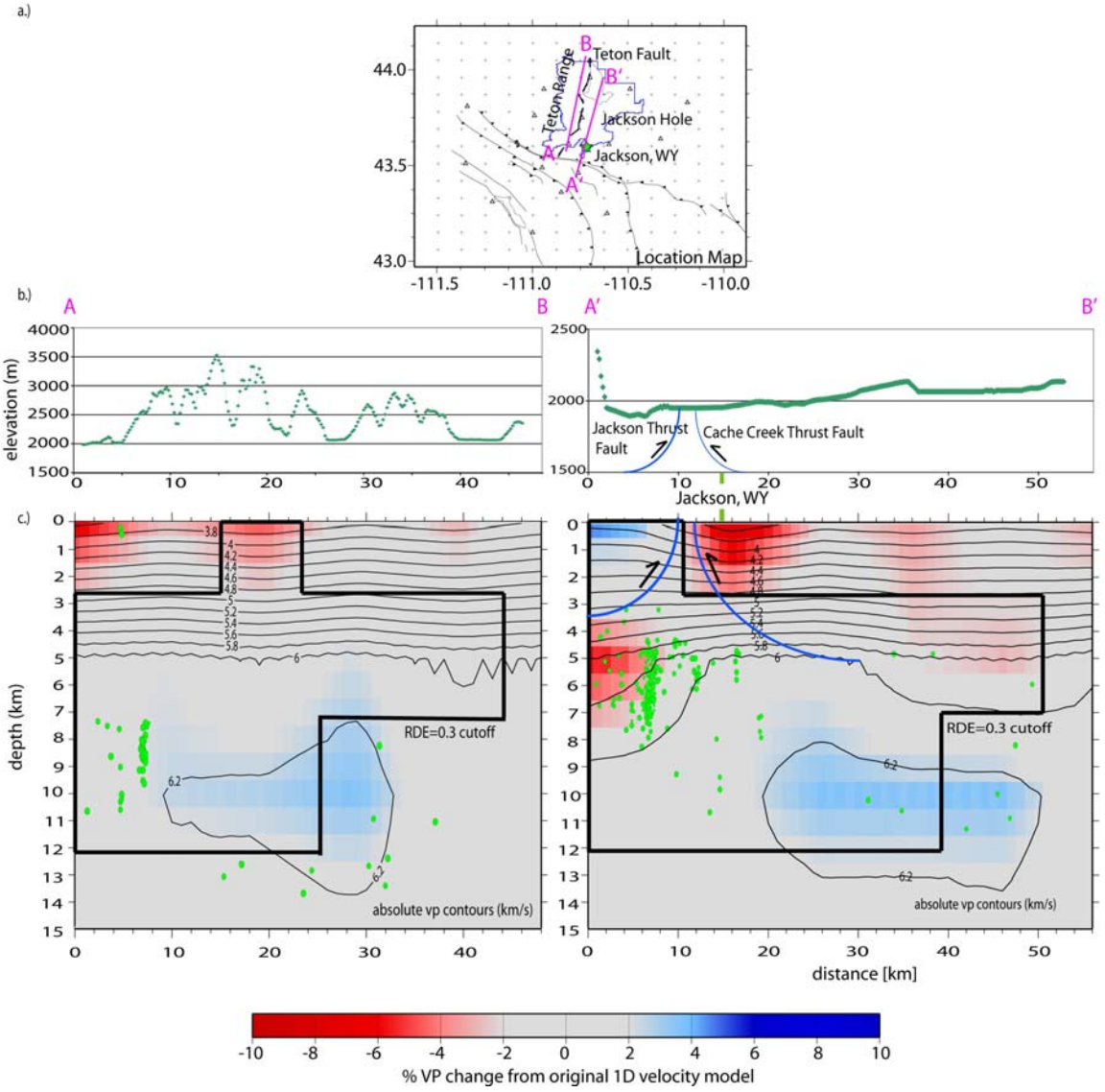

Figure 4.9. 3-D velocity model cross sections parallel to the Teton fault. The location map of the vertical cross section is located at the top in figure (a). The cross section location represented by the pink line continues along the A to B and A' to B' profiles. Figure (b) shows the topographic profiles along the cross sections in meters. Figure (c) shows the final 3-D inversion solution with velocity perturbations shown by the red and blue color scale, and overlain absolute velocity contours. There is 2.75 times the vertical exaggeration between the depth and distance axis. The areas of good resolution are located inside the bold black lines that show the areas of RDE greater than or equal to 0.3. The hypocenter locations of the high quality events along the profiles +/-5 km are shown in green circles. The Cache Creek and Jackson Thrust faults are projected at depth and are represented by the blue lines with black arrows showing the direction of movement by the headwall.

bedrock formation. These two anomalies may be part of one continuous bedrock structure that has not been offset by faulting, implying that the Teton fault terminates or becomes listric at 6 km depth. If the anomaly in the cross section running through the valley were offset then we would expect the anomaly to be located in the hanging wall and offset from the similar anomaly obviously in the footwall. However, we do not see any offset implying they are either; a) the Teton fault is listric and shallow dipping down to 6 km, b) the Teton fault terminates at 6km depth and no offset takes place in the bedrock at 7 km depth, or c) the Teton fault continues down to a slightly deeper depth around 10 km and vertical offset at depth is not well imaged. The gravity model profiles in Figure 4.6 suggest that theories b) or c) with regard to the high velocity anomalies are more likely the case; however, I believe you cannot rule out the possibility of the theory a) due to the lack of data density in the area.

4.2. Stress Field Inversion

4.2.1. Stress Field Orientation

The stress field orientations in the Teton Region derived by focal mechanism inversions are generally consistent with dominant normal faulting stress orientations in the east-west direction. However, the northern part of the Teton fault area showed oblique normal fault stress directions in a northeast southwest orientation. This anomalous stress orientation is interpreted as possibly due to the influence of the Yellowstone volcanic field just north of the northern Teton fault segment. Southern Yellowstone stress orientations are dominantly trending in this oblique northeastern stress orientation that is seen in the northern Teton region.

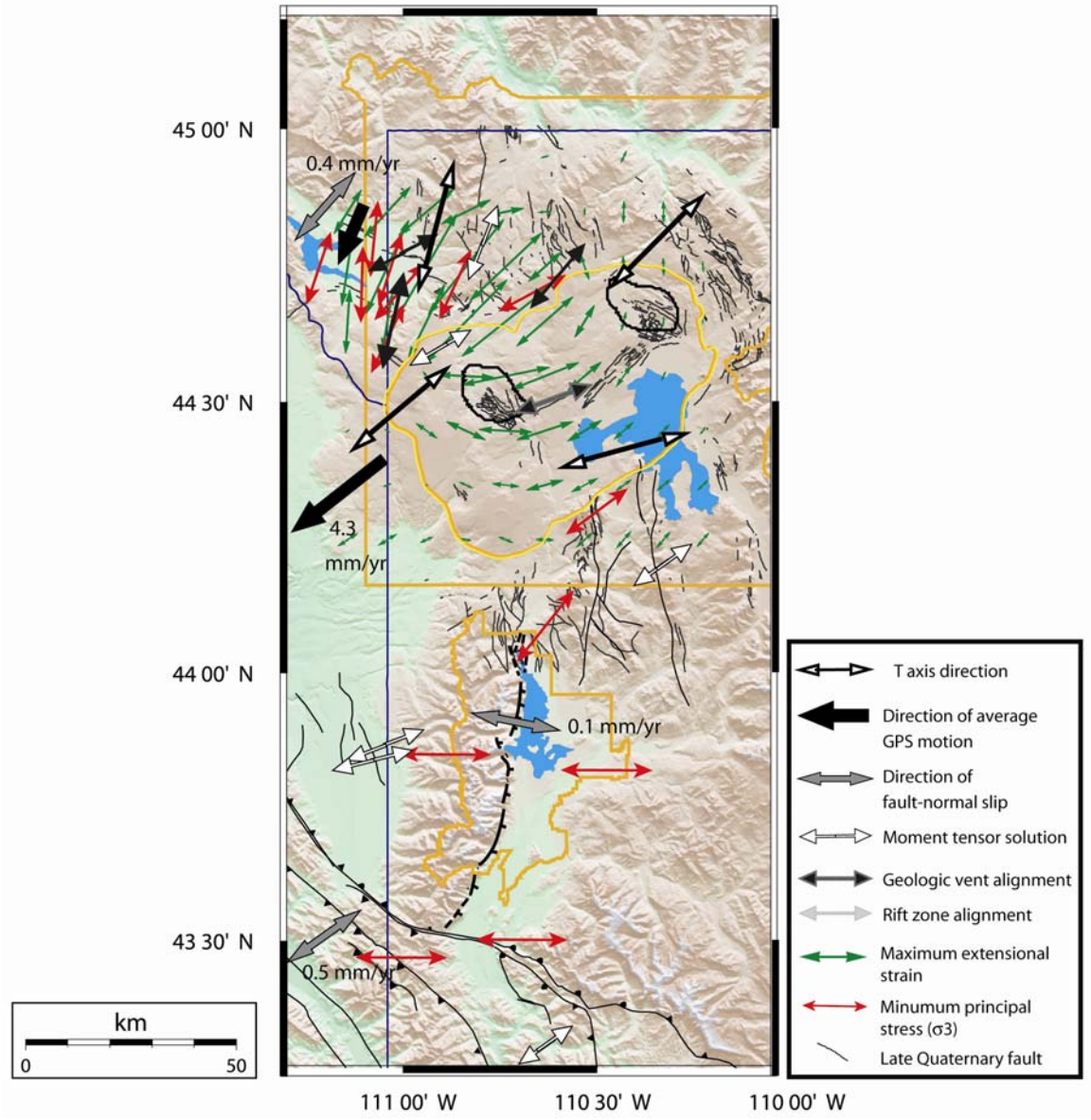

Figure 4.10. Seismic and geodetic stress indicators across Yellowstone and Grand Teton National Parks. Maximum extensional strain directions measured by GPS for the time period 1995-2000 [*Puskas et al*., 2000] are represented by the green arrows and their lengths are proportional to the strain rate. The minimum principal stress (σ3) directions are shown by the red arrows and where determined using inverted focal mechanisms. *Haller et al.* [2002] and *Wong et al.* [2000] were converted to horizontal extension rates assuming a fault dip of 60° and are labeled in small fonts. Fore comparison, minimum principal stress indicators from other studies are also shown. T-axis directions are from *Waite* [1999], focal mechanisms and vent alignments are from *Zoback* [1992], moment tensor solutions are from http://quakes.oce.orst.edu/moment-tensor, and mapped rift zones are from *Smith et al.* [1996].

Figure 4.10 displays the combined stress field orientations for the Yellowstone and Teton regions. The stress field orientations for the Yellowstone area were also computed from focal mechanisms, using the same methodology as in the Teton region. This transition from northeast-southwest extension in the northern Teton region to east-west extension in the central and southern Teton region gives rise to one possible hypothesis for the lack of seismicity along the Teton fault. Obviously there is a seismic gap along the Teton fault but the real question is why. One possibility is that the stress field that is driven by the Yellowstone volcanic system is affecting the northern Teton fault, as can be seen in the stress field orientations shown in Figure 4.8. Given the unique stress orientations in the northern Teton fault segment, they may perhaps be locking the fault in compression, which would also be loading the fault segment at the same time. The effect of Yellowstone on the Teton fault, and vice versa, has been suggested by scientists working in the region for quite some time [*Smith et al*., 1993b]. The biggest problem with the overall stress field along the Teton fault is that it is mainly determined by earthquakes that do not occur along the Teton fault and that are very small in magnitude. A network of GPS stations was established by the University of Utah to assess the contemporary deformation of the Teton fault and its relation to the overall strain field of the Yellowstone region.

4.2.2. Teton GPS-Derived Contemporary Deformation Field

A network campaign and continuous GPS sites was established by the University of Utah in the Teton valley that included 15 campaign stations and one continuous station, mainly located in the Jackson Hole valley and Gros Ventre Range (Figure 4.11).

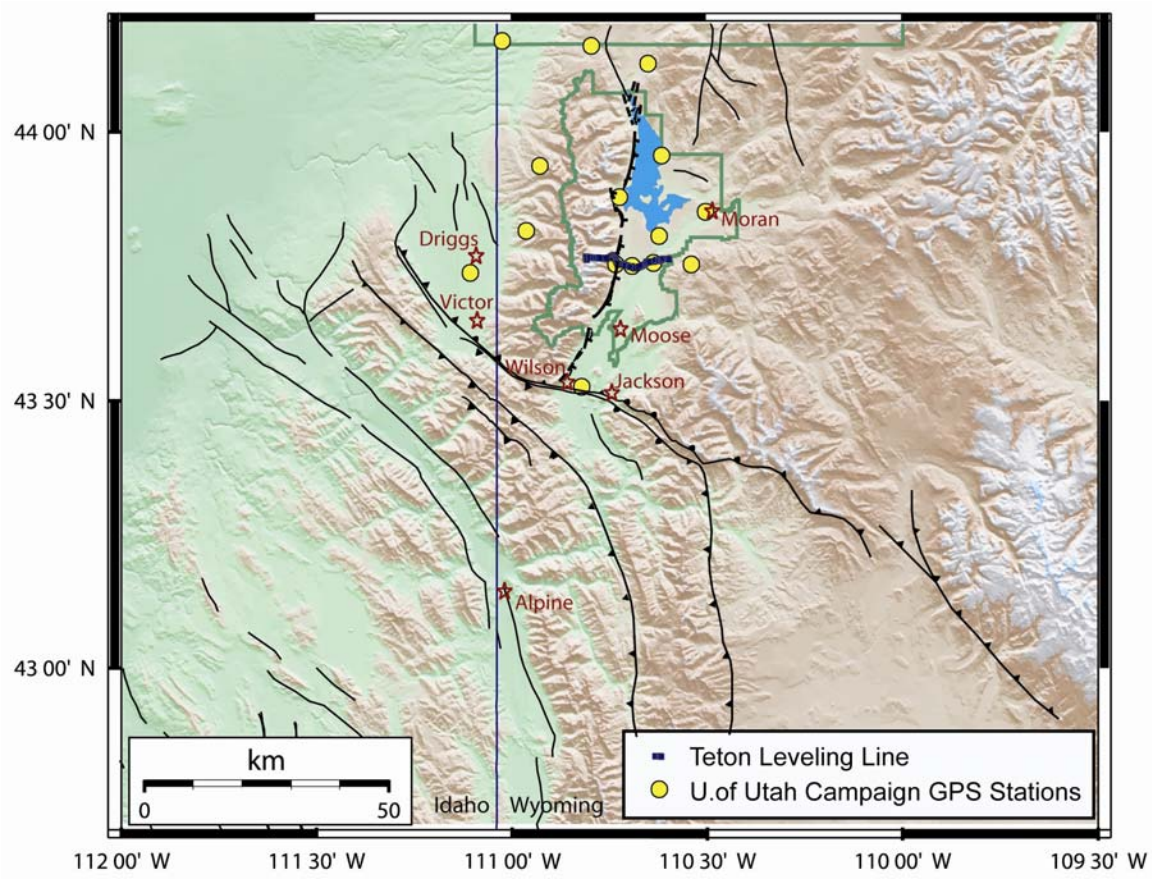

Figure 4.11. The University of Utah GPS campaign network, 1987-2003, and the Teton leveling line, 1988-2001. Campaign site stations are represented by yellow circles, and the leveling line sites are shown in dark blue squares. The major faults in the area are shown by the black lines, and the outline of the Grand Teton National Park is shown in dark green.

A 22 km-long first-order leveling line was established across the Teton fault (Figure 4.11) and surveyed from 1988 to 2001 with surveys taking place in 1988, 1989, 1991, 1993, 1997, and 2001 [*Sylvester et al.*, 2004]. The ground deformation determined by these two surveys revealed interesting and contradicting results with the regional stress field orientations we determined using focal mechanisms. Figures 4.12 and 4.13 display the average ground deformation motion directions in both the vertical and horizontal planes.

Combined results from the 1987-2003 campaign GPS surveys display an average valley floor uplift of ~0.5-1.5 mm/yr and a mountain block vertical uplift of ~2-3 mm/yr. However, combined surveys from 1987-1995 and 1995-2000 show mountain block uplift with various periods of valley floor uplift and subsidence. From these GPS rates we find an unusual compression of the hanging-wall moving west towards the footwall, and the hanging wall showing an average uplift across the valley with respect to the footwall. This type of deformation pattern would usually be seen in a compressional fault system and not in a normal fault system. This deformation motion is completely opposite to what we would expect to see and what we did see in the stress field determined by focal mechanisms in section 3.6.

The leveling line results also show a range of valley block subsidence and uplift through out the surveying years (Figure 4.14). *Sylvester* [2004] concluded that five of the six levelings are remarkably similar and suggest that the alluvium-filled valley of northern Jackson Hole (hanging wall) subsided 6-8 mm relative to bedrock of the Teton Range (footwall) relative to the 1989 survey. However, in 1997 a 2 km-wide zone adjacent to the fault rose 12 mm relative to the 1993 survey, and then dropped 16 mm by

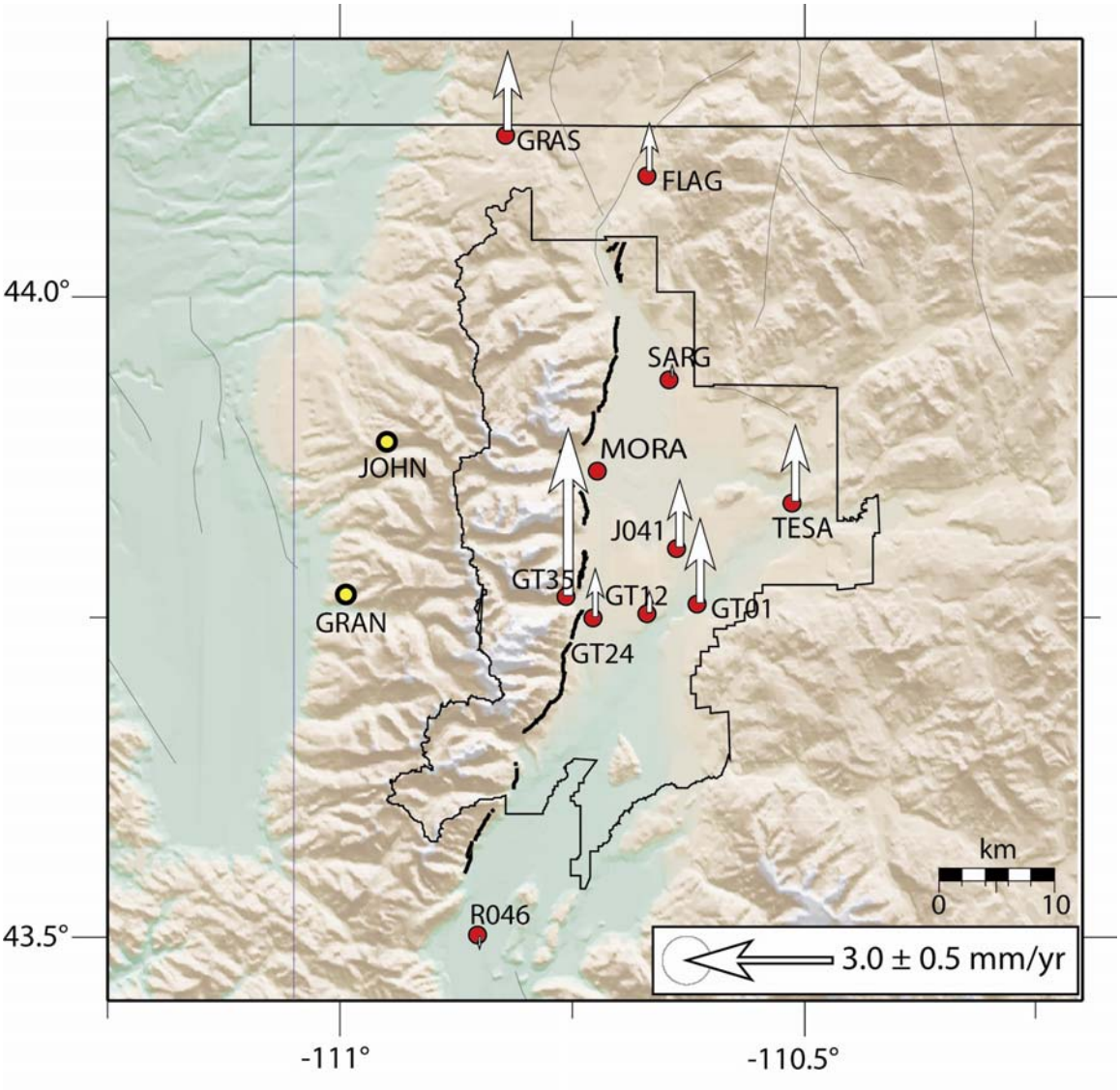

Figure 4.12. The University of Utah GPS campaign network, 1987-2003, vertical deformation results. Campaign site stations are represented by red and yellow circles. The yellow stations represent the stations held fixed in the mountain block allowing the valley block campaign stations to move with respect to the fixed footwall. The vertical deformation vectors are shown as white arrows with their arrow length being proportionate to the movement of the station in mm/yr. The major faults in the area are shown by the black lines, and the outline of the Grand Teton National Park is shown in black. Note compression is implied by vertical velocity vectors with respect to the mountain block.

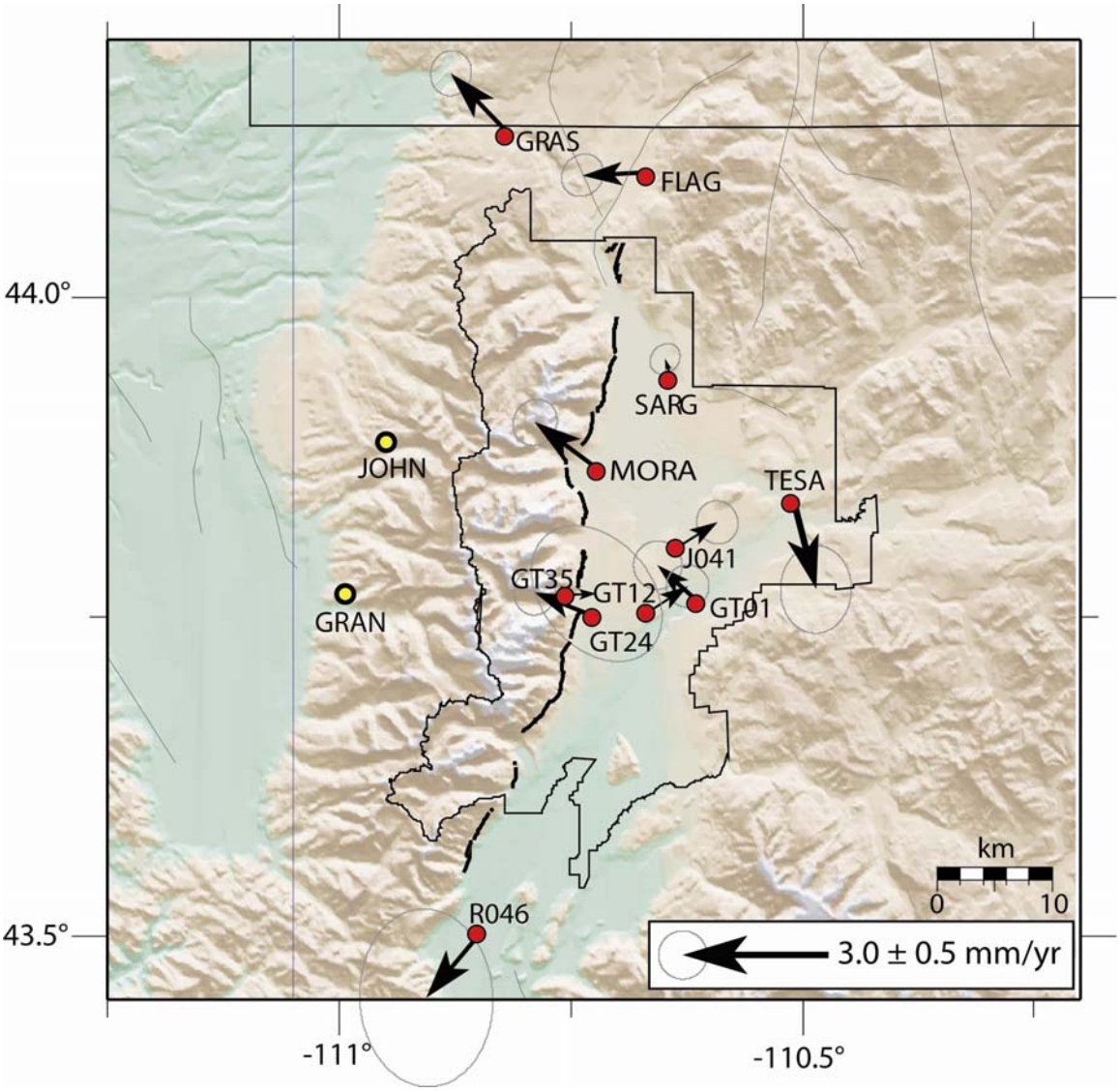

Figure 4.13. The University of Utah GPS campaign network, 1987-2003, horizontal deformation results. Campaign site stations are represented by red and yellow circles. The yellow stations represent the stations held fixed in the mountain block allowing the valley block campaign stations to move with respect to the fixed footwall. The horizontal deformation vectors are shown as black arrows with their arrow length being proportionate to the movement of the station in mm/yr. The major faults in the area are shown by the black lines, and the outline of the Grand Teton National Park is shown in black. Note compression is implied by west oriented velocity vectors with respect to the mountain block.

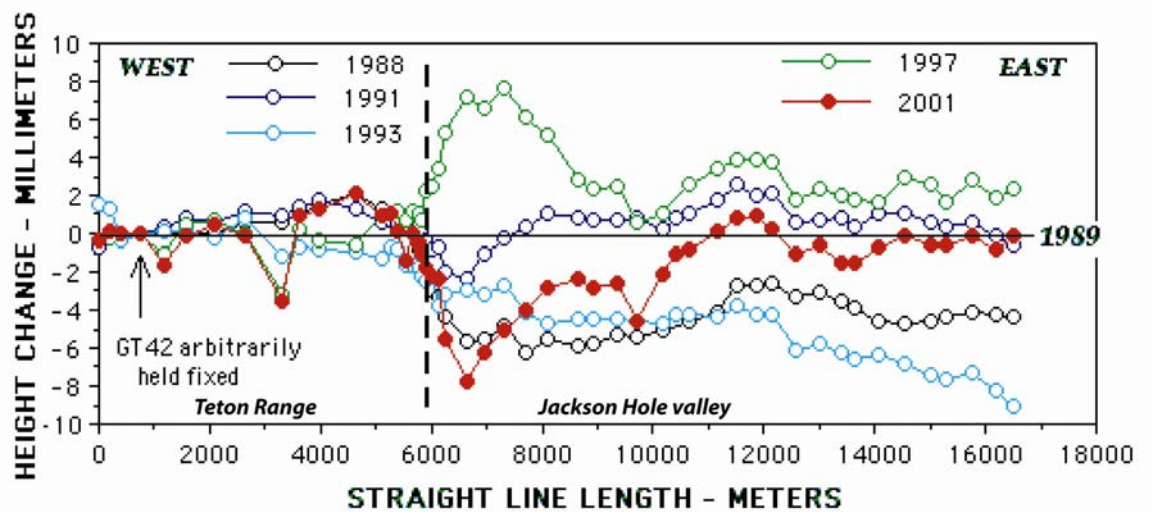

Figure 4.14. Teton first order leveling line survey results, 1988-2001 [*Sylvester et al*., 2004]. The height changes are measured in millimeters and the line length is measured in meters. All surveys are with respect to the 1989 survey datum, and site GT42 was arbitrarily held fixed. The black dash line represents the planar location of the Teton fault. The standard deviation of bench mark heights/km of leveling is 0.08 mm.

the 2001 leveling. This zone coincides with an area of low topography characterized by lakes ponded along the fault and south-flowing streams parallel to the range front, rather than eastward away from the range [*Sylvester et al.,* 2004]. This subsidence zone records hanging wall subsidence related to long term faulting, and the 1997 uplift of the valley floor and subsidence zone may reflect an unexpected, reverse loading and local crustal shortening between 1993 and 2001 [*Sylvester et al*., 2004].

The campaign GPS surveys from 1986 to 2000 support this hypothesis, indicating that the principal horizontal strain axis is locally E-W perpendicular to the fault, and crustal shortening is occurring from 1995-2000. Perhaps what we are seeing is just a localized time period of compression along the Teton fault, which would explain the lack of seismicity along any fault projection at depth. Regionally during 1987-1995, uplift and contraction of the Yellowstone caldera only 30 km north of the Teton Region were recorded during the same time as the valley uplift and extension across the Teton valley. During 1995-2000, subsidence of the Yellowstone caldera was recorded and GPS-derived ground motion vectors across Jackson Hole were directed west with almost 2 mm/yr of E-W motion (N. America fixed). The observed leveling changes may reflect a complex combination of other processes including local poroelastic effects, and nearfield drag of the hanging wall as it subsides overall in farfield extension [*Sylvester*, 2004]. The overall stress field of the Teton region might show extension through the use of the focal mechanisms from small magnitude events, but perhaps there are compressional time periods along the Teton fault that cause seismic gaps and are not resolved in seismic trends.

4.3. Teton Region PSHA Models and Future Research

An initial PSHA (Probabilistic Seismic Hazard Assessment) model was established for the Teton Region using the new relocated earthquake catalog determined by using the 3-D velocity model and probabilistic relocation method.

In order to model earthquake occurrence as a random process, the catalog must approximate random space-time characteristics. Due to the possibility of forshock-mainshock-aftershock sequences and swarms, it is necessary to identify and delete dependent events from swarms and forshock-mainshock-aftershock sequences. We deswarmed the new Teton Region catalog using the methodology of *Waite* [1999] using an earthquake deswarming matlab script written by *Waite* [1999] explained below.

Waite's deswarming script follows the empirical definition of a swarm as defined by *Mogi* [1963] and consists of the following: (1) the total number of earthquakes in a sequence is at least 20, and (2) the maximum of the daily number of events in the sequence (N_d) is greater than twice the square-root of the swarm duration in days (T):

$$N_d > 2\sqrt{T} \tag{2}$$

For deswarming of the Teton relocated catalog we used the values reported by *Waite* [1999] to be the best in distinguishing precursory swarms which used the following values: a 2-day look ahead time window, a 5 km radius window, and at least 20 events to be declared a swarm. Only five swarms were identified in the Teton catalog that fit the criteria defined by *Waite* [1999].

Once the catalog was deswarmed the new catalog was used in the program ZMAP [*Wiemer and Zuniga*, 1994] to decluster the catalog and determine cumulative a and b values. Using ZMAP's internal declustering program, which applies an algorithm written by *Reasenberg* [1985] that identifies aftershocks by modeling an interaction zone around each earthquake, 714 clusters were determined that contained 3940 events.

A magnitude of completeness for the Teton catalog was set to the lower magnitude cutoff of 2.0, with a cumulative *b* value of 1.08 +/- 0.05 and an a value of 2.08 (scaled to the annual frequency of the Jackson Lake seismic network) (Figure 4.15). This information and regional fault slip data were used in the creation of the PSHA model using HAZ38_2006 created by *Abrahamson* [2006] that determines estimates of peak ground acceleration and spectral amplitude for specified sources. This is only an initial model and later models should ideally include GPS deformation rates in their calculations.

Geologic moment rates for the Teton area are comparable to historic moment rates observed in other parts of the Intermountain Seismic Belt, indicating that long-term seismicity in the Tetons is similar to that of the other regions. Large earthquakes ($6.5 < M < 7.5$) are estimated to occur in the Teton Region every 130 to 155 years [*Doser and Smith*, 1983]. Magnitude 7.5 earthquakes are estimated to occur along the Teton fault every 800 to 1800 years [*Doser and Smith*, 1983]. Geologic moment rates for the Teton region determined by trenching results by *Byrd* [1995] indicate at loading rate of 0.16 mm/yr which with linear extrapolation from the last two ruptures leads a present day event capable of M 7 along the Teton fault (Figure 4.16). Byrd's loading rate along the Teton fault for the most recent events is considerably lower than the prehistoric post-

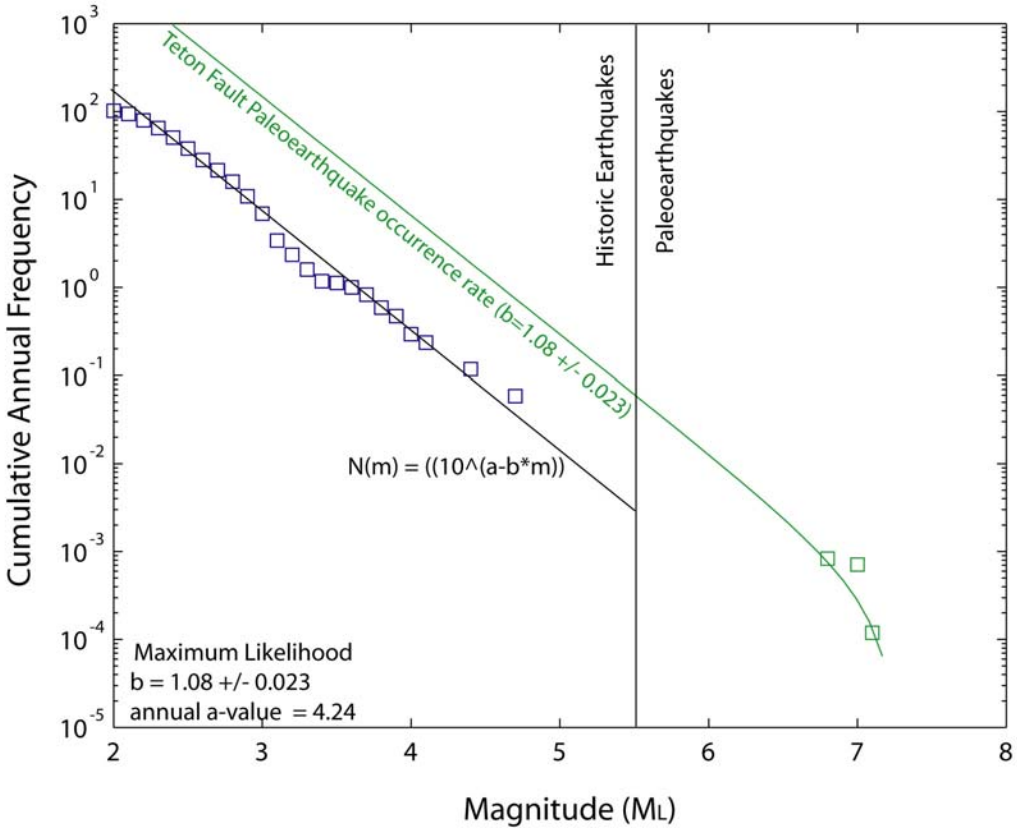

Figure 4.15. Earthquake recurrence model for the Teton region. The blue squares show the historical (1986-2002) cumulative annual earthquakes per magnitude with a minimum magnitude of 2. The blue line is the maximum likelihood best fit for the observed data using the Gutenberg-Richter equation. The b value for the Teton region is 1.08 +/- 0.023 with an annual a-value at the y = 0 intercept equal to 4.24. The green squares show the cumulative annual paleoearthquakes along the Teton fault determined from trenching as shown in Figure 4.16. The green line was determined using the truncated Gutenberg-Richter equation to best fit the paleoearthquake data then extrapolated back into the historic record using the same b value determined from the historical earthquake record.

Figure 4.16. Teton fault stress loading model and Teton trench cross section. Figure (a) shows the geologic composition of the Teton trench cross section completed by *Byrd* [1995]. Figure (b) shows the fault stress loading model for the Teton fault using postulated Paleoearthquake that would have been necessary in order to create the observed fault offsets along the Teton fault scarp (in blue), and the prehistoric ruptures determined from the trenching results (in red). The youngest recorded prehistoric rupture was a M6.8 earthquake 4,700 to 6,000 years ago that generated a 1.3 m offset. The next youngest rupture was a M7.1 earthquake 7,300 years ago that generated a 2.8 m offset. Using the prehistoric ruptures a fault loading rate of 0.16 mm/yr is calculated and extrapolated to the present time to estimate the next possible rupture on the Teton fault.

a.)

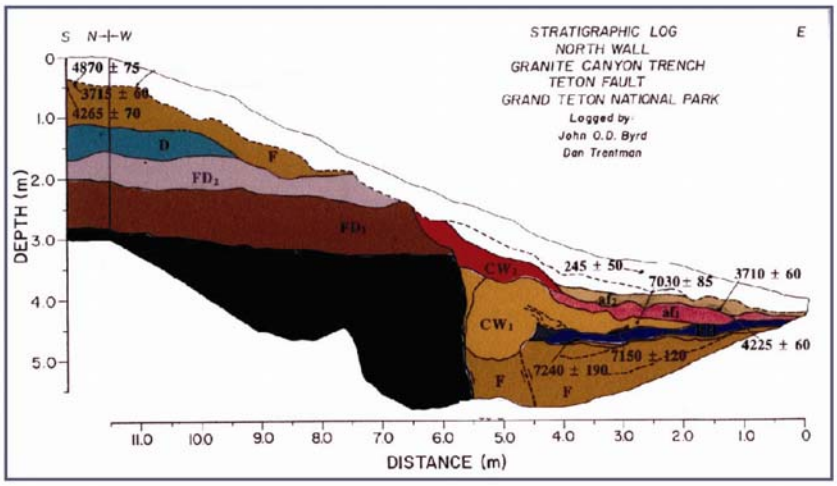
S N-I-W
E
STRATIGRAPHIC LOG
NORTH WALL
GRANITE CANYON TRENCH
TETON FAULT
GRAND TETON NATIONAL PARK
Logged by:
John O.D. Byrd
Dan Trentman
4870 ± 75
3715 ± 60
4265 ± 70
D
F
FD2
FD1
CW1
245 ± 50
7030 ± 85
3710 ± 60
af2
af1
CW1
4225 ± 60
7150 ± 120
7240 ± 190
F
F
DEPTH (m)
0
1.0
2.0
3.0
4.0
5.0
11.0
10.0
9.0
8.0
7.0
6.0
5.0
4.0
3.0
2.0
1.0
0
DISTANCE (m)

b.)

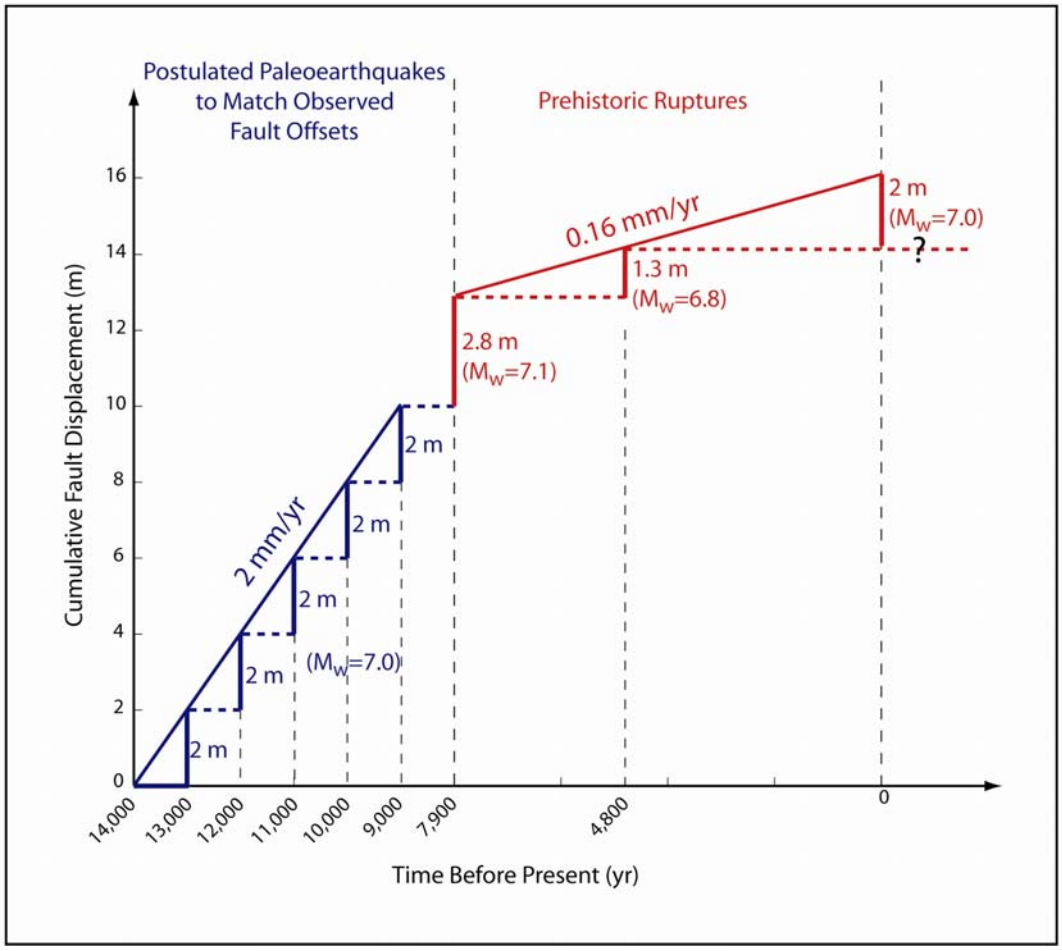
Postulated Paleoearthquakes
to Match Observed
Fault Offsets
Prehistoric Ruptures
0.16 mm/yr
2 m
(Mw=7.0)
?
1.3 m
(Mw=6.8)
2.8 m
(Mw=7.1)
2 mm/yr
2 m
2 m
2 m
2 m
(Mw=7.0)
2 m
Cumulative Fault Displacement (m)
0
2
4
6
8
10
12
14
16
14,000
13,000
12,000
11,000
10,000
9,000
7,900
4,800
0
Time Before Present (yr)

glacial loading rate of 2 mm/yr (Figure 4.16). These large differences in prehistoric slip rates could possibly be related to glacial unloading of normal faulted adjacent mountains which has been proposed by *Hatzel and Hampel* [2005]. Similar to the Teton fault, the Wasatch fault and three adjacent normal faults in the Basin and Range have documented geologic and paleoseimological data that marks an increase in slip rates in postglacial faulting offsets relative to current measured slip rates [*Hatzel and Hampel*, 2005]. However, the important question is where are we currently on the earthquake cycle for the Teton fault given either of these slip rates (Figure 4.17). This is a question that will only be answered once the Teton fault ruptures again.

Including the Teton Fault, other major active faults in the greater Teton and Yellowstone region were used in the seismic hazard analysis of the Teton region (Figure 4.18). These major Quaternary faults' information including current slip rates were gathered from the U.S.G.S. Fault and Fold Database. These 12 faults have the largest slip rates of any of the major faults in the area.

Above we have discussed the key input for the PSHA, which includes Quaternary fault sources, seismogenic sources, and frequency of occurrence. However, the attenuation relationship input is very important in determining the PSHA. The generally accepted attenuation relationship used for western U.S. extensional Basin and Range province is *Spudich et al.* [1999]. The crustal rock and soil attenuation relationship established by *Spudich et al.* [1999] was used in our preliminary PSHA as the connection from frequency magnitude plots and fault slip rates to the final ground amplifications for a given site.

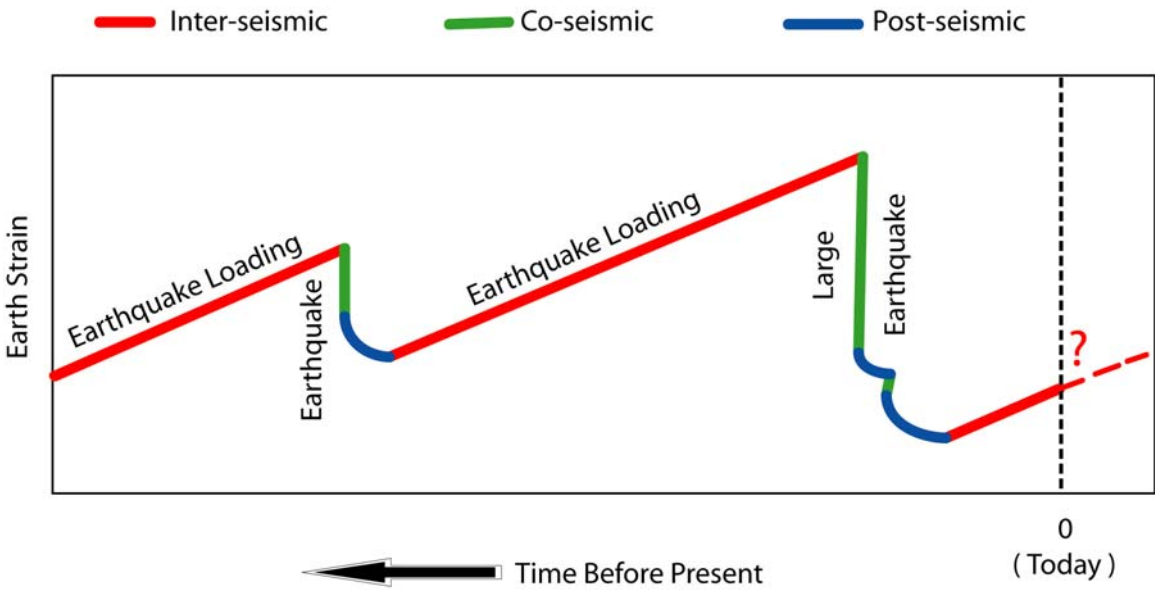

Figure 4.17. Earthquake cycle for the Teton fault. Interseismic periods are shown in red where fault loading is occurring. Coseismic periods are shown in green where a large earthquake releases strain along the fault. Postseismic periods are shown in blue. The Teton fault is currently in the Interseismic period, but it is not known how far along in the period it is.

Figure 4.18. Quaternary faults in the PSHA for the Teton/Yellowstone region. The bold black faults had the largest slip-rates of any faults in the area and were used in the PSHA calculation. The small bold black lines perpendicular to each fault show the fault's normal faulting dipping direction. The minor area faults not included in the PSHA are shown in gray. Yellowstone and Grand Teton National Parks are outlined in black, and all major lakes are blue. The Yellowstone caldera is outlined in orange and the Idaho/Montana and Wyoming/Montana borders are outlined in blue. Towns are labeled in maroon, and fault slip rates are in blue.

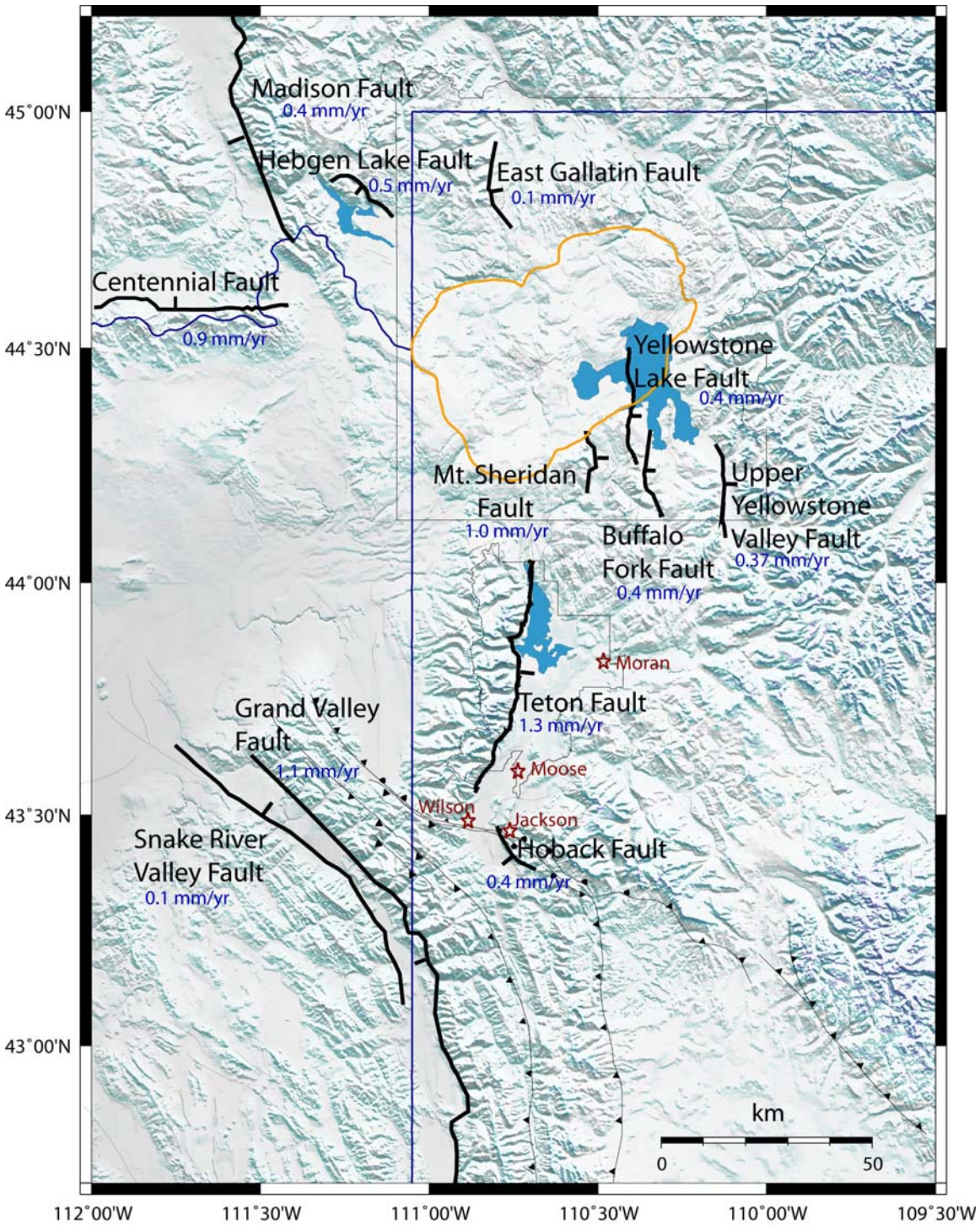
Madison Fault
0.4 mm/yr
Hebgen Lake Fault
0.5 mm/yr
East Gallatin Fault
0.1 mm/yr
Centennial Fault
0.9 mm/yr
Yellowstone
Lake Fault
0.4 mm/yr
Mt. Sheridan
Fault
1.0 mm/yr
Upper
Yellowstone
Valley Fault
0.37 mm/yr
Buffalo
Fork Fault
0.4 mm/yr
Moran
Teton Fault
1.3 mm/yr
Grand Valley
Fault
1.1 mm/yr
Moose
Wilson
Jackson
Hoback Fault
0.4 mm/yr
Snake River
Valley Fault
0.1 mm/yr
km
0
50
45°00'N
44°30'N
44°00'N
43°30'N
43°00'N
112°00'W
111°30'W
111°00'W
110°30'W
110°00'W
109°30'W

To generate the PSHA for the greater Teton region we also included Yellowstone since they are close together and the major faults that affect the hazard for both regions are typically included with one another. The PSHA code HAZ38_2006 created by *Abrahamson* [2006] from Pacific Gas and Electric was used in this research to create the Teton/Yellowstone PSHA. HAZ38_2006 determines estimates of peak ground acceleration and spectral amplitude for specified sources. Sources of hazard include: fault sources and slip rates, earthquake sources, and implicitly input of GPS via a proxy for slip rate). However for this study we did not include input of GPS via a proxy for slip rate due to the fact that this was a preliminary model and only traditional fault slip rates were used. Future PSHA models for the Teton region will include GPS input as well as local site conditions.

The fault and seismic sources in the hazard contain significant uncertainty in most of the parameters used to characterize source behavior. This code incorporates epistemic uncertainty in the analysis via a logic tree approach, allowing the user to specify several possible values for each of the parameters used to characterize the fault behavior and to assign discrete probabilities or weights to each of these values or models. The beginning of the logic tree used in this study is shown in Appendix I. Aleatory uncertainty also is accounted for in this code by defining probability density functions for the earthquake magnitude, location, and rupture dimensions. The equation that is calculated for the annual rate of exceedance y* of a given PGA value is calculated by:

$$\lambda_{y^*} \approx \sum_{i=1}^{N_s} \nu_i \cdot \left(\sum_{j=1}^{N_m} \sum_{k=1}^{N_k} \mathrm{P}\left(m_j \mid t=1\right) \cdot \mathrm{P}\left(r_k\right) \cdot \mathrm{P}\left(Y > y^* \mid m_j, r_k\right) \right) \tag{3}$$

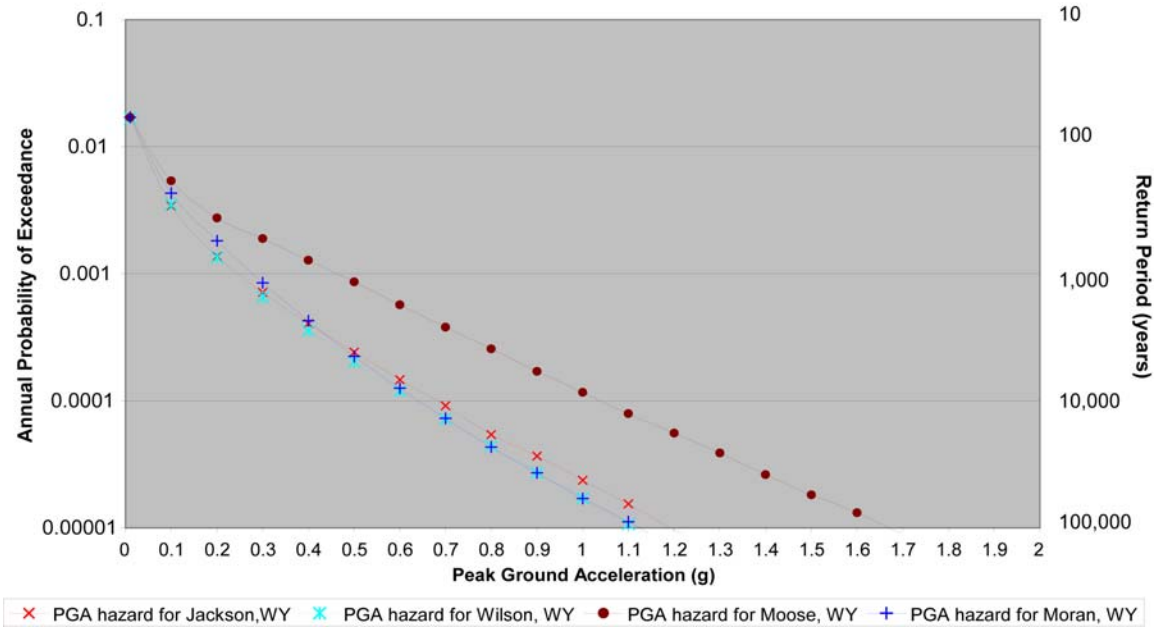

Figure 4.19. Probabilistic seismic hazard analyses of the Wyoming towns of Jackson, Moose, Moran, and Wilson in terms of ground motion as a function of annual exceedance probability. These four towns are located in the Jackson Hole valley east of the Teton fault. The x-axis values are relative to the gravitational constant of g = 9.8 m/s^2. This probability is the reciprocal of the average return period. The hazard for the town of Moose, WY is the largest given its close proximity to the central Teton fault segment as shown in Figure 4.18.

Four individual sites' hazards were computed for the Teton region at the towns of Jackson, WY, Moose, WY, Moran, WY, and Wilson, WY. These towns are all located in different parts of the Jackson Hole valley east of the Teton Range. The hazard curves for peak ground acceleration (PGA) were computed and are shown in Figure 4.19. Notice the largest average return rate of 1000 years is about 0.5g PGA for the town of Moose, WY located in the Jackson Hole valley at the southern entrance to Grand Teton National Park as shown in Figure 4.18. The hazard curves for the other three towns have lower PGA exceedance values of about 0.3g for a 1000-year return period.

A regional preliminary PSHA map was created using HAZ38_2006 for gridded sources every 0.1 degree from northern Yellowstone to the southern Teton region near Palisades Dam, WY. PSHA maps with PGA color scales were created for return periods of 500 yrs, 1000 yrs, and 2500 yrs (Figures 4.20 – 4.22), and were compared to the USGS PSHA for the same region for a 2500-year return period (Figure 4.23). Within the different return periods the highest hazards in the mapped areas are typically the same, being the Jackson Hole valley and the southeastern portion of Yellowstone National Park. The PSHA in the Teton Yellowstone region is dominantly controlled by the fault hazards along the faults with the highest recorded slip rates. The Teton fault dominates the region with the Buffalo Fork, Mt. Sheridan, Yellowstone Lake and Yellowstone River Valley faults. Other faults such as the Grand Valley, Snake River, and Centennial faults also become a larger hazard in 2500 years. The overall outcome of this preliminary PSHA map of the Teton Yellowstone region demonstrates the hazard that is associated with this area and it must be updated with more current safety regulations and building code ordinances to prepare for seismic hazards of this magnitude.

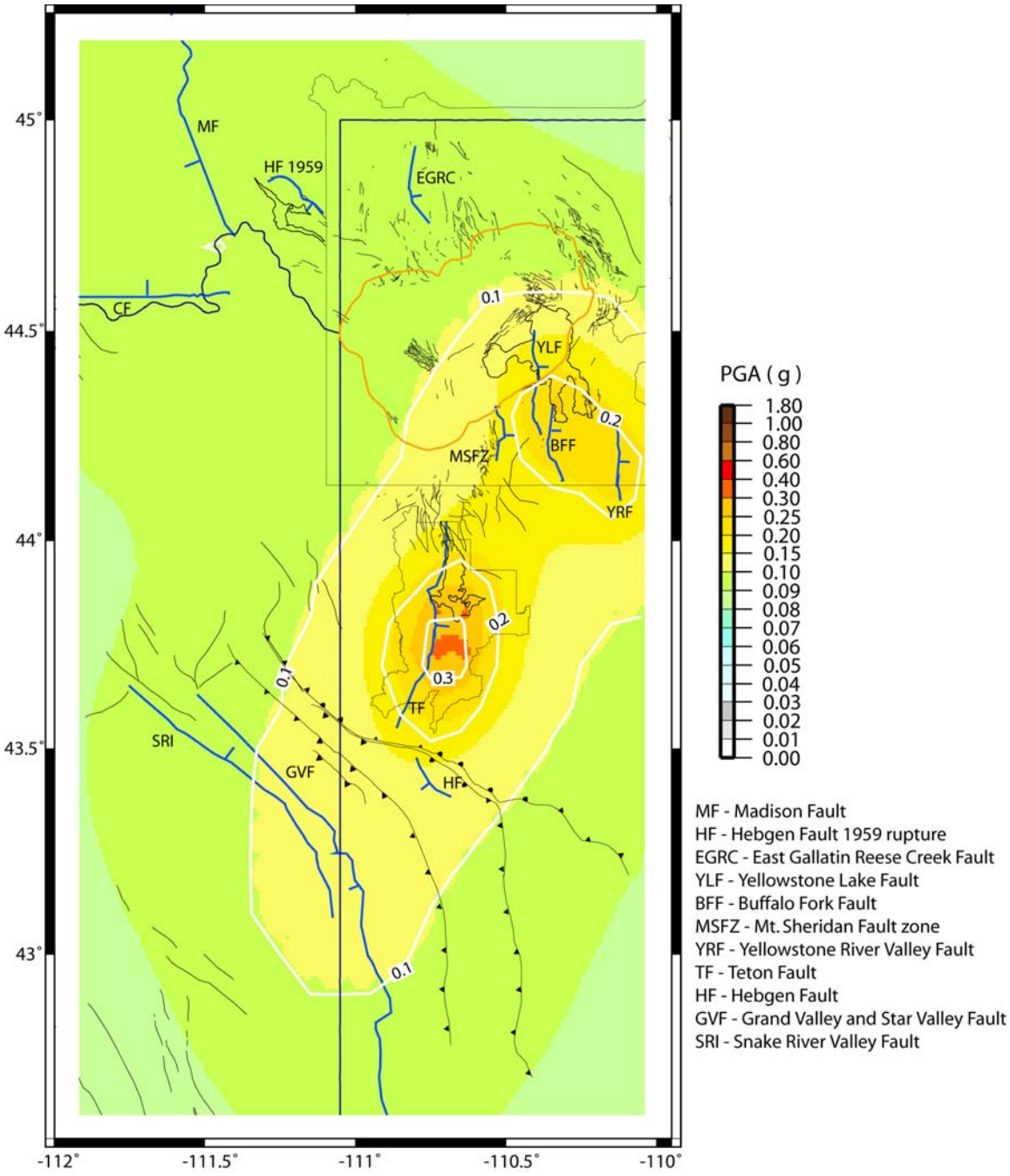

Figure 4.20. Probabilistic seismic hazard analyses of the greater Teton/Yellowstone region for peak ground acceleration with 10% probability excedance in 50 years (500 years). The color scale is based on PGA values relative to the gravitational constant of g = 9.8 m/s^2. The blue faults had the largest slip-rates of any faults in the area and were used in the PSHA calculation. The small blue lines perpendicular to each fault show the faults normal faulting dipping direction. The minor area faults not included in the PSHA are shown in gray. Yellowstone and Grand Teton National Parks are outlined in black, and all major lakes are outlined in black. The Yellowstone caldera is outlined in orange and the PGA contours are outlined in white.

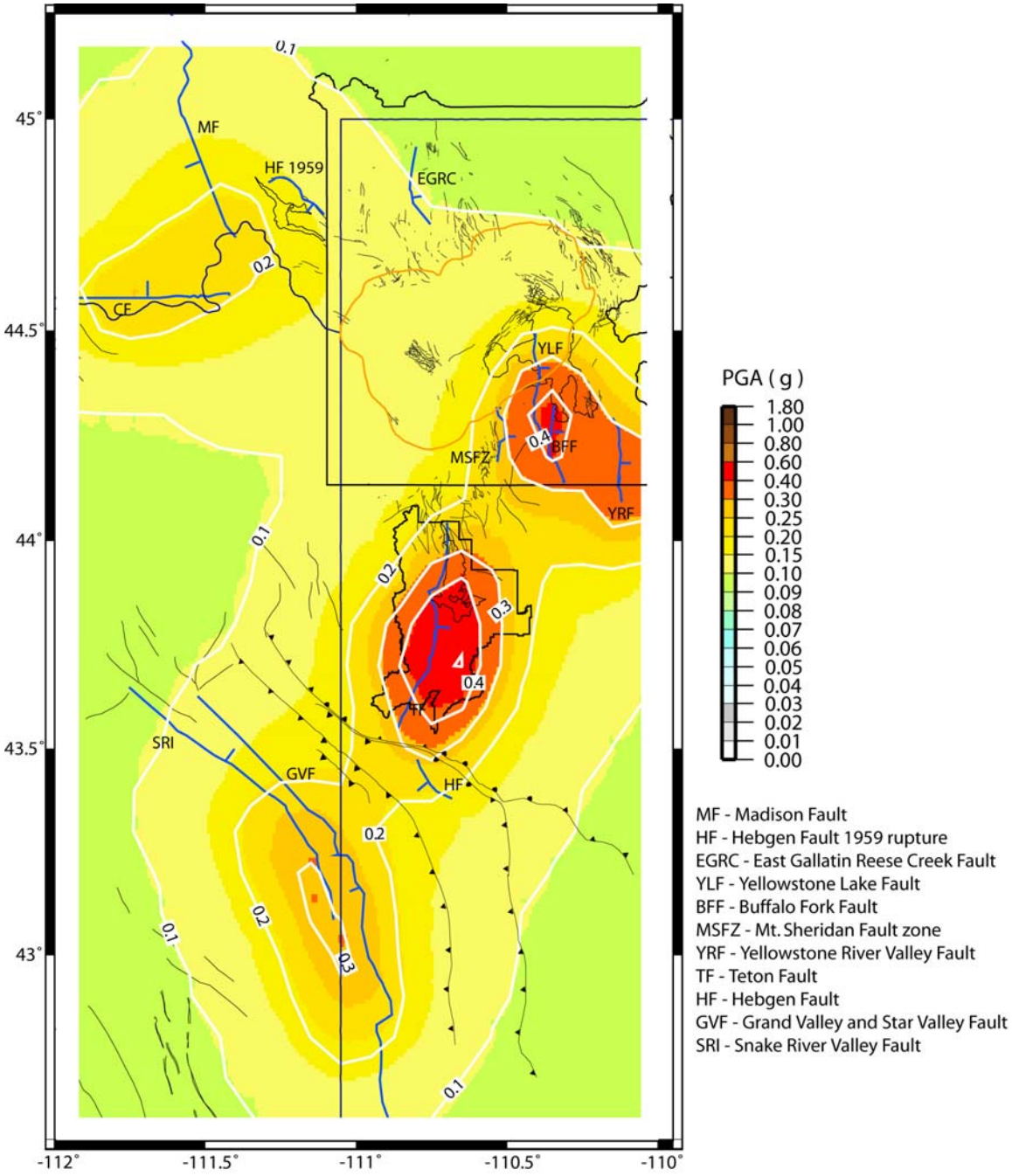

Figure 4.21. Probabilistic seismic hazard analyses of the greater Teton/Yellowstone region for peak ground acceleration with 5% probability excedance in 50 years (1,000 years). The color scale is based on PGA values relative to the gravitational constant of g = 9.8 m/s^2. The blue faults had the largest slip-rates of any faults in the area and were used in the PSHA calculation. The small blue lines perpendicular to each fault show the faults normal faulting dipping direction. The minor area faults not included in the PSHA are shown in gray. Yellowstone and Grand Teton National Parks are outlined in black, and all major lakes are outlined in black. The Yellowstone caldera is outlined in orange and the PGA contours are outlined in white.

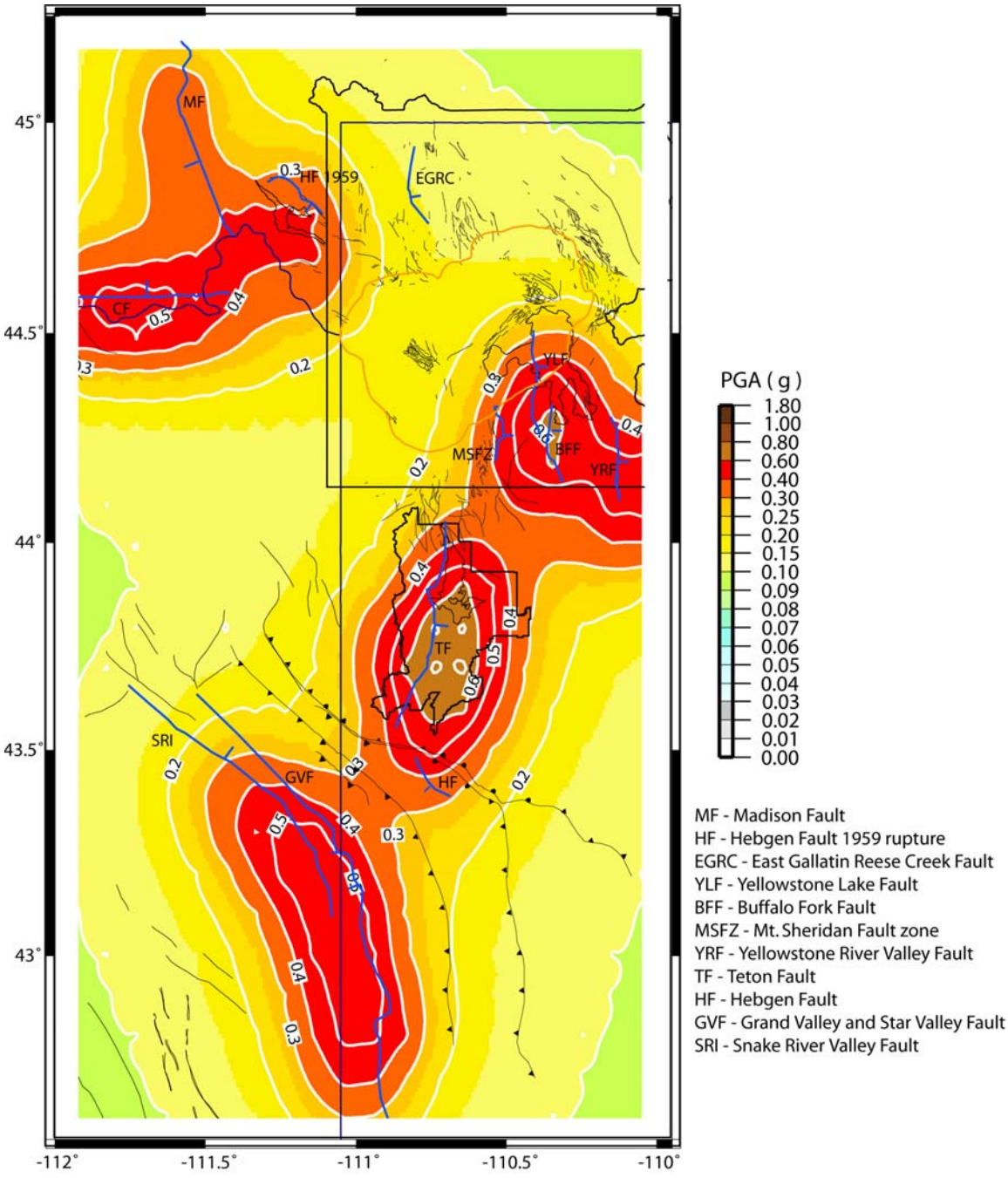

Figure 4.22. Probabilistic seismic hazard analyses of the greater Teton/Yellowstone region for peak ground acceleration with 2% probability excedance in 50 years (2,500 years). The color scale is based on PGA values relative to the gravitational constant of g = 9.8 m/s^2. The blue faults had the largest slip-rates of any faults in the area and were used in the PSHA calculation. The small blue lines perpendicular to each fault show the faults normal faulting dipping direction. The minor area faults not included in the PSHA are shown in gray. Yellowstone and Grand Teton National Parks are outlined in black, and all major lakes are outlined in black. The Yellowstone caldera is outlined in orange and the PGA contours are outlined in white.

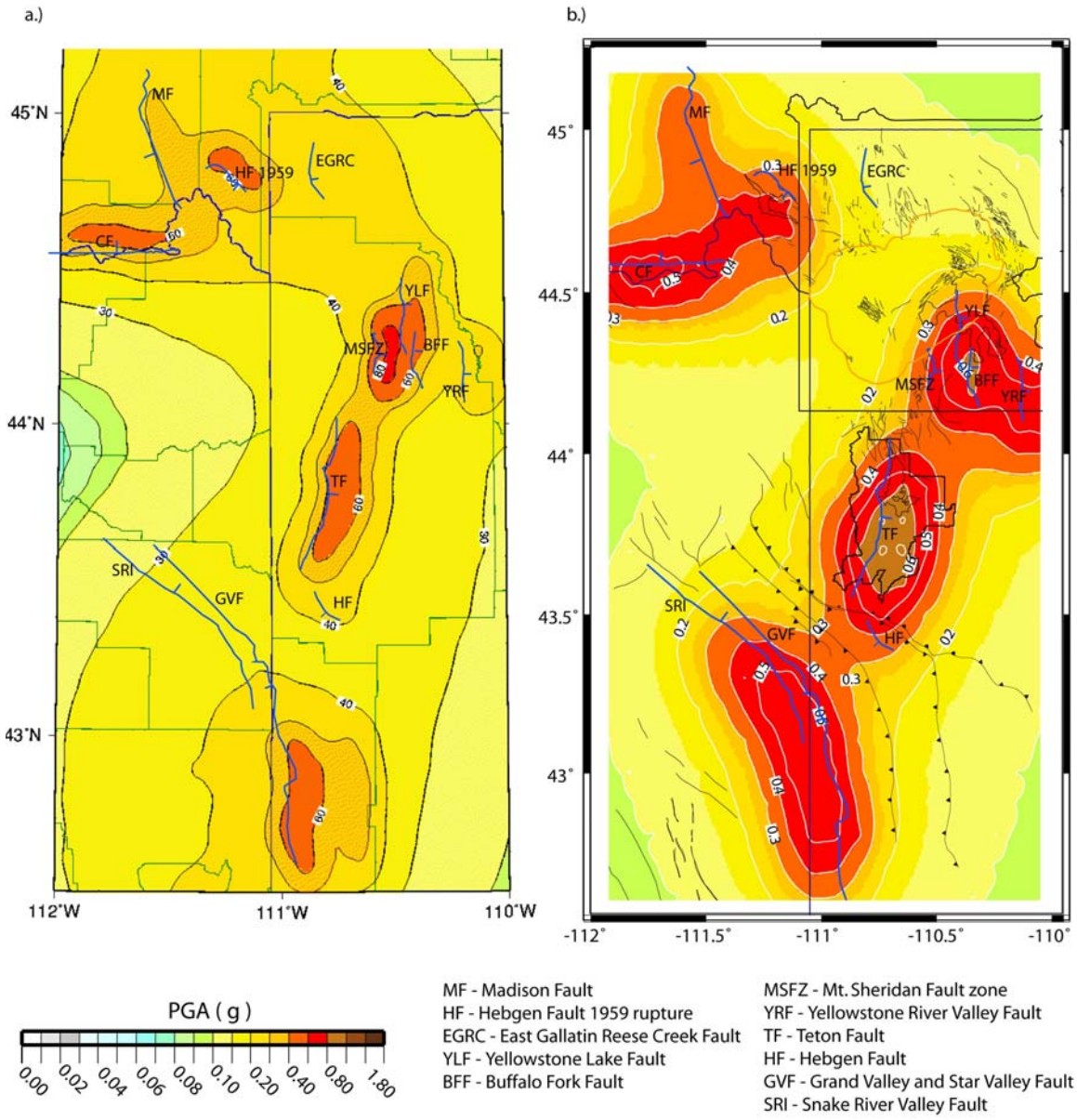

Figure 4.23. Teton/Yellowstone PSHA comparison to USGS Teton/Yellowstone PSHA. Probabilistic seismic hazard analyses of the greater Teton/Yellowstone region for peak ground acceleration with 2% probability excedance in 50 years (2,500 years) as determined by the USGS (figure a.) and by HAZ38 as determined in this study (figure b). The color scale is based on PGA values relative to the gravitational constant of g = 9.8m/s^2. The blue faults had the largest slip-rates of any faults in the area and were used in the PSHA calculation. The small blue lines perpendicular to each fault show the faults normal faulting dipping direction. The minor area faults not included in the PSHA are shown in gray. Yellowstone and Grand Teton National Parks are outlined in black, and all major lakes are outlined in black. The Yellowstone caldera is outlined in orange and the PGA contours are outlined in white.

CHAPTER 5

CONCLUDING REMARKS

Earthquake data from the U.S Bureau of Reclamation's Jackson Lake seismic network were used to produce a new higher accuracy earthquake catalog for the Teton Region employing a tomographic 3-D P-wave velocity model of upper and mid crustal structure. We note that focal depth data do not appear to be associated with the mapped or depth projected traces of Quaternary faults or along the Teton fault. Similar conclusions were obtained by *Smith and Sba*r [1974] and *Doser and Smith* [1983] for other regions in the intermountain seismic belt.

Seismicity in the Gros Ventre Range and Hoback regions might be related to reactivation of older Laramide basement structures in the Cache Creek, Jackson and Gros Ventre thrusting zones. The Teton fault has shown little to no seismic activity along mainly the northern and central fault segments, which exhibits the greatest and most recent prehistoric displacement. Whether this observation is due to the possible episodic nature of seismicity along the segment or other factors is not known, but the possibility that this segment is locked and storing strain energy cannot be ruled out.

Focal mechanisms provided data for stress field inversions that indicated dominant east-west extension in the southern and central Teton fault segments but with an unsuspected change to northeast-southwest extension in the northern segment

dominated by the Yellowstone volcanic system. GPS measurements and leveling results indicate the Teton fault shows intermediate stages of compression, generating a locked normal fault storing strain energy with no seismic activity. It has also been proposed by *Janecke* [1995] that the Teton fault is not a typical eastern Bain and Range fault, but is in response to lithospheric downwarp of the Yellowstone/Snake River Plain hotspot track that is most likely also akin to the Centennial fault as well.

Tomographic images did reveal velocity perturbations that could separate the footwall from the hanging wall structure of the Teton normal fault, but did not aid in determining the faulting dip angle of the Teton fault. However, basin structures and deeper bedrock structures were resolved down to 12 km depth. Perhaps the finer 5 x 5 km velocity model parameterization will better resolve the footwall-hanging wall velocity contrast and give a better estimate on the true dipping angle of the normal fault at depth.

The largest question associated with the Teton fault is the noticeable seismic gap. The Teton fault has the largest fault slip rate in the Basin and Range that has a seismic gap associated with its characteristics. There are several hypotheses that may account for the observed seismic quiescence and low strain rates across the Teton fault: 1) the Teton fault may indeed be quiescent, accumulating strain energy prior to a future earthquake; 2) the fault may be releasing strain through aseismic fault creep, although there is no evidence for this; 3) the short period of historic seismologic observations and poor epicentral control before 1962 preclude accurate assessment of the long-term seismicity; 4) the Teton fault may no longer be active and is not storing significant strain energy required for earthquake nucleation but that is unlikely given its profound late Quaternary history; or 5) the regional background seismicity surrounding the fault may be effectively

relieving stress accumulation directly on the fault [*Smith et al*., 1993a]. These hypotheses are logical and reasonable explanations of the seismic quiescence along the Teton fault.

However, in this study we have shown GPS-derived deformation and leveling data that reveal the Jackson Hole valley block moving in a westward direction with respect to the Teton Range mountain block. This implies the Teton fault is in a compressional state and could possibly be locked. This observation demonstrates the complexity of the Teton fault and how normal faults are capable of compressional loading causing seismic quiescence to occur. The real question I am more concerned with is that even though regional Teton seismicity is demonstrating normal faulting stress orientations, is the Teton fault capable of producing an oblique thrusting event? Given the GPS data it seems there is definite strain accumulation along the Teton fault in a compressional orientation. However is it enough to a generate a major earthquake along the Teton fault with a reverse fault focal mechanism? Paleoearthquake data reveal there is no evidence of reverse faulting occurring along the Teton fault. Perhaps the GPS deformation rates are just demonstrating the complexity of the seismic cycle of the Teton fault since they are only very small intervals of compression with respect to the overall geologic normal faulting record of the Teton Range.

Whatever the cause of the seismic quiescence along the Teton fault is, we believe the fault is still an active structure that is capable of generating large future earthquakes.

Future research along the Teton fault should include more waveform modeling of earthquakes located east of the Teton fault which can provide better constraints on Teton fault dip at depth than are currently available. I would also recommend seismic refraction/reflection studies of the Teton fault that extend observations of upper-crustal

structure from the Jackson Hole basin across the Teton fault westward into the Teton Range. I would concentrate seismic lines in areas where we have the most control with our 3-D velocity model so that we can compare results with our seismic velocity models and update them if necessary. The current analysis using dynamic models of the Teton fault should also provide more insight into the tectonic development of the Teton Range and should inspire others to continue working in the Teton region.

REFERENCES

Abers, G. A., and J. W. Gephart (2001), Direct inversion of earthquake first motions for both the stress tensor and focal mechanisms and application to southern California, *J. Geophys. Res*., *106*(B11), 26523-26540.

Abrahamson, N. (2006), HAZ38_2006, Pacific Gas & Electric, personal communication, Spring, 2006.

Aki, K., and P.G. Richards (1980), *Quantitative Seismology*, W. H. Freeman, New York.

Behrendt, J. C., B. L. Tibbetts, W. E. Bonini, and P. M. Lavin (1968), A Geophysical Study in Grand Teton National Park and Vicinity, Teton County Wyoming, *U.S.G.S. Professional Paper 516-E*, 23.

Blackwelder, E. (1926), Earthquakes in Jackson Hole, Wyoming: *Seismol. Soc. America Bull.*, *16*, 196.

Byrd, J. O. D. (1991), Paleoseismicity of the southern section of the Teton fault, Wyoming, *Geol. Soc. Amer. Abstr. Programs*, *23*, A481.

Byrd, J. O. D., R. B. Smith and J W. Geissman (1994) The Teton fault, Wyoming: topographic signature, neotectonics and mechanism of deformation, *J. Geophys. Res*., *99*, 20122-20140.

Byrd, J.O.D. (1995), Neotectonics of the Teton Fault, Wyoming. Ph.D. Thesis, University of Utah, Salt Lake City, Utah, 20 August.

Byrd, J. O. D., and R. B. Smith (1995), Near surface fault geometry and paleoseismicity of the Teton fault, Wyoming, submitted to *Geol. Soc. Amer. Bul*.

Christiansen, R.L., and H.R. Blank, Jr. (1972), Volcanic stratigraphy of the Quaternary rhyolite plateau in Yellowstone National Park, *U.S. Geol. Surv. Profess. Paper 516 E*, E14-E20 pp., U.S. Geol. Surv., Denver, CO.

Christensen, N.I., and W.D. Mooney (1995), Seismic velocity structure and composition of the continental crust: A global view, *J. Geophys. Res*., *100*, 9761-9788.

Coffman, J.L., and C.A. von Hake (Editors) (1973), Earthquake history of the United States, *U.S. Dept. of Commerce Publ. 41-1*, 208.

Dodge, D.A., G.C. Beroza, and W.L. Ellsworth (1995), Foreshock sequence of the 1992 Landers, California, earthquake and its implications for earthquake nucleation, *J. Geophys. Res*., *100*, 9865-9880.

Doser, D.L., and R.B. Smith (1983), Seismicity of the Teton-southern Yellowstone region, Wyoming, *Bull. Seis. Soc. Am*., *73*, 1369-1494.

Doser, D.I. (1985), Source parameters and faulting processes of the 1959 Hebgen Lake, Montana earthquake sequence, *J. Geophys. Res*., *93*, 15001-15016.

Eberhart-Phillips, D. (1986), Three-dimensional velocity structure in northern California Coast Range from inversion of local earthquake arrival times, *Bull. Seismol. Soc. Am., 76*, 1025-1052

Eberhart-Phillips, D. (1990), Three-dimensional P and S velocity structure in the Coalinga Region, California. *J. Geophys. Res*., *95*, 15343-15363.

Eberhart-Phillips, D., and M. Reyners (1997), Continental subduction and three-dimensional crustal structure: The northern South Island, New Zealand. *J. Geophys. Res*., *102* (B6), 11843-11861.

Eddington, P.J., R.B. Smith, and C. Renggli (1987), Kinematics of Basin-Range intraplate extension, in M.P. Coward, J.F. Dewey, and P.L. Hancock, editors "Continental Extensional Tectonics", *Lon. Geol. Soc., Spec. Pub*., *28*, 371-392.

Fehler, M., W.S. Phillips, R. Jones, L. House, R. Aster, C. Rowe (2000), A method for improving relative earthquake locations, *Bull. Seismol. Soc. Am*., *90*, 775-780

Fryxell, F. M. (1933), Earthquake shocks in Jackson Hole, Wyoming: *Seismol. Soc. America Bull.*, *23*, 167-168.

Gale, B.T. (1940), Communication, further earthquake shocks in Jackson Hole, Wyoming: *Seismol. Soc. Of America Bull.*, *30*, 85.

Got, J.L., J. Frechet, J.W. Klein (1994), Deep fault plane geometry inferred from multiplet relative relocation beneath the south flank of Kilauea, *J. Geophys. Res*., 99, 15375-15386.

Gilbert, J. D., D. Ostenaa, and C. Wood (1983), Seismotectonic study Jackson Lake Dam and Reservoir, Minidoka Project, Idaho-Wyoming: Bureau of Reclamation Seismotectonic Report, 83-8, 123.

Gephart, J.W. (1990a), Stress and the direction of slip on fault planes, *Tectonics*, 9, 845-858.

Gephart, J.W. (1990b), FMSI: A FORTRAN program for inverting fault/slickenside and earthquake focal mechanism data to obtain the regional stress tensor, *Comput. And Geosi*., 16, 953-989.

Haller, K.M., R.L. Wheeler, and K.S. Rukstales (2002), Documentation of changes in fault parameters for the 2002 National Seismic Hazard Maps-Conterminous United States except California, *U.S. Geol. Surv. Open-File Rep. 02-467*, 34 pp., U.S. Geol. Surv., Denver, CO.

Haslinger, F. (1998), Velocity structure, seismicity and seismotectonics of Northwestern Greece between the Gulf of Arta and Zakynthos, Ph.D. Thesis, ETH Zurich, Switzerland.

Haslinger, F., E. Kissling, J. Ansorge, D. Hatzfeld, E. Papadimitriou, V. Karakoastas, K. Makropoulous, H.G. Kahle, and Y. Peter (1999), 3D crustal structure from local earthquake tomography around Gulf of Arta (Ionian region, NW Greece). *Tectonophysics, 304*, 210-218.

Haslinger, F., and E. Kissling (2001), Investigating effects of 3-D ray tracing methods in local earthquake tomography. *Phys. Earth Planet. Int.,* 123, 103-114.

Hatzel R., and A. Hampel 92005), Slip rate variations on normal faults during glacial-interglacial changes in surface loads, *Nature*, *435*, 81-84.

Horiuchi, S., G.R., and A. Hasegawa (1995), Discrimination of fault planes from auxiliary planes based on simultaneous determination of stress tensor and a large number of fault plane solutions, *J. Geophys. Res*., *100*, 8327-8338.

Husen, S. (1999), Local Earthquake Tomography of a Convergent Margin, North Chile: A combined on – and offshore study. Ph.D. Thesis, ETH Zurich, Switzerland.

Husen, S., R. Quintero, E. Kissling, and B. Hacker (2002), Subduction-zone structure and magmatic processes beneath Costa Rica constrained by local earthquake tomography and petrological modeling, *Geophys. J. Int., 155*, 11-32.

Husen, S. and R. B. Smith (2003), Probabilistic earthquake relocation in three dimensional velocity models for the Yellowstone National Park Region, Wyoming, *Bull. Seismol. Soc. America*, in press.

Husen, S. (2003), Probabilistic earthquake location in complex 3-D velocity models: Application to Switzerland. *J. Geophys. Res., 108*(B2) (doi:10.1029/2002JB001778).

Husen, S. and R. B. Smith (2004), A revised earthquake catalog for the Yellowstone National Park Region, Wyoming, using probabilistic earthquake location, *Bull. Seismol. Soc. America*, in press.

Janecke, S. U. (1995), Eocene to Oligocene half grabens of east-central Idaho: Structure, stratigraphy, age, and tectonics: *Northwest Geology*, *24*,159-199.

Kissling, E. (1988), Geotomography with local earthquake data, *Rev. of Geophys,. 26*, 659-698.

Kissling, E., W.L. Ellsworth, D. Eberhart-Phillips, and U. Kradolfer (1994), Initial reference models in local earthquake tomography, *J. Geophys. Res*., *99*, 19635-19646.

Kissling, E., S. Husen, and F. Haslinger (2001), Model parameterization in seismic tomography: A choice of consequences for the solution quality, *Phys. Earth Planet. Int*., *123*, 89-101.

Klein, F.W. (1978), Hypocenter location program HYPOINVERSE; Part 1, Users guide to versions 1, 2, 3, and 4; Part 2, Source listings and notes, *U.S. Geol. Surv. Open-File Report*, 78-694.

Lageson, D.R., Adams, D.C., Morgan, L., Pierce, K.L., and Smith, R.B. (1999), *Neogene-Quaternary tectonics and volcanism of southern Jackson Hole, Wyoming and southeastern Idaho*, edited by Hughes, S.S., and Thackray, G.D., Guidebook to the geology of eastern Idaho: Idaho Museum of Natural History and the ISU Press, Idaho State University, pp. 115-130, Pocatello, ID.

Lavin, P.M., and W.E. Bonini (1957), Detailed gravity measurements in the Teton Range and Jackson Hole, Wyoming, *Geol. Soc. Am. Bull.*, *68*, 1760.

Lee, W.H.K., and J.C. Lahr (1972), HYPO-71: A computer program for determining hypocenter, magnitude and first motion pattern of local earthquakes, U.S. Geol. Surv., Menlo Park.

Leveque, J.-J., L. Rivera, and G. Wittlinger (1993), On the use of the checkerboard test to assess the resolution of tomographic inversions. *Geophys. J. Int*., *115*, 313-318.

Lomax, A., J. Virieux, P. Volant, and C. Thierry-Berge (2000), Probabilistic earthquake location in 3D and layered models, *Advances in seismic event location*, 101-134 pp., Kluwer Acad., Norwell, Mass.

Lomax, A., and A. Curtis (2001), Fast, probabilistic earthquake location in 3D models using Oct-Tree Importance sampling, *Geophys. Res. Abstr*., 3.

Love, J.D., J.C. Reed Jr., R.L. Christiansen, and J.R. Stacey (1973), Geologic block diagram and tectonic history of the Teton region, Wyoming-Idaho: U.S. Geological Surv., Map I-730.

Love, J.D. (1989), Yellowstone and Grand Teton National Parks and middle Rocky Mountains, International Geological Congress Guidebook t328, *Am. Geophys. Un*., 93.

Love, J. D., J. C. Reed Jr., and A.C. Christiansen (1992), Geologic map of Grand Teton National Park, Teton County, Wyoming, scale 1:62,500, *U.S. Geol. Surv. Misc. Invest. Ser*., Map I-2031.

Matter, F. (2005), High-Precision relocation of earthquake swarms at the Yellowstone caldera, Diploma Thesis, ETH Zurich, Switzerland.

Mogi, K. (1963), Some discussions on aftershocks, foreshocks and earthquake swarms – The fracture of a semi-infinite body caused by an inner stress origin and its relation to the earthquake phenomena, 3, Bull. *Earthquake Res. Inst. Tokyo Univ*., *41*, 615-658.

Moser, T.J., T. van Eck, and G. Nolet (1992), Hypocenter determination in strongly heterogeneous earth models using the shortest path method, *J. Geophys. Res,. 97*, 6563-6572.

O'Connell, D.R.H., C.K. Wood, D.A. Ostenna, L. Block, and R.L. LaForge (2003), Ground Motion Evaluation for Jackson Lake Dam Minidoka Project, Wyoming, Final Report, Report 2003-2, Seismotectonics and Geophysics Group, Technical Service Center, Bureau of Reclamation, Denver, Colorado.

Pavlis, H.G., and J.R. Booker (1980), The mixed discrete-continuous inverse problem: Application to the simultaneous determination of earthquake hypocenters and velocity structure, *J. Geophys. Res.*, *85*, 4801-4810.

Pechmann, J.C., J.C. Bernier, S.J. Nava, F.M. Terra, and W.J. Arabasz (2001), Correction of systematic time-dependent coda magnitude errors in the Utah and Yellowstone National Park region earthquake catalogs, 1981-2001, *EOS, Trans. Am. Geophys. Union, 82*, F809.

Reasenberg, P. (1985), Second-order moment of central California seismicity, 1969-1982, *J. Geophys. Res., 90*, 5479-5495.

Reasenberg, P., and D. Oppenheimer (1985), FPFIT, FPPLOT and FPPAGE: FORTRAN computer programs for calculating and displaying earthquake fault-plane solutions, *U.S. Geol. Surv. Open-File Report*, 85-739.

Richins, W.D., J.C. Pechmann, R.B. Smith, C.J. Langer, S.K. Goter, J.E. Zollweg, and J.J. King (1987), The 1983 Borah Peak, Idaho, earthquake and its aftershocks, *Bull. Seis. Soc. Am*., *77*, 694-723.

Roberts, S. V., and D. W. Burbank (1993), Uplifted and thermal history of the Teton Range defined by apatite fission-track dating, northwestern Wyoming, *Earth Planet. Sci. Lett*., *118*, 295-309.

Rowe, C.A., R.C. Aster, B. Borchers, and Young (2002), An automatic, adaptive algorithm for refining phase picks in large seismic data set, *Bull. Seismol. Soc. Am*., *92*, 1660-1674.

Rowe, C.A. 2000, Correlation-based phase pick correction and similar earthquake family identification in large seismic waveform catalogs, PhD thesis, New Mexico Institute of Mining and Technology, Socorro.

Rubin, A.M., and D. Gillard (1998), Dike-induced earthquakes: Theoretical considerations, *J. Geophys. Res., 103*, 10017-10030.

Smith, R.B., and M.L. Sbar (1974), Contemporary tectonics and seismicity of the western United States with emphasis on the Intermountain Seismic Belt, *Bull. Geol. Soc. Amer*., *85,* 8, 1205-1218.

Smith, R.B., J.R. Pelton, and J.D. Love (1976), Seismicity and the possibility of earthquake related landslides in the Teton-Gros Ventre-Jackson Hole area, Wyoming, *Contributions to Wyoming Geology, 14*, 57-64.

Smith, R.B., W.D. Richins, and D.I. Doser (1985), The Borah Peak earthquake: Seismicity, faulting kinematics and tectonic mechanism, in Workshop XXVII on "Evaluation of Regional and Urban Earthquake Hazards and Risk in Utah", *U.S. Geol. Survey Open-File Report*, 84-763, 73-112.

Smith, R.B. (1988), Seismicity and earthquake hazards of the Borah Peak-Hebgen Lake-Yellowstone-Teton region – Implications for earthquakes in extensional and active volcanic regimes, Abstracts with Programs, Ann. Meeting, *Geol. Soc. Amer*., A12.

Smith, R.B., R.E. Reilinger, C.M. Meertens, J.R. Hollis, S.R. Holdahl, D. Dzurisin, W.K. Gross, and E.E. Klingele (1989), What's moving at Yellowstone! The 1987 Crustal deformation survey from GPS, leveling, precision gravity and trilateration, Eos, *Amer. Geophys Union, 70*, 113-125.

Smith, R. B., J. O. D. Byrd, D. D. Susong, A. G. Sylvester, R. L. Bruhn , and J. Geissman (1990), An Evaluation of Earthquake Hazards of the Grand Teton National Park Emphasizing the Teton fault, Three Year Progress Report, prepared for the University of Wyoming-National Park Service Research Center, University of Wyoming, Laramie, Wyoming, 149.

Smith, R. B., and W. J. Arabasz, (1991), Seismicity of the Intermountain Seismic Belt, in D. B. Slemmons, E.R. Engdahl, M.D. Zoback, and D.D. Blackwell, editors "Decade Map vol. 1 Neotectonics of North America", *Geological Society of America*, 185-228, Boulder, Colo.

Smith, R. B., K. L. Pierce and R. J. Wold (1993a), Quaternary history and structure of Jackson Lake, Wyoming, from seismic reflection surveys, in A. W. Snoke, J. Steidtmann, and S. M. Roberts, editors "Geology of Wyoming", *Geological Survey of Wyoming Memoir No. 5*, 668-693.

Smith, R. B., J. O. D. Byrd and D. D. Susong (1993b), The Teton fault: Seismotectonics, Quaternary history and earthquake hazards, in A. W. Snoke, J. Steidtmann, and S. M. Roberts, editors "Geology of Wyoming", *Geological Survey of Wyoming Memoir No. 5*, 628-667.

Smith, R.B., and L.W. Braile (1994), The Yellowstone Hotspot, in D.P. Hill, P. Gasparini, S. McNutt, and H. Rymer, editors, *J. Volcanology and Geotherm. Research*, 61: 121-188.

Smith, R. B. and L. Siegel (2000), Windows Into the Earth: Geology of Yellowstone And Grand Teton Parks, *Oxford University Press*, 247.

Spudich, P., W.B. Joyner, A.G. Lindh, D.M. Boore, B.M. Margaris, and J.B. Fletcher (1999), SEA99-A revised ground motion prediction relation for use in extensional tectonic regimes, *Bull. Seismo. Society of America*, *89*, 1156-1170.

Susong, D.D., R.B. Smith, and R.L. Bruhn (1987), Quaternary faulting and segmentation of the Teton fault zone, Grand Teton National Park, Wyoming, Eos Transactions, *Amer. Geophys. Union, 68*, 1452.

Sylvester, A.G., Smith, R.B., Chang, W.C., J.O.D. Byrd, and C.H. Hitchcock (2004), Historic seismicity, geodetic evidence and possible mechanisms for observed interseismic stain of the Teton fault, Wyoming, system, *J. Geoph. Res.* (in preparation).

Tarantola, A., and B. Valette (1982), Inverse problems = Quest for information, *J. Geophys. Res*., *50*, 159-170.

Thurber, C.H. (1983), Earthquake locations and three-dimensional crustal structure in the Coyote Lake area, central California. *J. Geophys. Res*., *88*, 8226-8236.

Toomey, D.R., and G.R. Foulger (1989), Tomographic inversion of local earthquake data from the Hengill-Grensdalur central volcano complex, Iceland, *J. Geophys. Res*., *94*, 17497-17510.

Waite, G.P. (1999), Seismicity of the Yellowstone Plateau: space-time patterns and stresses from focal mechanism inversion, M.S. Thesis, University of Utah, Salt Lake City, UT.

Waite, G. P., and R. B. Smith (2004), Seismotectonics and stress field of the Yellowstone volcanic plateau from earthquake first-motions and other indicators, *J. Geoph. Res*, *109*, B02301, doi:10.1029/2003JB002675

Waldhauser, F., and W. L. Ellsworth (2000), A double-difference earthquake location algorithm: Method and application to the Northern Hayward Fault, California, *Bull. Seism. Soc. Am., 90***,** 1353-1368.

Waldhauser, F. (2001), hypoDD: A computer program to compute double-difference hypocenter locations, *U.S. Geol. Surv. Open File Rep., 01-113***,** 25.

Wiemer, S., and R.F. Zuniga (1994), ZMAP- a software package to analyze seismicity, *Eos Trans. AGU, 75*, 456.

Wong, I.G., S.S. Olig, and M. Dober (2000), Preliminary probabilistic seismic hazard analyses: Island Park, Grassy Lake, Jackson Lake, Palisades, and Ririe Dams, U.S. Department of the Interior, Bureau of Reclamation, Denver, Colorado.

Wood, C. (1988), Seismicity of the Teton region, Wyoming and Idaho; Perspective from a newly installed telemetered network, *Abs. Prog., Geol. Soc. Amer*., *20*, A14.

Zelt, C.A. (1998), Lateral velocity resolution from three-dimensional seismic refraction data, *Geophys. J. Int*., *135*, 1101-1112.

Zoback, M.L. (1992), First and second-order patterns of stress in the lithosphere: The World Stress Map Project, *J. Geophys. Res*., *97*, 11703-11728.